Review

Controlling Mineral Morphologies and Structures in Biological and Synthetic Systems

Fiona C. Meldrum, and Helmut Co#lfen

Chem. Rev., **2008**, 108 (11), 4332-4432 • DOI: 10.1021/cr8002856 • Publication Date (Web): 12 November 2008

Controlling Mineral Morphologies and Structures in Biological and Synthetic Systems

Fiona C. Meldrum*,† and Helmut Cölfen*,‡

School of Chemistry, Cantock's Close, University of Bristol, Bristol BS8 1TS, United Kingdom, and Max Planck Institute of Colloids and Interfaces, Colloid Chemistry, Am Mühlenberg, Forschungscampus Golm, D-14424 Potsdam, Germany

Received April 10, 2008

Contents

* To whom correspondence should be addressed. E-mail: Coelfen@mpikg.mpg.de, Fiona.Meldrum@bristol.ac.uk.
† University of Bristol.
‡ Max Planck Institute of Colloids and Interfaces.

1. Introduction

The unique and frequently beautiful morphologies that characterize many biominerals have long been a source of fascination. While research began by looking first at individual organisms and attempting to unravel the mechanisms by which their component minerals are produced, more recent times have seen efforts to replicate key fabrication strategies and structural features into materials design. Loosely grouping biominerals into three broad classifications provides a convenient basis for considering their morphological design. Amorphous minerals are the material of

10.1021/cr8002856 CCC: $71.00
Published on Web 11/12/2008

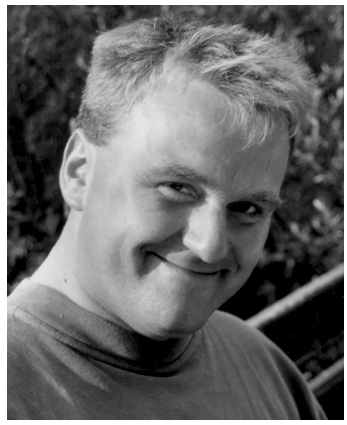

Helmut Cölfen studied Chemistry at the University Duisburg and completed his Ph.D. in Physical Chemistry in 1993 supervised by Werner Borchard. After a Postdoc at the National Centre for Macromolecular Hydrodynamics in Nottingham with Stephen Harding, he joined the Max-Planck-Institute of Colloids and Interfaces in 1995 and finished his habilitation on "Biomimetic Mineralization" in 2001 with Markus Antonietti. He is now private docent at the University of Potsdam and is employed as senior scientist and head of the analytical service in the Colloid Chemistry department of the MPI. His current research is focussed on Biomimetic Mineralization and Non-Classical Crystallization as well as Analytical Ultracentrifugation. His hobby is music in a band.

Fiona Meldrum completed her Ph.D. in 1992 and subsequently carried out a Postdoc with Janos Fendler at the University of Syracuse, U.S.A., from 1992 to 1994. She then held a Humboldt Research Fellowship at the MPI Polymerforschung, Mainz, Germany, in the group of Wolfgang Knoll from 1994 to 1996 and a research fellowship in the Department of Applied Mathematics, the Australian National University, Canberra, Australia, from 1996 to 1998. Fiona then returned to the U.K. in 1998 where she joined the Department of Chemistry, Queen Mary, University of London. She moved to the School of Chemistry, University of Bristol, in 2003, where she is currently a Reader. Her current research focuses on Bio-Inspired Mineralization, with particular interests in controlling crystal morphologies and crystallization in confinement.

choice for many of the most morphologically exotic biominerals, such as the silicaceous diatoms and radiolaria. With no preferred form, an amorphous material can be readily molded to give the desired product shape. Polycrystalline biominerals also exhibit a wide range of morphologies, and it is again intuitive that small crystalline building blocks can be organized to give complex forms. Our final category of biominerals, the single crystals, is perhaps the most intriguing. The term "single crystal" immediately suggests a geometric object defined by regular, planar faces, where the external form is a reflection of the internal symmetry of the crystal lattice. Biology, in contrast, can yield single crystals whose morphologies bear no relation to their crystallographic structure. Under biological control, a rhombohedral calcite crystal becomes bicontinuous and spongelike in morphology when produced as the skeletal plates of echinoderms, or curved with rounded surfaces in sponge spicules.

When writing an article describing biomineral morphologies, it is impossible to proceed without giving due consideration to D'Arcy Thompson's "*On Growth and Form*".[1] First published in 1917, this work looks to the disciplines of zoology and mathematics to rationalize the physical form adopted by biological structures. We will restrict ourselves here to a brief glimpse of Thompson's views on the formation of spicules and spicular skeletons, the morphologies of which he attributes to the physical forces acting on them during growth. These biominerals were considered to precipitate in an environment defined by contact between an assembly of cells or vesicles, the form of which depended on factors such as the packing and relative surface tensions of adjacent cells. Although no discussion of heredity or genetics was made in these arguments, which recognize that the structure and composition of the system vary and develop with time, this certainly does not entirely negate Thompson's ideas as the activities of genes are themselves governed by physical forces. Indeed, a combination of the ideas of genetics, with consideration of the physical forces inherent to the system, which could, for example, lead to self-assembly of a precursor matrix, may be necessary to construct a complete picture of morphogenesis.[2−4]

This paper provides a review of the general strategies used to control mineral morphologies, placing particular emphasis on biologically relevant minerals and minerals precipitated under biomimetic conditions. The article is structured into three major sections, beginning in section 2 with a discussion of the principal strategies that can be used to control the morphologies of amorphous and crystalline materials. Biominerals provide a wonderful demonstration of how mineral morphologies can be modified under ambient conditions to produce some truly remarkable forms, and section 3 will examine the biological strategies applied to achieve this. Finally, section 4 describes the application of biomimetic pathways to the formation of minerals with controlled morphologies. Within each of these sections, the morphological controls of amorphous, polycrystalline, and single-crystal solids are addressed separately. While some overlap is inevitable between these topics, separation of the discussion into their three main areas facilitates a comprehensive discussion of potential strategies for controlling mineral morphologies.

Morphological control of minerals is potentially an enormous topic, and as such, some selectivity over the material covered has had to be made. This has principally been achieved by placing particular emphasis on calcium carbonate and silica systems and illustrating with other materials where it was considered appropriate. Calcium carbonate provides an excellent example for illustrating morphogenesis strategies of single-crystal and polycrystalline materials. It is one of the most widely studied biominerals, because of both its high abundance and rich polymorphism, and it has been widely used as a model mineral in biomimetic experiments, leading to increased understanding of the mechanisms of biogenic control over mineral polymorph, orientation, and morphology. Providing a suitable example for illustrating morphogenesis strategies applicable to amorphous minerals, silica is of similar importance to calcium carbonate as a biomineral. It has also been used extensively for the synthesis of materials with complex shapes, with the advantage that its amorphous structure readily adapts to the form of any mold. Given that the volume of literature

concerning silica precipitation—and in particular the formation of porous materials—is so extensive, this article considers only general strategies used for the morphology control of silica minerals and does not address the large field of liquid-crystal-templated mesoporous silicas.

In summary, this article serves to demonstrate how study of the formation of biominerals, and indeed structural investigation of these materials, can lead to the development of new synthetic strategies for controlling mineral morphologies. For example, recent investigations of the mechanisms operative in biological calcification have shown that calcium carbonate deposition frequently occurs via an amorphous precursor rather than by direct ion-by-ion growth.[5−8] This route has been successfully applied to controlling crystal morphologies in vitro.[9−13] Further, in producing crystalline minerals with remarkable forms, and in particular single crystals with noncrystallographic morphologies, biology demonstrates the enormous range of crystal morphologies that it is possible to produce under ambient synthetic conditions. Indeed, faced with the spongelike form of sea urchin skeletal elements, which Thompson describes "as though... carved out of a solid crystal",[1] there has been much discussion about whether these structures are indeed single crystals of calcite or polycrystalline arrays.[14−17] Biology, therefore, demonstrates that we have many preconceived ideas about crystal morphologies and, in doing so, provides us with a precedent and indeed inspiration for crystalline structures that we may hope to achieve synthetically.

2. Overview of Crystal Growth and Morphological and Crystal-Structure Control

Before the various morphogenesis strategies for crystals and amorphous minerals are discussed, some general aspects should be recalled, which underlie all precipitation processes. Precipitation starts from dissolved atoms or molecules or, in the case of salts, from different ions. The thermodynamic driving force for the formation of a new phase is the supersaturation of the solution. This treatment is usually used in classical crystallization theory, but the general assumptions are also valid for amorphous phases.

The relative supersaturation S is defined as a dimensionless ratio of the actual concentration of the species c, divided by its equilibrium molecular solubility product k_{sp} under the given set of conditions:

$$S = \frac{c}{k_{sp}} \tag{1}$$

In the case of multiple species involved in crystallization, as for example in ionic crystals, c is the product of the concentrations of the individual components (or, more correctly, the activity product). It is important to note that the above definition of supersaturation preassumes the nature of the final precipitate, as its molecular solubility product is needed for the calculation of S. If a species, e.g., calcium carbonate, exists in five different crystalline polymorphs and at least one amorphous species, one and the same initial ion concentration can mean different supersaturations depending on which species is precipitated as a result of the different solubilities of amorphous matter and different crystalline polymorphs. These differences in supersaturation can be rather large—at least between a relatively much better soluble amorphous phase and crystalline polymorphs. Often, amorphous precursor phases are formed in a crystallization reaction, but if they are overlooked, the calculation of the supersaturation and, with it, of the driving force for the crystallization reaction will be wrong. This driving force is the change of the chemical potential and, thus, the free enthalpy (eq 2) of the crystallization reaction.

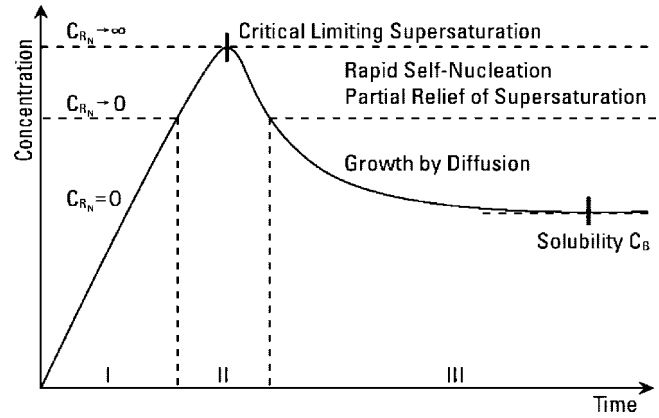

Figure 1. Schematic representation of the concentration of molecularly dissulfed sulfur before and after nucleation as a function of time. C_{R_N} is the concentration for a given nucleation rate R_N. Reprinted from ref 18. Copyright 1950 American Chemical Society.

$$\mu_2 - \mu_1 = \Delta\mu = -kT \ln S \tag{2}$$

with $\Delta\mu$ = change in the chemical potential during phase transformation of a phase with the chemical potential μ_1 into the new phase with the chemical potential μ_2, k = Boltzmann constant, and T = thermodynamic temperature.

Figure 1 presents the classical 1950 La-Mer curve for the crystallization behavior of sulfur in ethanol,[18] which can, however, also be considered for any precipitation reaction. Here, a reaction is linearly increasing the amount of sulfur, until a critical supersaturation is reached, and particles spontaneously form thereafter. Therefore, the sulfur concentration decreases again, until finally $S = 1$ or the equilibrium solubility is reached. If the time of the nucleation burst is short, nuclei of uniform size can be obtained, which is often desired in colloid synthesis.

Once supersaturated (i.e., $S > 1$), the primary particles can grow from solution but need a nucleus to grow from. In heterogeneous nucleation, surfaces or dispersed components, such as dust particles or crystal seeds, provide the starting point for the crystallization event. Heterogeneous nucleation is less energetically demanding and becomes relevant when the other options are kinetically excluded. The reason for this is that, for the formation of a new particle, energy is consumed for the generation of the new surface with the solution, whereas energy is gained in the form of bulk energy of the particle (e.g., lattice energy for crystal nuclei). Because a surface is already present in heterogeneous nucleation, the surface energy term will be decreased and, with it, the energy demand for nucleation. This strategy can be very advantageously applied for the defined nucleation of a new face on a chemically tailored surface. In homogeneous nucleation, on the other hand, the nucleus forms spontaneously from the solution itself when a critical supersaturation is reached. Usually, a short nucleation burst is desired, as this will maintain that all nucleated particles have the same size (Figure 1), before they grow further by diffusion.

These very basic concepts are valid for all precipitation reactions. However, already at the stage of the first precipitated product, the further morphogenesis pathways will diverge and,

with them, the strategy to obtain a defined and controlled morphology. The first big distinction certainly has to be made between crystalline and amorphous matter. The latter is unordered and, therefore, isotropic. Such a phase can, therefore, be molded into any shape by a suitable template and is, thus, highly advantageous for templating strategies. Examples are amorphous silica and other metal oxides from sol−gel reactions but also amorphous phases of ionic crystals like $CaCO_3$. Single crystals, on the other hand, are highly ordered, and therefore, their vectorial properties are anisotropic because of different packing motifs along different directions. This makes templating approaches more difficult, but adsorption of additives can be achieved in a face-selective way for these materials. This will lower the energy of the covered faces, which will lead to their expression. As a result, the crystal morphology can be tuned in this approach based on slow crystallization under thermodynamic control.

In addition to these two extremes, there are a wide variety of alternative routes to morphogenesis. These possibilities exploit polycrystalline matter. Nanoparticles can aggregate, which is a well-known and usually undesired phenomenon and can be avoided by particle stabilization. Nanoparticle matter can also be templated in a process similar to ceramic processing by molding and subsequent sintering. Nanoparticles are small compared to microscopic or macroscopic templates, and an assembly of these particles can, therefore, be constructed that adopts the form of the template. However, there are a variety of interactions possible between nanoparticles and additives or already between anisotropic nanoparticles themselves. This can allow for control of their self-assembly, which can be tuned in many ways. The important difference to the above-mentioned templating or face-selective additive adsorption approaches for morphology control is that the final morphology is not (yet) predictable just from the choice of the components. Although a self-assembly process can certainly be coded by face-selective additive adsorption onto a nanocrystal, there are usually several structural levels involved in such processes and certainly synergetic effects can also take place.

Interactions between nanoparticles and with a matrix may even lead to their orientation into crystalline registry. In such a case, they may fuse together to form a homogeneous single crystal. As nanoparticles can be molded into complex shapes, and many of the self-assembled nanoparticle superstructures are highly complex, the single crystals formed by crystallite fusion from such mutually oriented crystallites will adopt the gross shape of the precursor particle. This is the process of so-called "nonclassical crystallization", as single crystals formed via this pathway are always formed from precursor nanoparticles, which is mutually oriented into crystalline register before fusion into the larger single crystal. Usually, the morphogenesis pathways involving polycrystalline matter do not take place in the slow thermodynamically controlled regime but are fast and kinetically controlled. This is a reason why the crystal shape of such superstructures is much more difficult to predict. Further, due to multiple levels of hierarchy, these structures are also difficult to access by computer models.

2.1. Single-Crystal, Definition, Classical and Nonclassical Concepts

An ideal single crystal, or a "monocrystal", is a crystalline solid in which the crystal lattice of the entire sample is continuous and unbroken to the edges of the sample, with no grain boundaries. Because of a variety of entropic effects on the microstructure of solids, including the distorting effects of impurities and the mobility of crystallographic defects and dislocations, single crystals of meaningful size are exceedingly rare in nature and can also be difficult to produce in the laboratory. A single crystal has a rigid lattice of molecules, atoms, or ions in a characteristic location for the crystal with the unit cell as its smallest repeat unit. [19] Because of the regularity of its internal structure, a single crystal has a characteristic shape with smooth surfaces parallel to atomic planes in the lattice. Therefore, defined angles exist between the external faces as expressed in the law of constant interfacial angles, stating that the angles between corresponding faces of all crystals of a given substance and polymorph are constant.

This definition of a crystal describes single crystals as solid bodies with a defined geometrical outer surface characterized by smooth, planar faces. However, as we shall see in the following paragraphs, it is quite possible to template single crystals with curved surfaces, and such morphologies are characteristic of many biominerals. This already contradicts the classical picture of a single crystal. In the introductory discussion, it became evident that the classical definition of a crystal is seldom valid. Much more common is a disturbed growth of a crystal with the associated lattice imperfections. This is apparent in a reduction of the coherence lengths of the crystalline domains, which can be measured via peak broadening of an X-ray diffractogram with high quality beams of a synchrotron light source.[20,21] It is, however, difficult to distinguish a single crystal from a polycrystal with nanocrystal building units in crystallographic register. Such a crystal is termed a "mesocrystal" (abbreviation for "mesoscopically structured crystal"; see also section 2.1.3). Both of these crystal types exhibit a single crystal diffraction pattern and cannot be distinguished from each other simply by diffraction because the domain spread of both structures can be very low. The coherence length can, however, vary largely. Thus, the problem arises as to how to distinguish a single crystal from a mesocrystal or polycrystal. This is demonstrated in Figure 2. All three shown structures exhibit diffraction patterns with single spots without a considerable domain spread, which would be evident as arcs in the diffraction pattern.

However, only Figure 2 (left) is in agreement with the classical definition of a single crystal. The coherence length of geological calcite single crystals with the typical rhombohedral shape is indeed very high with 800 nm and a domain spread of only 0.003°.[21,24] The sponge spicule (Figure 2 (center)) is curved but nevertheless has a coherence length of 130 nm, and the domain spread is still very low with 0.07°. The calcite mesocrystal (Figure 2 (right)) has the lowest coherence length of 60−80 nm, and the nanocrystalline building units can be observed in electron microscopy.[22] The latter two crystals do not agree with the facetted shape of a single crystal, although they behave as such in diffraction experiments. In view of these difficulties, a practical definition of a single crystal can only be made via its diffraction behavior: *A single crystal is a solid body with a large coherence length, which shows a diffraction behavior characteristic of a perfect three-dimensional alignment of its building units.*

It is, nevertheless, difficult to define a strict boundary between a single and mesocrystalline substance on the basis of the coherence length, as structure of these materials can clearly vary in a continuous manner. An example of such a

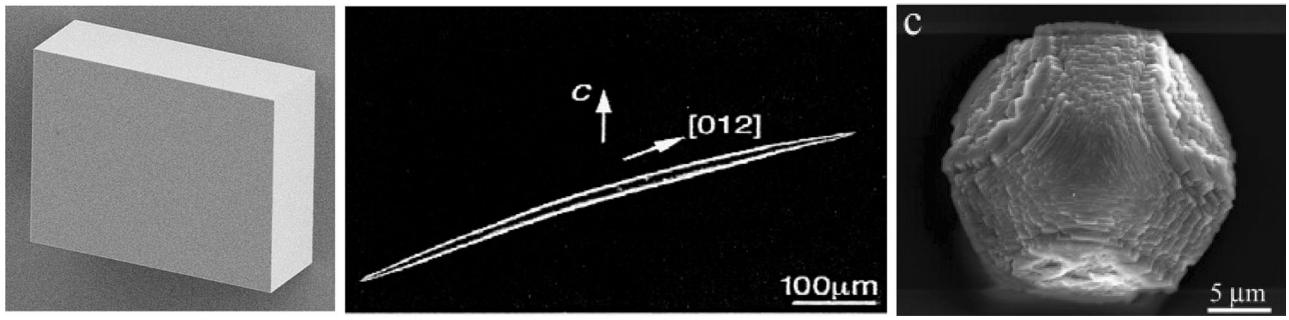

Figure 2. (Left) Synthetically grown calcite single crystal; (Center) curved monaxon spicule of the sponge Sycon; and (Right) synthetic calcite mesocrystal. Reprinted with permission from refs 22 and 23. Copyright 2007 American Chemical Society and 2008 John Wiley & Sons.

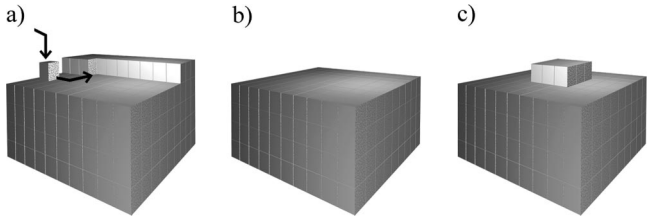

Figure 3. Ideal layer-by-layer crystal growth: (a) migration of a unit toward a kink on the surface, (b) completed layer, and (c) surface nucleation. Reprinted with permission from ref 19. Copyright 2001 Butterworth-Heinemann at Oxford.

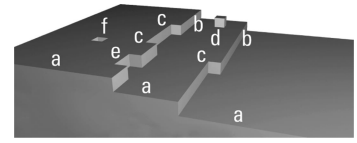

Figure 4. Kossel's model of a growing crystal surface showing (a) flat surfaces, (b) steps, (c) kinks, (d) surface adsorbed growth units, (e) edge vacancies, and (f) surface vacancies. Reprinted with permission from ref 19. Copyright 2001 Butterworth-Heinemann at Oxford.

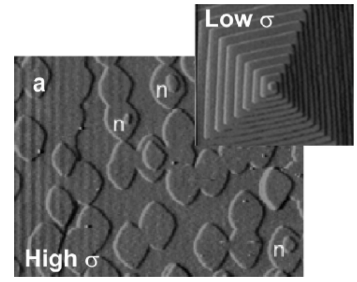

Figure 5. AFM images showing examples of 2D nucleation at high supersaturation for calcite. σ is the supersaturation in this image. At low supersaturation, the layer-by-layer growth and a screw dislocation are evident. Reprinted with permission from ref 32. Copyright 2003 Mineralogical Society of America.

borderline case could be the sponge spicule in Figure 2 (center). However, if nanocrystalline building units can be observed in electron microscopy, the structure is a mesocrystal. For a single crystal, the coherence length is, on the other hand, more defined via defects and not grain boundaries of nanoparticle subunits as in the case of a mesocrystal (for more details on mesocrystals, see section 2.1.3). This definition shows that a mesocrystal can satisfy the definition of a single crystal but that the converse cannot hold true.

2.1.1. Crystal Growth under Thermodynamic and Kinetic Control and Equilibrium Morphologies

In the classical picture of crystallization, the flat surfaces of a crystal grow via layer-by-layer adsorption of solute atoms or molecules onto an existing crystal face, as was originally suggested by Volmer.[25] When an atom/molecule arrives at the crystal surface from solution, it is not immediately integrated into the crystal lattice but is able to migrate on the crystal surface in two dimensions. These units form the so-called adsorption layer with a typical thickness of about 1 nm.[19] The migrating units on the crystal surface become integrated into the crystal lattice at "active centers" where the attraction of the moving units to the lattice is greatest. These are steps and kinks on the growth surface (Figure 3a). The attachment of a growth unit to a kink is the most favored scenario so that the kink moves along the step until it is completed and a new step is started.

The nucleation of a new layer starts from surface nucleation of an island on the plane face (Figure 3c), which grows further by attachment of further atoms/ions to the steps and kinks of the new layer until the surface is completed (Figure 3b). This layer-by-layer growth mode of a crystal surface is expressed in the model of Kossel (Figure 4).[26]

However, the growth of a surface is rarely perfect, and a number of imperfections exist in the form of vacancies (parts e and f of Figure 4) or dislocations, with screw dislocations being a particularly important example. In addition, even at equilibrium, the steps have kinks due to thermally activated detachment of molecules from the steps onto either the step edges or the terraces or even back into solution.[27−29] Consequently, the step edges are not static; molecules are constantly attaching and detaching, even at equilibrium.[30,31] As a consequence, growth steps are not as ideal as implied by the Kossel model but are fuzzy. Growing crystal surfaces can nowadays be very favorably imaged by scanning-force microscopy (SFM), while the growing layers can be depicted with high resolution (Figure 5, low *S*). In a similar manner, the surface nucleation in the form of islands (Figure 3c) at high *S* can be imaged using SFM, as shown in Figure 5, high *S*. These different growth conditions can already lead to deviations from the equilibrium morphology for a crystal, as the system does not have time to equilibrate. However, these kinetic morphologies are difficult to control via the reaction conditions.

Under equilibrium conditions, the micro- and macroshape of single crystals is related to the intrinsic structure of the unit cell, and the crystal shape can reflect the unit-cell replication and amplification. However, the crystal morphology often varies significantly from the shape of the unit cell. From a thermodynamic viewpoint, the diverse crystal morphologies of the same mineral are due to the differences in surface energies of the crystal faces, which in turn are dependent on the external growth environment, as revealed early last century by Wulff.[33] Generally speaking, the growth

rate of a crystal face is usually directly related to its surface energy if the same growth mechanism acts on each face. Faces that have high surface energies will grow quickly, have small surface areas, or vanish completely upon crystal growth to the final morphology. Faces with low surface energies will grow slowly and dominate the final shape. This treatment assumes that the equilibrium morphology of a crystal is defined by its minimum surface free energy, which can be calculated as the sum of the products of surface energy and surface area of all exposed faces (Wulff's rule).[33]

$$\sum_i \gamma_i A_i = F_S \tag{3}$$

with γ_i = surface energy of the surface i, A_i = area of surface i, and F_S = surface free energy.

Generally, the interface energy of a crystal surface results from its unsaturated, "dangling" surface bonds, minus the interaction of the crystal surface with the surrounding medium, such as solvation or hydration in the case of a liquid medium. As a rule of thumb and for isotropic structures, the surface "bond strength" (summarizing, ionic, van-der-Waals, and all secondary interactions without a detailed molecular picture) can be estimated from the cohesion energy of the material, as is, for instance, revealed from the evaporation energy ΔE_{vap} or the Hildebrandt solubility parameter δ ($\delta^2 \approx \Delta E_{vap}$). The surface tension γ then can be approximately calculated from the molar cohesion energy by dividing with the area demand per molecule (derivation analogous to that in ref 34),

$$\gamma = \frac{\Delta E_{vap}}{2 N_A A_{mol}} \tag{4}$$

with N_A = Avogadro's number and A_{mol} = cross section per molecule.

Surface tension in this picture is the strength of dangling bonds per unit area. It is obvious that very polarizable and high melting substances like ionic crystals have a high surface tension, while bare van der Waals solids like organic crystals have a lower surface energy. The strength of dangling bonds can be compensated for by secondary interactions with the solvent, which are especially strong for very polar surfaces and water as a solvent. Again, the change of the surface energy $\Delta\gamma$ with a solvent or additive can be estimated from its molar free energy of adsorption ΔE_{ads}.

$$\Delta\gamma = \frac{\Delta E_{ads}}{N_A A_{mol}} \tag{5}$$

Molecularly, the adsorption process can also be illustrated as a partial saturation of the surface bonds of the crystal, e.g., by ions with the opposite charge or coordinative bonding in the case of metals. This formal, nonmolecular, but illustrative picture of surface tension does not reflect the complexity and multiplicity of chemical bonding. In addition, effects such as surface reconstruction (i.e., formation of a structure deviating from the bulk structure) or surface roughness to minimize the mutual interactions are not considered. In the case of anisotropic structures (and all crystals are anisotropic by definition), faces and their surface behavior can be very different. For crystals, we can find ionic faces (with an excess charge), electrically neutral but dipolar faces, highly polarizable faces, or simple hydrophobic faces, with all of them having a different surface energy, potentially existing in one and the same chemical crystal system. This is demonstrated in Figure 6.

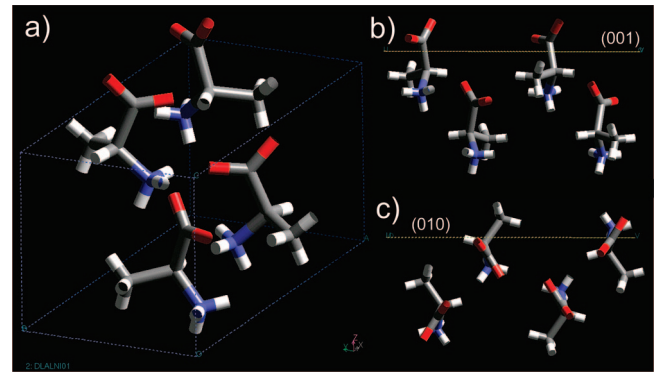

Figure 6. (a) DL-Alanine unit cell: C = gray, O = red, N = blue, and H = white. (b) (001) surface cut of DL-alanine (yellow dashed line) showing that (001) is a charged face. (c) (010) surface cut of DL-alanine (yellow dashed line) showing that this face is hydrophobic, electrically neutral, but dipolar and polarizable. Reprinted with permission from ref 23. Copyright 2008 John Wiley & Sons.

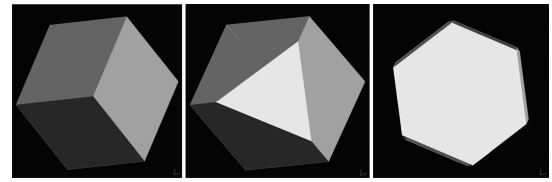

Figure 7. Change of the rhombohedral equilibrium $CaCO_3$ morphology with six exposed {104} faces (gray) by lowering the surface energy of the {001} faces (white). The morphology change from rhomboeder to a hexagonal platelet is evident and is maintained just by face-selective interface energy decrease of the two {001} faces. Images modeled with Cerius[2] (Accelrys).

According to Wulff's rule, the shape of crystals will be affected by changing the surface energy of the surfaces. If this can be done in a face-selective way, the equilibrium morphology of a crystal can be tuned in a defined and predictable way. For this, various additives, i.e., inorganic ions or organic additives, can be used, as can the solvent/solvent mixture itself (for more details, see section 2.1.2). This strategy of crystal morphogenesis has been recognized for a long time and has even found industrial application mainly based on empirical observations. The change of the equilibrium shape of a $CaCO_3$ crystal due to the lowering of the surface energy of the charged high-energy (001) face is illustrated in the schematic sequence in Figure 7.

An experimental manifestation of Wulff's rule can be obtained from the reconstruction of high-energy crystal faces in a good solvent. This is shown for the case of calcite in water.[35] The calcite (001) and (012) faces are high-energy surfaces because they are the most polar calcite surfaces. Such faces can be generated in high quality with solid surface templates, but surface reconstruction is to be expected from the thermodynamic viewpoint in the absence of surface-stabilizing additives.[35] Indeed, the surface reconstruction can be followed by scanning-force microscopy (SFM) when the (012) surfaces were put into deionized water for different times (Figure 8, upper). The mean roughness of the surfaces at the start of the experiment is 1.1 nm. It was found that, after 30 min, the mean roughness had increased to 5.7 nm, while after 2 h, the surfaces were very rough and composed of neutral (104) surface spikes with characteristic shape. Obviously, it is energetically more favorable to expose larger

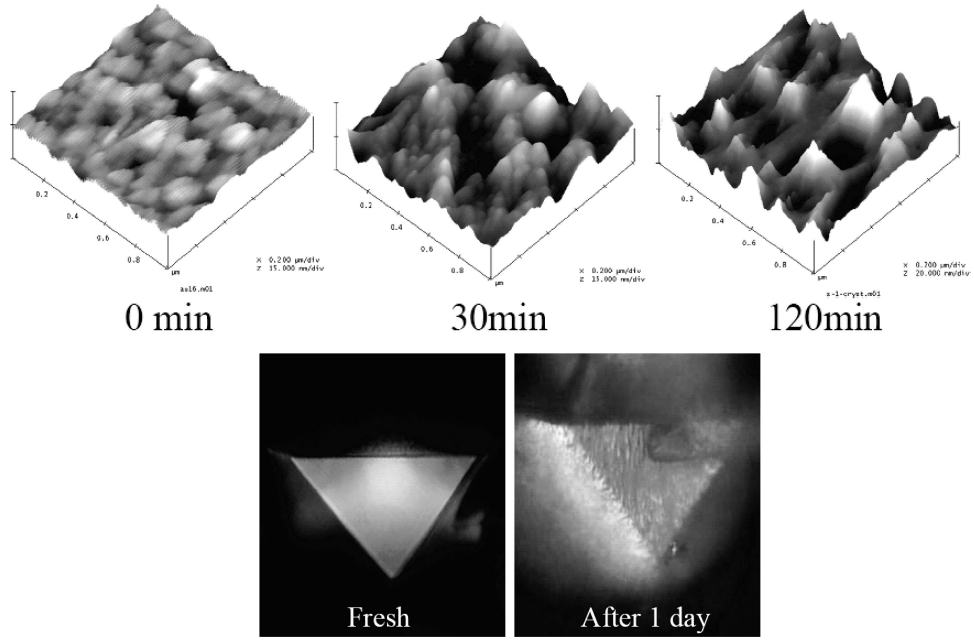

Figure 8. (Upper) Time-dependent SFM-imaging of calcite (012) surfaces (1×1 μm^2). Note that the zero point corresponds to the beginning of the measurement and not the beginning of exposure of the calcite surface to water. (Lower) Surface reconstruction of a calcite (012) surface observed with polarized light microscopy. Reprinted with permission from ref 35. Copyright 2008 American Chemical Society.

areas of a (104) sawtooth pattern than a flat (012) face. (Figure 8, upper, surface roughness = 95 nm). The reconstruction of the (012) to the (104) faces is so pronounced that its final stages are visible with a light microscope (Figure 8, lower). If the same experiment is repeated in the poor solvent ethanol, no reconstruction of the (012) surface was observed, which shows that the surface reconstruction of high-energy faces indeed is related to the solvent.

It is well-known that the purely thermodynamic equilibrium treatment based on Wulff's rule does not predict the experimentally found crystal morphologies in all cases. This is because crystallization and the resulting morphologies are often kinetically dominated, and defect structures like screw dislocations or kinks have a special importance for the dynamics of crystal growth. Nevertheless, Wulff's rule provides a good basis for understanding additive-based crystal morphology changes from a fundamental viewpoint, and it is especially helpful to explain changes of crystal morphology if an additive is selectively adsorbed on only one family of crystal faces.

Kinetic control can also express itself in crystal morphologies and architectures. Control of the kinetics of crystallization can result in the formation of different polymorphs, which can themselves have different characteristic morphologies. In general, kinetic polymorph control is based predominantly on the modification of the activation-energy barriers of nucleation, growth, and phase transformation (Figure 9).[37] In such cases, crystallization is often a sequential process involving structural and compositional modifications rather than a single-step pathway.[8,36,38,39] Intermediate particles have multiple possibilities for further reaction including dissolution-recrystallization, aggregation, solid-phase transformation, or other mesoscopic transformations, which allow for multiple possibilities for the control of mineral shape as will be discussed further in this review. The kinetic cascade displayed in Figure 9 is a manifestation of Wolfgang Ostwald's "step rule". This rule allows an empirical prediction of the sequence of formed phases in a

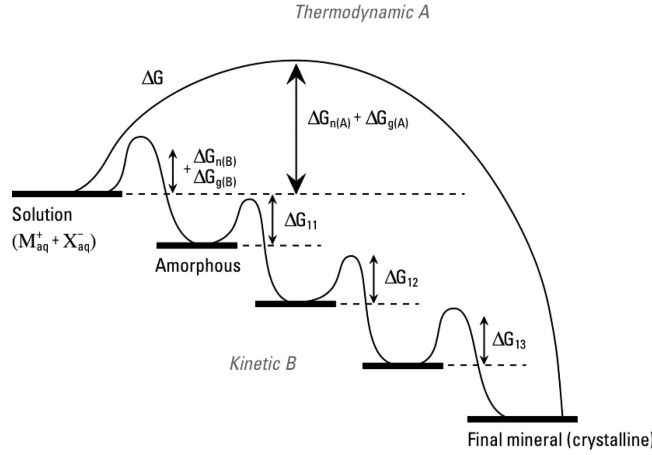

Figure 9. Simplified scheme of the crystallization pathways under thermodynamic and kinetic control. Whether a system follows a one-step route to the final mineral phase (pathway A) or proceeds by sequential precipitation (pathway B) depends on the free energy of activation associated with nucleation (n) and growth (g). Reprinted with permission from ref 36. Copyright 2003 Wiley-VCH.

crystallization event. Usually, the least dense phase is formed first and transforms to the next dense phase, until finally, the most dense phase, which is usually also the most stable phase, is formed. This kinetic transformation sequence is strictly in order of increasing thermodynamic stability. All possible polymorphs do not usually appear along such lines.

Polymorph transformations following the Ostwald step rule for $CaCO_3$ are first nucleated as the metastable spherical vaterite polymorph, and then transform gradually into the stable rhombohedral calcite polymorph.[40] Note that the third anhydrous polymorph, aragonite, is not observed along this sequence, as it is notoriously hard to nucleate.

The stabilities of the intermediate products and their transformation to the next stable species according to Ostwald's step rule depends on the solubility of the minerals

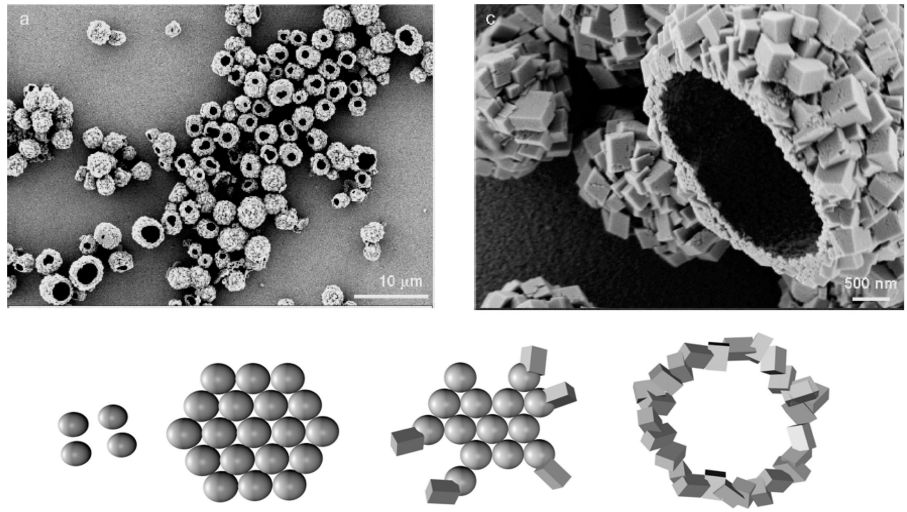

Figure 10. Hollow spherical metastable vaterite aggregates transform into hollow stable aggregates of calcite rhombohedra by a dissolution−recrystallization process in the presence of a block copolymer.[41] The growth sequence is the formation of vaterite nanoparticles (upper left), which form spherical aggregates (upper right). These aggregates partly dissolve and calcite rhombohedra are nucleated on the surface of the vaterite aggregate. After the sacrificial vaterite aggregate is completely dissolved, a hollow sphere composed of calcite rhombohedra is formed (lower image). Reprinted with permission from ref 41. Copyright 2003 American Chemical Society.

and on the free energies of activation of nucleation in different environments. All of these factors can be strongly influenced by additives. The corresponding changes in composition and structure usually occur by dissolution-renucleation processes. This can be exploited for morphogenesis. If sufficient nucleation centers are provided on the dissolving metastable phase, it can be used as a template to nucleate the stable phase on a sacrificial metastable phase. One example of this controlled mineralization strategy is the formation of calcite hollow spheres grown around sacrificial vaterite spheres (Figure 10).[41] Similar results were reported by Mann et al., where hollow vaterite spheres were synthesized using amorphous $CaCO_3$ spheres generated in the presence of poly(styrene sulfonate), as precursor materials.[42]

Kinetic control of crystallization can be achieved by a high supersaturation promoting a rapid particle nucleation of the kinetically favored crystal modification according to Ostwald's step rule or by modifying the interactions of nuclei and developing crystals with solid surfaces and soluble molecules.[43] Kinetically driven crystallization, especially at high supersaturations, most often involves an initial amorphous phase that may be nonstoichiometric, hydrated, and susceptible to rapid phase transformation. Amorphous calcium carbonate (ACC), for instance, is in general highly soluble, has a low density of almost half of the crystalline mineral, which indicates a high level of hydration,[44] and rapidly transforms to calcite, vaterite, or aragonite unless kinetically stabilized. ACC is used as precursor in biomineral formation but can also be exploited in kinetically controlled synthesis of crystals. In biomineralization, a significant number of stabilized ACC biominerals are now documented, including plant cystoliths,[45,46] snail shells,[47] aragonitic mollusk shells,[7,48] nacre,[49] ascidian spicules,[50−52] precursors of the carbonated apatite inner tooth layer of chitons,[53] and crustacean exoskeletons.[54]

An effective medium for controlled mineralization are gels, as they provide a matrix that reduces the rate of ion transport by decreased diffusion as compared to the bulk solution. This enables a reduction and control of the nucleation rate as well as suppression of convection, leading to large, defect-free single crystals.[55−58] If sufficiently slow ion transport to the growth sites can be maintained, thermodynamic control and crystal growth under equilibrium conditions or with kinetic control under near equilibrium conditions can be achieved.[58] The advantage of gel systems is that their cross-linking density and, hence, the associated rate of ion diffusion in the gel medium can be adjusted. At a high cross-linking density, the formation of diffusion-limited morphologies including skeletal, dendritic, and branched forms can be observed.[58] Also, other complex morphologies and periodic precipitation in the form of Liesegang rings can be observed—especially if the gel interacts with the mineral.[59−62] Figure 11 schematically shows the effect of the gel density respective supersaturation onto the formed crystal morphologies. Densification of the gel matrix decreases the diffusion rate, builds up a diffusion field making growing surfaces unstable, and, thus, promotes the formation of irregularly branched polycrystalline aggregates. Theoretical studies have also indicated that a decrease in the diffusivity changes the morphology of a diffusion-limited aggregate from an anisotropic shape into an irregularly branching pattern.[63] Control of ion diffusion thus leads to the observed morphology sequence from polyhedral to dendritic forms with decreasing order, as schematically shown in Figure 11. Therefore, control of reactant diffusion not only can switch between thermodynamic and kinetic control but also can control a branching of structures as well as the aggregation of nanoparticles. The above considerations show that it is extremely important to consider which crystallization pathway will operate as defined by selection of the experimental conditions and additives, as this can in turn determine the product crystal morphologies.

2.1.2. Thermodynamic Control: Additives—Organic and Inorganic

To achieve thermodynamic control over a crystallization reaction and to allow for the classical crystallization pathway with layer-by-layer growth, a low supersaturation has to be chosen to avoid polynucleation and kinetic control. When controlling crystal morphologies using additives under a thermodynamic regime, it is also important that the concentration of additives is low, as high additive concentrations will lead to a surface coverage of the growing nucleus and,

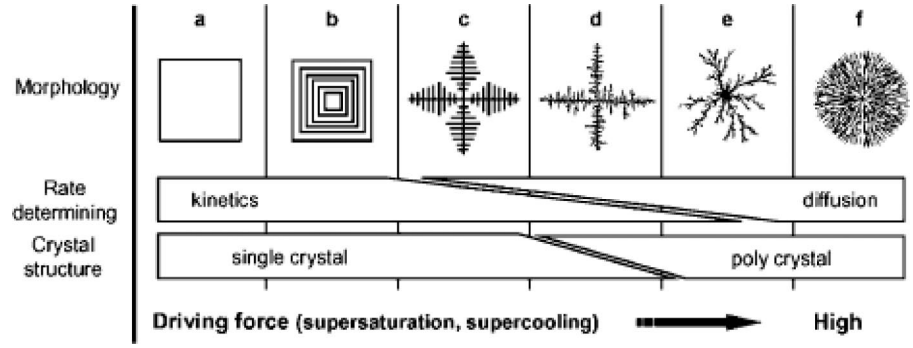

Figure 11. Schematic model of morphological evolution with an increase in the driving force: (a) polyhedral form produced in the kinetic-controlled system near equilibrium, (b) skeletal morphology by the Berg effect, (c) single-crystalline ordered dendrite with crystallographic symmetry, (d) partially disordered dendrite having a single-crystalline ordered trunk and disordered polycrystalline side branches, (e) disordered polycrystalline dendrite as shown in diffusion-limited aggregation, and (f) dense branching morphology. Reprinted with permission from ref 58. Copyright 2003 American Chemical Society.

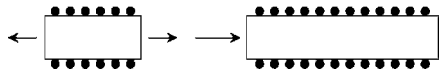

Figure 12. Adsorption of an additive (filled circles) onto a crystal surface lowers its surface energy and, thus, its growth rate. The crystal predominantly grows at the uncovered faces. Reprinted with permission from ref 23. Copyright 2008 John Wiley & Sons.

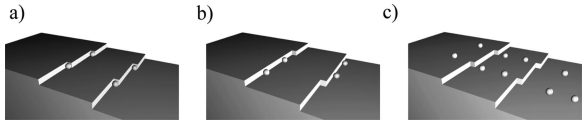

Figure 13. Sites for impurity adsorption on a growing crystal based on the Kossel model: (a) kink, (b) step, and (c) surface after additive adsorption.[64] Reprinted with permission from ref 19. Copyright 2001 Butterworth-Heinemann at Oxford.

therefore, a quenching of its growth. In order to achieve modification of crystal morphologies, in this way the additives must selectively adsorb to certain faces only, such that the surface energies of this family of faces only is reduced. This behavior will be expressed in modification of the equilibrium crystal morphology, as expressed by Wulff's rule. Wulff's rule can also be applied if all outer faces are identical or influenced by the additive in a similar fashion. Because the growth rate is related to the surface energy of the system, the overall crystal growth rate is reduced, which leads to much finer particles. This is why most recipes using strongly adhering additives, e.g., surfactants or ligands, result in stable nanoparticles, which can be accessed as such. Figure 12 shows the effect of additives upon the crystal morphology when selectively adsorbed only onto two crystal faces. Only the uncovered faces with their higher surface energies will now grow (Figure 12).

It is, however, not necessary to cover an entire surface with additives to block its further growth. The layer-by-layer growth of a single crystal according to Kossel's model[26] (Figure 4) has important consequences for the effect of additives onto the growth of a crystal face. Additives can adsorb at various sites of the growing crystal as shown in Figure 13 and both lower the surface energy of the crystal face and inhibit step edges from further growth. The influence of an additive onto crystallization is, therefore, both thermodynamic and kinetic in character.

Additive adsorption to steps or kinks has the direct result that adsorption of even tiny quantities of an additive can retard or even block the growth of a complete crystal surface, as shown in Figure 13. This effect will be expressed in the final morphology of the single crystal. An example of

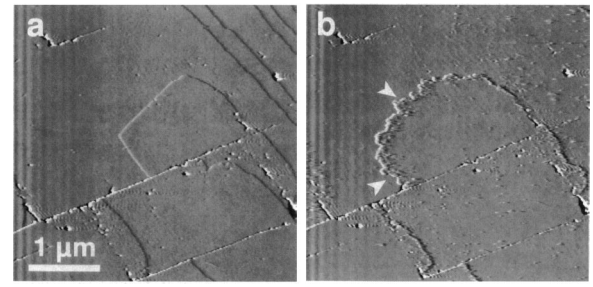

Figure 14. (a) Calcite (104) surface without proteins. Light gray and dark gray lines are obtuse and acute step edges, respectively. Step edges are generally straight and smooth, with sharp corners. Some kinks are visible in the acute step edges in the upper right corner. (b) Calcite surface with proteins. Step edges have become rounded (suggesting an isotropic step edge speed) and more convoluted. The step edge appears highlighted, as by a raised lip of proteins. Strong white-and-black features (that are identical in (a) and (b)) are defects in the crystal that can act as barriers to step-edge motion. Conditions: pH 8.1, 2 μg/mL proteins, flow rate = 4 μL/s, 9.3 s/image, contact mode. Reprinted with permission from ref 66. Copyright Biophysical Society.

proteins adsorbing to the step edges of a growing calcite (104) surface is illustrated in Figure 14. It can be seen that the step edges become rounded, which is equivalent to a macroscopic habit modification of a crystal by additive adsorption. On the other hand, adsorbed additives can also nucleate the growth of new layers as found for the protein perlucin.[65] The nucleation of new layers will also modify the macroscopic crystal morphology.

If the growth of the face is not completely blocked, the additives can become incorporated into the crystal after they are overgrown by subsequent layers. This can be nicely demonstrated for the case of polymer latexes, which are functionalized to adsorb onto certain crystal faces so that they get incorporated into the crystals.[67,68] Once removed from the crystal by dissolution or calcination, a porous crystal with "Swiss cheese" morphology is obtained, which clearly shows the inclusion of the latex additive as shown in Figure 15.

2.1.3. Kinetic Control: Aggregation/Oriented Attachment/Mesocrystals

In contrast to thermodynamic crystallization control, where classical crystallization ideas are used to consider crystal growth under low reactant and additive concentrations, kinetic control becomes increasingly important with increasing reactant and additive concentrations. At high supersatu-

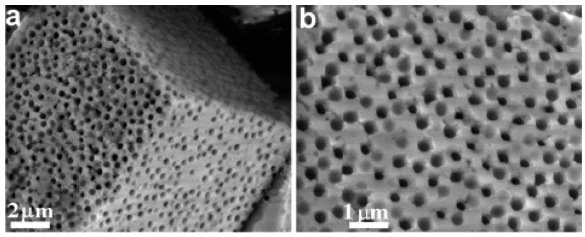

Figure 15. Scanning electron microscopy (SEM) images of $CaCO_3$ particles with porous surface obtained by templating and tetrahydrofuran (THF) extraction of P(St-MMA-AA) latex particles with a size of 380 nm (a, b). Image reproduced with permission from ref 68. Copyright 2005 American Chemical Society.

rations, the driving force for precipitation is high, and kinetic crystal forms are usually the first precipitated species according to Ostwald's step rule shown in Figure 9. This can be an emulsionlike structure in the case of $CaCO_3$, which decomposes to nanoparticles.[69] Because of the high supersaturation of the precipitating material, many crystal nuclei can form and grow to nanoparticles. As a result, aggregation-based pathways become important for the kinetically controlled regime, where single nucleation events drive the formation of single crystals under thermodynamic control. This aggregation can be hindered if high concentrations of a stabilizing additive are applied, leading to the formation of nanoparticle dispersions. This case of stabilized nanoparticles is of less interest in the context of this review. On the other hand, additives can adsorb onto specific faces of nanocrystals, thus coding for a subsequent aggregation process. This case is of considerable interest for the morphological control of crystalline structures. If the nanoparticles self-assemble in a way that they adopt a mutual orientation in crystallographic register, they can potentially fuse crystallographically under the elimination of two neighboring crystal surfaces. This can lead to single crystals. As this crystallization pathway toward single crystals is based on nanoparticles rather than on atomic or molecular building units as in the classical crystallization mechanism, such particle-based crystallization pathways are called "nonclassical crystallization".

Nonclassical crystallization is a concept that has been developed in the past few years, as reviewed in articles.[70,71] It was driven by experimental evidence that showed that several crystallization reactions can obviously not be understood on the basis of classical crystallization schemes. Processes of nanoparticle aggregation, self-assembly, and final mesoscopic transformations, which incorporate all restructuring processes taking place on a length scale of between 1 and 1000 nm, therefore nicely complement the classical picture of crystal growth via ions, atoms, or molecules. Examples of crystallization processes that can only be interpreted in terms of nonclassical crystallization are as follows:

• Formation of intermediary clusters or phase separation to liquid precursors as the primary building blocks;

• Crystallization via amorphous intermediates involving transient amorphous building blocks, which can undergo mesoscopic transformations;

• Oriented attachment of nanoparticulate building blocks, i.e., the directed aggregation of nanoparticles with possible subsequent crystallographic fusion of high-energy crystal faces; and

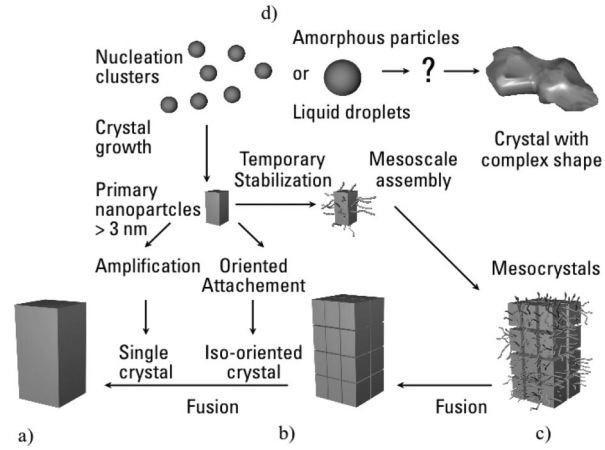

Figure 16. Schematic representation of classical and nonclassical crystallization. Pathway (a) represents the classical crystallization pathway where nucleation clusters form and grow until they reach the size of the critical crystal nucleus growing to a primary nanoparticle, which is amplified to a single crystal (path a). The primary nanoparticles can also arrange to form an iso-oriented crystal, where the nanocrystalline building units can crystallographically lock in and fuse to form a single crystal (oriented attachment, path b). If the primary nanoparticles get covered by a polymer or other additive before they undergo a mesoscale assembly, they can form a mesocrystal (path c). Note: Mesocrystals can even form from pure nanoparticles. There is also the possibility that amorphous particles are formed, which can transform before or after their assembly to complicated morphologies (symbolized by the question mark in path d). Reprinted with permission from ref 23. Copyright 2008 John Wiley & Sons.

• Mesocrystallization involving the 3D self-organization of nanoparticles in crystallographic register to a highly ordered mesostructure.

This list is likely to be far from complete as particle-based crystallization pathways are an emerging research topic. Figure 16 schematically illustrates these processes and links them with the classical picture of crystallization.

From Figure 16, it becomes clear that several products of nonclassical crystallization mechanisms have a transient character and that they evolve to the product structure via mesoscopic transformations. The particle-mediated nonclassical crystallization path makes crystallization practically independent of ion products or molecular solubility; it can occur without pH or osmotic pressure change in the crystallization medium and opens new spatiotemporal strategies for crystal morphogenesis. This is possible because the precursor particles can be formed independently even at different locations (i.e., in a different flask) and can be stored and transported to the locus of mineralization/crystallization, keeping this site unaffected from precipitation effects (elevated ion concentrations or pH changes). Nanoparticles can also undergo self-assembly to superstructures long after the molecular supersaturation has dropped to 1, so that no crystallization is to be expected according to the classical nucleation picture.[72,73] It is obvious that those benefits make nanoparticle-mediated nonclassical crystallization especially relevant for biological systems. However, the precursor particle-mediated nonclassical crystallization pathways are difficult to detect because they are often only of a transient nature.

2.1.3.1. Oriented Attachment. Primary nanoparticles can spontaneously self-organize to a superstructure with a common crystallographic orientation. This is the process of oriented attachment (Figure 16b). In this mechanism, nano-

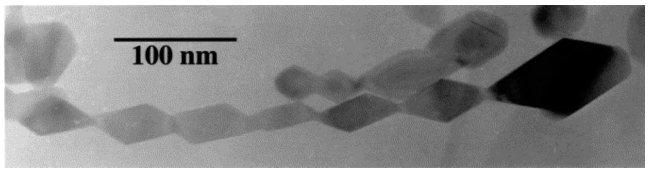

Figure 17. Transmission electron microscopy (TEM) micrograph of a single crystal of anatase that was hydrothermally coarsened in 0.001 M HCl, showing that the primary particles align, dock, and fuse to form oriented chain structures. Reprinted with permission from ref 74. Copyright 1999 Elsevier Science Publishers.

particles aggregate first but still have the possibility of retaining their mutual orientation. When the particles come into crystallographic register with high-energy faces, they can fuse and eliminate these faces.

The first experimental observations of this unconventional coarsening behavior and morphology evolution were of nanocrystalline titania prepared under hydrothermal conditions.[74,75] This work has stimulated many other observations and finally led to the formulation of the oriented-attachment mechanism. This mechanism, which is kinetically second order in the number of primary particles,[76,77] describes the spontaneous self-organization of adjacent particles with a common crystallographic orientation. Crystallographic fusion of these particles then occurs at a planar high-energy interface, leading to the formation of single crystals with unusual morphologies, as shown in Figure 17. This model makes it clear that nanoparticle alignment has many similarities to a controlled polymerization process, where the defined nanoparticles take the role of the organic monomers. This similarity between controlled assembly and controlled polymerization has also been stressed by other authors.[77,78] Controlled nucleation or initiation in a short period of time sets the base of a process that is terminated by the depletion of material or external stimuli, such as electric fields or curvature or stress fields.

Oriented attachment is particularly relevant in the nanocrystalline regime. With relatively high specific surface areas, bonding between the particles allows the system to win a substantial amount of energy by eliminating two high-energy surfaces by crystallographic fusion[79,80] and by increasing the system entropy due to displacement of molecules adsorbed on the previous fusing surfaces. There are, in principle, two main ways to achieve the mutual orientation of the nanoparticles. One is an effective collision of particles with mutual orientation, while the second is coalescence induced by particle rotation in weakly coagulated samples where the nanoparticles still have rotational freedom.[81] The particle fusion process can happen in an appropriate intermediate interaction region. The colloidal stabilization of the particles has to be so weak that two nanoparticles can approach each other within the primary minimum where they mutually attract by van der Waals forces. However, the flexibility and dynamics must still be high enough to rearrange to the low-energy configuration represented by a coherent particle−particle interface.[79] This "weak attraction" leads to crystallographic fusion of the two particles, eliminating the two high-energy surfaces.

The decrease in system energy upon particle alignment has been calculated by Read and Shockley in their classic paper[82] and was found to be in good agreement with earlier experimental results by Dunn and Lionetti.[83] Their results show a very rapid rise of energy with increasing angle between grain boundaries in the range of 0°−15°, which reaches almost the maximum relative system energy ε. Crystals with an angular mismatch of more than 15° have practically the same energy as randomly oriented polycrystals. Below 10°, a huge thermodynamic driving force is exerted to drive particle alignment into crystallographic register as long as the particles are still mobile enough to rotate and correct their positions. The meaning of this curve is that particles that collide in random orientation at an arbitrary angle must have the possibility to wiggle around until eventually a lattice mismatch angle $<15°$ is reached. If this is the case, the large thermodynamic driving force will perfectly align the particles in crystallographic register. For practical mineralization conditions, this means that a low ionic strength favors the oriented aggregation. It supports electrostatic repulsion by maintaining a more extended electric double layer and gives the particles time to mutually align before they are cemented together. This could indeed be demonstrated for calcite rhombohedra, which were found to align in crystallographic register at a low ionic strength, whereas upon salt addition, the aggregation was random.[84]

This metastability of colloidal particles can be controlled not only according to the reaction conditions but also by addition of appropriate quantities of additive, i.e., a stabilizer or controlled aggregation agents, termed the "assembler". A step in this direction was reported for the surface functionalization of stable titania nanoparticles with low-molecular-weight ligands (the "assembler"), which predetermine the assembly behavior of the nanoparticles. Anatase nanoparticles with diameters of about 3 nm were coated with various multidentate ligands.[85,86] Upon redispersion in water and reversible deprotection of specific surfaces by refluxing at elevated temperatures, the nanoparticles self-organized into pearl-necklace structures several hundreds of nanometers in total length.

The oriented-attachment mechanism can also be advantageously used for the fabrication of defect-free one-dimensional single crystals. Such fibers can be up to hundreds on nanometers long if appropriate additives are used.[73] The reason for the formation of defect-free single crystals in the presence of additives is the face-selective polymer adsorption onto a small nanocrystal. Face-selective additive adsorption can also be used to form nanofibers according to Wulff's rule. However, if there are voids in the polymer adsorption, branching can occur, which becomes more likely the longer the fibrous structures get.[87] This complication can be avoided by the oriented-aggregation mechanism.

Oriented attachment is not only described for the zero- to one-dimensional case (Figure 18a)[88,89] and the one-dimensional case (Figure 18b)[90] but can also occur in two dimensions (Figure 18c)[89,91,92] and three-dimensional cases (Figure 18 parts d and e),[93,94] as schematically shown in Figure 18. Some examples will now be provided to illustrate the application of oriented-attachment processes to the development of more exotic morphologies. CdS particles in the form of rings were formed from the assembly of CdS (wurtzite) nanoparticles, each of which has an intrinsic hexagonal symmetry.[95] After selectively stabilizing the {001} planes with a suitable additive, hexagonal building units with six equal chances to attach to neighboring crystallites are obtained, and they can arrange to form ring patterns by oriented attachment of the side faces of the hexagonal platelets.[95] These rings show single crystalline diffraction pattern, indicating perfect orientation of the building units.

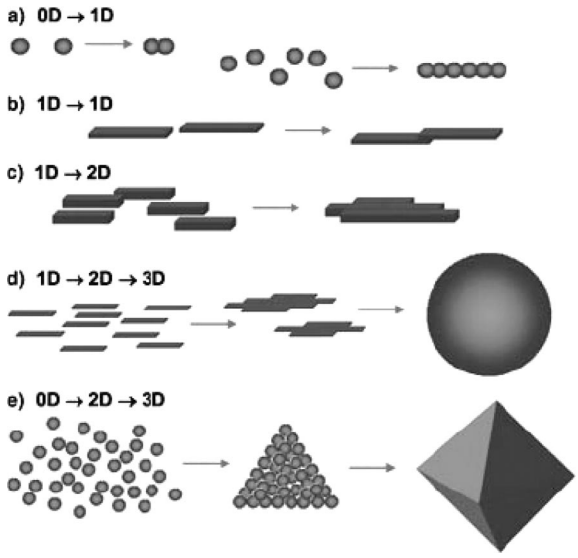

Figure 18. Various organizing schemes for self-construction of nanostructures by oriented attachment. Reprinted with permission from ref 93. Copyright 2004 Wiley-VCH.

This suggests that oriented attachment can also be used in a defined way for multifunctional building units.

Such a strategy was recently applied to the synthesis of hollow cones of ZnO in a hydrothermal process.[96] The formation process starts with the assembly of a hexagonal base ring followed by upward growth, which constructs the sloped wall. Finally, a top closure is added to the tube structure, resulting in a hollow cone with one open end. Oriented attachment can also be combined with a template to direct the oriented-attachment process, as recently reported by Yu and co-workers.[97] Reduction of SeO_2 with ethylene alcohol in the presence of cellulose acetate in a solvothermal reaction yielded selenium rods. Reduced Se was initially adsorbed on the celluloseacetate fibers, and directed anisotropic Se growth and oriented attachment then occurred along the fiber template to give the product raftlike organic−inorganic superstructures containing very crystalline Se nanowires. Oriented attachment was also reported for the case of heterostructures of the crystallographically similar SnO_2 and TiO_2 systems.[98] This example shows that the oriented-attachment mechanism can also be applied to a mixture of particles, providing that the nanoparticles are crystallographically similar.

The list of clearly identified cases of oriented attachment is ever-increasing in length and comprises a variety of chemical systems such as TiO_2,[74,85,86,88] FeOOH,[99−101] Co_3O_4,[102] CuO,[94,103] CoOOH,[104] SnO_2,[81] CeO_2,[105,106] Ag,[107] ZnO,[89] ZnS,[76,108] $CaCO_3$,[91,109] PbSe,[110] and Pt[111] $Cd(OH)_2$/CdO.[112] A large number of examples have also recently been summarized in some excellent review papers.[70,77,113]

2.1.3.2. Mesocrystals. The term "mesocrystal" is an abbreviation for "mesoscopically structured crystal". Mesocrystals are colloidal crystals that are built up from individual nanocrystals. The nanocrystals are aligned in a common crystallographic register (see also Figure 16c) such that the mesocrystal scatters X-rays or electrons like a single crystal and shows birefringence properties characteristic of a single crystal.[114] A mesocrystal can be molded into any outer shape, including novel engulfing symmetries, which are not encoded by the unit cell or even curvature. It is possible that this definition of a mesocrystal may be somewhat too strict, as recently, a continuous transition between a mesocrystal and a polycrystalline aggregate with unordered building units was observed if the building units rotate out of crystallographic register.[22] A detailed discussion is beyond the scope of this review, and the above mesocrystal definition is useful to define most of the mesocrystals discussed here.

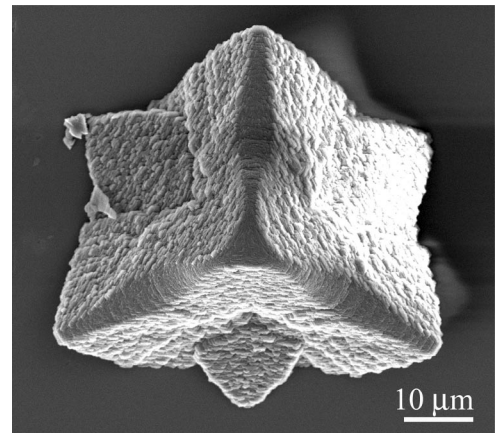

Figure 19. Calcium carbonate crystal precipitated from a solution containing 1 mM Ca and PEO_{22}−$PNaStS_{49}$ at a concentration such that the [Ca]/[S] molar ratio was 1.25:1. For further details about these mesocrystals, see ref 22. Copyright 2007 Dr. Fiona Meldrum.

Mesocrystals are a very interesting generalization of colloidal crystals, as they extend the well-recognized class of colloidal crystals formed from monodisperse, spherical tectons to those constructed from nonspherical building units. Further, these units can also show considerable polydispersity in size and shape, which offers significant new possibilities in terms of superstructure formation. It is clear that nonspherical nanoparticle building units with structural multiplicity should provide additional opportunities for self-assembly, as a LEGO-kit with more than one structural element simply has a higher flexibility of construction.

Figure 19 depicts a nice example of a calcite mesocrystal, which appears to be composed of two twinned tetrahedra, slotted into each other. It is obvious that such a morphology cannot be generated for a calcite single crystal with its typical rhombohedral shape (see Figure 2), and the rough surfaces clearly show the nanoparticle building units. These nanoparticle building units must possess a low interfacial tension toward the mother liquor (in this case, with a stabilizing block copolymer), which is a mandatory prerequisite for their existence. Higher interfacial energies lead to high colloidal attraction, rapid flow of the separation layer, and crystallographic fusion of the mutually aligned nanoparticles to a coherent single crystal. These product crystals do, however, carry a memory of their nucleation and surface recrystallization from a mesostructure as they are often hollow, boxlike, and still partly filled with a particulate material. It is very likely that mesocrystals are far more common than currently assumed, and that they are often mistaken for classic single crystals because of difficulties with detection and the fact that their morphologies and diffraction patterns can be practically identical to classic single crystals.[114] Literature evidence for mesocrystals is, therefore, mainly indirect, and in many cases, mesocrystals are not recognized as such.

In most practical cases of crystallization, the speed of the crystallization events immediately makes the classical picture of molecule- or ion-mediated crystallization unrealistic. For example, Rieger et al. have proven that particle formation from highly supersaturated boehmite solutions is determined

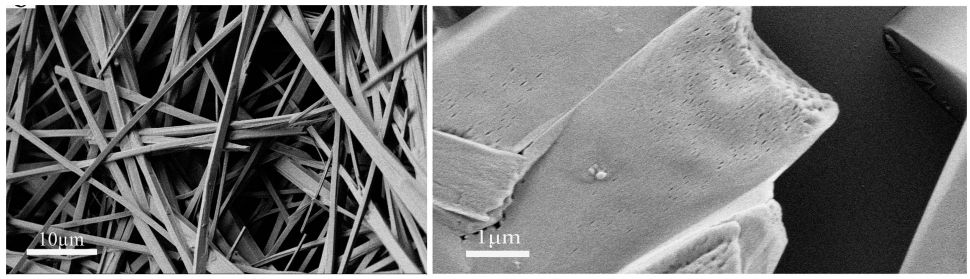

Figure 20. (Left) DL-Alanine single crystals derived at room temperature, pH 9.2, via molecular crystallization. (Right) DL-alanine mesocrystals obtained in saturated DL-alanine solution at room temperature for 5 h while the pH of the solution is 6.2. Reprinted with permission from ref 117. Copyright 2006 American Chemical Society.

by the mixing process, which is by orders of magnitudes too fast to be covered by the schemes of classical nucleation and growth theories.[115] Even in the crystallization of a mineral such as $BaSO_4$, which would generally be assumed to crystallize along classical crystallization pathways, there is strong experimental evidence that crystallization can also progress via organized mesoscale aggregation and alignment.[116]

Amino acids have been shown to provide excellent model systems for the study of the required conditions for mesocrystal formation and for the transformation of the mesocrystal to a single crystal. Here, the lattice energy of the organic crystals is lower than that of inorganic crystals, which decreases the driving force for crystallographic fusion and, therefore, enables the experimental observation of the mesocrystal intermediates. In addition, the solubility of amino acids can be varied easily not only by temperature variation but more importantly by pH changes. High supersaturations can, therefore, be reached quite rapidly, and mesocrystals can be formed in the absence of any directing or stabilizing additives. As demonstrated by conductivity experiments and light scattering, molecular supersaturation is realized quite rapidly, resulting in the formation of a metastable form of alanine, presumably as amorphous nanoparticles or liquid droplets.[117] These nanoparticles or liquid precursors then partly crystallize and grow to a mesocrystal via colloidal aggregation due to crystallization. Similar precursor particles have been found for several other systems, both experimentally[8,114,115,118,119] and theoretically.[120,121]

This crystallization pathway is in contrast to the single-crystal formation via charged molecular precursors that occurs in regimes of higher molecular solubility, at pH values deviating from the isoelectric point, or at higher temperature. However, too much undercooling, or quenching the system too far into thermodynamic instability, limits the lifetime of the amino acid mesocrystals. Although lower molecular solubility and a higher number of colloidal precursor particles are, in principle, even more supportive of a mesostructure process, the forces driving the recrystallization of the mesocrystal to a single crystal are also higher, thus making the mesocrystals short-lived intermediate objects, only. The final outcome of DL-alanine crystallization along the classical and mesocrystal pathway is shown in Figure 20. Single-crystal needles with smooth surfaces are the typical DL-alanine morphology and can be derived from the molecular crystallization pathway (Figure 20 (left)). In contrast, the coherent single crystal, which is formed from its mesocrystal precursor (Figure 20 (right)), displays smooth outer faces that are perforated with pores, resulting from previous voids in the mesocrystal. Further, a cross section through the crystal also reveals the nanoparticle subunits in the interior.

Formation of a coherent DL-alanine single crystal via its mesocrystal precursor took place on a time scale of several hours and was followed experimentally via small-angle neutron scattering (SANS).[122] Neutron scattering from particles of at least 1 micron in size showed a Q^{-3} power law behavior in the beginning, which is characteristic of porous structures with surface roughness, and then later a transition to Q^{-4} behavior, which is characteristic of a two-phase system with sharp interfaces. Thus, detection of this transition for the inner structure of the mesocrystal reveals elimination of grain boundaries and the flattening of the pore walls on the way to the final porous coherent single crystal.[122] This example definitively shows that a single crystal can be formed via a mesocrystal precursor. Mesocrystal formation inside a template with arbitrary shape can, therefore, lead to formation of a single crystal with this shape via a nonclassical crystallization pathway.

There are a number of different mechanisms of mesocrystal formation. They are discussed in detail elsewhere[23] but shall be briefly mentioned here to illustrate which mechanisms can be employed for mesocrystal formation. The simplest mechanism to form a mesocrystal is to fill nanosized compartments in an organic matrix with crystalline matter while the separated nanoparticles are oriented by the organic matrix. This (more static) matrix-mediated nanoparticle growth on a fibrous organic matrix was, for instance, suggested for the growth of corals.[123] Related to this is mesocrystal formation in a gel matrix, which can lead to orientation of the formed nanocrystallites. Nevertheless, the majority of known cases of mesocrystal formation originate from nanoparticles in solution, which aggregate and arrange in crystallographic order—even without any additives.

Currently, three principal possibilities are discussed in the literature that could account for the striking mutual 3D alignment of the nanocrystals in crystallographic register. These are illustrated in Figure 21. The first possibility requires the existence of ordering directional physical fields like electric, magnetic, or dipole fields, or possible polarization forces (Figure 21). The nanoparticles must be anisotropic with respect to their interaction potentials so that an ordering can take place. Such anisotropy could, for example, be oppositely charged counter faces on a crystal, a magnetic or dipole moment along one nanocrystal axis, or differences in the polarizability of different faces. The anisotropy could already be present in the nanocrystal itself[117,124] or be induced by face-selective additive adsorption.[125] In addition to physical fields with longer range, there are also contact forces and the above-discussed mechanism of oriented aggregation.

A second possibility for 3D nanoparticle alignment in crystallographic register is the formation of a crystallographic

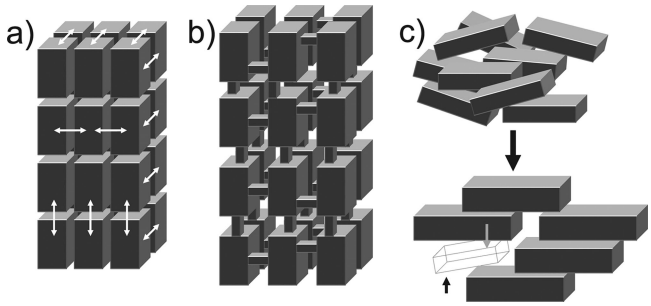

Figure 21. Three principal possibilities to explain the 3D mutual alignment of nanoparticles to a mesocrystal. (a) Nanoparticle alignment by physical fields or mutual alignment of identical crystal faces. The arrows indicate the mutual alignment by physical fields or the faces. (b) Epitaxial growth of a nanoparticle employing a mineral bridge connecting the two nanoparticles. (c) Nanoparticle alignment by spatial constraints. Upon growth of anisotropic nanoparticles in a constrained environment, the particles will align throughout growth according to the space restrictions as indicated by the open drawn particle in the arrangement of already grown particles in the lower image of (c). Reprinted with permission from ref 23. Copyright 2008 John Wiley & Sons.

connection between the so-called mineral bridges (Figure 21). This concept was first used to explain the mutual *c*-axis orientation of aragonite tablets in nacre, where some experimental evidence for the mineral bridges was given.[126] An assembly of crystals connected by mineral bridges would, in fact, be a coherent single crystal so that this concept is the most straightforward attempt to explain the mutual crystallographic orientation of nanocrystals. According to Oaki and Imai, formation of a mesocrystal with mineral bridges starts with the formation of nanocrystals.[127] Polymer adsorption onto the nanoparticle surface then quenches further growth. At this stage, mineral bridges can nucleate at the defect sites within the growth-inhibition layer on the nanocrystal, and a new nanocrystal grows on the mineral bridge. Its growth is again quenched by the polymer, new mineral bridges form, and the process is sequentially repeated until the mesocrystal is built up. It is, however, also possible that the mineral bridges form after the alignment of the nanoparticles in crystallographic register and that they act to permanently fix the mesocrystal structure.

An alternative to this additive-mediated formation of mineral bridges is the formation of crystallographically connected nanoparticles in a solid-state reaction from amorphous nanoparticle precursors. Amorphous nanoparticles are detected as precursor phases for many minerals—both bio- and biomimetic minerals (see sections 3 and 4). The density of amorphous particles is generally lower than that of the crystalline phases. This means that crystallization of an amorphous nanoparticle in an aggregate will lead to volume shrinkage. Nevertheless, its crystallization can induce the crystallization of adjacent nanoparticles, which will lead to a crystallographic connection in the form of a mineral bridge. Repetition of this process leads to a mesocrystal with crystallographically connected nanoparticle building units (see Figure 21b). The voids between the nanoparticles would originate from the volume shrinkage upon crystallization. Such mesocrystals can be expected to exhibit a high internal porosity. The mineral bridge concept can easily explain the crystallographic orientation of the nanocrystals in a mesocrystal, but mineral bridges of only a few nanometers in diameter are extremely difficult to detect experimentally from TEM thin cuts.[127] Nevertheless, they have been observed experimentally in a number of cases. [128−130]

The third possibility for the formation of mesocrystals is a simple geometric argument as outlined in Figure 21c. When crystalline nanoparticles grow and are not spherical in shape, simple entropic arguments (known from the Onsager theory of liquid crystallinity) can explain their alignment in a constrained reaction environment upon particle growth, as shown in Figure 21c for the transparent particle. The particles first crystallize into a relatively disordered and loose structure of crystalline nanoparticles. Upon further growth in a confined reaction space, they cross the critical volume fraction to form a lyotropic liquid crystal, and the structures mutually have to align. The higher the volume fraction, the higher is the entropic force driving the order parameter, and the more regular is the packing. This argument for mesocrystal formation just requires the presence of a constrained reaction environment with a constant influx of reactants. The constrained reaction environment can be a preformed cavity (such as a vesicle or gel) but can also be generated by the mutual attraction of first crystallizing particles to generate a packing for the alignment of further growing nanoparticles. It is possible that features of more than one of the above three principal possibilities can occur in the formation of a mesocrystal as found for the example of $(NH_4)_3PW_{12}O_{40}$ mesocrystals, which finally form so-called porous, spongelike crystals.[130]

There appear three different reaction pathways leading to the formation of mesocrystals from individual initially separated nanopaticles that depend on surface energy and interaction potentials of the primary nanoparticles: (a) nanocrystals with high surface energies and interaction potentials will undergo oriented alignment and crystallographic fusion, as the flow out of the liquid separation layers can be quite fast; (b) for surface energies in the intermediary region or medium-effective stabilizers, mineral bridges can form and fix the aligned nanoparticles toward a porous hybrid superstructure; or (c) binding of the surface layer is too strong or immobilized (such as for glassy amorphous surface layers) so that the aligned situation is thermodynamically or kinetically stable. In this case, the nanoparticles stay aligned but are separated and do not form a joint crystalline system.

Whether or not a mesocrystal is formed and can be observed thus depends on a number of factors like crystal symmetry and also the existence of different attractive and repulsive colloidal forces. The observation of a mesocrystal—at least as an intermediate—highly relies on a counterplay between long-range attractive and short-range repulsive forces. A considerable number of forces exist that can influence the mesocrystal formation process. Therefore, it appears that many of the mesocrystal-formation mechanisms reported to date are quite distinct.

2.1.4. Control of Reaction Conditions

The above section clearly demonstrates that reaction conditions are of great importance not only for selection of the crystallization pathway but also for determining the mechanism by which the final crystal will be formed and, therefore, how its morphology will be influenced. This was demonstrated for the crystallization of amino acids under different pH conditions. Other experimental variables, which are directly related to the supersaturation are reactant concentration, temperature, or pressure, as they determine the amount of dissolved species in solution. For $CaCO_3$, temperature and pressure dependence are manifested in

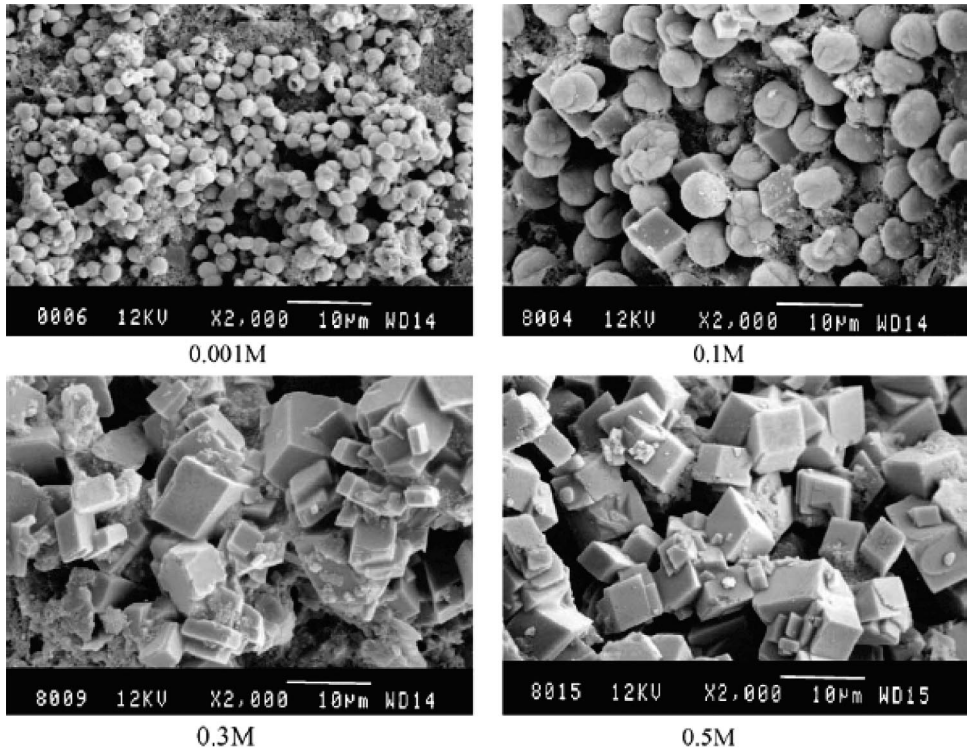

Figure 22. SEM images of $CaCO_3$ precipitated at different initial $CaCl_2$ concentrations. Note the constant scale bars. Reprinted with permission from ref 138. Copyright 2006 Elsevier Science Publishers.

crystallization techniques such as the Kitano method,[131] which relies on the carbonate−bicarbonate equilibrium for the supply of carbonate for $CaCO_3$ crystallization, and a recent variation of this method.[132] For both methods, the CO_2 partial pressure above the crystallizing solution is important in influencing the supersaturation, and therefore, the reaction is determined by temperature and pressure. Larger temperature and pressure variations can even change the precipitated polymorph according to the phase diagram of $CaCO_3$.[133−135] This will be discussed in further detail in section 2.1.5.

The importance of the experimental parameters in $CaCO_3$ crystallization was systematically studied for $CaCO_3$ crystallization via CO_2 bubbling into a $CaCl_2$ solution. The pH has a marked influence on the polymorph and morphology of the crystals produced.[136] With increasing pH, the precipitation time decreased and irregular vaterite aggregates were found (pH < 10), whereas at pH 9, spherical particles with different sizes were found.[136] If amorphous calcium carbonate (ACC) is prepared at different pH-values, as a precursor material for subsequent thermal $CaCO_3$ crystallization, the crystallization temperature increases strongly with the pH of the preparation from 480 to >600 K.[137] This is explained by an increased degree of atomic ordering of ACC with decreasing pH, although X-ray diffraction (XRD) does not show diffraction peaks. The increased order at the lower pH supports nucleation at a lower temperature.

The concentration of $CaCl_2$ has a significant influence on the morphology of the crystals formed because it determines the supersaturation (see Figure 22).[138] Vaterite particles (1−2 μm) are precipitated at low $CaCl_2$ concentrations, and the proportion of calcite and the size of the particles increases with an increase in the $CaCl_2$ concentration (Figure 22). Calcite formation is also favored at higher $[Ca^{2+}]/[CO_3^{2-}]$ ratios. Higher flow rates of CO_2 increased the amount of vaterite in the sample according to expectations, and a change from pure calcite to high vaterite yields could be achieved by simply varying the flow rate.[138] Increase of the temperature led to aragonite formation. Furthermore, other experimental factors including the bubbling time and stirring speed also showed a small influence on the morphologies of the finally derived crystals.[138] This example shows how many parameters must be considered in a crystallization reaction and how difficult it is to predict the morphology for a given set of experimental conditions. The influence of the experimental parameters can be much more subtle to control the crystallization pathway. Looking at a broader range of crystallization processes, redox chemistry can also play a role, as can catalysts such as enzymes and chemical decomposition of precursor molecules or a solvent mixture. Redox chemistry is especially valid for iron and other heavy metal minerals, as soluble Fe^{2+} salts can be (partly) oxidized to form sparingly soluble iron oxide minerals like magnetite, maghemite, akagenite, iron oxyhydroxide, ferrihydrite, and many others.[139] As this review focuses primarily on $CaCO_3$ and silica, this pathway will not be discussed in further detail here

Chemical decomposition of precursor species, possibly under the action of catalysts such as enzymes, is also sensitive to the experimental conditions—especially the pH and temperature. This is valid for both $CaCO_3$ and silica formation, which generally proceed via a polycondensation reaction and, therefore, a chemical reaction of precursor molecules. Decomposition of precursor molecules is widespread in several strategies for $CaCO_3$ crystallization. Probably the best known is the ammonium carbonate decomposition method, which is temperature dependent.[91] This is a commonly used crystallization method because it can be applied to small volumes of solution and it can yield high-quality $CaCO_3$ crystals. However, for each carbonate, two ammonia molecules are produced, which raises the pH of the crystallization solution with time. Significantly, ammonia

ions can act as an additive for $CaCO_3$ crystallization, influencing the polymorph and morphologies of the $CaCO_3$ crystals.[91] A similar solution composition can be expected if CO_2 is produced from urea by enzymatic decomposition with ureases, as here two moles of ammonia are also produced with each mole of carbon dioxide. Enzymes can also be used for the mineralization of $CaCO_3$ or silica in the absence of decomposition of precursor species. For $CaCO_3$, carbonic anhydrase is used in biomineralization processes to catalyze the formation of bicarbonate from dissolved carbon dioxide, and it acts with one of the fastest reaction rates of all enzymes.[140] The carbonate−bicarbonate equilibrium as well as the enzyme activity are strongly pH-dependent. For example, a β-carbonic anhydrase was found to be active at pH 8.4 but not at pH 7.5.[141] Thus, pH variation can be used to vary the amount of $CaCO_3$ formed and, with it, the reaction kinetics.

Another method for the production of $CaCO_3$ is the alkaline decomposition of dimethylcarbonate into carbon dioxide and two moles of alcohol.[142] This method was found to be well-suited for the production of amorphous $CaCO_3$[142,143] but has the inherent drawback that the solvent composition changes with decomposition of the dialkylcarbonate. The solvent composition in a mixed solvent has a significant influence on the crystallization, as it determines the solubility of the mineralizing species, the supersaturation, and, ultimately, the crystallization path. However, the role of solvents is more complex because a solvent molecule can also act as an additive by preferential adsorption onto crystal faces. The use of a solvent as an additive for face-selective adsorption has not yet been significantly exploited but potentially can be applied as other additives for crystal morphogenesis. The use of mixed solvents for crystallization control has, however, been increasingly studied in recent years.

Several research groups have studied the use of solvents to control the growth of $CaCO_3$ and other crystals, often using further additives such as block copolymer in the solvent mixture, often leading to variations in morphology.[144−151] However, as the exact role of the solvent mixture and its composition on crystal morphogenesis is not yet very well-understood, addition of further additives only allows morphology changes in an exploratory manner. The influence of the solvent composition on the supersaturation S of a charged crystallizing compound, and therefore on the choice of the crystallization pathway, can be quantitatively expressed and depends largely on the concentration c and dielectric constant of the solvent mixture ε as expressed in eq 6,[150]

$$\ln S = \ln c + \frac{z_+ z_- e^2}{4\pi\varepsilon_0 \varepsilon kT(r_+ + r_-)} = A + \frac{B}{\varepsilon} \qquad (6)$$

where ε_0 = permittivity in vacuum, r^+, r^- = radii of the charged ions with the charges z^+ and z^-, and e = elementary charge (1.602×10^{-19} C). A and B are constants for a given concentration of ions in solution.

By changing the solution composition in an ionic solution with a given concentration, only ε varies significantly, which influences the supersaturation, as shown in the simplified form of eq 6. For various alcohol/water and ethylene glycol/water mixtures, ε varies almost linearly with the solvent composition.[150] Therefore, changes in the supersaturation can be calculated for a given solvent composition. For CeO_2 nanoparticles, the correlation of $1/\varepsilon$ with the inverse particle size was possible.[150] In the case of alcohol/water mixtures, ε decreases the more hydrophobic the alcohol is and with increasing alcohol content in the mixture. This will increase the supersaturation S and, therefore, the tendency to form the kinetic reaction products rather than the thermodynamic ones (see also sections 2.1.2 and 2.1.3). Addition of solvents such as ethanol, isopropanol, and diethylene glycol to the aqueous solution for $CaCO_3$ crystallization led to an acceleration of the crystal growth rate and the formation of the kinetic polymorph vaterite. As the solvent becomes poorer for $CaCO_3$, ε is decreased (as can be easily seen in eq 6) and, thus, S increases[152] In addition, vaterite was stabilized in the solvent mixture. A phase change from a mixture of calcite and aragonite to pure aragonite and then to almost pure vaterite was observed and controlled by the choice of the ratio of ethanol to distilled water in an ethanol/water mixed-solution system. This demonstrates that the solvent plays an important role in polymorphic discrimination and for determination of the microstructures of $CaCO_3$ crystals.[153]

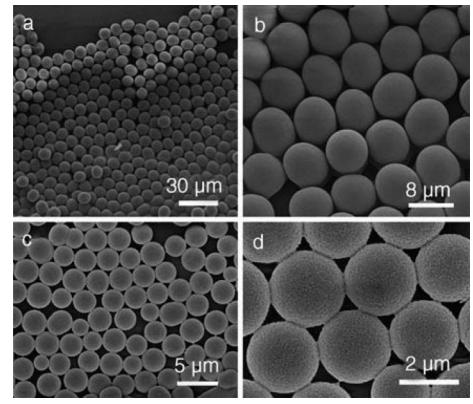

Figure 23. SEM images of $CaCO_3$ microspheres obtained from different solvent mixtures (volume ratios) in the presence of [PEG-b-pGlu] = 1 g L^{-1}: (a) DMF/water = 1:1; (b) magnified SEM image of (a); (c) DMF/ethanol = 5:1; and (d) magnified field-emission scanning electron microscopy (FESEM) image of (c). Reaction time = 3 days. Reprinted with permission from ref 154. Copyright 2006 Wiley-VCH.

Very recently, Yu et al.[154] investigated the effect of different organic solvents or their mixtures on controlling morphology and microstructure of $CaCO_3$ in the presence of an artificial peptide-type block copolymer, PEG(110)-*b*-pGlu(6), as a crystal-growth modifier. The synergistic effect of PEG-*b*-pGlu and the solvent mixture on the growth of calcium carbonate was fully investigated, and the results demonstrated that the composition of the solvent mixture and the ratio of the solvents present have a significant influence on the morphology and polymorph of $CaCO_3$ crystals in the presence of this polymer. Highly monodisperse $CaCO_3$ microspheres (vaterite) were produced in a mixture of dimethyl formamide (DMF)/water and a polymer concentration of 1.0 g L^{-1} (Figure 23). The high-magnification SEM image shown in Figure 23b shows microspheres with diameters ranging from 5.3 to 6.0 μm and with smooth surfaces. Monodisperse vaterite $CaCO_3$ can also be prepared in a mixture of DMF and ethanol, as shown in Figure 23c, but the obtained vaterite microspheres have rough surfaces and are smaller, with diameters ranging from 1.5 to 2.4 μm (Figure 23d). Moreover, these microspheres are not stable and transform into rhombohedral calcite after prolonged crystallization times. Clearly, the solvent mixture plays a key role in controlling the growth, size, and shape of the $CaCO_3$ crystals with different polymorphs.

The above considerations clearly demonstrate that control of standard experimental parameters such as temperature, solution pH, or composition can have a pronounced effect of crystal morphogenesis. The experimental parameters determine the crystallization pathway and, with it, the possibilities for morphogenesis, if additional additives are applied.

2.1.5. Polymorph Control

Polymorphism is the ability of a crystalline system to exist in more than one crystal structure, and it has been recognized for centuries. Polymorphism was observed over 170 years ago when Wöhler and von Liebig examined a boiling solution of benzamide in 1832.[155] On cooling, the benzamide initially crystallized as silky needles, but on standing, the needles slowly converted to rhombic crystals.[155] In terms of thermodynamics, there are two types of polymorphism. For an enantiotropic system, the relative stability of a pair of solid forms inverts at some transition temperature beneath the melting point, while a single form is always more stable beneath the melting point in a monotropic system.[156] This means that any transition from one polymorph to another will be irreversible below the melting point for a monotropic system. For an enantiotropic system, the solids may convert reversibly between the two polymorphs on heating and cooling.

Polymorphism has great technological significance due to the dependence of material behavior such as hardness or optical properties on the solid-state structure. In particular, organic crystals exhibit a variety of polymorphs with different properties. Polymorphism is important in many fields like pharmaceuticals, agrochemicals, pigments, dyestuffs, foods, and explosives and is especially relevant for pharmaceutical compounds because dissolution rates depend on the polymorph and patents are filed for a particular polymorph.[157] Therefore, one of the long-standing challenges of crystallization is the ability to predict and control the occurrence of polymorphism. In the case of $CaCO_3$, three anhydrous polymorphs (trigonal calcite, orthorhombic aragonite, and hexagonal vaterite, in order of decreasing stability at ambient conditions) and two hydrated polymorphs (monoclinic hexahydrate ikaite and calcium carbonate monohydrate) are known. In terms of morphogenesis, control of the crystal polymorph provides a route to controlling morphology, as all of the three anhydrous $CaCO_3$ polymorphs have different characteristic morphologies. While calcite forms rhombohedra, aragonite is needlelike and vaterite forms polycrystalline spheres comprising aggregates of high-surface-energy nanoparticles, which are formed in the kinetic regime (see Figure 24).

Traditional strategies for selection of polymorphs often involve changing solvents, temperature, and other growth conditions in an attempt to control crystal formation by changing from thermodynamic toward kinetic control or vice versa,[144,145,153] although polymer additives can also be used.[159−163] Using $CaCO_3$ crystallization as an example, the calcite aragonite phase diagram [133,134] is not so useful because it describes high temperature and pressure regimes. Instead, a phase diagram was established showing the stability regions of calcite, aragonite, and ikaite in aqueous solutions at different pressures and temperatures (Figure 25).[135]

The $CaCO_3 \cdot H_2O$ observed in natural and laboratory environments is unstable with respect to calcite and aragonite under all conditions investigated and will generally convert to aragonite at low temperatures and to calcite at temperatures in excess of 100 °C.[165] Similarly, vaterite is metastable toward calcite and aragonite.[166] Consequently, calcium carbonate monohydrate and vaterite are only available via kinetic routes and must be prevented from transforming into a more stable polymorph in solution. Monohydrate is nearly as unstable as ACC and typically plays the role of a precursor phase, with concomitant loss of morphology on transformation. Well-known strategies to induce aragonite precipitation include the application of higher temperatures[167−169] and/or the addition of Mg^{2+} ions to the crystallizing solution. Mg^{2+} ions are smaller and more strongly hydrated than Ca^{2+} ions and induce aragonite precipitation at ambient pressure by inhibiting calcite crystal growth.[170−176] Pure $CaCO_3$ polymorphs can be synthesized using a constant composition method.[177] pH and temperature were found to be the most important variables for polymorph control. At room temperature, calcite was obtained at pH > 12, aragonite was obtained at pH 11, and vaterite was obtained at pH < 10, although the aragonite phase was not phase-pure.[177]

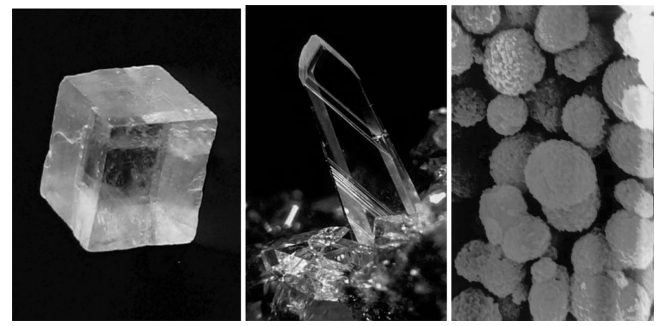

Figure 24. (a) Geological calcite with its typical rhombohedral form. (b) Aragonite geological elongated crystal. Reprinted with permission from Photo Atlas of Minerals. Copyright Lou Perloff and the Gem & Mineral Council. (c) SEM image of micron-sized vaterite spheres. Reprinted with permission from ref 158. Copyright 1997 Royal Society of Chemistry.

In biomineralization, polymorph selection is a key issue because the different polymorphs offer the possibility of different materials properties. Excellent examples of polymorph control are found in organisms such as mollusks, which can selectively deposit a specific polymorph of $CaCO_3$ (aragonite or calcite) under the control of biopolymers, always at about constant outer conditions.[178] Aragonite, for example, which is difficult to synthesize under ambient conditions but can offer beneficial mechanical properties, can be nucleated in the presence of soluble proteins extracted from an aragonite nacre layer.[179,180] The same level of control has, up to now, not been achieved by chemists, although elegant examples of selective polymorph production using monolayers[181−186] or synthetic polymer additives[163,187,188] (and references therein) have been demonstrated for special cases, although mixtures of polymorphs are often obtained.[189] Many questions still remain regarding the functions of biopolymers extracted from biominerals, although mixtures of biopolymers extracted from specific mineral components of an organism often exhibit targeted activity.[179,180] For example, biomineralization proteins such as AP7 and AP24, which were believed to be active in nucleating aragonite, were actually shown to be effective in inhibiting calcite precipitation.[190,191] In contrast, adsorption of these polymers onto a surface can lead to the formation of aragonite, in direct analogy to nacre formation. A synthetic analogue for

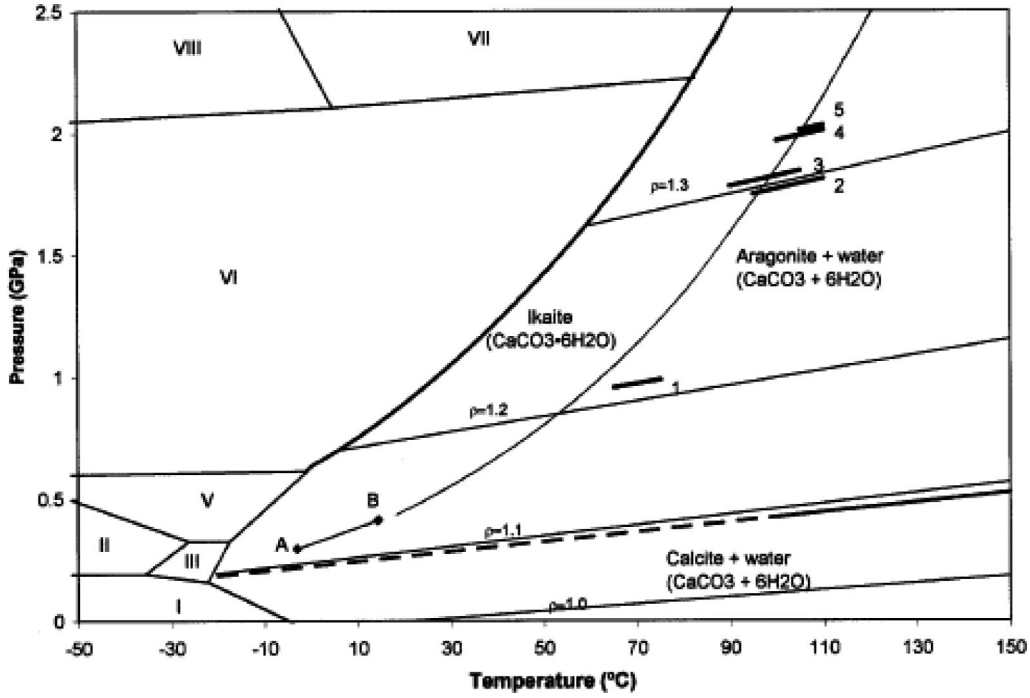

Figure 25. Phase diagram for the $CaCO_3-H_2O$ system extended to 2.5 GPa and 150 °C. The A−B portion of the ikaite ↔ aragonite + water boundary is taken from Marland.[164] Experimental points are represented by heavy lines, each extending over a range of observations along an isochore based on the melting point of ice measured at the end of each observation. The short, heavy solid lines represent the isochoric $P-T$ conditions over which both ikaite and aragonite + water coexist. The lighter straight lines are isochores for densities (ρ) = 1.0, 1.1, 1.2, and 1.3 g/cm^3. The phases of H_2O ice (shown as areas with Roman numerals) and their melt curves are superimposed on the phase diagram for the $CaCO_3-H_2O$ system. Reprinted with permission from ref 135. Copyright 2005 Mineralogical Society of America.

aragonite formation on polymer-covered surfaces can be seen in the nucleation of aragonite after adsorption of hyperbranched polyglycerol on alkane-terminated self-assembled monolayers (SAMs).[192]

Despite the general understanding of polymorph control by specific biopolymer interactions gained from the study of selected biominerals, control of polymorphism is still largely an empirical process. Ostwald's step rule is usually employed to cause the crystallization reaction to proceed along the kinetic pathway and then to stop the reaction when the desired polymorph has been formed. Transformation into a more stable polymorph in contact with a solvent usually occurs via dissolution-recrystallization as reported for stearic acid,[193] magnesium phosphate hydrates,[194] L-histidine,[195] and also $CaCO_3$. [168] Transformation into a more stable polymorph, however, can also take place as a solid-state reaction, although these processes usually have higher activation energies and are, therefore, only found for systems with low cohesion energies in the crystal or slightly below the melting point. Solid-state transformations can, therefore, occur in mobile glasses and are particularly common for organic crystals at annealing temperatures close to their melting point.[196] Such transitions are already exploited on an industrial scale, e.g., in dyestuff pigment synthesis.

For the $CaCO_3$ system, the energies for the solid-state transformations of the metastable polymorphs into calcite are high. The vaterite-to-calcite phase transformation has an activation energy of 252.8 ± 48.7 kJ mol^{-1}, and aragonite to calcite has a corresponding one of 234.5 ± 5.6 kJ mol^{-1}.[197] Therefore, the dissolution-recrystallization pathway is chosen. However, the transformation of ACC into a crystalline polymorph is still disputed. ACC is stable when kept dry and highly unstable toward transformation in aqueous solution. The solid-state transformation of ACC into calcite takes place at 276 °C with a transition enthalpy of −15.0 ± 3 kJ mol^{-1},[198] although there is obviously an activation energy barrier to the transformation. Nevertheless, extended X-ray absorption fine structure (EXAFS) investigations have shown that, even in ACC, a local order exists that often resembles the polymorph into which the ACC will subsequently crystallize.[46,47,199] Thus, the question of polymorph control is still an open one. Recently, Epple reported a continuous $CaCO_3$ synthesis procedure, which could yield all of the anhydrous crystalline polymorphs in pure form. This was achieved by variations of reaction temperature, reactant concentrations, and their mixing and residence time in the reactor.[200] However, it has not yet been possible to develop a synthesis that yields all of the metastable polymorphs in pure form under one operating temperature. Some studies have, however, almost succeeded in this goal, but the precipitated polymorphs were not entirely pure.[177] A first step toward this goal was reported for the polymer-controlled crystallization of $CaCO_3$ on chitosan substrates using temperature and molar mass variation of a poly(acrylic acid) to control $CaCO_3$ deposition.[201] Polymorph selection was achieved by changing the addition time of the radical initiator to a calcium carbonate supersaturated solution containing sodium acrylate at ambient temperature.[202]

More simple is polymorph control by variation of the reactant concentrations in a given reaction system for polymer-controlled crystallization.[203] Here, amorphous $CaCO_3$ nanoparticles were found as precursors for all polymorphs so that the classical calculation of molecular supersaturation S was irrelevant, as it was always lowered by the formation of amorphous precursor nanoparticles. ACC transformation reactions occurred, both for calcite and vaterite, following the kinetic reaction cascade. Homogeneous nucleation, as well as particle growth, are essentially

carried out using the amorphous nanoparticles as a reservoir of precursor material, and these processes, therefore, depend upon the concentration of the nanoparticles. A second consequence of the particle-mediated reaction pathway is the appearance of the two polymorphs as complex structured mesocrystals with well-defined morphologies, where the primary tecton unit size reflects the size of the amorphous nanoparticles. Switching between calcite and vaterite was obtained by a strong crystallization-inhibiting polymer additive and kinetic discrimination, followed by stabilization of the vaterite against recrystallization by the polymer. At very low ACC concentrations, aragonite is heterogeneously nucleated on the surface of the reaction vessel as single crystals.

The above examples show that control of polymorphism is a complex interplay between thermodynamic and kinetic factors and that it can often be achieved using additives. Further, whether crystallization proceeds via ion/atom/molecule growth at low reactant concentrations or via particle-mediated crystallization pathways at higher concentrations can be important in determining the product polymorph and morphology. Because amorphous precursor phases can be generated for a number of crystalline systems—especially in the experimentally most relevant kinetic crystallization regime—the principles governing the formation of product crystals via amorphous precursor phases should be applicable to a range of other systems.

2.1.6. Single Crystals from Amorphous Precursors

Amorphous precursor phases have many advantages when it comes to the generation of the complex crystalline morphologies that characterize many biominerals. Because amorphous materials can be molded and formed into any shape, as occurs in pottery or in glass blowing, they can be easily exploited to generate complex crystal morphologies. Indeed, it is striking that many of the most elaborate biomineral morphologies are formed from amorphous silica (see also section 3). Furthermore, this crystallization strategy maintains an effective material transport to the crystallization site and precludes formation of high ionic strengths and related osmotic pressures. Additionally, by introducing amorphous precursor particles into the template site, there is no need to remove large solution volumes directly at that location.

Amorphous precursor particles are favored at high supersaturations and form as the first species. According to the Ostwald rule of stages, the least stable and least dense modification also has the lowest activation barrier of formation. It is, meanwhile, experimentally well-established that formation of amorphous clusters and droplets is practically unavoidable in ionic solutions with concentrations far above the saturation level.[38,204] Quite generally, the supersaturation relaxes much faster than the presence of crystals can be detected. At this time, the amorphous precursor can be used for molding into shape before crystallization occurs. Amorphous particles can, however, only be formed at concentrations above their dissolution threshold, which is, due to the laws of phase thermodynamics, significantly higher than the corresponding value of the crystalline species. This ensures that there is a certain experimental window (between the equilibrium dissolution concentrations of crystalline and amorphous species) where only classical ion-mediated crystallization can be found, as is required for the formation of large single crystals. The higher the supersaturation, the higher is the concentration of amorphous clusters that are formed, and this reaction mechanism will be promoted. Amorphous precursor phases are particularly charateristic of low-solubility minerals. This is simply due to the fact that a lower solubility automatically increases the apparent supersaturation even at moderate molarities, but also kinetically stabilizes the amorphous nanostructures against redissolution.

The role of amorphous nanoparticles as particle intermediates was first identified in 2001,[205] although the observation of amorphous precursor phases in a crystallization reaction predates this.[50,206] In synthetic bioinspired mineralization systems, amorphous precursor particles are now found to be omnipresent,[207] and they most often constitute the early nanoparticle phase. There are two principal possibilities for the transformation of amorphous precursor particles into a single crystal. Either they act as a material depot for subsequent dissolution and recrystallization in a classical crystallization reaction, or they fuse together before or after crystallization and finally form the single crystal in a nonclassical crystallization reaction. The nucleation of the crystalline species is the critical part in the formation of a large single crystal. If there are multiple nucleation events in an aggregate of amorphous precursor particles, a polycrystalline aggregate will be formed unless the nanocrystals are temporarily stabilized so that a position and orientation correction can take place, as discussed previously (section 2.1.3). This would then be the case of single crystal formation via a mesocrystal intermediate. However, because the mechanisms of mesocrystal formation are not yet well-understood, this strategy cannot yet be applied in a predictable way. The current choice for the synthesis of a large single crystal with complex shape in a template structure, when the crystallization proceeds via an amorphous precursor phase, is the generation of a single nucleation center.[11] This can be an acidic center on the template with an otherwise unordered structure, which does not induce heterogeneous nucleation. The acidic center then can induce the nucleation of the amorphous precursor phase.

One general point to consider for the generation of single crystals via amorphous precursors is the volume shrinkage upon crystallization, which occurs because the density of a crystalline phase is generally higher than that of the unordered amorphous phase. If the template is rigid, this must unavoidably lead to voids being created, usually between the template and the formed crystal. Nevertheless, the template structure is imprinted into the morphology of the crystal. For $CaCO_3$, there is an additional problem in that synthetic ACC is hydrated with the formula $CaCO_3 \cdot H_2O$.[5] This means that a considerable amount of water needs to be removed upon crystallization of ACC. This can be achieved using sumps between the template and the formed crystal, as demonstrated by Aizenberg et al.[11] Despite these difficulties, rigid templates can be used to imprint the morphology of the formed crystal.

Other softer templates like vesicles or liquid crystalline structures can also be used for the morphogenesis of single crystals from amorphous precursors. The formation of single crystals from amorphous precursors appears especially valid for biominerals, and amorphous precursors were revealed for a variety of biomineral systems including magnetite in chiton teeth,[208] magnetite in magnetotactic bacteria,[209] calcite in sea urchin spicules[50] and spines,[8] aragonite shells in mollusks,[7,48] carbonated apatite,[53] and possibly skeletons of corals[210] and crustaceans.[211] (see section 3). The synthetic

strategy of templating via amorphous precursor phases can also be advantageously applied to generate single crystals with defined complex morphologies (section 4.1.7.2).

2.2. Polycrystalline Structures

Control of crystal morphologies can be achieved even when the building units of an aggregate are not oriented with respect to each other. In the case of $CaCO_3$, a good example is provided by vaterite spheres, which are formed from unordered nanoparticles (Figure 24c).[158] Under this heading, we will discuss all structures that are composed of nanoparticles, but which are not mutually oriented within the same crystallographic register and, therefore, do not show single-crystalline scattering behavior. The distinction between the aggregation of crystallites and amorphous precursors is somewhat arbitrary as the transition of the amorphous precursor into crystalline matter is usually not identified. It is not typically identified whether or not crystals are formed via the aggregation of amorphous precursor particles.

2.2.1. Aggregation of Crystallites

Aggregation of nanocrystallites can lead to the formation of a wide range of morphologies, but it is very hard to control an aggregation process in terms of morphology and size of the final aggregate. Usually, the result of an aggregation process is an undefined aggregate, unless additives are employed that can control or direct the aggregation process. Indeed, there is a fine balance between fast, uncontrolled aggregation of the nanoparticles, which occurs in the absence of stabilization, and colloidal stabilization, which will completely prevent aggregation. For the control of nanoparticle aggregation, the particles must be only temporarily stabilized—just long enough after formation to find their position in the controlled aggregate morphology. For the $CaCO_3$ case, this stabilization cannot usually be achieved by charges because most $CaCO_3$ crystallization reactions introduce spectator ions. Instead, stabilization by an additive is desirable.

Most of the literature relating to complex polycrystalline morphologies probably concerns the application of additives. In contrast, very little is yet known about how to control aggregation to give desired morphologies. We will, therefore, discuss here examples of the formation of polycrystalline aggregates where the mechanism of morphogenesis was well-characterized. The most important strategy for the control of a complex morphology of an aggregate is the application of templates. Providing an example of this strategy, gas bubbles and emulsion droplets present in a reverse microemulsion were shown to act as effective templates for the generation of polycrystalline vaterite spheres with spongelike morphologies.[212] A more detailed discussion of this mechanism is provided in section 4.2.4.2.

As a second example, combination of a gas bubble templating method, temporary polymer stabilization of nanoparticles, and surface tension variation of the polymer stabilizer solution led to a systematic morphogenesis cascade of polycrystalline $CaCO_3$ aggregates with complex and controllable morphologies.[213,214] In this case, the surface activity of the polymer was tuned according to the degree of phosphorylation. The polymer, therefore, played the role of both a temporary nanoparticle stabilizer and a surface-active molecule that could change the surface tension of the polymer solution. Provided that sufficient time was provided for controlled nanoparticle aggregation in crystallization, a cascade of complex morphologies was obtained. Particles that form via aggregation of temporarily stabilized nanoparticles at gas bubbles at the air/solution interface can be tuned in their morphology by a simple variation of the solution surface tension.[213,214] This is outlined in Figure 26. CO_2 gas bubbles resulting from the Kitano crystallization method remain at the air−water interface and act as templates for the aggregating $CaCO_3$ nanoparticles in the solution (Figure 26A), thereby forming a ring (Figure 26B). The ring closes and gets heavier until the surface tension cannot hold the structure at the air−water interface anymore and the newly formed aggregate sinks to the bottom of the vessel where further growth is quenched (Figure 26 parts C−F). This process leads to large flowerlike aggregates at high surface tensions, shuttlecock morphologies at intermediate surface tensions, and partly hollow half-spheres at low surface tensions. The rim of the shuttlecock is formed for a caving-in structure outlined in Figure 26D, whereas already the lower part of the shuttlecock sinks without rim formation for the lowest surface tension (Figure 26 parts E and F).

Hollow polycrystalline calcite microspheres can be produced with organic templates such as poly(acrylic acid) (PAA) and sodium dodecylsulfate (SDS),[215] although the nature of the template is not entirely clear here. If soluble polymers are applied as additives in a crystallization reaction in the absence of an insoluble matrix to guide the mineralization process, the morphogenesis is usually based on a self-organization process of the formed nanoparticles. This can be controlled by the polymer and even coded if a face-selective polymer adsorption can be achieved on the nanocrystal building units. This will be discussed in sections 4.1.4, 4.1.5, and 4.2.2. Morphogenesis mechanisms in the presence of soluble additives are typically more complex than those that rely upon a template, as the additive may adopt multiple roles in the crystallization process. For example, a polymer can sequester ions, control the nucleation and nanoparticle growth, guide the self-assembly of nanoparticles, and so forth. The role of additives in achieving morphogenesis is, therefore, treated in separate sections of this article.

2.2.2. Polycrystalline Materials from Amorphous Precursors

A template is typically required to achieve the controlled morphogenesis of polycrystalline materials from amorphous precursors. In the absence of a template, aggregation of nanocrystals leads to uncontrolled morphologies, although some of them may have a fascinating and complex form. At this point, it is probably appropriate to make a statement about controlled and uncontrolled morphogenesis processes. It is clear that there are many significant questions to be answered in the field of additive-controlled crystal morphogenesis and that many control mechanisms are simply as yet unknown. Therefore, many complex morphologies will be described in section 4, and we will focus here on the application of controlled templating strategies to achieve morphogenesis.

An important strategy leading to morphological control of polycrystalline structures that are formed via amorphous precursor phases is the so-called polymer-induced liquid precursor (PILP) process, which was first described for $CaCO_3$ by Gower.[118] Because of their liquid nature, these precursors are especially well-suited for morphogenesis using templates because they can easily adapt to any shape and

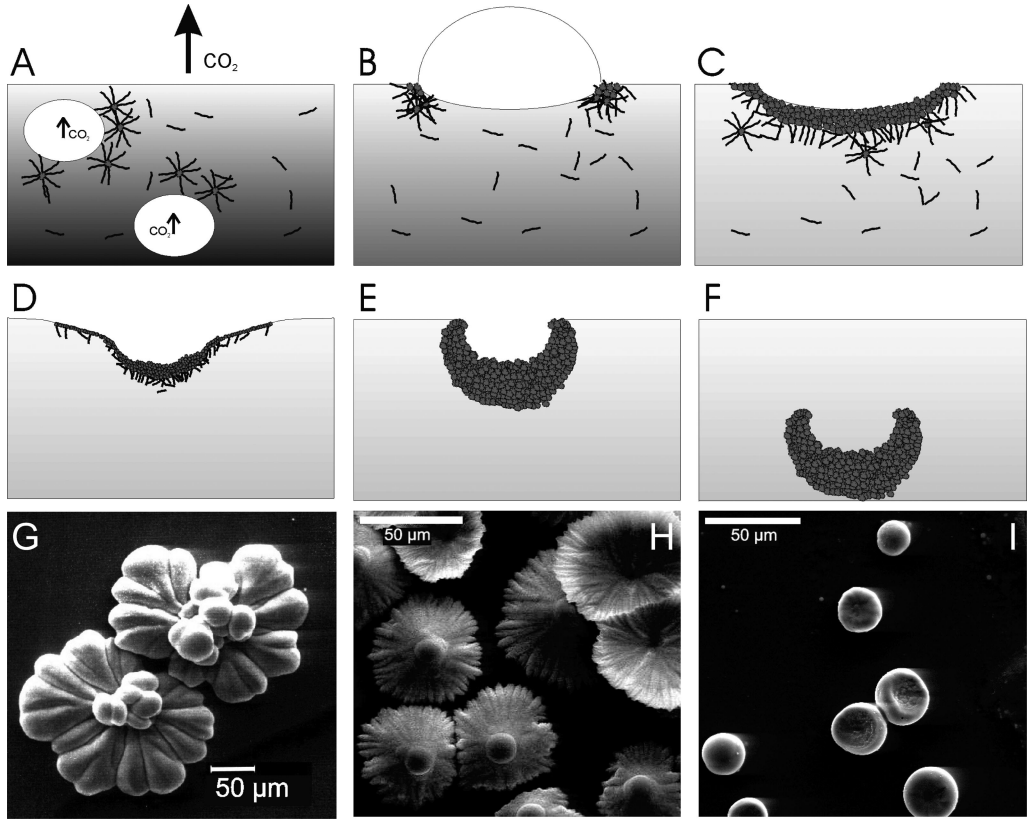

Figure 26. Schematic presentation of the formation of polycrystalline complex $CaCO_3$ morphologies using phosphorylated block copolymers for temporary nanoparticle stabilization and CO_2 gas bubbles as templates, which are generated in the Kitano method for $CaCO_3$ crystallization.[131] (A) $CaCO_3$ nanoparticles are generated near the air−water interface and stabilized by the block copolymer while CO_2 gas bubbles are also developing. (B) The gas bubbles can stay at the surface, and a rim of aggregating nanoparticles forms around them. (C) With time, the rim closes and the structure gets heavier by attachment of further nanoparticles. (D, E, F) It is now a matter of surface tension, how big the aggregate structures can grow until they loosen from the air−water interface and sink to the bottom of the vessel. (G−I) SEM images of the polycrystalline $CaCO_3$ structures, which are formed with decreasing surface tension caused by a decreasing phosphorylation degree of the block copolymer. Reprinted with permission from refs 213 and 214. Copyright 2002 Wiley-VCH and 2004 American Chemical Society.

can even enter small cavities by capillary forces. As there will be a separate review on this topic by Gower in this issue, we will not discuss PILPs in detail here, but some overview of this design strategy as applied to the templated formation of polycrystalline $CaCO_3$ structures is necessary for completeness. Liquid/liquid phase separation is a general effect when two components become nonmiscible with each other, e.g., salts and water. The decomposition always leads to a solvent-rich and a solvent-poor phase, and near the critical demixing point, liquid/liquid phase separation is the default case. It can be observed as an undesirable effect during protein crystallization from solution[216] and has been known for mineral salts such as $CaCO_3$ for more than a century.[217−219] In the case of $CaCO_3$, separation of the PILP phase from the saturated crystallization solution can be induced by addition of tiny amounts (μg mL^{-1} range) of polyelectrolytes such as PAsp or PAA, which clearly increase the water content of the salt-containing phase. The droplets formed can be observed in the crystallization solution by light microscopy once they have coalesced to microscopic size (Figure 27).

The role of the polymer in this process appears to be in sequestering and enriching the calcium ions in a rather water-rich environment, while simultaneously delaying crystal nucleation and growth within the droplets to form a metastable emulsion.[220,221] If $CaCO_3$ PILP droplets are deposited on a substrate, they coalesce and form a coating and then subsequently crystallize to give calcite films

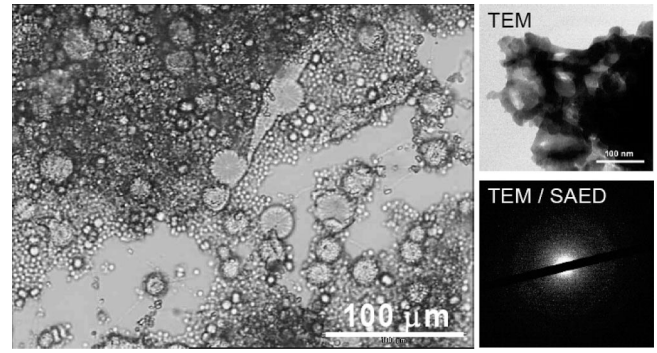

Figure 27. (Left) Light microscopy of $CaCO_3$ PILP droplets in a crystallization solution of 20 mM $CaCl_2$ + 20 μg/mL of PAsp on a glass plate. CO_2 is slowly added via the gas phase. (Right) TEM and TEM/SAED pictures of a PILP solution after shock freezing in N_2 and subsequent freeze-drying show the amorphous character. Reprinted with permission. Copyright 2006 Dr. Nicole Gehrke, Berlin.

comprising separate single-crystal domains.[220] If Mg^{2+} is added, Mg-calcite films can be formed whose composition and crystallinity can be controlled between fully crystalline and amorphous according to the Mg concentration.[222] The Mg^{2+} content incorporated into the calcite lattice (8−26%) was much higher than in the reference experiments, which employ classical crystallization methods.

PILP precursors can also be used to deposit amorphous precursor films on a substrate that is composed of 20−30

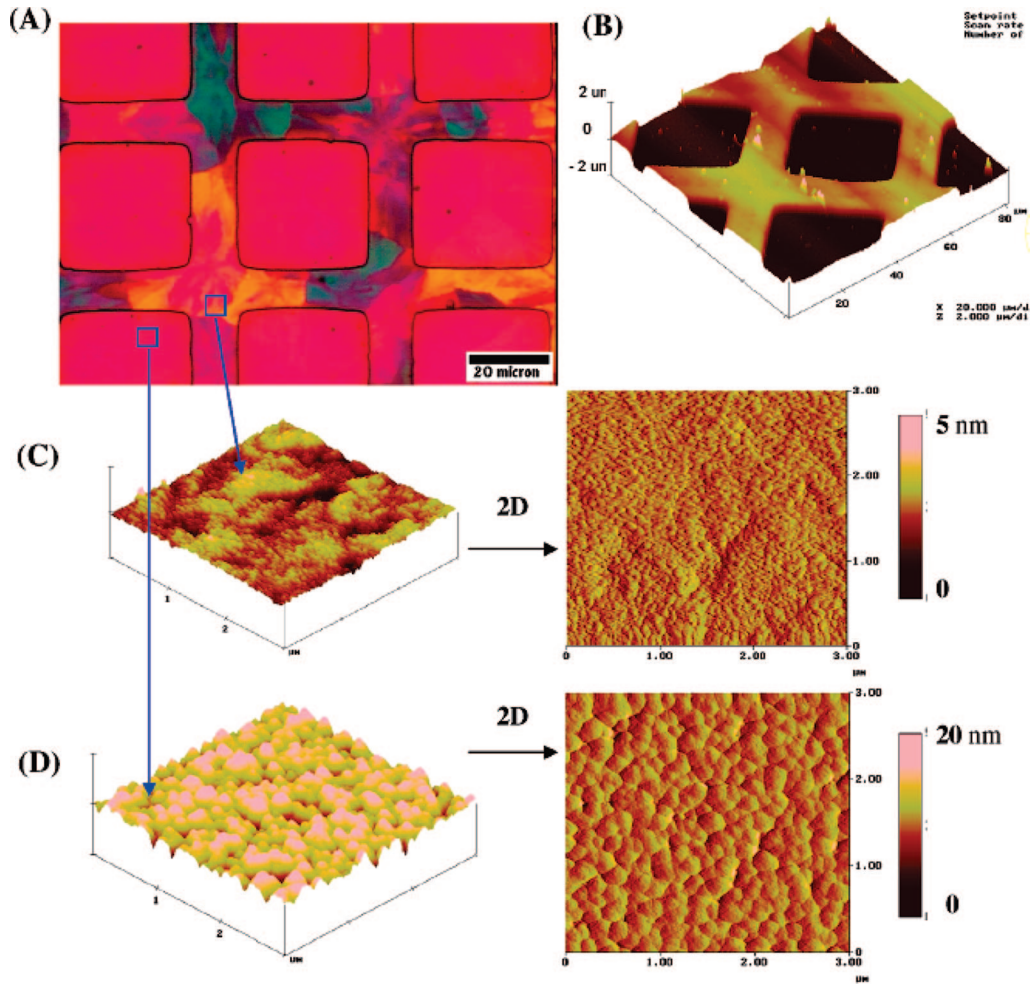

Figure 28. Comparison of calcite film topology when PILP phase is deposited on different surfaces. (A) Polarized light micrographs show that, in this particular experiment, PILP phase deposited on both the COO^--terminated SAMs (grid regions) and on the bare gold surface (interior square regions) but was much thicker on the former, as indicated by the different brightnesses of the birefringence. (B) Three-dimensional AFM height image scanned across an 80 μm × 80 μm surface area showing different film thicknesses for PILP phase deposited on COO^--terminated SAMs versus on bare gold surface. Scale bar is 20 μm/division in the $x-y$ plane and 2 μm/division in height. (C) and (D) AFM images scanned across the surface of a 3 μm × 3 μm area (as indicated with the blue boxes in (A) within each patterned region ((left) 3-D "height-mode" image to show quantitative height deviation; (right) "deflection-mode" image to show lateral dimensions of colloidal surface), showing colloidal particle morphology with different size ranges and surface roughnesses (rms (roughness) = 4.7 nm for film on the COO^--terminated region vs 17 nm on the bare gold surface). As can be seen in (C), PILP film deposited on COO^--terminated SAMs was formed from significantly smaller particles than that formed on the bare gold surface (D), even though the final film thickness was much greater. Reprinted with permission from ref 224. Copyright 2007 American Chemical Society.

nm ACC nanoparticles and PAA. These films are initially composed of amorphous nanoparticles that transform into a partially crystalline film by drying at room temperature for several days and heating to 400 °C.[223] The product film comprises crystalline domains with differing crystallographic orientations and typical sizes of between 50 and 200 μm, as revealed by polarization microscopy. Overgrowth of the polycrystalline patchwork film with $CaCO_3$ in the absence of polymer resulted in single and multiple layers of highly oriented multicrystalline calcite crystals, finally leading to a laminated $CaCO_3$ coating.[223] The crystal domain texture changed abruptly at the border between different domains but stayed constant within each domain, supporting a mechanism of epitaxial overgrowth. The coatings show iridescence, indicating that the multilayers of highly parallel calcite tablets exhibit periodicity of a few hundred nanometers, which is in the range of the wavelength of visible light. This methodology, therefore, provides an interesting, low-cost, and bioinspired pathway toward photonic materials.[223]

Formation of amorphous films from a PILP precursor has also been observed at a monolayer template when Mg^{2+} was used as an additional additive.[225] Crystallization yielded calcite/aragonite films comprising crystalline domains. It is also possible to pattern $CaCO_3$ films formed via a PILP precursor if a patterned self-assembled monolayer (SAM) is used as the substrate on which the film is deposited.[224] These films are formed by adsorption of colloidal precursor droplets from solution. Figure 28A shows various orientations of the crystallized films in the polarized light micrograph, and the AFM height image in Figure 28B clearly shows that the carboxy-terminated SAM regions served as templates for $CaCO_3$ deposition. The films are very smooth with a surface roughness of only 4.7 nm (Figure 28C) for the carboxy-terminated SAM regions and 17 nm for the bare gold surface, showing the existence of very small particles building the film.

Particles or even emulsion droplets can also be coated by PILPs.[226] PILPs were also found to mineralize collagen, where the PILP precursors were amazingly even able to enter the nanometer-sized gap zones of collagen, resulting in a structure partly resembling that of bone.[227] These results suggest that bone mineralization might also proceed via a

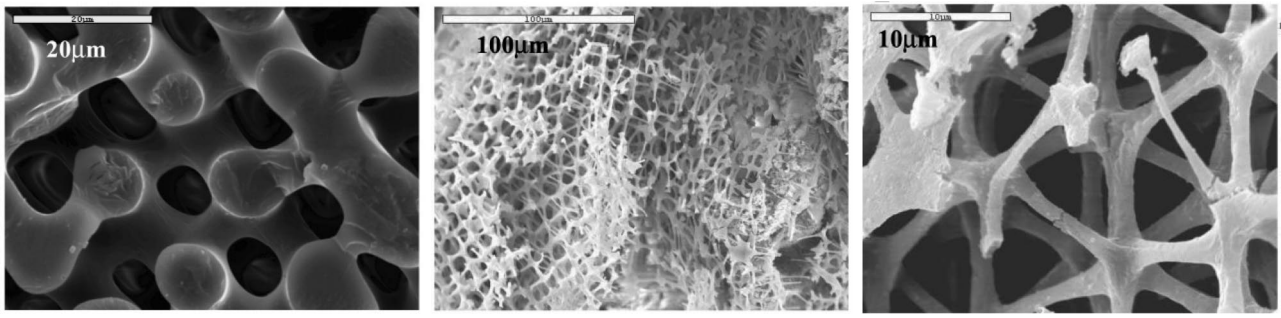

Figure 29. (a) SEM image of a section of the PHEMA replica of a sea urchin spine shows a microstructure very similar to that of an original sea urchin spine where the pores are interconnected with pore diameter of ~10 μm. (b) $CaCO_3$ mineralized in the PHEMA gel via a PILP precursor shows a bicontinuous structure very similar to the outer core region of the original sea urchin spine, with 3D interconnected pores similar to that of the original sea urchin spine. Note that the $CaCO_3$ polycrystal took the shape of the micropores inside the hydrogel replica. Reprinted with permission from ref 12. Copyright 2006 American Chemical Society.

PILP precursor stage, and indeed, the authors speculated that all Ca-based biominerals may form via a PILP phase.[221] Replicas of complex structures such as that of a sea urchin spine could also be achieved, demonstrating the remarkable possibilities to achieve complex morphologies by templating PILP phases (Figure 29).[12] The replicas are structurally less perfect than those prepared as a single crystal in a similar template using the classical crystallization pathway (see section 4.1.7). This may be related to volume shrinkage effects upon crystallization of an amorphous precursor phase.

In addition to PILP phases, amorphous $CaCO_3$ can also be used to generate polycrystalline structures on and within templates. An example is the application of SAMs as a mimic of the insoluble matrices commonly exploited in biomineralization processes. Tremel and co-workers described some work on polymer-guided $CaCO_3$ crystallization on SAM templates. If a carboxy-terminated SAM on a gold surface was used in combination with high-molar-mass PAA in solution, polycrystalline vaterite wires up to tens of μm were obtained. These structures were believed to form via the attachment of ACC nanoparticles to PAA nanowires anchored on the SAM. The PAA nanowires were in turn suggested to comprise several Ca^{2+} cross-linked polymer chains. The ACC-coated fibers in turn subsequently crystallized to vaterite, yielding the polycrystalline wire structures.[228]

PAA and PAsp are not only valuable for production of PILPs but also can act as crystallization inhibitors. This strategy can be used to produce ACC precursor particles, which in turn form sacrificial aggregates of ca. 20−30 nm ACC nanoparticles for further structure development. Hollow vaterite spheres can then be produced by crystallization of vaterite on the outer surface of the sacrificial ACC template. This was demonstrated by Tremel et al. for PAsp[229] and later by Cho et al., who formed ACC spheres in the presence of very low levels of PAA, which surface-crystallized to give hollow vaterite spheres due to the greater density of the crystalline $CaCO_3$ as compared to the sacrificial ACC.[230](Figure 30) The vaterite hollow spheres subsequently further aggregated, forming a spongelike vaterite film. (Figure 30h).

2.3. Amorphous Minerals

Amorphous minerals provide a distinct, but no less important, category of minerals versus the single crystal and polycrystalline materials considered in the previous sections. Indeed, amorphous biominerals, of which silica is by far the most abundant, represent approximately 20% of known biominerals.[231] Many of the most morphologically complex biominerals, such as the skeletons of diatoms and radiolaria, comprise amorphous silica.[231] As an amorphous material, silica has no preferred form and, therefore, can be shaped as desired to give noncrystallographic morphologies. This property of amorphous phases is exploited for the realization of many of the most complex biomineral morphologies but is also of relevance for synthetic systems if templates are applied. Therefore, no specific mineralization strategies are discussed in this section for the morphogenesis of amorphous materials with complex form. Amorphous minerals are discussed in detail in sections 3.4, 4.1.8, 4.2.3, and 4.3.

3. Biological Routes to Controlling Morphology

The term biomineralization is extremely broad, covering the formation of over 60 known biominerals within all five of the animal kingdoms.[37,231] Of these minerals, approximately 20% are amorphous and 80% are crystalline, although the number of amorphous minerals may be an underestimate due to the problems of detecting amorphous materials when they are present in combination with crystalline phases.[5,232] As a demonstration of how mineralization processes can be controlled to produce structures with truly remarkable morphologies and exceptional functional properties, biominerals are unparalleled. Indeed, so remarkable are the morphologies of some structures—for example, the spongelike form of the single-crystal skeletal elements of echinoderms—that it was long disputed whether the form of a single crystal could be molded in this way.[14−17] Nature, therefore, has much to offer those working in crystal growth, demonstrating what can be achieved synthetically and providing insight into possible strategies.

Given the range of different biominerals produced, their contrasting physical and chemical properties, and the incredible diversity in morphologies, there is clearly no single route by which control over mineral morphologies is achieved in biology. A number of key strategies are, however, readily identified, which have evolved according to the synthetic tools available to biology and the properties of the product biominerals. While high temperatures and pressures and extreme chemical conditions such as high and low pH values can be used in synthetic systems to control mineral morphologies, biology is necessarily limited to ambient conditions. Biological systems are, however, expert at synthesizing organic molecules and directing the assembly of three-

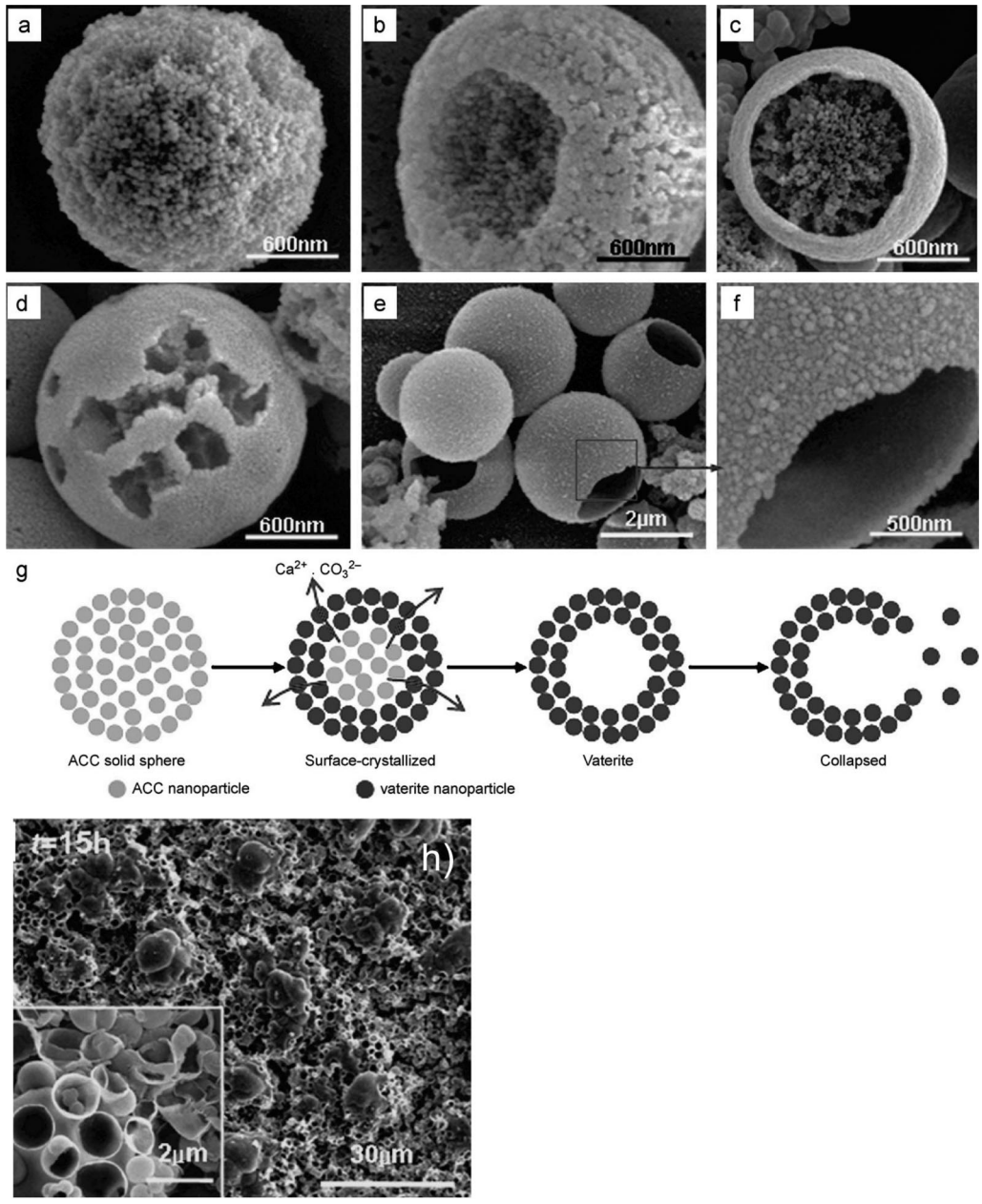

Figure 30. SEM images of etched calcium carbonate particles for various precipitation times: (a)−(d) etched solid spheres; (e) hollow spheres; (f) high-magnification image of the surface of (e); (g) scheme of hollow-sphere formation.; and (h) spongelike film composed of vaterite sphere. Reprinted with permission from ref 230. Copyright 2007 Elsevier Science Publishers.

dimensional organic structures, and it is this ability that provides the foundation for a wide spectrum of morphological control strategies. Considering, for example, two contrasting mechanisms, adsorption of soluble organic molecules on specific crystal faces or growth steps can result in morphological variation, while crystallization within a rigid organic template can mold the gross morphology to give noncrystallographic forms.

This section will review the principal mechanisms used by organisms to control the morphological development of single-crystal, polycrystalline, and amorphous minerals. A brief description of biomineralization processes will be given in section 3.1, which will be followed by a discussion of some of the general routes used to achieve morphological control of biominerals. Included in this section is a consideration of the role of organic molecules, polymorph selection, and, finally, control of crystal orientation. Organic molecules as insoluble organic matrices and soluble control macromolecules provide the foundation for all control strategies, and their roles will be described first. Where crystals are polymorphic, the selection of specific polymorphs provides an immediate route to morphological control. As described in section 2.1.1, crystals display equilibrium morphologies defined by their lattice symmetry and the relative energies of the low-index faces. Different polymorphs are thus characterized by different equilibrium morphologies, providing organisms with an immediate mechanism of morphology control. Discussed under this topic is also the potential role of amorphous precursor phases in achieving morphological control of a crystal product. Finally, selection of specific crystal faces at nucleation provides a further basic mechanism for the determination of crystal morphologies, and some of the biological mechanisms by which this is achieved are described.

A more detailed examination of the mechanisms used to control the morphologies of single-crystal (section 3.2),

polycrystalline (section 3.3), and amorphous biominerals (section 3.4) will then be presented and will be supported by discussion of specific biominerals. Again, many of the mechanisms discussed are based on calcium carbonate, as its abundance and diversity of form have made it arguably the best-studied biomineral. Iron-based biominerals are also significant, and magnetite precipitation within magnetotactic bacteria will be used as an illustration of the morphological control of single crystals. Of the amorphous biominerals, amorphous silica is by far the most significant, being widespread among plants, Protoscista such as diatoms and radiolaria, and occurring in some lower animals such as sponges. Precipitation of silica by organisms will be contrasted with that of amorphous calcium carbonate, which is characteristically short-lived in synthetic systems but can be either stable or transient in biology.

3.1. General Mechanisms

Biomineralization has been divided into two fundamentally different classes, based on the degree of biological control exerted.[37] The precipitation of a mineral as a result of simple interaction between an organism and its environment is termed "biologically induced mineralization" and is characterized by little control over the mineralization process or mineral morphologies. A common example is the decoration of bacteria by minerals such as iron and manganese oxides.[233] The surface of the bacteria contains macromolecules with reactive groups including carboxylates and phosphates, which can bind metal ions present in the environment. The bound metal ions serve as nucleation sites for precipitation, induced by local changes in the pH or redox potential due to the bacterial metabolism, or by the presence of reactive ligands such as sulfide.

In "biologically controlled mineralization", the organism directly controls the mineralization process, having evolved specific strategies to produce minerals of selected size, morphology, structure, and orientation. [37,231] These strategies rely upon organic molecules to control mineralization: confining a space, forming an organic matrix framework, controlling ion input, constructing a nucleation site, controlling crystal orientation and growth, and terminating crystal growth. Some or all of these processes may be involved in the precipitation of a given mineral. Exhibiting a degree of control that is currently beyond that which can be achieved synthetically, these biological mechanisms offer a unique inspiration for "biomimetic" crystal growth experiments and provide the basis for the design and synthesis of novel materials.

3.1.1. Soluble and Insoluble Organic Molecules

The organic macromolecules involved in regulating biomineralization processes can be categorized either as insoluble matrix molecules or soluble "control" macromolecules.[232] Fundamental to all biologically controlled biomineralization processes is that mineralization always takes place within a designated space that is delineated by a structured organic matrix. This can vary from simple intracellular lipid vesicles in the case of in magnetotactic bacteria to more complex extracellular macromolecular frameworks such as the organized collagen fibrils in bone. The organic matrix defines the mineral-deposition site and enables an organism to control the composition and concentration of the precipitation solution. Additional soluble control additives may also be present. As an important mechanism of morphological control, the three-dimensional form of the mineralization site can dictate the final morphology of the precipitated biomineral by spatial constraint, effectively molding the morphology of the product mineral.[5,37,234] When considering precipitation within a confined volume, changes in the activity or positioning of ion pumps and channels during mineralization may also lead to crystal growth in preferred directions. Similarly, when the precursor material is in the form of storage granules of enriched ions or amorphous material, morphological control can be achieved by introduction of these particles at specific locations in the mineralization site.[6]

The organic framework is often further functionalized by adsorption of soluble macromolecules, providing an additional mechanism for controlling crystal nucleation and growth.[232,235] Many biominerals comprise oriented arrays of crystals, and there is good evidence that the crystal nucleation face is selected by a nucleating organic matrix. This result is also strongly supported by synthetic crystal growth experiments that have achieved epitaxial growth of calcite crystals from a number of highly organized organic matrices[183,236−239] and unique selection of particular calcite nucleation faces from organic matrices, which are believed to possess a specific charge density.[184,186,223] It is noteworthy that the rate of nucleation can also be increased and the morphology of calcium carbonate can be altered by the presence of immobilized macromolecules, while the same proteins in solution can retard crystallization, a difference in behavior that has been attributed to conformational changes and rigidity on binding to a solid substrate.[240−243]

Control macromolecules also function as soluble additives, adsorbing to crystals during growth and modulating polymorphs, morphologies, and textures. Biogenic calcium carbonates and calcium phosphates represent some of the best-studied systems and typically contain organic macromolecules at levels of up to a few wt %.[231] Isolation of these macromolecules and regrowth of calcium carbonate in their presence has demonstrated both selectivity of the macromolecules for specific crystal planes and control over polymorph.[244−250] The macromolecules present in calcium carbonates are usually highly acidic,[231] and as such, purification and characterization of these macromolecules has proven extremely challenging. Recent application of a gel electrophoresis fixing and staining protocol has, however, provided a real step forward in separating the components of the macromolecule assembly.[251,252] Molecular genetic techniques are also beginning to be used to probe biomineralization processes and are likely to bring significant progress in identification and understanding of the roles of specific proteins in controlling mineral formation.[253−256]

The macromolecules isolated from calcium carbonate biominerals usually contain fractions that are rich in aspartic acid and glutamic acid and often contain bound polysaccharides.[232,242] These acidic macromolecules typically contain blocks of repeated sequences, such as runs of poly-Asp and sequences with poly-Asp at every other residue, commonly separated by either glycine or serine.[252,257] The repeating negative charges offered by the Asp residues may bind to Ca^{2+} ions, leading to control over crystal growth, and it may also be significant that poly(aspartic acid) can adopt a β-sheet structure on binding to Ca, which may enable a specific interaction with crystal faces. [257,258]

An unambiguous demonstration of the role of soluble macromolecules in controlling crystallization comes from

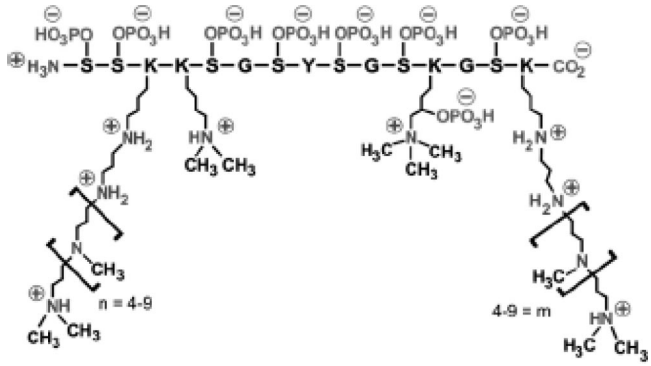

Figure 31. Chemical structure of silaffin-1 A from *Cylindrotheca fusiformis*. Reprinted with permission from ref 269. Copyright 2006 Wiley-VCH.

production of stable amorphous calcium carbonate (ACC) by some organisms.[5] Stable ACC was produced on calcium carbonate precipitation from solution containing small amounts of macromolecules extracted from stable ACC in sponge and ascidian spicules.[51] In contrast, the proteins extracted from the calcitic portion of the sponge spicules induced the formation of calcite crystals. Further, the macromolecules present in ACC appear to be quite distinct from those present in crystalline $CaCO_3$ phases and are characteristically rich in glutamic acid and hydroxyamino acids.[51,259]

Organic macromolecules have also been isolated from a range of silica biominerals, including diatoms, [260−263] plants,[264] and sponge spicules.[265,266] All species of diatoms so far analyzed contain long-chain polyamines composed of propyleneimine units, which are covalently bound either to putrescine or to lysine residues of low-molecular-mass proteins termed silaffins.[260,262,263,267−269] Diatoms characteristically synthesize complex mixtures of polyamines, which show a range of chain lengths and differences in the degree of *N*-methylations. There are also differences in the positioning of secondary amino functionalities and site-specific incorporation of a quaternary ammonium functionality. Notably, there appears to be quite a high degree of structural variation between polyamines isolated from different diatom species.[262,263] The silaffins themselves are polypeptides that have covalently bonded, long-chain polyamides side groups and that also show quite considerable variation in structure with diatom species. The structure of a typical silaffin is given in Figure 31, which shows polyamine chains attached to lysine groups and a high degree of phosphorylation. Silaffins are, therefore, highly zwitterionic, a structural feature that is believed to facilitate their self-assembly into large aggregates.[269] Indeed, in vitro studies have demonstrated the ability of these silaffin proteins and long-chain polyamines to regulate silica precipitation (as discussed in more detail in section 3.4.2).[261,263,270,271]

In sponge spicules, the occluded organic macromolecules take the form of a central protein filament known as a silicatein. [265,266] The silicatein protein filaments are in the order of 1−2 mm long and 30 μm in diameter and exhibit a regular repeating structure comprising three similar subunits, termed α-, β-, and γ-silicatein. Silicateins comprise approximately 25% of the hydroxy amino acids serine, threonine, and tyrosine, which typically appear in clusters, 15% glycine and about 20% acidic amino acids.[266] The hydroxyl-rich structure is postulated to be important in the silicification process as is supported by the in vitro activity of extracted silicatein proteins in directing the polymerization of silica and silicones, under conditions where an acid or base catalyst would be required in their absence. [265] Both the density and conformation of the hydroxyl residues are likely to be important in promoting this process.

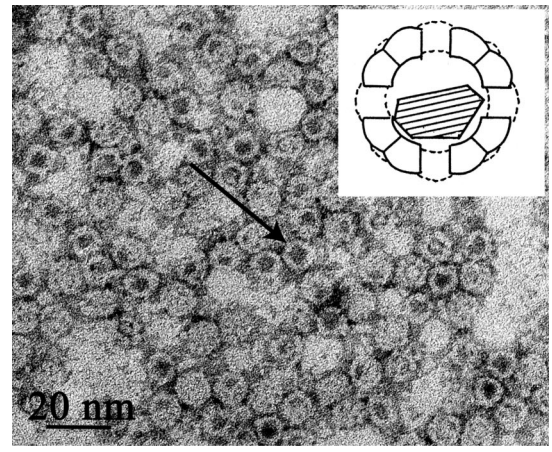

Figure 32. Transmission electron micrograph of horse spleen ferritin that has been negatively stained with uranyl acetate to show the protein shell and ferrihydrite core (an individual protein molecule with core is arrowed). The inset shows a schematic diagram of the ferritin protein.

3.1.2. Control over Crystal Polymorph

Many minerals exist in a number of closely related forms, such as the iron oxides and hydroxides or the polymorphs of calcium carbonate, and organisms have developed strategies to actively select particular mineral polymorphs. Two situations must be considered: when precipitation occurs (i) in the absence of and (ii) via precursor phases. Considering the former case first, polymorph selection must occur at nucleation.[232] This could be achieved by preferred nucleation of a metastable phase at a structured nucleation site, interaction with soluble additives at nucleation (such that inhibition of the stable form occurs), and determination of the composition and pH of the solution from which the mineral precipitates (see also sections 2.1.1 and 2.1.5). An excellent example of polymorph control at nucleation is provided by the protein ferritin. Ferritin comprises a spherical protein shell containing a particle of ferrihydrite, $5Fe_2O_3 \cdot 9H_2O$, and its structure/function relationships have been well-studied (Figure 32). [272,273] The protein actively selects the ferrihydrite polymorph, forming this phase during in vitro reconstitution of the apoprotein, where lepidocrocite (γ-FeOOH) would form in its absence. Fe(II) is initially bound at a ferrioxidase site located within an H-chain subunit where oxidation to Fe(III) is catalyzed, prior to transport to a nucleation site comprising six negatively charged groups on the inner surface of the protein shell. Hydrolysis of Fe(III) ions at the nucleation site then generates the poorly ordered ferrihydrite mineral.

Examples where a product biomineral forms via one or more precursor phases are also common. Recrystallization follows the Ostwald Law of Stages, and each subsequent phase precipitated is more stable than its predecessor (see also section 2.1.1). Again, a classic example involves iron oxide phases and is that of the development of chiton teeth.[274] The beauty of chiton teeth is that they are present in the animal in a continuous sequence of structural development, providing the opportunity for examining the different stages of mineralization. The initial stage of tooth development in

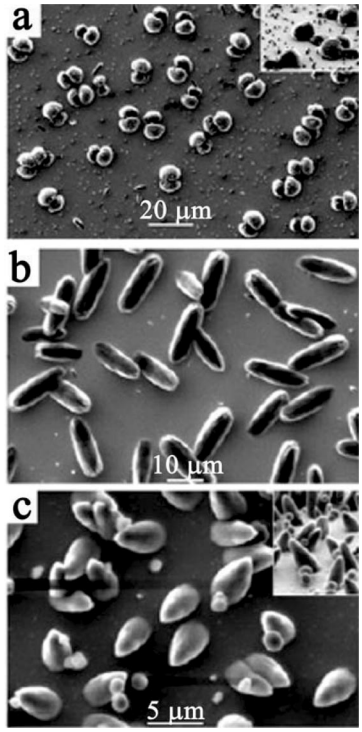

Figure 33. Calcite crystal precipitated on self-assembled monolayers of (a) $HSC_{10}-CO_2H$, (b) $HSC_{15}-CO_2H$, and (c) $HSC_{11}-SO_3H$ at a Mg/Ca ratio of 2, demonstrating the different effect of the additive on crystals in different orientations. Reprinted with permission from ref 282. Copyright 2005 Wiley-VCH.

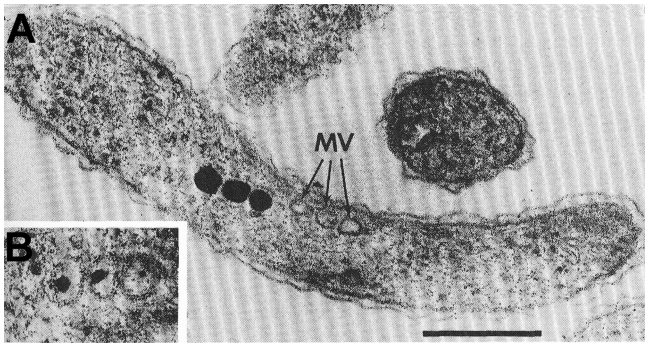

Figure 34. Section through a magnetotactic bacterial cell showing (A) three mature magnetite crystals and three empty magnetosome vesicles (MV); (B) vesicles containing immature magnetite particles. Scale bar = 250 nm. Reproduced with permission from ref 37 (Mann, S. *Biomineralization: Principles and Concepts in Bioinorganic Materials Chemistry*; Oxford University Press: Oxford, U.K., 2001). Copyright 2001 Oxford University Press (www.oup.com).

Chitonida is the formation of an organic framework with morphology identical to the product tooth. Ferrihydrite ($5Fe_2O_3 \cdot 9H_2O$) is then deposited within the organic matrix and subsequently transforms to magnetite (Fe_3O_4). Residual ferrihydrite then transforms to lepidocrocite (γ-FeOOH) and amorphous calcium phosphate, which crystallizes to dahllite or francolite, and finally fills the rest of the tooth.

Polymorph control of calcium carbonate provides an interesting example. The equilibrium morphologies of the three crystalline polymorphs, namely, rhombohedra for calcite, needles for aragonite, and spherical polycrystalline aggregates for vaterite, are quite distinct. Therefore, in selecting a particular polymorph, an organism has an immediate mechanism for morphological control. Additional use of soluble macromolecules can then open the door to a much wider range of possible forms. Thus, it is no surprise that, when an organism wishes to precipitate a large single-crystal calcium carbonate structure, it selects calcite. Of particular significance to the understanding of biological calcification mechanisms, it is now recognized that the crystalline calcium carbonate polymorphs frequently precipitate via a transient ACC precursor phase.[5−8] Because the amorphous phase has no preferred form, it can be readily molded and then crystallized to give a product with non-crystallographic form.

There are no known examples of transformation between calcite and aragonite, indicating that polymorph selection must occur at nucleation.[232] Investigation of the influence of soluble macromolecules on polymorph selectivity has suggested that these molecules are involved in the selection of calcite or aragonite.[179,180,251,275] Studies have focused on proteins extracted from mollusk shells, which typically exhibit spatially distinct calcite and aragonite zones and undergo a dramatic transition from calcite to aragonite precipitation during development. Demonstrating the role of the soluble proteins, calcite spherulites precipitated on the nucleating protein sheets of the abalone *Haliotis rufescens* in the presence of proteins extracted from the calcitic layer of the shell, while aragonite-derived proteins induced the formation of aragonite crystals.[179] Growth of calcite seed crystals in solutions of these proteins yielded similar results in that the aragonitic proteins resulted in an overgrowth of aragonite needles on the calcite crystals, while the calcitic proteins caused calcite overgrowth. Transition of layers from calcite to aragonite and back to calcite again was also demonstrated on addition of the appropriate proteins.[179]

Interestingly, a protein extracted from the aragonitic crossed-lamellar component of a gastropod shell induced the formation of vaterite in solution, leading to the suggestion that this protein may be important in a mechanism where ACC transforms to the product aragonite phase via a vaterite-type intermediate.[250] Applying molecular genetic techniques to probe the formation of calcium carbonate otoliths in the ears of teleost fishes, a protein comprising 35% acidic residues was identified that was termed "starmaker".[256] Interference with the in vivo function of this protein demonstrated that it was involved in both the morphogenesis and polymorph control of the otoliths. While the otoliths are aragonite in the wild-type animal, a polymorphic change to calcite was observed in the absence of starmaker.

Showing that the local microenvironment created by the insoluble organic matrix may also play a role in polymorph control, calcium carbonate was precipitated in an organic matrix that mimicked the structure of the organic matrix present in the mollusk nacreous layer.[180,251,275] Constructed from layers of β-chitin and silk fibroin, and permeated with soluble macromolecules extracted from the calcitic or aragonitic layers of mollusc shells, calcite precipitated inside the chitin when calcitic macromolecules were used, and aragonite was produced when aragonitic macromolecules were employed. This system also provided a suitable assay to test the function of purified protein fractions extracted from calcite and aragonite biominerals, showing that only one fraction of the macromolecules extracted from the aragonite layer of the mollusk *Atrina rigida* induced aragonite precipitation within the chitin framework.[251]

Discussion of the activity of the proteins in these examples was made considering calcite or aragonite to be the first phase precipitated. Because it is becoming increasingly apparent

that biogenic calcification often proceeds via a transient ACC precursor phase, some review of the proposed mechanisms may be required. However, that macromolecules are active in achieving polymorph control is not questioned. Indeed, examination of the short-range structural order of stable and transient ACC using X-ray absorption spectroscopy has shown that ACC from different organisms can exhibit different short-range structures.[45−47,276−279] Significantly, there is also evidence that this structure may act as a blueprint for the final transformation product of transient ACC.[5,47]

In some ways, distinction between the role of macromolecules in achieving polymorph selectivity in the presence, or in the absence, of an amorphous precursor phase is a matter of semantics. Whether the macromolecules act to induce nucleation of a selected polymorph de novo, or whether they cause precipitation of a transient ACC phase structurally designed to recrystallize to the desired polymorph, it is the organic macromolecules that appear to be key in achieving polymorph selectivity.

3.1.3. Control over Crystal Orientation

Selection of a particular crystal face at nucleation provides another basic mechanism of controlling crystal morphologies. Combining oriented nucleation with the effect of soluble additives enables yet greater control. As a demonstration of this effect, calcite crystals were precipitated on a range of different self-assembled monolayers (SAMs) in the presence of Mg^{2+} ions as a growth additive.[280−282] Extremely homogeneous arrays of crystals, whose morphologies were substrate-dependent, were produced. Interestingly, the crystals displayed different morphologies according to the structure of the SAMs under identical growth conditions, demonstrating that the morphological changes were dependent not only on the additive but also on the crystal orientation. This effect was attributed to differences in the accessibility of crystal surfaces and growth steps according to the crystal orientations.[282]

Oriented crystal growth is a key feature of many biominerals, and resolution of the mechanisms by which this is achieved has proven to be an enduring and challenging goal. This can be attributed, for a large part, to the experimental difficulties inherent in investigating the structural relationship between the surface on which a crystal grows in vivo and the crystal nucleation face. Nucleation is typically considered to occur on an organic matrix, leading to two distinct categories of oriented crystal arrays: those oriented in one direction only (i.e., where the nucleation face only is selected) and those oriented in all three dimensions (i.e., where there is a crystallographic relationship between the crystal nucleation face and the organic matrix). The only reasonable way to achieve *total* control over the orientation of an *individual* nucleating crystal would appear to be via an epitaxial relationship between the crystal nucleation face and an organized organic matrix. This situation arises, for example, in the formation of the single-crystal units of coccoliths, each of which is oriented in three dimensions from nucleation (see section 3.2.2.2 for a more detailed description of the formation of coccoliths). Selection of a particular nucleation face can, however, be achieved in the absence of a structural match between the crystal and the substrate. Experiments employing model organic monolayers where no epitaxial match is possible have shown that a specific crystal face can be selected at nucleation according to the charge density of the monolayer only. [186,283,284]

In the latter description, we have emphasized the role of epitaxial matching in achieving total orientational control over a *single* crystal. Aragonitic bivalve shell nacre has long been held as the classic example of a biomineral comprising crystals oriented in three dimensions, and the mechanism of orientation control has been widely discussed in terms of an epitaxial relationship between the crystal nucleation face and the preformed organic matrix.[285,286] Recent studies on bivalve nacre, examining the development of the crystallographic orientation and morphology with time, have provided compelling evidence that a mechanism relying on competitive growth of crystals in the direction of the growth front results in increasing ordering with deposition of core lamellae and can ultimately result in 3D-orientation of the aragonite tablets.[287,288] While competitive growth may enable orientation of a polycrystalline mineral, this mechanism clearly cannot be active for single-crystal biominerals, where the orientation is defined by a single nucleation event. For this situation, epitaxial growth on a structured organic matrix would appear to be as valid a mechanism as ever. The structure and formation of mollusc shell nacre will be discussed in detail as an example of a well-controlled polycrystalline solid in section 3.3.1.

3.2. Single-Crystal Biominerals

In this section, we will explicitly consider mechanisms used by organisms to control the morphologies of single crystals. While it is fairly intuitive how an amorphous material, which has no preferred form, can be molded to produce a complex structure, the ability of organisms to modify the morphologies of single crystals is truly stunning. Morphological control ranges from relatively minor modifications to the basic equilibrium form of a crystal, such as that viewed in the magnetite crystals precipitated by magnetotactic bacteria, to the formation of small crystals whose gross form bears no relationship to the underlying crystal symmetry, as exemplified by the individual calcite single-crystal elements of coccoliths, to single crystals with complex three-dimensional structures such as sea urchin skeletal elements. Indeed, so remarkable are the morphologies of echinoderm skeletal elements that it has long been debated whether these structures are indeed single crystals or highly organized polycrystalline arrays.[14,16,17,128,289,290] All of these three examples will be discussed in this section.

Three principal strategies are identified and discussed: (i) interaction of soluble macromolecules with developing crystals (section 3.2.1), (ii) templating of crystal morphologies (section 3.2.2), and (iii) formation of single crystals via amorphous precursor phases (section 3.2.3). It is emphasized that these mechanisms are used in addition to the fundamental processes of polymorph and orientation control discussed in the previous section. As a route to morphological control, the action of soluble organic macromolecules and certain significant inorganic ions has received considerable attention.[37,231,291] In the case of calcium carbonate, which forms the basis of the majority of studies (largely due to its high abundance), the intracrystalline macromolecules typically show a specific interaction with growing calcium carbonate crystals in vitro, binding to certain sets of crystal planes only and modifying morphologies.[244,246,248,292] While clearly active in modifying morphologies, the changes in crystal morphologies produced by these soluble macromolecules are necessarily fairly basic modifications of the equilibrium crystal form. In contrast, occlusion of these

additives within a crystal can result in significant changes in the texture[21,24] and mechanical properties,[293] and it is possible that this is a more important role than potential morphological changes.

Complex and noncrystallographic morphologies are characteristic of crystals formed within confined volumes, where the structure of this environment acts to mold the form of the product mineral. Indeed, in common with amorphous materials, crystals with unusual morphologies and curved surfaces are typical of growth within vesicles.[231] Many biominerals, such as the calcite scales produced by coccoliths,[294] form within vesicles with defined shapes and grow until they impinge upon the vesicle. The size and shape of the vesicle may also develop during the crystal-growth process. However, while it is fully intuitive that the form of an amorphous material can be defined by a soft organic membrane, it is perhaps surprising that the same mechanism is effective in dictating the form of a crystal whose energetically favored form comprises well-defined faces. Excellent evidence for the viability of this mechanism is, however, provided by biomimetic crystallization studies where calcite single crystals with spongelike morphologies and curved surfaces were produced within molds with the corresponding form (as discussed in detail in section 4.1.7).[234,295−297]

It is becoming increasingly evident that many crystalline calcium carbonate biominerals may actually form via an amorphous precursor phase rather than by direct precipitation.[5] While there are a number of possible advantages of producing biominerals in this way, including, for example, the potential for more rapid precipitation rates, it is the possibility of facile morphological control that intrigues. Taking an amorphous precursor with no preferred form, shaping as desired, and then allowing crystallization provides an extremely attractive route to morphological control. Indeed, this mechanism is operative in the formation of sea urchin larval spicules[6,50,298] and of the complex three-dimensional form of sea urchin spines.[8] It is important to emphasize again, however, that the presence of an amorphous precursor is not a prerequisite to the development of single-crystal biominerals with complex shapes and curved surfaces.

3.2.1. Organic and Inorganic Soluble Additives

3.2.1.1. Organic Additives. The possible role of the macromolecules occluded within calcium carbonate biominerals in controlling mineral morphologies has been studied in some detail, showing that interaction of these soluble molecules with growing calcite crystals can result in specific morphological changes, characterized by the display of new, well-defined faces.[244,246,248,292] This behavior has been interpreted using two main approaches: adsorption of additives to particular crystal faces[299] and adsorption to step edges and terraces.[300,301] In the former mechanism, macromolecules are preferentially absorbed onto crystal faces where a structural match exists between the functional groups on the macromolecules and the atomic arrangement on the crystal planes, causing the additive to interact with and stabilize these faces.[299] Following adsorption to specific crystal faces, the macromolecules become overgrown and are occluded within the crystals, as demonstrated by calcite crystals grown in the presence of fluorescence-labeled sea urchin macromolecules.[302] AFM studies of calcite growth in the presence of additives have formed the basis of the second mechanism, in which morphological effects are rationalized in terms of the interaction of additives with atomic steps. It should be emphasized that these two descriptions actually display considerable overlap, with stereospecific binding of additives occurring to different step edges.[303]

Support for adsorption of macromolecules to specific crystal planes comes from high-resolution synchrotron X-ray diffraction (XRD) studies of a series of calcite single-crystal biominerals.[21,24,292,304,305] In this approach, the crystal defects, as described by the coherence length and the domain spread, were attributed to occluded macromolecules, providing information on the location of the macromolecules. Investigation of the domain shapes of a number of calcite sponge spicules demonstrated a marked correlation with the gross morphology of the spicules, such that longer coherence lengths were present in crystallographic directions close to the morphological axes of the spicules.[24,292] Significantly, in spicules whose morphologies were inconsistent with the internal lattice symmetry, symmetry-related faces displayed different coherence lengths, suggesting that control beyond specific protein−crystal interactions was operative.[304] This anisotropic interaction of additives is consistent with a crystal growing from a specific crystallographic plane, such that access of additives to the symmetry-related faces becomes nonidentical.

Measurement of the crystallographic texture of synthetic calcite single crystals grown in the presence of macromolecules extracted from biogenic calcite crystals supported the above model of additive−crystal interaction.[21,290] Macromolecules extracted from the young and mature spines had identical effects on calcite crystal morphologies, inducing the formation of well-developed, stepped $\{10l\}$ ($l \approx -1.5$) faces, in addition to {104} faces. [21] XRD study of these crystals showed that coherence lengths were smaller in the {100} as compared with the {110} direction, which was consistent with preferential adsorption of proteins on the {100} as compared with {110} planes, as suggested by the morphological studies.

Atomic force microscopy (AFM) has proven to be a powerful technique for investigating the interaction of additives with growing crystal in solution and has provided direct evidence for the presence of specific interactions between isolated biological macromolecules and calcium carbonate crystals.[66,249,306] Imaging of the {104} faces of a calcite seed crystal in saturated calcium carbonate solution showed straight step edges with some kinks, as well as sharp corners between different step edges. Brief exposure to intracrystalline proteins extracted from the calcitic layers of the red abalone *Haliotis rufescens* resulted in rounding of the corners between step edges and in the step edges becoming more convoluted and kinked.[66] The proteins agglomerated at the step edges and appeared to attach more strongly to the step edges than to the terraces. Interestingly, proteins extracted from the aragonitic layer of the abalone behaved quite differently, resulting in the deposition of aragonite, as opposed to calcite, on the calcite nuclei. The step edges became highly convoluted and the terraces became extremely rough before crystal growth terminated.

Tying in with the model of additives adsorbing to specific crystal faces, a clear demonstration of the role of stereochemical binding in producing morphological variations was produced on studying the interaction of chiral amino acids with growing calcite crystals using AFM.[303] Interaction of D-aspartic acid and L-aspartic acid with the crystal steps was asymmetric, with the specific amino acid enantiomers binding

to the step edges that offered the best geometric and chemical fit. This effect changes the step-edge free energies and, in turn, results in macroscopic crystal-shape modifications. In general, for additives to affect a crystal morphology, they must interact with the reactant species either in solution or at the step edge, such that the kinetic barriers and/or the energetic driving forces of the crystal-growth process are modified.[300]

Recent work has demonstrated that the size of an additive and its hydrophilicity are both important quantities in determining the influence of additives in affecting crystal growth.[307,308] Indeed, when looking at the effect of soluble macromolecules on crystallization in more detail, it is a common characteristic that they accelerate the crystal-growth rate at low concentrations while retarding it at higher concentrations.[249,291] Acceleration in the growth of calcite seeds in the presence of extracted abalone nacre proteins was initially attributed to proteins bound at step edges promoting ion attachment,[249] although further consideration of the link between the additive structure and the acceleration of the step velocity indicated that a more significant affect of the additive may be in modifying the barriers to dehydration of the solvated growth units.[307] As an alternative mechanism, it has also been suggested that the additives may act as nucleation centers for unseeded crystallization when present in small quantities but may inhibit crystal growth by binding to the surfaces at higher solution concentrations.[309]

3.2.1.2. Inorganic Additives. In addition to discussing the influence of organic additives on crystal morphologies, it is important to consider also the role of certain cations. Calcite biominerals usually contain magnesium as a solid solution within the calcite lattice, and the role which magnesium may play in the morphological control of calcium carbonate has been considered.[52,310,311] The mechanism of magnesium incorporation in calcite biominerals has proven to be something of an enigma. Typically present at levels of a few percent to around 20%,[231,312−315] values of up to 44% have been observed in sea urchin teeth.[231] While biology can achieve such levels of magnesium incorporation not only within polycrystalline, but also in single-crystal, calcite, precipitation of calcite from solution in the presence of sufficient magnesium concentrations generally results in the precipitation of aragonite rather than calcite.[316−322] This behavior is attributed to the higher hydration energy of Mg^{2+} than Ca^{2+} and to the fact that magnesium can be incorporated in the calcite but not in the aragonite lattice.[146,316,317,323,324] To achieve the precipitation of calcite rather than aragonite, and to occlude significant quantities of Mg in the product calcite phase, it has been suggested that biogenic magnesium calcite may be precipitated via an amorphous precursor phase rather than direct from solution.[52,325] Stabilization of such an amorphous phase is likely to be achieved through a cooperative effect between soluble organic macromolecules and magnesium.[52,310] It has also been suggested that, in an in vivo environment, complexation of Mg^{2+} ions with organic macromolecules may present the Mg^{2+} ions in a dehydrated state, thereby promoting incorporation within the calcite lattice.[246] The feasibility of this mechanism is supported by the formation of Mg-calcites with Mg contents up to 14 mol % from water/alcohol solutions in which the Mg^{2+} ions are less hydrated.[146] Further, recent studies on the precipitation of calcium carbonate in the presence of Mg^{2+} ions and soluble organic macromolecules extracted from a seastar *Pisaster giganteus* have suggested that the organic macromolecules facilitate the formation of Mg-calcite via an amorphous precursor phase.[326]

Mg^{2+} ions have been demonstrated to cause a morphological modification of calcite single crystals, resulting in the generation of elongated, seedlike particles with roughened, facetted faces.[146,246,311] The effect of the Mg^{2+} ions has been interpreted as a specific interaction with calcite faces approximately parallel to the *c*-axis, causing elongation along this direction,[327] and also by an alternative mechanism where differential interactions of the Mg^{2+} ions with four different step directions occur.[328] In the latter case, AFM study of the growth of a calcite seed crystal in the presence of Mg^{2+} ions showed step-specific interactions at low Mg/Ca ratios. At high Mg/Ca ratios, both acute and obtuse steps were modified, but differential Mg^{2+} incorporation at these two steps caused a reduction in growth rates at their intersection, resulting in the formation of new step directions and pseudofacets, oriented close to an (010) face. The morphological modification, therefore, derives from strain at the boundary between the compositionally distinct steps. Some variation in the morphology of magnesium calcite has also been noted according to the anions present in solution, an effect that was attributed to different degrees of distortion of the calcite lattice caused on incorporation of different anions.[329]

3.2.2. Templating of Single-Crystal Morphologies

3.2.2.1. Magnetite and Greigite Single Crystals in Magnetotactic Bacteria. The precipitation of magnetite crystals by magnetotactic bacteria provides an example of precise regulation over crystal size, coupled with moderate morphological control. Magnetotactic bacteria are a diverse group of microorganisms that are characterized by their ability to display magnetotaxis, enabling them to respond to an applied magnetic field.[330−332] Each bacterium possesses a net magnetic dipole, which derives from chains of magnetically aligned magnetite (Fe_3O_4) or greigite (Fe_3S_4) crystals running along the length of an organism.[330] Formation of the crystals is under precise biological control, such that they exhibit narrow size distributions (magnetosome crystals display average sizes of 35−120 nm and consequently constitute permanent, single magnetic domains) and species-specific morphologies.[330,331] Examination of the morphologies of crystals produced by many bacterial strains has identified a number of different crystal forms (examples of which are shown in Figure 35), many of which are characterized by a uniaxial elongation that is coincident with the magnetic axis.[330,333−335] A three-dimensional image of a magnetosome, produced by tomographical reconstruction of transmission electron microscope images, is given in Figure 36, clearly showing the form of a single magnetite crystal and the existence of some well-defined crystal faces. This morphological modification is fascinating since both magnetite and greigite have cubic crystal lattices, which thus translate into equilibrium growth forms that reflect this internal symmetry such as cubic {100} forms or octahedral {111} forms. Development of a uniaxial elongation therefore breaks the symmetry of the crystal and cannot be rationalized by simple interaction with soluble additives.

The strategies used to induce magnetite precipitation and to control the size, morphology, and location of the crystals within the bacteria have received considerable attention. Each of the crystals precipitates within an individual "vesicle", which is formed prior to magnetite precipitation, thereby

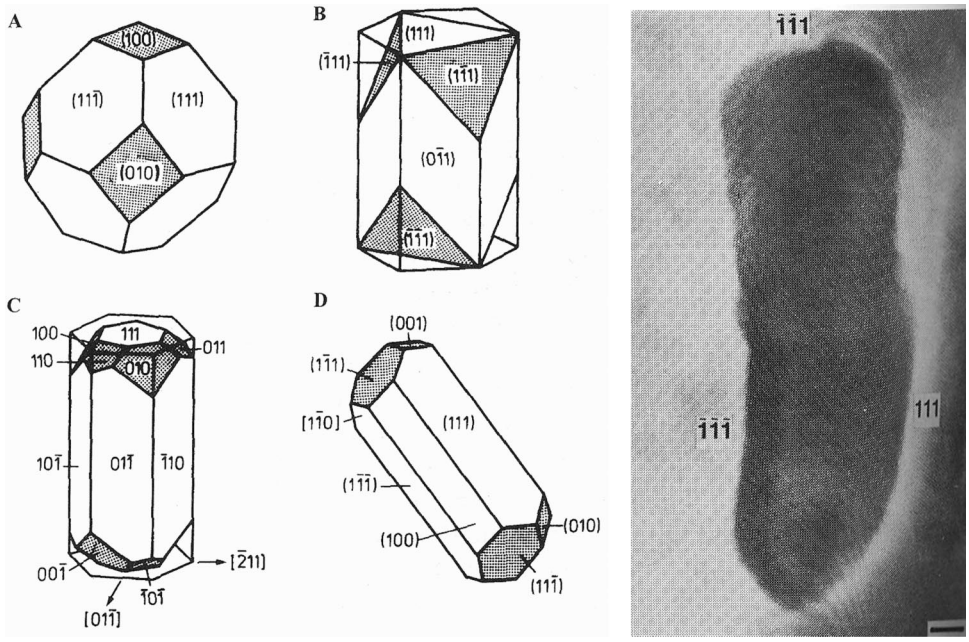

Figure 35. Morphological types of bacterial magnetite single crystals: (A) cuboctahedron, (B) and (C) hexagonal prisms, (D) elongated cuboctahedral, and (E) bullet-shaped bacterial magnetite single crystal with side and end (111) faces. Scale bar = 10 nm. Reprinted with permission from ref 37 (Mann, S. *Biomineralization: Principles and Concepts in Bioinorganic Materials Chemistry*; Oxford University Press: Oxford, U.K., 2001). Copyright 2001 Oxford University Press (www.oup.com).

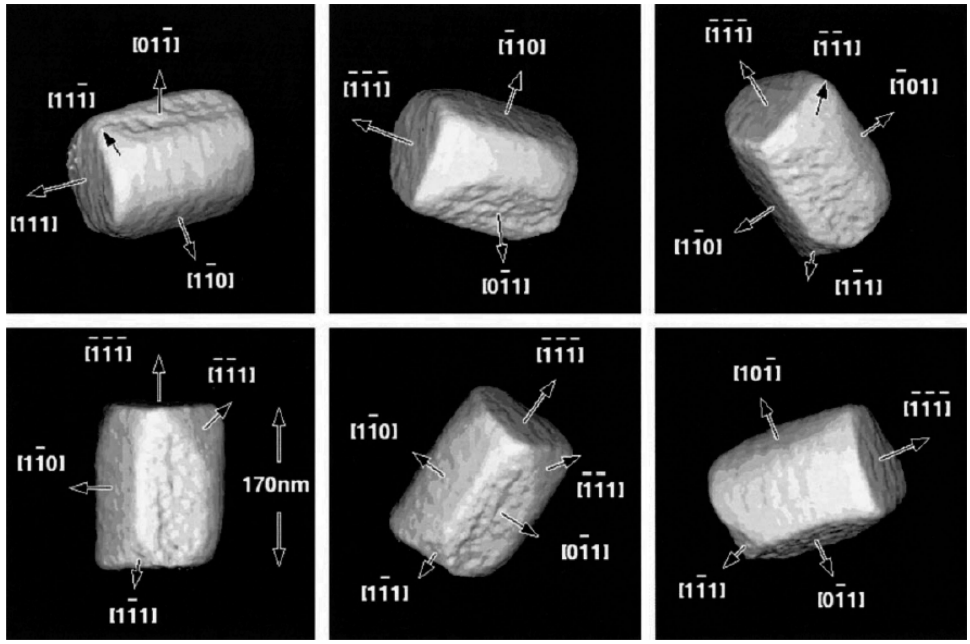

Figure 36. Tomographic reconstruction of a magnetite nanocrystal from an undescribed coccus collected from Sweet Springs Nature Reserve, Morro Bay, CA, reconstructed from a tilt series of STEM HAADF images obtained at 300 kV on a Philips CM300 FEG TEM over a range of ±56°. The tableau shows the three-dimensional morphology of the crystal viewed from a range of directions. Reprinted with permission from ref 336. Copyright 2001 National Academy of Sciences U.S.A.

producing a membrane-coated crystal termed a magnetosome. We have highlighted the term vesicle above due to recent electron cryotomographic (ECT) imaging studies of *Magnetospirillum magneticum* that have shown that the membrane-bound compartments in which the crystals precipitate are in fact invaginations of the cell membrane rather than isolated vesicles (Figure 37).[332,337] The magnetosomes are also supported by cytoskeletal filaments that provide further structural support. The size and morphology of the magnetite crystals is believed to be principally controlled by the magnetosome vesicle.[330] A preformed vesicle may act as a mold for the final crystal size and form, physically constraining further growth. Anisotropic flux of ions through the magnetosome membrane, or asymmetric distribution of specific proteins in the membrane, may also promote growth in certain directions.

The mechanism of magnetite precipitation in these organisms has not yet been fully resolved. Evidence from Mössbauer studies[338] and high-resolution transmission electron microscopy[339] has suggested that the magnetite crystals may not precipitate directly but rather form via a low-density hydrous Fe(III) oxide and ferrihydrite precursors precipitated within the magnetosome. The possibility of ferrihydrite formation in the periplasm surrounding the magnetosome,

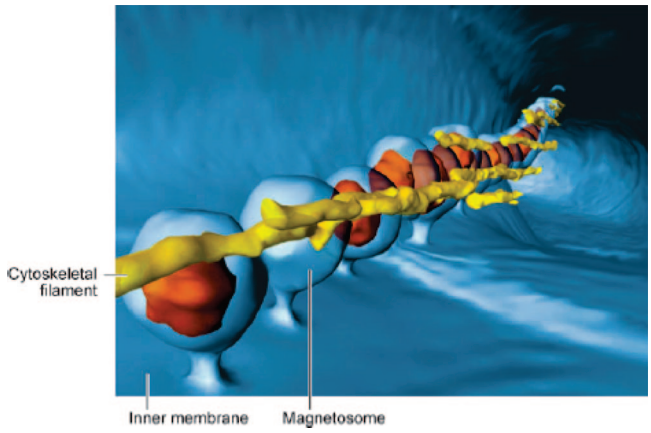

Figure 37. Three-dimensional organization of magnetosomes. An ECT reconstruction of *Magnetospirillum magneticum* sp. AMB-1. The background is the inner membrane, and magnetosomes can be seen as invaginations of the inner membrane. A network of cytoskeletal filaments surrounds the magnetosome chain. Reprinted with permission from ref 332. Copyright 2007 Elsevier Science Publishers.

followed by transport to the magnetosome interior through the opening into the magnetosome, has also been discussed, but is not as yet supported by experimental evidence. It is, however, equally possible that a barrier exists between the periplasm and magnetosome compartments.[332,337] Recent experimental evidence obtained from analysis of magnetite deposition in *M. gryphiswaldense* has, however, indicated that, in this species, Fe(III) is taken up and rapidly converted into Fe_3O_4 in the absence of a precursor phase.[340] It is likely that the crystallization process is mediated by the magnetosome membrane, which contains at least one major protein with molecular weight 22−24 kDa, which appears common to all strains. This specific protein is likely to have specific functions in the accumulation of iron, in the nucleation of the iron oxides, and in redox and pH control.[341] Significant progress has been made in genome-sequencing of several magnetotactic bacteria, which is expected to lead to breakthroughs in understanding of mineralization in these organisms. [332]

3.2.2.2. Calcite Single Crystals in Coccolithophorids. Coccolithophorids are a major group of marine algae that are characterized by their ability to produce calcium carbonate scales, which decorate the exterior surface of the cell.[231,342] Produced intracellularly, the coccoliths are transferred to the outside of the cell, where they form an elaborate exoskeleton, termed the coccosphere. Coccoliths are classified in terms of two distinct ultrastructure types, namely, the heterococcoliths, which consist of radial arrays of complex crystal units, and the holococcoliths, which are formed from arrays of a large number of small, morphologically simple single-crystal units.[342] In this section, we will look specifically at the formation of the coccoliths of *Emiliania Huxlei*, which provides a well-studied organism producing complex single-crystal morphologies via intravesicular growth.

The coccolith scales of *Emiliania Huxlei* each comprise about 30−40 hammerheaded units that are organized in a ring to give a double-rimmed structure (Figure 38). The remarkable thing about these units is that, despite their complex form, each is a single crystal of calcite. Indeed, in common with the skeletal elements of echinoderms, whose unusual form led to considerable discussion about whether they were single crystals or polycrystalline arrays, it was not until high-resolution transmission electron microscopy

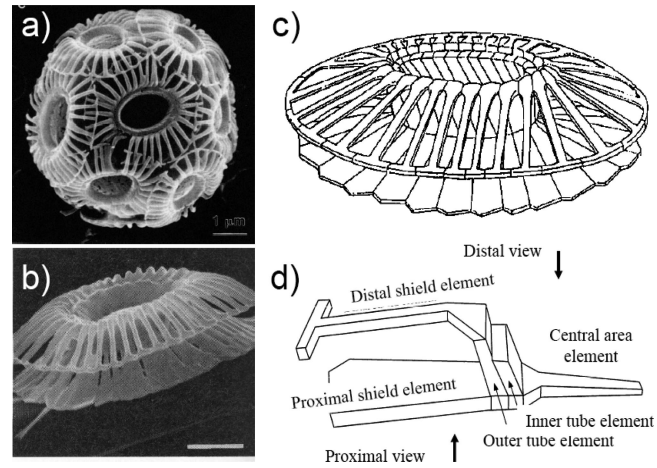

Figure 38. (a) Coccosphere of *Emiliana huxleyi*; (b) coccolith scale viewed approximately side-on. The scale consists of a ring of about 30 hammerheaded calcite crystals that together produce a double-rimmed structure. Scale bar = 1 μm. (c) Drawing of coccolith based on an elliptical array of discrete structural units. (d) Individual structural unit from a coccolith plate showing calcite single crystal with various growth elements. Reprinted with permission from ref 37 ((Mann, S. *Biomineralization: Principles and Concepts in Bioinorganic Materials Chemistry*; Oxford University Press: Oxford, U.K., 2001). Copyright 2001 Oxford University Press (www.oup.com).

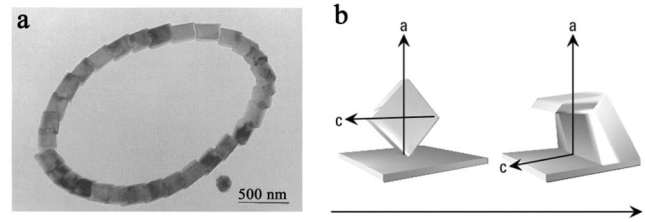

Figure 39. (a) Protococcolith ring of *Emiliania huxleyi* and (b) time-dependent changes in the morphology of a developing hammerhead-shaped crystal unit in a coccolith. Figure (a) reprinted with permission from ref 37 (Mann, S. *Biomineralization: Principles and Concepts in Bioinorganic Materials Chemistry*; Oxford University Press: Oxford, U.K., 2001). Copyright 2001 Oxford University Press (www.oup.com). Figure (b) reprinted with permission from ref 23. Copyright 2008 John Wiley & Sons.

(HRTEM) demonstrated that the crystal lattice of the hammerheaded units was continuous that their status as single crystals was completely accepted.[343] The form of the hammerheaded structural units is described in terms of a basal plate (the proximal shield element) and a hammerhead-shaped upper plate (the distal shield element), which are separated by a central wall. While the morphology of the base plate retains much single-crystal character, with the display of a basal (010) face and (−108) end faces, the upper element is curved with rounded faces. The calcite *c*-axis lies parallel to the direction of elongation of the elements and in the plane of the proximal shield element, while the *a*-axis lies perpendicular to the plane of the ring. The units are then organized in the coccolith such that the *c*-axis is oriented at 20° to ring radius. This orientation is always in a clockwise direction, endowing the coccolith with morphological chirality.[344] The orientation of these units must be defined at nucleation.[342]

The complex form of the coccolith primary units is generated by intravesicular growth, and the vesicle itself is shaped through proximity to various cellular organelles.[345] Studying formation of the coccolith units at different stages of development has provided a detailed picture of their

formation and emphasizes how different biological control mechanisms can be phased in over time, giving rise to an elaborate product morphology.[345,346] Development of the protococcolith ring of *Emiliana huxleyi* begins with formation of an organic base-plate scale and the assembly of vesicles along the rim of this plate. Nucleation then occurs within the vesicles in a highly oriented fashion to generate a ring of interlinked calcite crystals whose crystallographic alignment defines the final orientation of the mature hammer-headed crystals. At this point in development, the organism exerts little control over the crystal morphology, and the calcite crystals are 40 nm thick rhombohedral plates, which are inclined to the plane of the ring. With further growth in the spatially constrained reaction environment, the morphology of the crystal becomes defined by the form of the vesicle. The plates grow to a height of 100 nm, where they impact the boundaries of the vesicle, and radial outgrowths along the *c*-axis from the top and bottom faces generate a Z-shape. These units become interlinked by selective growth along the inside rim, and further radial growth from the base and top of the element produces the proximal and distal shield elements. The coccolith vesicle is in close contact with the developing crystal, and the form of this shaped organic environment defines the final morphology of the mature coccolith elements. Finally, when the coccolith plate has fully developed, it moves to the cell wall where it is extruded from the cell to form a spherical shell of coccoliths.

Given the current interest in amorphous calcium carbonate as a general precursor phase to crystalline calcium carbonate polymorphs (see section 2.1.5), it is interesting to speculate a little about the possible role of ACC as a precursor in coccolith formation. Looking at calcification in the coccolithophorid *Pleurochrysis carterae*, 25 nm Ca-rich, calcium/polyanion particles are produced in vesicles and are then transferred to the coccolith saccule during mineralization.[347] Particles are present prior to mineral deposition and throughout growth of the coccolith. The particles do not adhere to the growing crystal in high density, and it is suggested that they simply act as a carrier of the Ca^{2+} ions, releasing the cations possibly through the action of a polyanion-degrading enzyme or pH change. At termination of growth, the coccolith crystal is coated with an amorphous, carbohydrate-rich layer. Notably, the polyanions are not incorporated into the mineral phase, although the product coccolith is coated with an amorphous, polysaccharide-rich coating. Clearly, these particles closely resemble the ACC precursor particles observed in sea urchin larvae. However, as a marked distinction with that organism, there is no evidence that the calcite mineral does not precipitate directly, suggesting that the particles seen simply provide a Ca-rich source, enabling more rapid crystallization. Notably, analogous electron-dense particles have not been observed in *Emilania huxleyi*.[347] In *Emilania*, the coccolith saccule is attached to a reticular body, whose large surface area may provide a high concentration of Ca pumps to enable rapid mineralization. A further interesting observation on coccolith mineralization is that gentle demineralization of an *E. huxleyi* coccolith leaves an organic replica of the entire structure (Figure 40).[348] The composition of this framework is not known. That such a well-defined organic matrix remains after demineralization raises the possibility that the single crystal units of these coccoliths grow within a gel-like medium, the viscosity of which may contribute to maintenance of the coccolith vesicle shape and enable the organism to produce the calcite crystals with high reproducibility.

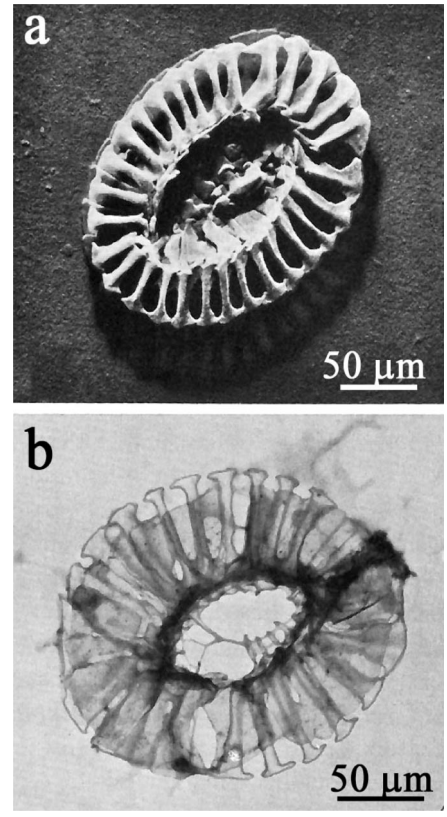

Figure 40. Transmission electron micrographs of (a) isolated coccolith (shadowed) and (b) organic framework left after demineralization of an isolated coccolith of *Coccolithus huxleyi.* Reprinted with permission from ref 348. Copyright 1970 Appleton−Century−Crofts.

3.2.3. Sea Urchin Skeletal Elements. The skeletal elements of sea urchins exhibit truly remarkable single crystal morphologies.[349] Despite the finding of crystallographically oriented nanoparticles in sea urchin spicules by Oaki and Imai[128] or Sethmann et al.,[350] which indicate them to be mesocrystals,[114] we will treat them here as single crystals because high-resolution X-ray diffraction studies are consistent with this definition. Additionally, Oaki and Imai[127] have shown that they form from amorphous precursors with possible mineral bridge connections between the nanoparticle building blocks. They are, therefore, a framework of crystallographically connected nanocrystals, which satisfies the definition of a single crystal (for a schematic structure, see also Figure 21b).

Each spine and skeletal plate is a single crystal of calcite, and yet examination of the microstructure reveals a complex, spongelike structure containing channels of diameter 10−15 μm and bounded by continuous curved surfaces. The surface of some species of echinoid skeletal plates also resemble a triply periodic minimal surface (TPMS), namely, a cubic P-surface, which has a pair of identical subphases on either side of the surface such that the volume fraction of each phase is 0.5 (Figure 41).[14,351] Minimal surfaces are defined as possessing zero-mean curvature, such that the principal curvatures are equal in magnitude but opposite in sign at every point. Triply periodic minimal surfaces have structures that are also periodic in three independent directions.[351] TPMS are common throughout the natural world, having been observed, for example, in surfactant−water systems,

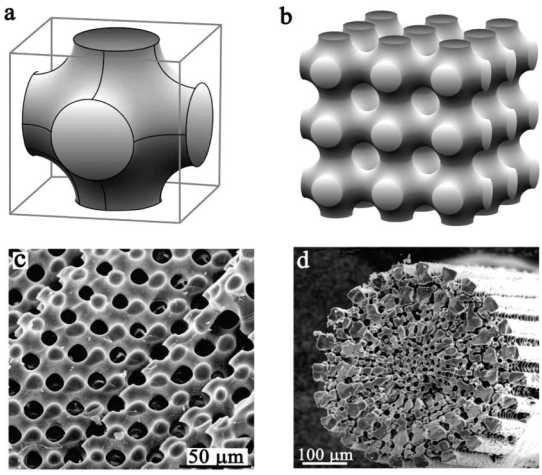

Figure 41. (a) Schematic diagram of the primitive unit cell and (b) periodic structure of Schwarz's P surface, (c) a cross section through a sea urchin skeletal plate showing the resemblance to the P surface, and (d) a cross section through a sea urchin spine. Figures (a) and (b) reprinted with permission from ref 353. Copyright 2007 Royal Society of Chemistry.

silicate mesophases, block copolymers, and cell membranes.[351,352] Notably, all of these structures are produced in self-assembly processes. It is, therefore, interesting to speculate about possible mechanisms that could drive the formation of the environment in which echinoderm skeletal elements precipitate.

As is characteristic of crystalline biominerals with smooth, curved surfaces, echinoderm skeletal elements form within vesicles, whose gross morphologies define the form of the product biomineral.[231] While this has been recognized for a long time, recent studies on the development of sea urchin larvae and on the regeneration of adult spine tips have revolutionized our understanding of the calcification process itself, demonstrating that calcite formation in both larvae and adult sea urchins proceeds via an amorphous calcium carbonate precursor phase.[6,8,50,298]

Sea urchin larval spicules initially present a triradiate morphology and curved surfaces.[354] Mineralization begins by formation of an oriented, regular rhombohedral crystal of calcite and continues through the addition of ACC particles, forming smooth rounded rods that grow out in the direction of the *a*-axis (Figure 42). The ACC particles are formed in the endomembranous system and are then transported into the spiculogenic compartment.[6] X-ray diffraction studies of isolated spicules demonstrated that ACC is present in relatively large amounts during the first stages of spicule growth and that transformation into crystalline calcite occurs with time. [50] Notably, the transformation process of the biogenic ACC is much slower than that for synthetic ACC, but it is also significantly faster than the crystallization of dried spicules isolated from the larvae, suggesting that the organism actively controls the crystallization process. An interesting observation pertaining to the mechanism of ACC formation and crystallization is that the inner membrane of the syncytium is tightly bound to the surface of the growing spicule,[354] suggesting that growth of the spicule occurs by transfer of ACC into the spiculoghenic cavity, rather than from its in situ precipitation.[6] The absence of an aquous phase is also consistent with thermogravimetric analysis, which shows that this transient ACC phase is anhydrous, in sharp contrast to stable biogenic ACC and synthetic ACC.[298] Interestingly, no continuous crystallization front is observed within the spicule, which indicates that crystallization may occur via a solid-state transformation process, in which domains of short-range order align and coalesce, rather than by dissolution-reprecipitation.[5,6] Examination of the regeneration of fractured spine tips in adult sea urchins demonstrated that calcification in adult sea urchins similarly occurs via an ACC precursor phase.[8]

It is interesting to compare the mechanism of formation of the sea urchin skeletal plates with that of the coccolith single-crystal units. In both cases, an oriented rhombohedral calcite crystal is formed first, which defines the ultimate orientation of the product biomineral. At this stage, no morphological influence is exerted on the form of the crystal. Complexity in crystal shape develops with time, when the crystal impinges on the boundaries of the crystallization

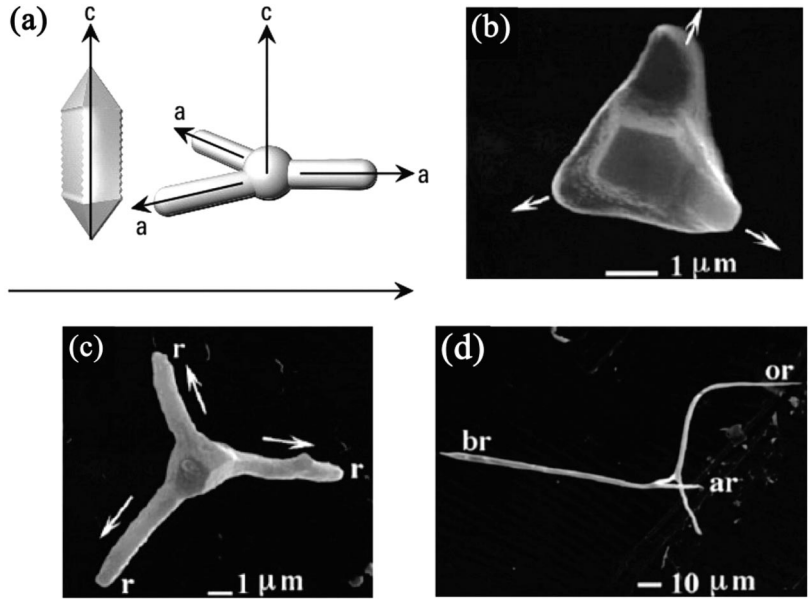

Figure 42. Time-dependent changes in the morphology of a developing sea urchin larval spicule. (a) Schematic diagram of spicule development, (b) 20 h embryo sea urchin larval spicule of *Paracentrotus lividus* with an initial rhombohedral calcite crystal and three radii starting to grow. (c) Triradiate spicule (25 h embryo) and (d) fully developed pluteus spicule (48 h embryo) composed of the central triradiate portion and three rods growing roughly in the *c*-axis direction. Figure (a) reprinted with permission from ref 23. Copyright 2008 John Wiley & Sons. Figures (b) and (c) reprinted with permission from ref 50. Copyright 1997 Royal Society of Chemistry.

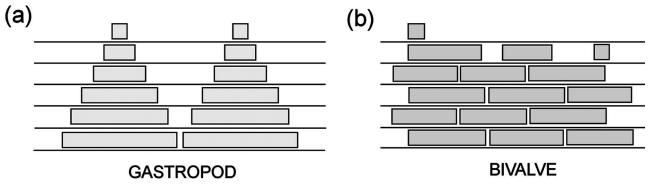

Figure 43. Schematic diagram of nacre structure: (a) columnar nacre in gastropods and (b) sheet nacre in bivalves. Reprinted with permission from ref 37 (Mann, S. *Biomineralization: Principles and Concepts in Bioinorganic Materials Chemistry*; Oxford University Press: Oxford, U.K., 2001). Copyright 2001 Oxford University Press (www.oup.com).

environment. While it is perhaps tempting to attribute the noncrystallographic form and curved surfaces of the sea urchin crystals to the existence of an amorphous precursor phase that can be shaped with ease, in vitro experiments have clearly demonstrated that an amorphous precursor is not required to produce these complex morphologies (see section 4.1.7). Direct precipitation of a mineral within a confined geometry can yield single crystals with morphologies identical to sea urchin skeletal plates.[234,295−297] Thus, while it is likely that ACC acts as a precursor to crystalline calcium carbonate phases in many more organisms than currently identified, exhibition of a noncrystallographic morphology is not in itself a demonstration of the operation of this mechanism.

3.3. Polycrystalline Biominerals

Many biominerals with complex morphologies are polycrystalline structures generated by organized assembly of single-crystal components. An excellent example of this is the sphere of calcite scales (coccoliths) formed by the single-cell algae *Emilania huxleyi* (Figure 38). A general description of this organism has been given in section 3.2.2.2, where the mechanism of formation of each of the 30−40 single crystal hammerhead-shaped calcite crystals that form the scales was described. In this section, we will address how the more complex structures of the individual scales and, ultimately, the entire coccosphere are formed.

3.3.1. Nacre Formation in Mollusks

Aragonitic mollusk shell nacre provides a classic example of an oriented biomineral. Constructed from tablets of aragonite that are separated by organic sheets, the structural organization of nacre differs between the three principal mollusc classes (Figure 43 and Figure 44). Nacre in gastropods is described as "columnar nacre" and comprises stacks of aragonite crystals oriented such that the *c*-axes of the crystals are perpendicular to the shell surface, and the *a* and *b* axes are coaligned within a given stack. The stacks of crystals are randomly oriented. In bivalves, the nacre takes on a "bricks and mortar" appearance where all three axes of the individual aragonite tablets are mutually aligned and is described as "sheet nacre". In common with bivalves, nacre in *Nautilus* (a cephalopod) shows 3D alignment, but it exhibits a columnar structure. The growth behavior is such that towered and terraced growth occurs simultaneously.[287,355]

The individual aragonite tablets are separated by interlamellar organic sheets constructed from thin layers of β-chitin, associated with silk fibroin-like proteins and acidic macromolecules (Figure 45).[285,286] The structure of the organic matrix has been much studied and historically was believed to comprise thin layers of β-chitin sandwiched between layers of β-sheet silk fibroin-like proteins, which were oriented orthogonal to the chitin fibrils and which supported acidic macromolecules. The *a*-axes of the aragonite lattice are aligned with respect to the chitin fibers, and the acidic macromolecules were postulated to display β-sheet domains and exhibit a well-defined structural relationship with respect to the insoluble framework. Crystals were then considered to nucleate at specific sites on the preformed insoluble matrix due to binding of the Ca^{2+} ions to the matrix in an organization mimicking the Ca^{2+} ions in the *ab* face of aragonite. This structural match thereby selected the nucleation face and its orientation (Figure 46).[285,286]

Recent work using cryo-TEM to study the nacreous layer of a bivalve *Atrina serrata* in the hydrated state has, however, suggested that the silk is actually in the form of a hydrated, nonordered gel, located between, rather than within, the sheets of chitin fibrils.[357] The acidic macromolecules adopt

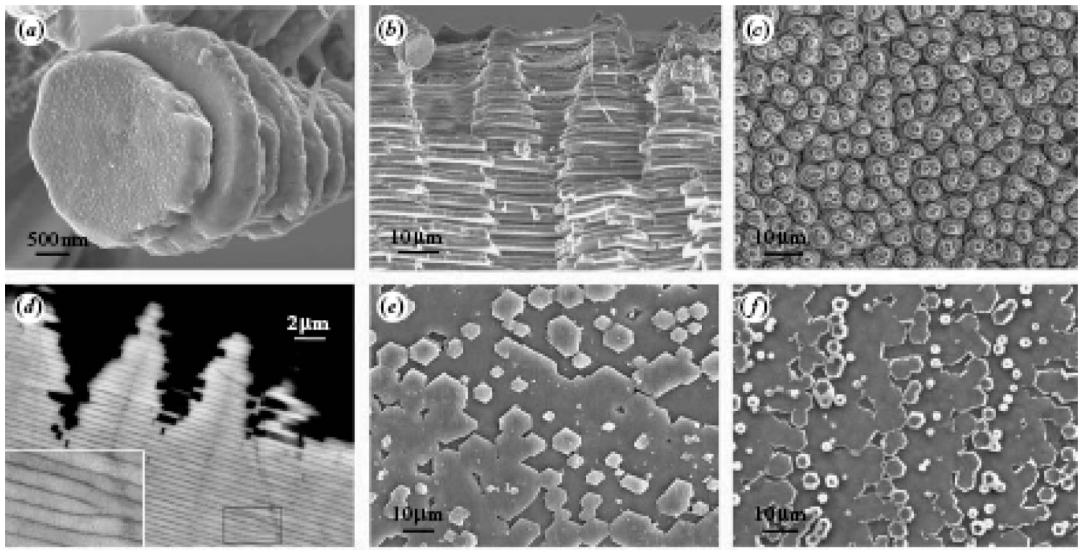

Figure 44. Scanning electron micrographs of nacre morphologies (a−d) gastropod nacre: *Calliostoma zyziphynus* showing (a) a tower of tablets and (b) a fractured transverse section. (c) *Bolma rugosa* displaying towers of tablets and (d) *Gibbula pennanti* back-scattered electron scanning of a transverse section: (e, f) bivalve nacre; (e) *Anodonta cygnea* and (f) *Atrina pectinata* displaying growth fronts made up of tablets. Reprinted with permission from ref 356. Copyright 2006 The Royal Society.

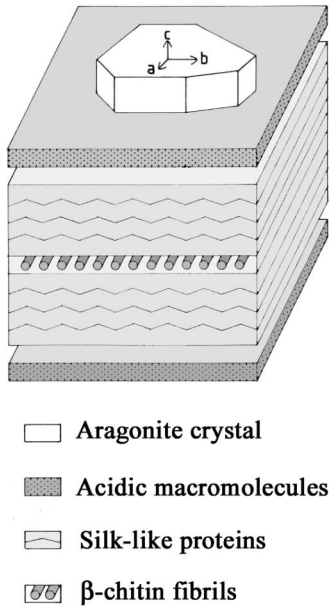

Figure 45. Schematic diagram of the historical model of the composition of individual organic matrix sheets of mollusk shell nacre. Adapted from ref 285. Copyright 1984 The Royal Society.

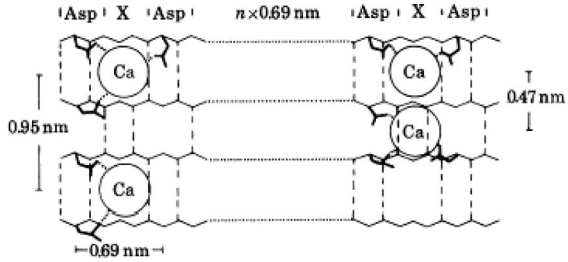

Figure 46. Schematic diagram of the possible binding modes of Ca^{2+} ions to the surface of a β-sheet containing aspartic acid residues. The distances given to those measured by XRD of the insoluble matrix protein fraction which adopts a β-sheet conformation. Reprinted with permission from ref 285. Copyright 1984 The Royal Society.

a β-sheet conformation in the presence of calcium ions and appear to be located in high density at the center of each aragonite tablet. Surrounding this probable nucleation site is a domain rich in sulfate groups, which has been suggested to exhibit an ionotropic effect, increasing the cation concentration at the carboxylate groups forming the nucleation site (Figure 47).[358] Mineralization is then believed to proceed via an amorphous precursor phase.[178] While there is currently no definite proof of this mechanism, there is good circumstantial evidence, based on the fact that calcification in mollusk larvae proceeds via an ACC precursor[7] and the fact that ACC- or vaterite-containing granules have been located in adult mollusks. [178] Further, high-resolution imaging of individual aragonite tablets from the gastropod *Haliotis laevigata* has revealed a thin (~5 nm) layer of ACC surrounding each tablet, which could indicate crystallization via an amorphous precursor phase. On crystallization, organic additives and impurities present within the ACC phase may be expelled from the newly formed crystalline material, ultimately producing an impurity-rich amorphous zone on the outer surface of the plates.[359]

The mechanism of crystal growth and orientational control in nacre is under hot debate. In all molluscs, the first-formed aragonite tablets nucleate on an organic sheet, oriented with

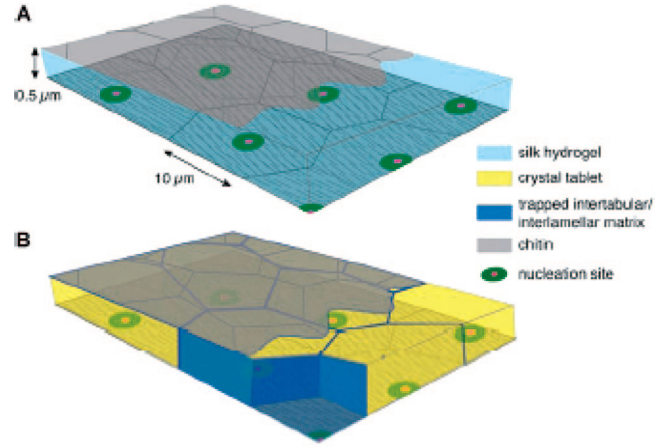

Figure 47. Schematic representation of the suggested model for nacre formation (A) before mineralization and (B) after mineralization. (A) Assembled organic matrix prior to mineral deposition. The microenvironment is formed by two layers of β-chitin, with a gel comprising silklike protein filling the space in between. Part of the upper chitin layer (upper right) has been removed to show the silklike protein gel filling. Nucleating proteins are adsorbed on the β-chitin sheet. Note that the polygonal outlines of imprints are created only during mineralization and have been added to this scheme for added clarity only. (B) Mineralized nacreous layer. Nucleation of aragonite is induced on and by the acidic proteins, and as the mineral grows, water and silk are displaced. The latter is eventually trapped between adjacent tablets and between the tablet and the chitin layer. Reprinted with permission from ref 178. Copyright 2006 Wiley-VCH.

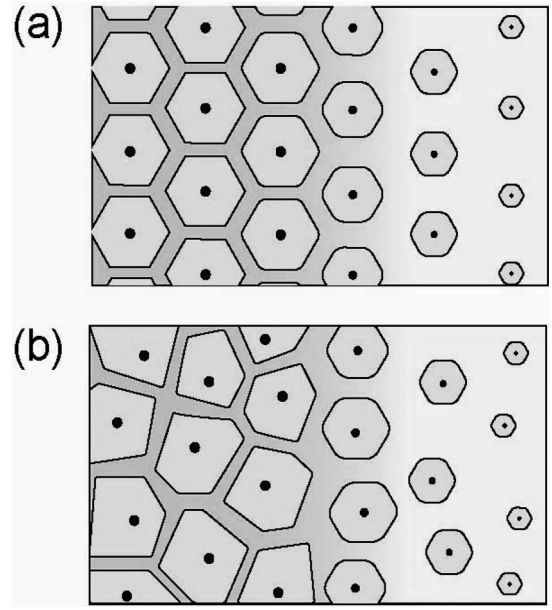

Figure 48. Model of the mineralization front within the film of extrapallial fluid: (a) a Voronoi diagram for a plane lattice of nuclei and (b) a more realistic case with the same amount of nuclei but less well-ordered. Adapted from ref 360. Copyright 2005 Elsevier.

the *c*-axis perpendicular to the shell surface. The crystals then grow along the *c*-axis until they impinge on the chitin-based organic matrix that defines the thickness of the crystals as ~0.5 μm.[356,361] The crystals continue to grow in the $a-b$ plane until they contact each other, defining their polygonal morphologies. The tiling of nacre in *Pinctada margaritifera* has been shown to correspond well to a Voronoi diagram in which every point in a given tablet is closest to the nucleation center of that crystal.[360] Figure 48 shows how the morphol-

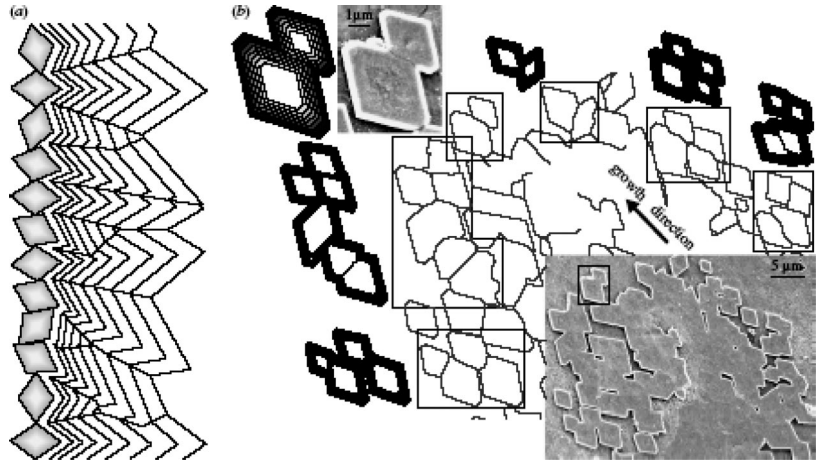

Figure 49. (a) Model of competition between hypothetical nacreous tablets in the plane of the lamella (i.e., that containing the crystallographic *a*- and *b*-axes). The boundaries between growing crystals are drawn along the intersections between equivalent growth increments. Only those crystals whose longest diagonals (*b*-axes) are parallel to the growth direction of the lamella (to the left) survive preferentially. (b) Geometrical reconstruction of boundaries between crystals using the same procedure as in (a).We have reproduced several cases in the growth front of a lamella of *P. hirundo* (lower right photograph). Nacre tablets are rhombic ({110} faces, with slightly developed {010} faces), with the *b*-axis along the longest diagonal. A sketch is also provided for clarity. In all selected cases (framed), the contacts between crystals fit quite closely with those produced by the model. Reprinted with permission from ref 288. Copyright 2006 The Royal Society.

ogy of the tablets can vary according to the distribution of nuclei, such that an hexagonal array of nucleation centers gives rise to perfect hexagonal crystals, while irregular tablet morphologies are generated from a more irregular distribution of nuclei.

The mechanism by which orientational control is achieved is not clear. Selection of an (001) face at nucleation can be attributed to the nucleating organic matrix exhibiting the appropriate charge density to nucleate this face.[288] In gastropods, where the tablets within a stack are perfectly aligned, but where separate stacks show no mutual alignment, there is good evidence that crystallographic alignment is achieved by growth through pores in the organic sheets separating the adjacent aragonite tablets.[126] Individual stacks are then effectively single crystals. In bivalves, where a high degree of alignment is observed in the $a-b$ plane, the mechanism by which orientational control is achieved is even more intriguing. Morphological and crystallographic examination of nacre in a number of molluscs has suggested that the degree of alignment in the $a-b$ plane and the morphological regularity of the crystals improves with increasing thickness of the nacreous layer, until a steady stage is reached at $\sim$500 μm from the prism-nacre boundary.[287,288] This was interpreted in terms of competition between growing crystals in the direction of the growth front. The rhombohedral, {110} bound aragonite tablets grow fastest along the *b*-direction, such that crystals oriented with this axis parallel to the growth direction dominate (Figure 49). Providing that the orientation of the crystals in each nacreous layer is translated to the crystals in the subsequent layer, continued growth ultimately leads to each nacreous layer displaying a high degree of orientational order in the $a-b$ plane, as well as in the *c*-direction. Indeed, it has been postulated that mineral bridges between crystals in adjacent lamellae may also exist in bivalve nacre, but that these may be more widely spaced than in gastropod nacre.[356] That orientation in the $a-b$ plane is achieved for molluscs but not gastropods can be attributed to their contrasting growth mechanisms. While growth of nacre in molluscs is sheetlike, in gastropods it is columnar. Crystals in the same lamella in adjacent columns grow separately and only contact each other after the growth front has advanced well in front of their location, such that growth of individual tablets cannot affect the orientation of adjacent crystals.[288,356]

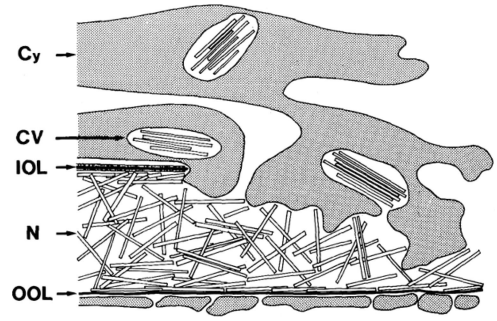

Figure 50. Schematic diagram of the formation of the porcelaneous test of *Calcituba polymorpha*. Bundles of calcite needles form within vesicles (V) in the cytoploasm (Cy). The first deposited needles (N) are arranged in an oriented fashion on the inner surface of an outer organic layer (OOL) and then become randomly oriented in the test wall. A final layer of oriented crystals is deposited last, parallel to the inner organic lining (IOL). Reprinted with permission from ref 363 (Hemleben, C. H.; Anderson, O. R.; Berthold, W.; Spindler, M. In *Biomineralization in Lower Plants and Animals*; Leadbeater, B. S. C., Riding, R., Eds.; Clarendon Press: Oxford, U. K., 1986; Vol. 30, p 237). Copyright 1986 Oxford University Press (www.oup.com).

3.3.2. Foraminifera—A Biogenic Mesocrystal

A second example of a polycrystalline biomineral displaying a high degree of orientational order is provided by the foraminifera. Foraminifera are a highly diverse type of marine protozoans, comprising approximately 4000 different living species, and are either planktonic, living in surface water, or benthic, living on the ocean bed.[231,362] These single-celled organisms have either an organic or mineral-based test that comprises one or more chambers.[363] There are three general types of mineral test. Agglutinated tests are formed from particles picked up from the environment and cemented together to form a test, porcelaneous carbonate tests (imperforate tests) comprise calcium carbonate needles produced within the organism and subsequently transferred to the

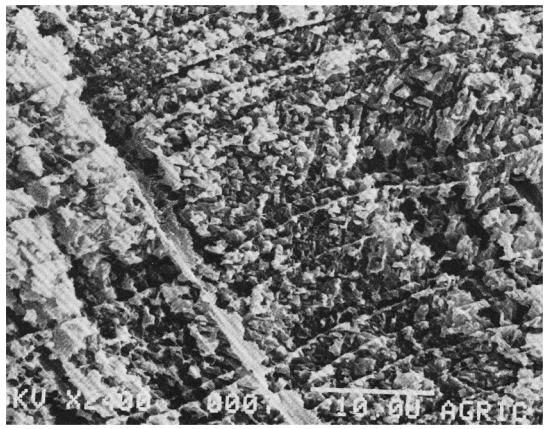

Figure 51. Scanning electron micrograph of the fixed, etched, and critical point dried shell of the benthonic foraminifer, *Heterostegina depressa*, showing the lamellae separated by organic matrix layers. Note that the shapes of individual crystals are very difficult to identify (scale bar = 10 μm). Reprinted with permission from ref 362. Copyright 1986 CRC Press.

surface of the organism, while hyaline carbonate tests (perforate tests) are deposited directly at the site of wall construction in association with an organic membrane.[231,363,364] Hyaline tests are further described as (i) granular, when the calcite particles comprising the test are oriented with their {104} faces approximately parallel to the test wall,[362,365] (ii) radial, where the test is textured such that the component calcite granules are oriented with their *c*-axes perpendicular to the inside surface of the wall, and (iii) single crystal, when the entire calcitic test behaves as a single crystal under X-ray diffraction and polarized light.[364]

Considering first the general mechanisms operating to precipitate porcelaneous tests, the test of *Calcituba polymorpha* is formed from magnesian calcite needles. These are precipitated as bundles in intracellular vesicles and are then transported from the cytoplasm to a large compartment enclosed by an organic sheath, which provides the site of wall deposition. The first crystals deposited in the shell are oriented with respect to the substrate, forming an organized layer, while the remainder of the wall is filled with a random arrangement of crystals (Figure 50).[363] In contrast, the radial wall of hyaline tests form by quite a different process in which mineralization takes place directly at the wall deposition site. Calcification occurs within vesiclelike structures located on either side of a primary organic membrane, which expand and fuse with continued mineralization until a continuous bilamellar calcite wall is formed. The test wall then thickens until it achieves its final dimensions (Figure 50).[363] In each newly formed chamber, the inner lamella forms the interior of the new chamber, while the outer lamella covers both the new and existing chambers.[366] Further, some radial shells have been shown to contain both high and low magnesian calcite, and it has been suggested that high-Mg calcite forms the primary layer, while secondary layers are low-Mg calcite.[362,366]

Examination of the microscopic structure of hyaline tests has demonstrated that they comprise a mosaic of crystal units either oriented with their *c*-axes perpendicular to the inner wall in the case of radial tests or with the c-axes irregularly arranged in granular tests.[364,365] The shapes of these crystalline units are poorly defined, and their sizes vary widely, from approximately 200 nm to several μm, and the boundaries between crystals are poorly defined and irregular, suggesting a penetration of adjacent crystals into each

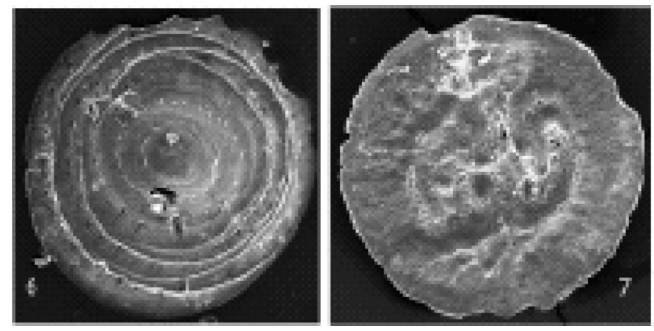

Figure 52. Radial shell of *Patellina corrugata Williamson*, D = 500 μm. Reprinted with permission from ref 368. Copyright 2003 The Palaeontological Association.

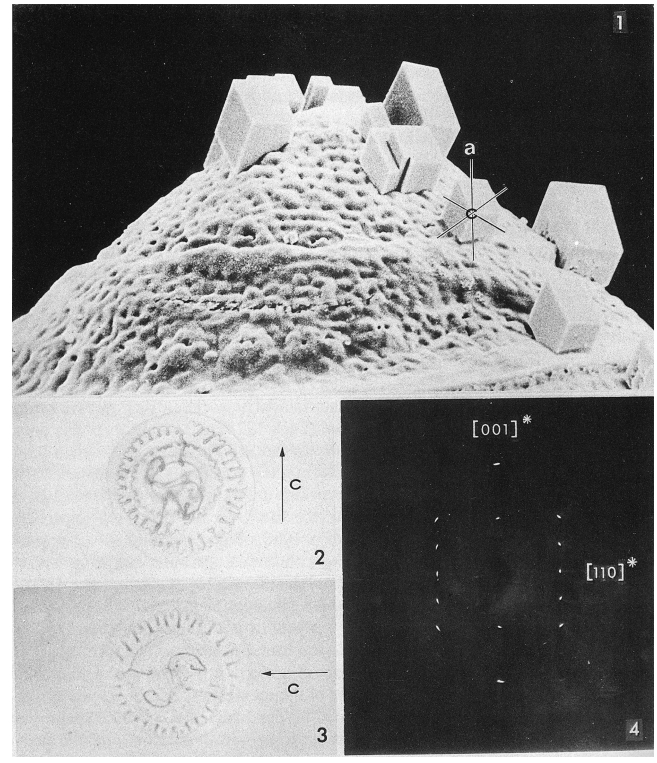

Figure 53. (1) Scanning electron micrograph of *Patellina corrugata* secondary overgrown with calcite crystals. (2, 3) An individual of *Patellina corrugata* viewed in polarized light with crossed-nichols and a gypsum plate. Both views are extinction positions at right angles showing maximum (2) and minimum (3) relief. (4) Buerger precession X-ray photograph showing the single-crystal pattern from *Patellina corrugata.* Reprinted with permission from ref 367. Copyright 1977 The Cushman Foundation.

other.[362] This is also expressed in the rough external appearance of foraminifera shells (Figure 51). Possibly the most fascinating type of foraminifera test are those which behave as single crystals and are described as belonging to the group *Spirillinacea*.[231] Although structural examination of these foraminifera tests shows that they are clearly polycrystalline, comprising crystalline subunits, these crystallites are highly aligned, yielding a mineral with properties consistent with a single-crystal material.[367] Polarization microscopy of the radial shell of *Patellina corrugata* (Figure 52) showed uniform extinction between crossed polars (Figure 53), while diffraction patterns of individual shells were of single-crystal type. Overgrowth experiments with calcite crystals also yielded mutually oriented calcite rhom-

bohedra, further demonstrating the mutual alignment of the crystallites forming the shell. Clearly, the gross morphology of the *Patellina* shells bears no relationship to the crystallography of the underlying crystallite array.

Unfortunately, little is known about the formation of the shell of *Patellina*, although it is likely to show many similarities to the mechanisms described for other hyaline foraminifera. The crystallographic orientation observed in radial tests has been attributed to face-selective nucleation of calcite crystals on the primary organic membrane.[17] It also possible that intergrowth of crystal subunits could play a role in enhancing the degree of crystallographic alignment. The gross morphology of the test is necessarily defined by the constrained environment in which the crystal forms. The relationship between the structure of *Patellina corrugata* and a number of synthetically produced calcite "mesocrystals" is striking. Cölfen et al. have described the synthesis of calcite particles that diffract as single crystals and yet which comprise an oriented array of subunits ("mesocrystals"), using block-copolymer additives to mediate the formation of these structures.[114] Perhaps coming even closer to this biomineral structure are the remarkable calcite polycrystalline aggregates precipitated in gels by Loebmann et al.[369−371] Both of these examples are described in detail in section 4.1. Notably, these synthetic mesocrystals display morphologies that reflect the crystal symmetry of the calcite units, due to their unconstrained growth into the bulk solution.

3.4. Amorphous Biominerals

Some of the most beautiful and structurally complex biominerals, which are exemplified by the inorganic frameworks produced by diatoms and radiolaria, are formed from amorphous silica. Indeed, with no preferred morphology, this mineral would seem an ideal choice for construction of these materials. We will here address the topic of morphological control of silica biominerals, using silicification in diatoms as an example. Diatoms are extremely abundant in freshwater and marine environments, and the mechanisms involved in the precipitation of their silica skeletons have been investigated in some detail.[261,268] Further, in vitro studies of silica precipitation in the presence of macromolecules extracted from diatom silica have provided real insight into the possible role of self-assembly processes in driving pattern formation in diatom frustrules.

3.4.1. Silicification in Diatoms

To start by briefly discussing the mineral skeleton (frustrule) of diatoms, the alga is encased within two interlocking valves, one of which (the epitheca) overlaps the other (the hypotheca) like a lid, together with a number of girdle bands that surround the valves (Figure 54). The top of the frustrule is perforated with many pores, the patterning of which is species-specific, that allow transfer of chemical species between the cell and its environment.[372] Diatoms reproduce through cell division where the nucleus first divides and two new valves are formed within the cell wall. The pair of parent valves then separate and fit over the new valves, such that each daughter cell contains a parental epitheca and a new hypotheca. The dividing population of diatoms therefore reduces in size with time, but size is maintained by sexual reproduction.[233,373]

Development of the characteristic morphology of a diatom frustrule can be illustrated by looking at the diatom *Cosci-*

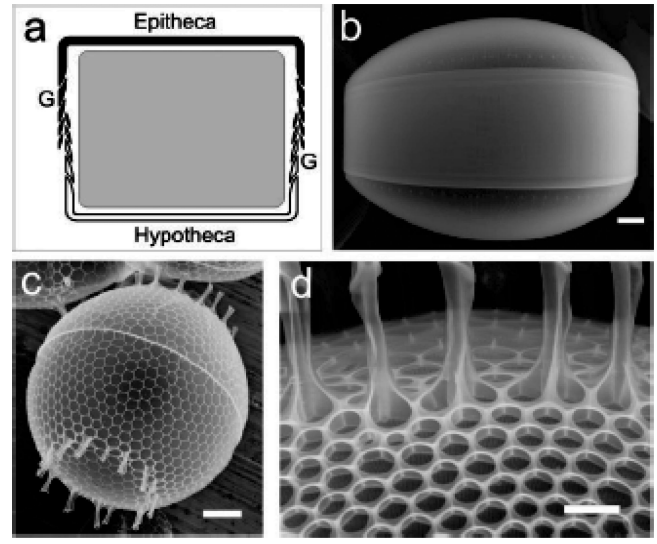

Figure 54. Structure of a diatom cell wall. (a) Schematic cross section through a centric diatom cell: G, girdle bands. (b) Scanning electron microscopy (SEM) image of *Coscinodiscus granii* cell walls (scale bar = 20 μm). (c) SEM image of *Stephanopyxis turris* cell walls (scale bar = 10 μm). (d) *Stehanopyxis turris* cell wall at higher magnification (scale bar = 5 μm). Reprinted with permission from ref 269. Copyright 2006 Wiley-VCH.

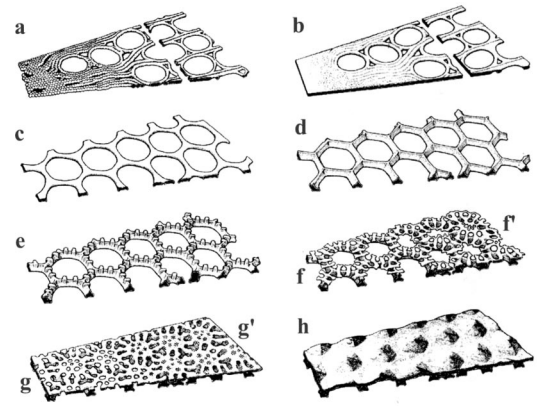

Figure 55. Schematic diagram of valve formation in *Coscindiscus wailesii*. (a) Initial deposition of silicified strands and formation of areolae in base layer, giving rough structure of silica. (b) Initial smoothing of deposited silica, (c) final smoothing of base layer, (d) perpendicular growth of areolar walls, (e) growth of silicified "teeth" from the tops of the areolar walls (f), (f′), (g), and (g′). (h) Growth of silica perpendicular to silicified teeth. Reprinted with permission from ref 375. Copyright 1983 Blackwell Publishing (www.interscience.wiley.com).

nodiscus wailesii, in which the silicon skeleton forms in a precisely timed sequence of interactions (Figure 55).[374,375] Silicification in all diatoms occurs within a specialized vesicle, the silica deposition vesicle (SDV), the shape of which is determined by various components of the cell. An initial pattern for the location of future silica deposition is formed by a close-packed array of large vesicles attached to the cell wall (the areolar vesicles) that determine the location of the shell pores and vesicles of the endoplasmic reticulum (ER), which defines the location of the basal silica layer. The SDVs then form with tubular morphologies and extend first in the plane of the cell wall between the areolar vesicles and then vertically between the vesicles. Polymerization of silicic acid and deposition of silica proceeds continuously with growth of the SDV. Vertical growth stops when the areolar vesicles detach from the cell wall, allowing the SDV

to expand laterally and become attached to the cell wall. The vacant pores become filled with small vesicles, which generate a mold for further patterned silica deposition.

3.4.2. In Vitro Studies of Silicification in Diatoms

Remarkable progress has been made in understanding the biological mechanisms governing both silicification processes and pattern formation in diatoms. This has been largely driven by successful isolation of the macromolecules entrapped within diatom silica and investigation of their influence on silica precipitation in vitro. Silaffin NatSil-1A isolated from *Cylindrotheca fusiformis* is extremely active in promoting silica precipitation in vitro, causing silica precipitation within a few minutes by accelerating polycondensation of silicic acid and acting as a flocculating agent.[261,270] This activity is driven by the formation of supramolecular aggregates of natSil-1A in solution comprising ~700 peptide molecules, which appear to provide a template for silicic acid polycondensation.[376] Further, the active functional groups on the silaffins appear to be the long-chain polyamines, as polyamines alone can promote silica formation in a similar way to silaffins in the presence of inorganic phosphate or other polyvalent anions.[260]

Further investigation of the activity of long-chain polyamines has demonstrated their significance in directing silica formation. Polyamines extracted from the frustrules of *Stephanopyrix turris* precipitated silica nanospheres from a silicic acid solution after a few minutes, but only in the presence of multivalent anions such as phosphates.[270] Indeed, the size of the silica particles could be controlled according to the concentration of phosphate ions. Silica precipitation in the presence of synthetic polyallylamines showed a similar dependence on phosphate concentration and clearly demonstrated the importance of microscopic phase separation in inducing silica precipitation.[376] Nono-, oligo-, or poly(silicic acid) molecules may be adsorbed onto, or dissolved in, the polyamine droplets, forming a coacervate that is subsequently mineralized.[376]

The most intriguing question relating to diatom mineralization has to be the mechanism of pattern formation. Diatoms of the genus *Coscinodiscus* display highly intricate, symmetric patterns comprising a hierarchy of self-similar hexagonal motifs (Figure 56a). The valve pattern of *C. asteromphalus* is yet more complex, appearing as a superposition of at least four hexagonal superstructures (Figure 56b).[269] Pattern formation in *Coscinodiscus* can be interpreted by a mechanism based on phase separation of polyamines in the silica deposition vesicle (SDV).[261] A close-packed organization of microdroplets in the flat SDV generates a hexagonal monolayer that acts as a template for the formation of a honeycomblike silica framework, with silica precipitation occurring at the interface between the solution and the microdroplets (Figure 57a). Silica formation necessarily consumes some of the polyamines, which causes smaller droplets to separate from the surface of the original microdroplet (Figure 57b). Silicification continues on these new structural features, again reducing the amount of polyamines present. Finally, the entire remaining polyamine droplet subdivides into an hexagonal array of small droplets, and silica precipitation is templated by these structures (Figure 57c). Iteration of this mechanism would ultimately lead to the nanoscale patterning observed in the *Coscinodiscus* valves.[376]

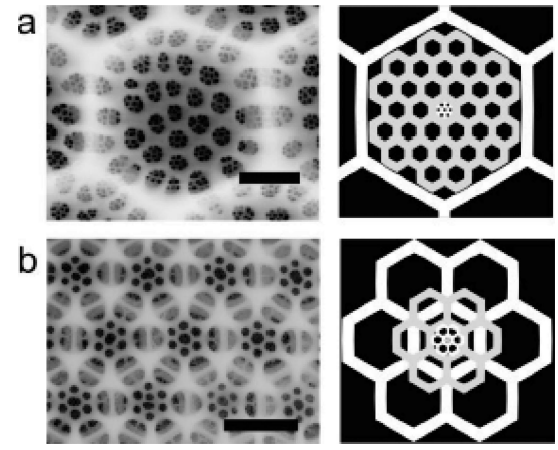

Figure 56. (a) Scanning electron microscopy (SEM) image of *Coscinodiscus asteromphalus* and the interpretation of the valve pattern by superimposition of three hexagonal silica frameworks. (b) SEM image of *Coscinodiscus granii* and the interpretation of the valve pattern by superimposition of four hexagonal silica frameworks (scale bars = 1 μm). Reprinted with permission from ref 269. Copyright 2006 Wiley-VCH.

This proposed mechanism is supported by strong experimental evidence.[269,376] While long-chain polyamines and phosphate ions can together direct the formation of silica sols from silicic acid solution, this route alone does not produce structures analogous to the silica networks produced by diatoms (Figure 58a). However, phase-separated polyamine-based microdroplets *can* act as templates for such honeycomb forms when silica sols are employed as the silica source in the place of silicic acid. In this case, silica precipitation occurs around the droplets rather than inside them, as occurs with silicic acid as the silicon source. In the absence of phosphate ions, long-chain polyamines support the formation of silica-based particles in silicic acid solution. These particles exhibit well-defined sizes and are stable for periods in excess of 24 h. Use of these sols as the silica source for silica deposition on the phase-separated polyamine-based microdroplets then yields a silica monolith with internal honeycomb structure (Figure 58b). The long-chain polyamines are, therefore, key to silicification in diatoms, controlling both the rate and mechanism of silica precipitation and formation of the elaborate patterns so characteristic of these biominerals.

4. Bioinspired Routes to Controlling Crystal Morphologies

The previous section described how biology controls the development of mineral morphologies and provided several examples of the strategies used in nature to generate biominerals with complex shapes and structures. These tools include the application of templates and confined reaction environments; spatially controlled mineral deposition; the presence of soluble additives as crystallization modifiers, inhibitors, or nucleation agents; and the vectorial alignment of smaller crystalline subunits. Additional interest in these strategies also comes from their potential application to the bottom-up synthesis of advanced materials, where biominerals can be used as a source of inspiration for the design and fabrication of future materials. On the basis of these ideas, a rapidly developing research field has evolved that is generally termed *bioinspired* or *biomimetic materials chemistry*.[377,378] Bioinspired morphosynthesis provides an important and environmentally friendly route to generate materials with controlled morphologies. Inorganic or organic

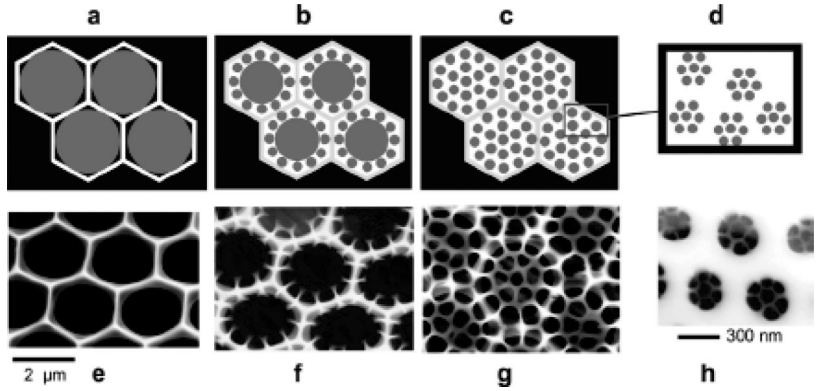

Figure 57. Schematic drawing of the templating mechanism by the phase-separation model (a−d) and comparison with the stages of the developing cell wall of *C. wailesii* (e−h). (a) Monolayer of polyamine-containing droplets in close-packed arrangement within the silica-deposition vesicle guides silica deposition. (b, c) Consecutive segregations of smaller (about 300 nm) droplets open new routes for silica precipitation. (d) Dispersion of 300 nm droplets into 50 nm droplets guides the final stage of silica deposition. Silica precipitation only occurs within the water phase (white areas). The repeated phase separations produce a hierarchy of self-similar patterns. (e−h) SEM images of valves in statu nascendi at the corresponding stages of development. Reprinted with permission from ref 261. Copyright 2002 American Association for the Advancement of Science.

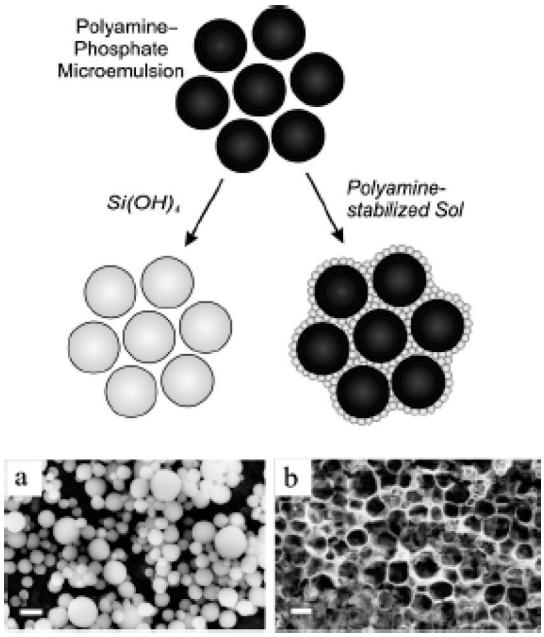

Figure 58. Silica formation guided by emulsion droplets formed in the polyamine/phosphate system. The hypothetical scheme on top explains the formation of different silica morphologies if silicic acid or a polyamine-stabilized silica sol is used as the silicon source. The silica morphologies found in corresponding experiments are shown in the SEM images: (a) silica morphology produced with monosilicic acid and (b) silica morphology produced with a polyamine-stabilized silica sol. Scale bars = 1 μm. Reprinted with permission from ref 269. Copyright 2006 Wiley-VCH.

additives can be used to modify crystal growth via classical or nonclassical crystallization pathways, while templates can be applied to limit and define the gross morphology of mineral precipitated within. During the past decade, exploration and application of these bioinspired strategies have enabled complex materials with specific sizes, shapes, orientation, compositions, and structural organizations to be fabricated.[36,379−386]

It is no surprise then that application of biomimetic mineralization principles has enabled the synthesis of complex crystal morphologies, which were previously restricted to the natural world. Further discussion of this subject can be found in various reviews including refs 3, 187, 207, 377, 378, and 387−398.

4.1. Single Crystals and Mesocrystals

This section will discuss the application of biomimetic strategies to the morphological control of single crystals. According to the definition of a single crystal by its single crystal diffraction behavior and the exhibition of large coherence length, mesocrystals with large building units also fall into this category. Because a continuous transition in structure can exist between mesocrystals and single crystals,[22] mesocrystals that show single-crystalline scattering behavior will be discussed under this heading. Additives can influence a crystallization reaction, and therefore the product crystal morphology, from the earliest stages of precipitation as a nucleator or nucleation inhibitor. The same molecule can serve as either a nucleator or an inhibitor, depending on its concentration. An example of this behavior is in the nucleation of calcium oxalate in the presence of glutamic acid,[399] where glutamic acid served as nucleator in the very low concentration regime (2.5−5 ppm) but as a nucleation inhibitor at higher concentrations. The same is true for a large number of additives, both of low molecular weights and polymeric. However, as the influence of the additive on the finally obtained crystal morphology is subtle and often unknown, this morphogenesis pathway is not further discussed here. The same argument is valid for many cases of indirect morphological control where the product crystal is produced via polymorphic transformation, although polymorph control by additives is in itself well-established.[400]

4.1.1. Low-Molecular-Mass Organic Additives

Low-molar-mass additives provide an effective method for changing the morphology of a crystal by face-selective adsorption. They have the advantage that they can be defined by their molar mass and chemistry and, in contrast to polymeric additives, exhibit only a few potential binding sites. This can be an advantage over polymeric additives with multiple binding sites with the same or even different chemical functionalties in copolymers. The application of small, specifically designed molecular additives to control the growth of organic crystals is a well-documented research area.[401] However, the application of this route to inorganic mineral growth is more difficult because of the lack of complexity of the individual components and the simple nature of the surface packing patterns, which make a face-

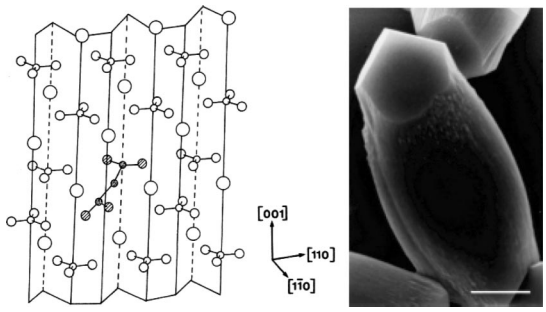

Figure 59. (Left) Perspective drawing of the calcite {1 −1 0} face showing a possible binding site for a malonate anion. (Right) SEM micrograph of a spindle-shaped calcite crystal grown from supersaturated calcium bicarbonate solution in the presence of malonate. Crystal faces approximately parallel to the *c*-axis are severely inhibited by the additive. Reprinted with permission from ref 405. Copyright 1990 Royal Society of Chemistry.

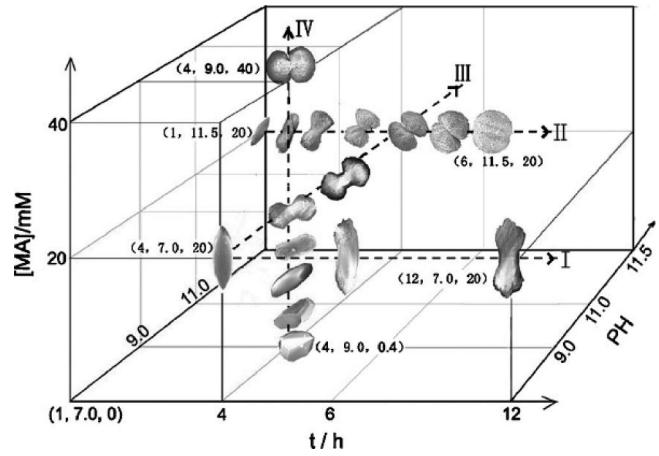

Figure 60. Dependence of $CaCO_3$ morphology on reaction time *t*, pH, and concentration of malic acid. Reprinted with permission from ref 406. Copyright 2007 Elsevier Science Publishers.

selective additive interaction difficult. Nevertheless, low-molar-mass organic additives can be highly selective of the crystal face.[402] Face-selective adsorption on inorganic crystals is typically achieved via electrostatic interaction, but, in principle, all other molecular interactions can also be active. It has been shown that the efficiency of monofunctional organic molecules for face-selective adsorption onto $CaCO_3$ increases with their overall negative charge.[402] In addition, the distances between ligands and their conformations were found to be important for multifunctional molecules.

Tian et al.[403,404] reported the use of simple citrate ions to control the growth of a ZnO crystal, and unusual oriented helical ZnO nanorods and columns were prepared by selective citrate adsorption to the ZnO basal planes forcing the crystal to grow into thin plates. The spiral growth of these plates led to the formation of oriented helical nanorods and columns.[403] The morphology observed in the helical ZnO nanostructure showed a strong resemblance to the growth morphology of nacreous calcium carbonate in red abalone (gastropod *Haliotis rufescens*).

Low-molecular-weight carboxylic acids are a natural choice for $CaCO_3$ because of the similarity of the carboxyl groups on the additive and carbonate groups in the mineral. Carboxylates and the corresponding acids can, therefore, selectively adsorb onto $CaCO_3$ faces, causing a change in morphology. A good example is that of α-ω-dicarboxylic acids, which adsorb to the {1 −1 0} faces of calcite if the carboxy groups are ionized. This inhibits the growth of these faces, leading to the formation of elongated calcite crystals.[405] This selective adsorption is possible because the carbonate ions in the {1 −1 0} faces are oriented perpendicular to the surface, which enables incorporation of carboxy groups by bidentate binding to Ca^{2+}. This is shown in Figure 59. However, the face-specific binding is only possible at low additive concentrations. At higher concentrations, nonspecific binding also takes place and the morphogenesis by face-selective adsorption is lost. The face-selective adsorption capability can be increased by additional charge functionalization of the carboxylic acids as shown in the superior binding of aspartate and γ-carboxyglutamate to succinate and glutamate.[405]

Similarly, *c*-axis elongated calcite single crystals with {104} caps were produced by malic acid adsorption onto {011} calcite faces. The aspect ratio of the crystals could be controlled by varying the malic acid concentration, with the higher additive concentration leading to more elongated crystals.[310,406] Application of low-molecular-weight additives together with Mg^{2+} led to more pronounced morphological changes[310] and variations in morphology. A number of complex polycrystalline structures were also observed, as will be discussed in section 4.2.1. To provide a brief overview here, an increase in the concentration of malic acid led to a gradual transition to polycrystalline, dumbbell-shaped particles.[406] Further development into spherical structures also occurred with time. The observed morphologies also depended on pH, such that a morphology map could be established that allows the empirical prediction of the obtained morphology for a given set of experimental parameters, as shown in Figure 60. *c*-Axis elongated calcite single crystals with {104} caps by selective low-molecular-weight additive adsorption were also reported when $CaCO_3$ was precipitated in the presence of ethylenediaminetetraacetic acid (EDTA).[407]

Another remarkably illustrative case for face-selective additive adsorption is the dyeing of crystals, such as KH_2PO_4 or poppy acid. This is because the dye adsorption can be directly monitored by optical microscopy or even the naked eye provided that the crystals are large enough. For an excellent review on the whole field of dyeing crystals, we can recommend ref 408. Around 1900, Gaubert was the first to find out that organic dye molecules interact quite selectively with distinct growth zones of crystals.[409] For example, methylene blue recognized the {021} faces of phthalic acid and the {101} faces of poppy acid.[410] Further, in addition to interacting with specific faces of a grown crystal, dyes can also become incorporated within a crystal or can modify the rate of crystallization when they are present throughout the crystallization process. As a result, they can taint a whole growth sector where the dye selectively interacts with different crystal faces. A really nice example of this is the K_2SO_4 crystal. Dyes with sulfonate functionalities can selectively interact with different growth faces because of the match of the sulfonate groups with sulfate groups in the crystal lattice, thereby causing the dye to become included in different growth sectors, as shown in Figure 61.[411] This modifies the crystal habit as shown in Figure 61 (left).

Considering the multiplicity of different dye structures, the range of molecular sizes, and the possible presence of extended aromatic structures on ionic flat surfaces, it is hard to believe that this interaction is provided by epitactic recognition alone. In our opinion, dehydration entropy and

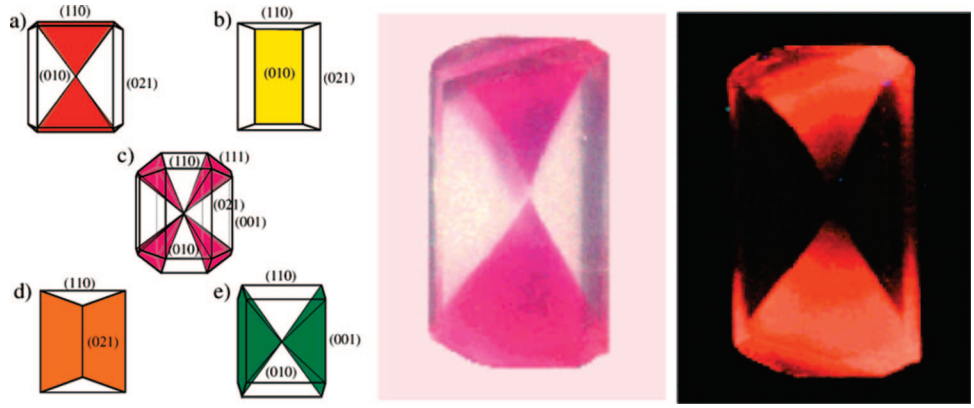

Figure 61. (Left) K_2SO_4 crystals can be selectively dyed in each of the principal growth sectors. Examples include the following: (a) acid fuchsin, (b) pyranine, (c) and (d) orange 2, and (e) naphthol green. (Center) Photograph of sulforhodamine B in the {110} sectors of K_2SO_4. (Right) Fluorescence from the same crystal. Reprinted with permission from refs 408 and 411. Copyright 2000 Elsevier and 2001 American Chemical Society.

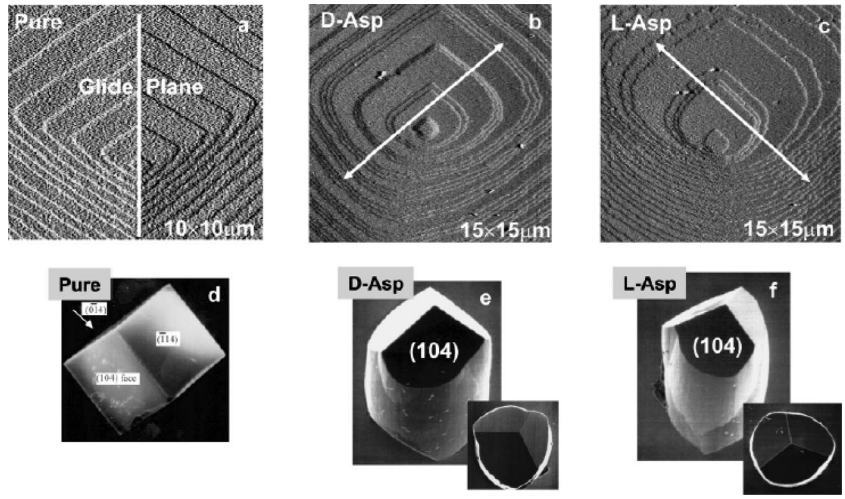

Figure 62. Example of system that exhibits behavior expected for addition of a growth-modifying additive. AFM images of calcite grown in (a) pure solution, (b) solution containing D-aspartic acid, and (c) solution containing L-aspartic acid. The shape changes dramatically and even shows a left−right shape dependence that corresponds to that of the additive. (d−f) show that the resulting crystal shape reflects these changes. Reprinted with permission from ref 303. Copyright 2001 Nature Publishing Group.

polarization interactions will also significantly contribute to the selectivity of dye adsorption. On the other hand, it is clear that the dyes are embedded in the crystal and that the embedding probability obviously depends on the size of the crystal. This again demonstrates the role of long-range contributions (such as polarization forces) in addition to simple surface recognition in enabling the dye to "differentiate" between different sites on a crystal. The selective interaction of dyes with crystal surfaces not only leads to habit modification but can also be used for analytical purposes to reveal crystal-growth mechanisms. This is of special interest in the field of biomineralization. Addadi and Weiner showed that fluorescein-labeled aspartic acid-rich proteins selectively recognized the {001} faces of calcite.[412] DeOliveira and Laursen showed that an aspartic acid-rich peptide labeled with fluorescein could be designed to recognize the {1 −1 0} faces of calcite,[413] and Aizenberg and co-workers used the fluorophore calcein as a marker in the growth of sponge spicules.[304,414]

The adsorption of additives onto crystal surfaces can be highly selective, and even chiral surface textures can be produced with a chiral additive. An example is presented in Figure 62, which shows the effect of right-handed and left-handed aspartic acid on the shapes of growth hillocks and the resulting macroscopic crystals.[303] It is obvious that the shape of the growth hillocks is dramatically altered and the symmetry about the calcite glide plane is broken such that L-aspartic acid gives one chirality, while D-aspartic acid gives the opposite chirality. There are new step directions that can be altered from one side of the glide plane to the other when the amino acid enantiomer is switched from L to D. This observation was explained by changes in the step-edge energies caused by the adsorption of the chiral additives. The selectivity of the adsorption of chiral molecules onto calcite surfaces can even be exploited for polymorph control, as was recently shown by Tremel and co-workers.[415] Addition of D-alanine to growing $CaCO_3$ produced the calcite polymorph, whereas L-alanine produced vaterite, which could be explained by the chiral interaction with growth steps.[415]

Reverse microemulsions/micelles also provide a route to the morphological control of crystals, as demonstrated by the synthesis of $CaCO_3$ and $BaCO_3$ nanowires with extremely high aspect ratios of 1000 and more. These structures were formed through the directed aggregation of nanoparticles in a mesoscopic transformation.[416] Although the precise role of the applied Triton X100 surfactant could not be fully elucidated, nanowire formation was shown to proceed via the initial formation of individual nanoparticles, followed by their aggregation to give fractal aggregates, then short wires, and ultimately long wires. This process clearly

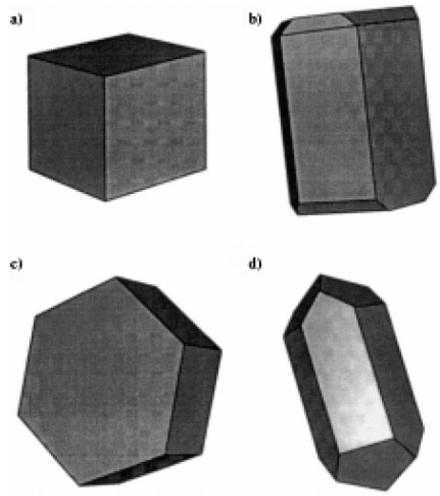

Figure 63. Predicted morphologies based on atomistic simulation of calcite surfaces in the presence of various additives. (a) {10.4} rhombohedral (no additives), (b) {100} faces stabilized by Mg^{2+}, (c) {001} tabular, stabilized with Li^{+}, (d) prismatic rhomb {1−1.0}/{10.4}, stabilized with HPO_4^{2-}. The morphologies are in agreement with experimental results. Reprinted with permission from ref 417. Copyright 1993 Elsevier.

indicates the importance of mesoscale transformation in the development of structure over several length scales.

The morphologies of $CaCO_3$ crystals can, in principle, also be controlled with Langmuir and self-assembled monolayers (SAMs), as these oriented surfactant structures allow for polymorph control as well as oriented nucleation of the crystal.[184] However, because this only allows for the production of a single crystal with one defined truncated edge, monolayer work will only be discussed in relation to the specific case of control of the morphology of single crystals using a 2D template, as discussed in section 4.1.6.

4.1.2. Simple Additives—Ions

Organic as well as inorganic ions, such as Mg^{2+}, Li^{+}, and HPO_4^{2-}, can have a marked effect on crystallization, particularly with regard to habit modification, as observed for instance for $CaCO_3$.[417] This has already been discussed above in section 2.1.2 and is caused by the fact that crystals can lower their surface energies by substitution of surface ions by foreign ions. Consequently, these faces become more strongly expressed in the crystal morphology. For example, atomistic simulations showed a marked energetic preference of the {110} faces of calcite for Mg^{2+}, which therefore become expressed in the product crystal morphology (Figure 63b). However, the role of Mg^{2+} in modifying $CaCO_3$ precipitation is somewhat more complex than simple ion adsorption or substitution onto crystal faces, as it also favors a polymorph change to aragonite or becomes incorporated into the calcite lattice forming magnesium calcite. This is especially important for biomineralization processes and is, therefore, discussed in more detail in section 3.

The substitution of Ca^{2+} ions with Li^{+} ions results in an effective negative charge, which can be compensated for by the addition of Li^{+} in interstitial sites or by incorporation into the crystal lattice.[417] Atomistic simulations showed that the highly charged {001} faces become the most stable ones after Li^{+} incorporation, while all neutral crystal faces become destabilized. Consequently, {001} becomes morphologically dominant (Figure 63c). HPO_4^{2-} replaces CO_3^{2-} most favorably on the {100} faces, which are then expressed in the

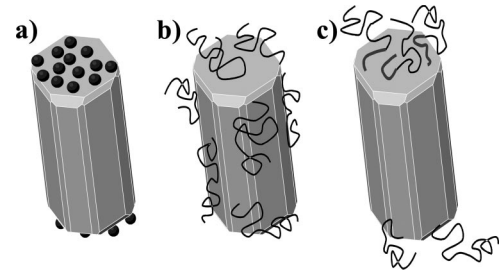

Figure 64. Face-selective adsorption of ions or low molar mass additives (a), steric particle stabilization by polymers (b), and face-selective adsorption and particle stabilization by DHBC (c). Reprinted with permission from ref 207. Copyright 2004 Royal Society of Chemistry.

crystal morphology, along with the standard {104} faces (Figure 63d).[417] Such studies on crystal growth indicate that ionic additives can act in a classical and, thus, predictable way as selective surface-poisoning agents, which is further supported by the results of functionalized latex adsorption onto growing crystals.[67,418] The crystal faces with which the ions interact can be deduced from the final morphologies of the crystals.

4.1.3. Polymer Additives in Classical Crystallization

The influence of small molecule additives on the shapes and structures of inorganic crystals has been well-documented. More sophistication in morphology control is, however, generated when the additives are more complex, polymeric or peptidic in nature, and where they can be designed to bind to specific crystal faces. Recent reports show that so-called double hydrophilic block copolymers (DHBCs)[162,419] are highly effective for stabilization of specific planes of crystals including Au,[420] ZnO,[421−423] calcium oxalate,[162] $PbCO_3$,[424] and $BaSO_4$.[425] This is due to the separation of the interacting and binding blocks in the polymer molecule. DHBCs, therefore, behave as improved surfactants for the temporary stabilization of hydrophilic matter in an aqueous environment. This is illustrated in Figure 64.

From the viewpoint of particle stabilization, DHBCs have an optimized molecular design that combines the advantages of electrostatic particle stabilization with those of steric particle stabilization by polymers. In addition, they are able to selectively adsorb onto certain crystal faces and can, therefore, control particle shape upon further growth. This can also be achieved with ions or low-molar-mass additives (Figure 64a) but then the particle is not sterically stabilized. On the other hand, polymers can also be adsorbed, thereby stabilizing the particle (Figure 64b), but if the polymers are long, they cover several crystal faces rather than being selectively adsorbed. However, a DHBC with a short sticking block combines the advantages of face-selective adsorption with those of particle stabilization due to the longer stabilizing block (Figure 64c). Although these considerations are more valid for nanoparticles, DHBCs can also be successfully used as growth modifiers of microcrystals.

DHBC design is actually analogous to the structures of proteins involved in biomineralization such as statherin or Asp-rich proteins,[252] which have blocks of acidic moieties that interact with a crystal, and other blocks that provide additional functionality.[419] Face-selective polymer adsorption does, however, depend on concentration. At low polymer concentrations, the polymer can select among several faces for adsorption. As adsorption and desorption take place, an

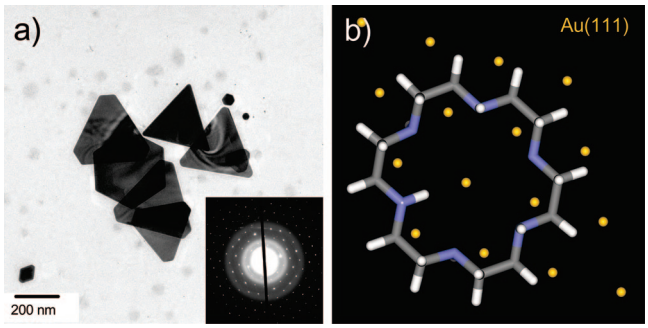

Figure 65. (a) TEM image and electron diffraction pattern of Au nanoparticles synthesized by self-reduction of 10^{-4} M $HAuCl_4$ solution in the presence of the block copolymer PEO-*b*-1,4,7,10,13,16-hexaazacycloocatadecan (hexacyclen) EI macrocycle. (b) Molecular modeling of the Au (111) surface and a hexacyclen molecule in vacuum, which show excellent match of this molecule to the hexagonal atom arrangement on Au (111): yellow, Au; blue, N; gray, C; and white, H. Figure drawn to scale. Reprinted with permission from ref 420. Copyright 2004 American Scientific Publishers.

error-correction routine can become functional, which leads to the adsorption of the polymer on faces where the interaction energy is the largest. If the polymer concentration is increased above a certain level, nonspecific binding will also take place simply because there is too much polymer for face selection and the error correction routine can no longer function. Instead, mineral nanoparticles will be temporarily stabilized and can be used as building units for subsequent self-assembly into superstructures. Similar considerations apply for homopolymers such as polyelectrolytes. Van der Leeden et al. proposed that low additive concentrations in solution can serve as heterogeneous nucleation centers, but upon concentration increase, the same molecules can inhibit further growth of formed nuclei and nanoparticles.[309] This was indeed observed for polyelectrolytes and proteins that act as inhibitor in solution but as nucleator when immobilized on a surface.[43,243,426]

A very illustrative case that shows the potential of DHBCs for controlling crystal morphologies is the controlled morphosynthesis of gold nanostructures in the presence of a PEO-*b*-1,4,7,10,13,16-hexaazacycloocatadecan (Hexacyclen) ethyleneimine macrocycle.[420] A typical image in Figure 65 shows the very thin and, thus, electron-transparent triangles, truncated triangular nanoprisms, and hexagons of gold produced in the presence of this polymer. The particles display high crystallinities as confirmed by the selected area electron diffraction pattern. The results suggest that this polymer can effectively stabilize the (111) faces of Au nanoparticles, which leads to the preferential exposure of these faces and to the formation of the observed very thin plates. This preferential, selective, and strong polymer adsorption onto the (111) faces can be understood on the basis of molecular modeling results, which show a good geometrical match of the interacting nitrogens in the hexacyclen part to the Au hexagons on the (111) face, which effectively minimizes the surface energy. The span distance of the neighboring NH_2 groups well-matches the distance between the neighboring Au atoms within the (111) face, as shown in Figure 65b. It is obvious that the free energy of adsorption and the related lowering of surface energy can be quite high in this case.

Such geometric considerations and model calculations are, however, hard to generalize, as interactions contain not only short-range mutual bonding motifs but also long-range contributions and—most importantly—solvent entropy effects, which are the key for most supramolecular recognition events in water. Application of the same DHBC hexacyaclen-*b*-PEO additive for $CaCO_3$ crystallization did not result in crystal morphologies with well-defined morphologies. A poor match between the hexacyclen molecules and the expressed crystal faces was determined.[427]

Polar peptides and proteins provide an ideal class of additives with which to investigate the interaction of an additive with specific crystal faces and, therefore, to produce well-defined changes in crystal morphologies. They are monodisperse in size and chemical functionality and can form defined secondary structures that can match the surface structures of distinct crystal faces. Laursen and DeOliveira showed an excellent example of using protein secondary structures to control the orientation of chemical functionality and, thus, protein binding to a targeted crystal face. An α-helical peptide (CBPI) with an array of aspartyl residues was designed to bind to the {1 −1 0} prism faces of calcite.[413] The observation of the effect of CBP1 and other peptides on calcite crystal growth was skillfully done by adding the peptide to rhombohedral seed crystals growing from a saturated $Ca(HCO_3)_2$ solution. When CBP1 was added to seed crystals as shown in Figure 66A, and growth was allowed to continue, with the calcite crystals elongated along the (001) direction (*c*-axis) with rhombohedral {104} caps (Figure 66B). After washing the crystals with water and replacing the mother solution with fresh saturated $Ca(HCO_3)_2$ solution, a regular rhombohedron formed by a "repair process" occurred with subsequent growth on the putative prism surfaces (Figure 66C). CBP1 is only about 40% helical when at a temperature of 25 °C, and studded crystals were formed under these conditions by epitaxial growth perpendicular to each of the six rhombohedral surfaces (Figure 66, parts D and E). After washing these crystals and regrowing them in fresh $Ca(HCO_3)_2$ solution, repair of the nonrhombohedral surfaces was again observed. In each study, a new rhombohedron was formed, and thus, six regular rhombohedra overgrew the original seed (Figure 66B).

Single-crystal vaterite nanorods have also been synthesized by a facile solution route using polyacrylamide (PAM) as the crystal-growth modifier.[428] It was found that the reaction time and pH had a great influence on the morphologies and crystal structures of the final products. When the reaction time increased, hollow hexagonal single-crystal vaterite disks were formed, and it was suggested that this metastable vaterite phase may have been stabilized by the polymer molecules. Hexagonal vaterite disks were obtained when the pH was increased. This experiment was also extended to the synthesis of single-crystal $BaCO_3$ nanorods,[428] which indicated that this solution method could also be exploited to synthesize other one-dimensional nanostructured materials.

There are multiple further examples of face-selective binding of polymers to single crystals, leading to changes in crystal morphologies. However, the principles of this strategy remain the same as those discussed previously for low-molecular-mass additives and polymer additives. It has to be remembered that face-selective additive adsorption can only lead to morphologies that are encoded in the crystal structure of the system. In contrast, mesocrystals or polycrystalline aggregates are not so closely defined by the basic crystal symmetry and are, therefore, free to adopt virtually any shape. Face-selective polymer adsorption is also useful

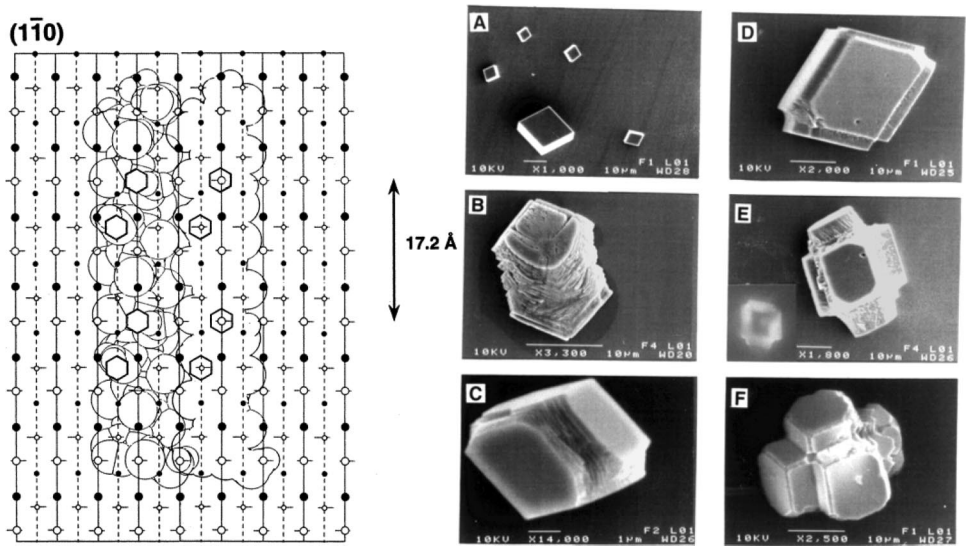

Figure 66. (Left) The footprint of two α-helical peptide (CBP1) molecules binding to the (1$\bar{1}$0) prism faces of calcite. The filled circles are Ca^{2+} ions, and open circles are CO_3^{2-} ions. Large circles are ions in the plane of the surface, and small circles are 1.28 Å behind this plane. The hexagons indicate that peptide carboxylate ions occupy CO_3^{2-} sites on the corrugated surface. (Right) SEM micrographs showing the effect of CBP1 on the growth of calcite crystals. (A) Calcite seed crystals showing typical rhombohedral morphology. (B) Elongated calcite crystals formed from seed crystals in saturated $Ca(HCO_3)_2$ containing ca. 0.2 mM CBP1. (C) "Repair" and re-expression of rhombohedral surfaces when crystals from (B) are allowed to grow in saturated $Ca(HCO_3)_2$ after removal of CBP1 solution. (D and E) Respective earlier and later stages of growth of calcite crystals from rhombohedral seed crystals at 25 °C in saturated $Ca(HCO_3)_2$ containing ca. 0.2 mM CBP1. (F) "Repair" and re-expression of rhombohedral surfaces when crystals from (E) are allowed to grow in saturated $Ca(HCO_3)_2$ after removal of CBP1. Reprinted with permission from ref 413. Copyright 1997 American Chemical Society.

to code nanoparticles for a subsequent self-organization process, which will be discussed further in section 4.2.5.

4.1.4. Polymer Additives and Mesocrystals

There are numerous examples of mesocrystal systems in the recent literature, and their number is rapidly increasing. It is, therefore, impossible to give a comprehensive overview here—even if the choice of systems is only restricted to those that are generated with polymer additives. We have, therefore, chosen to focus on $CaCO_3$ mesocrystals here. The easiest way to produce and observe mesocrystals is through the application of polymeric additives. These can kinetically stabilize the metastable mesocrystal by hindering the crystallographic fusion of the nanoparticle building units due to polymer coverage of crystal faces. Similar stabilization can also be observed with surfactant or low-molecular-weight organic additives. Polymers, however, are usually more effective and broadly applicable because of the following:

(1) Polymers can control nanoparticle nucleation and store material in precursor complexes or metastable precursor phases. This results in the formation of material depots that can be immediately transformed into the nanoparticles forming the mesocrystal.

(2) They can temporarily stabilize (steric or electrosteric stabilization) the primary nanoparticles, preventing their uncontrolled aggregation before they can mutually align into crystallographic register and mesocrystal formation can take place.

(3) They can selectively adsorb onto defined crystal faces and, thus, "code" the nanoparticles for their mutual alignment.

(4) Polymers have multiple adsorption sites and can, therefore, bind more strongly than their low-molar-mass counterparts.

A good example of a nonclassical crystallization pathway leading to $CaCO_3$ mesocrystal formation that uses a polystyrenesulfonate (PSS) additive has recently been described.[125,429] The strong binding effect of PSS to free calcium ions shifts the mechanism from traditional ionic growth to mesoscale assembly. Variation of the concentration of calcium chloride and PSS solutions by a CO_2 gas-diffusion technique resulted in the formation of unusual $CaCO_3$ superstructures, which transformed from the typical calcite rhombohedra to rhombohedra with rounded edges, to truncated triangles, and finally to convex−concavely bent doughnut-like superstructures (Figure 67). These mesocrystals are formed by selective adsorption of the polyanion onto the highly polar calcite {001} nanoparticle faces.[125,429] For this system, it is remarkable that the morphologies and particle superstructures can be varied over a wide range in a systematic way by simply adjusting the two reactant concentrations (Figure 67).

At the lowest polymer concentration and $CaCO_3$ supersaturation, crystals were found that resembled the default rhombohedral calcite single crystals (Figure 67a). Increase of the polymer and Ca^{2+} concentrations led to selective PSS adsorption on the highly polar (001) face of calcite. This, in turn, leads to the formation of nanoparticles with dissimilar charges on the opposite (001) faces and, therefore, the formation of dipolar nanocrystals (although calcite is not dipolar at all due to its symmetry). A detailed explanation for the formation of countercharged {001} can be found in the original literature reference 125. The nanoparticles then form a mesocrystal by controlled stacking of the dipolar nanoparticle subunits (Figure 67). Variation of the $CaCO_3$/PSS ratio resulted in highly systematic variation of the mesocrystal morphology and led to the formation of a whole family of crystals with rounded edges. Higher PSS concentrations led to increasing exhibition of the highly polar (001) face, resulting in a multicurved convex−concave structure with broken symmetry along the (001) direction. Finally, a central hole is formed on one side. Development of the morphology in Figure 67g goes against the classical picture of crystallization. According to the ideas of classical crystal-

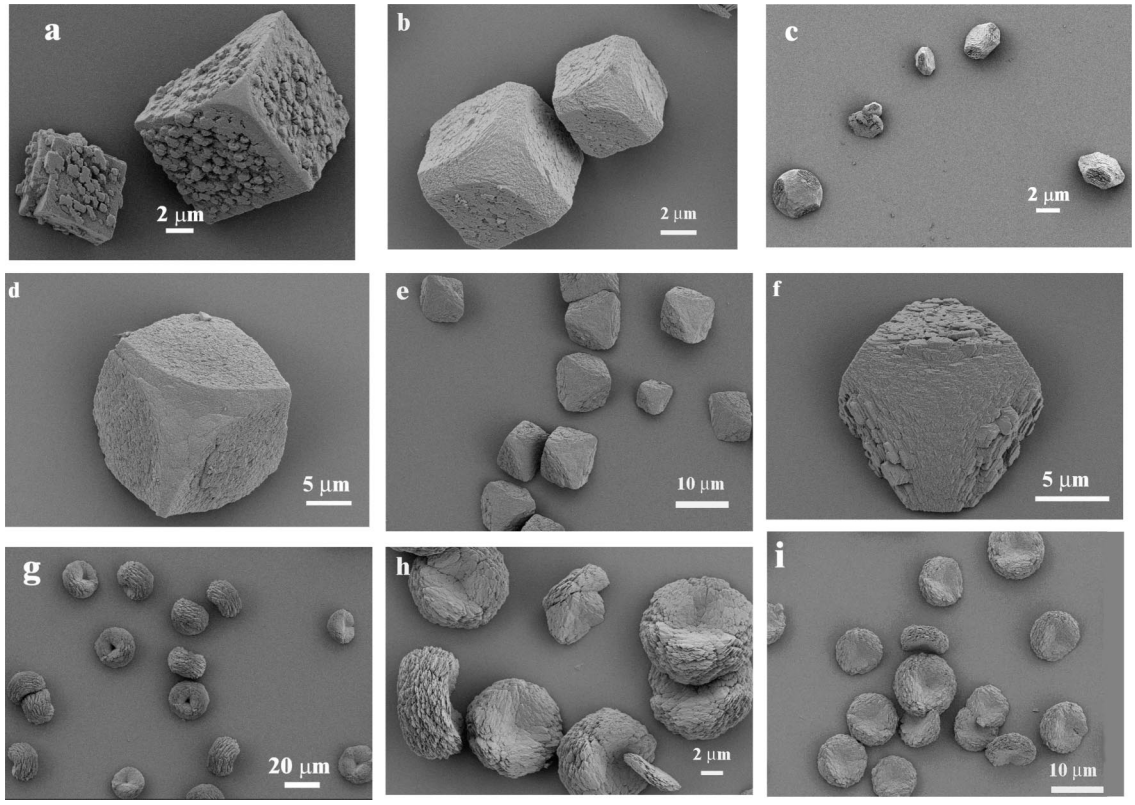

Figure 67. Typical SEM images of calcite mesocrystals obtained on a glass slip by the gas-diffusion reaction after 1 day in 1 mL of solution with different concentrations of Ca^{2+} and polystyrene−sulfonate: (a) $[Ca^{2+}] = 1.25$ mmol/L, [PSS] = 0.1 g/L; (b) $[Ca^{2+}] = 1.25$ mmol/L, [PSS] = 0.5 g/L; (c) $[Ca^{2+}] = 1.25$ mmol/L, [PSS] = 1.0 g/L; (d) $[Ca^{2+}] = 2.5$ mmol/L, [PSS] = 0.1 g/L; (e) $[Ca^{2+}] = 2.5$ mmol/L, [PSS] = 0.5 g/L; (f) $[Ca^{2+}] = 2.5$ mmol/L, [PSS] = 1.0 g/L; (g) $[Ca^{2+}] = 5$ mmol/L, [PSS] = 0.1 g/L; (h) $[Ca^{2+}] = 5$ mmol/L, [PSS] = 0.5 g/L; (i) $[Ca^{2+}] = 5$ mmol/L, [PSS] = 1.0 g/L. Reprinted with permission from ref 125. Copyright 2006 Wiley-VCH.

lization, such a hole should immediately vanish due to Ostwald ripening effects, and symmetry is encoded in the primary unit cells and thermodynamics, as described by the Wulff law of crystal growth (see also section 2.1.1).[33] Such a hole (=no effective mass transport) with a pile (=increased effective mass transport) on the opposite side strongly supports the picture of dipolar long-range interactions controlling the growth and mesoscale assembly of such structures. Wulff's rule only considers short-range interfacial energies (i.e., energies in the plane) as the driving force, but inclusion of long-range energy contributions might indeed explain the different mesocrystal morphologies. The mesocrystals shown in Figure 67 are highly porous with surface areas well exceeding 100 m^2/g but yet show a high degree of internal orientation, as indicated by the rather perfect tensorial birefringence under crossed polarizers.[429] The above example gives clear evidence that mesocrystals can self-assemble, even from subunits with complicated shapes, via edge or face energy minimization.

A similar morphological sequence to that shown in Figure 67 was obtained when $CaCO_3$ was precipitated in presence of a double hydrophilic block copolymer poly(ethylene oxide)-*block*-poly(syrene sulfonate) (PEO_{22}−$PNaStS_{49}$).[22] A wider ranger of reaction conditions were, however, utilized. Ca concentrations of 10 mM (Figure 68a) and 5 mM (Figure 68b) generated defined, rounded polycrystalline structures. The emergence of a curved, triangular top face at 5 mM indicates that the crystals are not uniaxially aligned but that they follow a joint field orientation. A Ca^{2+} concentration of 2.5 mM (Figure 68c) resulted in rounded mesocrystals with 6-fold symmetry, a that which has been described previously. The constituent crystalline units of this growth form are, due to a lower Ca^{2+}-concentration, significantly smaller, leading to somewhat smoother surfaces. At a Ca concentration of 1 mM (Figure 68d), the particles already possessed well-defined rhombohedral morphologies with significantly roughened faces, modified with the characteristic corner and edge truncations due to the presence of adsorbed polymer. Morphologies similar to single crystals were observed at low Ca^{2+} concentrations. Rhombohedral calcite particles with remarkable corner and edge truncations were produced at 0.5 mM (Figure 68e) and 0.1 mM (Figure 68f) Ca, with the particle faces produced at 0.1 mM being almost entirely smooth. This morphological sequence of particles shows that one cannot safely determine whether or not the particles form via an aggregation-based mechanism. The outer morphology of a recrystallized mesocrystal is often rough because of the primary nanoparticle building units and is typically that of the mesocrystal intermediate. However, as the final product morphology is often indistinguishable from a single crystal formed by ion-by-ion growth, identification can only be achieved by time-resolved analysis of the formation mechanism or by analysis of the internal structure of the particles at the nanoscale.

Microfocus XRD experiments performed on individual crystals revealed that the $[Ca^{2+}] = 2.5$ mM particle, despite showing a rounded profile and rough surfaces (Figure 68c), diffracts like a single crystal. Only a few isolated spots were observed in the diffraction pattern, while the apparently spherical [Ca] = 10 mM particles showed powder rings with strong texturing, indicating a substantial degree of preferred orientation for these crystallites. These two examples show that particles which are obviously composed of many subcrystals can exhibit different degrees of supercrystalline

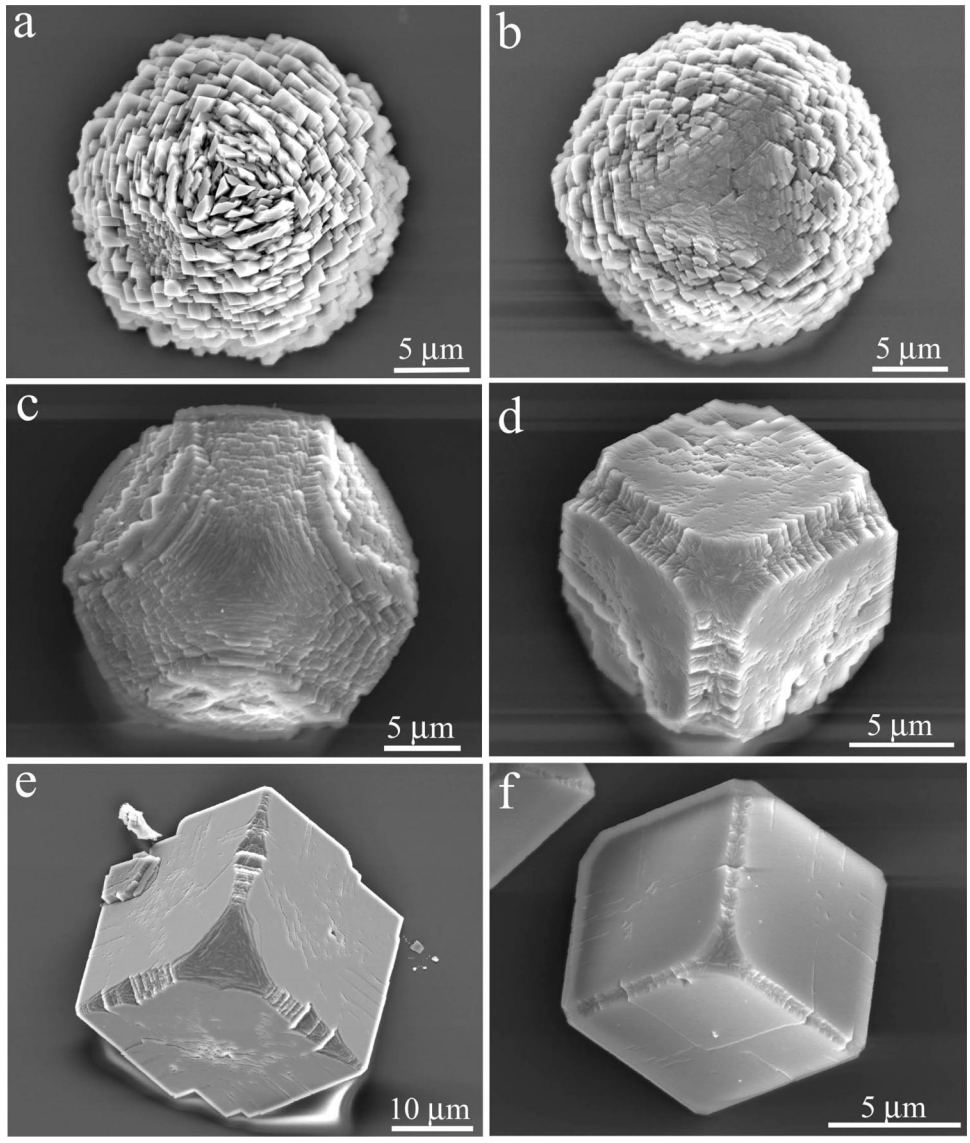

Figure 68. Calcium carbonate crystals precipitated from a solution containing Ca and $PEO_{22}-PNaStS_{49}$ at a fixed [Ca]/[S] molar ratio of 1.25:1 and Ca concentrations of (a) 10 mM; (b) 5 mM; (c) 2.5 mM; (d) 1 mM; (e) 0.5 mM; and (f) 0.1 mM. Reprinted with permission from ref 22. Copyright 2007 American Chemical Society.

order. The first case with its rough surfaces and identifiable polycrystallinity is a classical mesocrystal, while the more spherical structures are obviously constructed from parabolic or hyperbolic lattice lines such that no translational invariance is observed. The occurrence of bent or splayed mesostructures in organized crystal superstructures is a common observation. Because the particle in Figure 68c already diffracts like a single crystal, the single-crystalline scattering behavior of the higher-ordered particle aggregates in Figure 68 parts d−f is not surprising. This example shows a continuous transition between a single crystal and polycrystalline aggregate with polycrystalline scattering bevaviour.[22] Increase in size of the building units comprising the calcite single crystals from ions via clusters to nanoparticles yields the mesocrystal intermediate with its single-crystal diffraction behavior (Figure 68c). Deviation of the nanoparticle subunits from the perfect 3D crystallographic orientation of this mesocrystal, either by orientation along field lines (dumbbell formation) or increasing disorder in the nanoparticle aggregate, then finally leads to spherical aggregates with a large angular spread in the orientation of the nanocrystals. This finally results in the ringlike diffraction pattern of a polycrystal with random orientation.[22]

Vaterite mesocrystals with hexagonal morphologies and uniform sizes have recently been synthesized in the presence of an *N*-trimethylammonium derivative of hydroxyethyl cellulose via aggregation-mediated crystallization.[109] The obtained uniform hexagonal particles displayed sharp facets and edges and were formed by the aggregation of spherical nanoparticle or hexagonal nanosheet subunits, depending on the polymer concentration. As in the above calcite case, selective adsorption of polymer molecules on specific faces of crystals plays an important role in this mescrystal formation process.[109]

In a series of studies, Oaki and Imai reported on a number of mesocrystal systems. In these examples, mineral bridges between the individual nanoparticle building units are discussed as a tool to induce crystallization and orientation[430] (see also section 2.1.3.2). These bridges are a plausible explanation for the perfect crystallographic alignment of the building units, because they can transfer the crystal orientation from one nanocrystal to the next. For example, acute

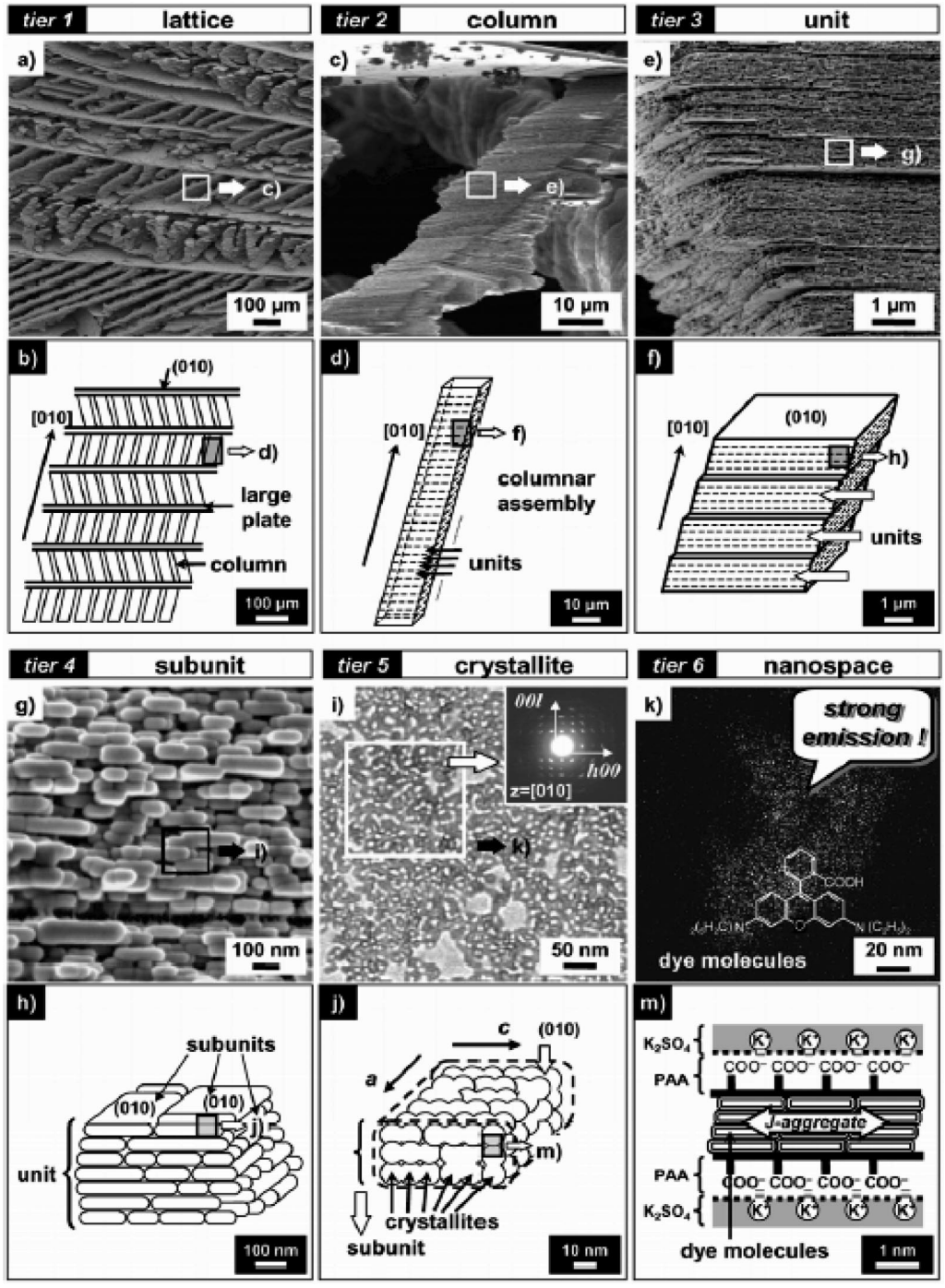

Figure 69. Overview of the hierarchical architecture in the K_2SO_4−PAA system and its schematic illustrations at six different size scales (c_{PAA} = 10 g/L). (a, b) Field-emission scanning electron microscopy (FESEM) image and a schematic representation of the macroscopic lattice architecture consisting of large thin plates and columns (tier 1); (c, d) columnar assembly between plates (tier 2); (e, f) units in the columns (tier 3); (g, h) subunits inside a unit (tier 4); (i, j) field-emission transmission electron microscopy (FETEM) image and schematic representation of crystallites with the same orientation in a subunit (inset: corresponding selected area electron diffraction (SAED) patterns taken along the (010) direction (tier 5)); (k, l) energy-filtered TEM (EFTEM) image and schematic illustration of the organization of dye molecules in a nanostorage space (Tier 6). Reprinted with permission from ref 431. Copyright 2005 Wiley-VCH.

calcite morphologies could be produced on a surface in the presence of PAA using this principle.[129] It was argued that the soft and adhesive PAA polymer serves as mortar between the inorganic nanobricks. PAA was also selected for the production of alternative mesocrystals.

A remarkable example of a mesocrystal produced using this concept was reported for the K_2SO_4−PAA system. [431] Here, no less than six hierarchical levels of structure formation were observed from the nanometer scale to the scale of several hundreds of μm. This is a typical feature of biominerals but has seldom been reported in synthetic systems (Figure 69).[431] The superstructure design at each level was controlled by changing the polymer concentration, and the observed hierarchy was attributed to the interaction between crystals and polymers.[431] On the lowest structural level, the polymer interlayer between individual nanoparticles was accessed by staining with dye molecules, which could themselves form J-aggregates (Figure 69 tier 6). These nanoparticles then formed a mesocrystal subunit (Figure 69 tiers 4 and 5), which stacked with other subunits to form a

plate unit (Figure 69 tier 3). The plate units in turn stacked in a columnar way (Figure 69 tier 2), and the columns themselves finally ordered to generate a lattice in the microscopic object (Figure 69 tier 1). The structure of the microscopic object is quite extraordinary because transport of units in the size range of tens of μm is not promoted by diffusion. Such large inorganic particles will sediment as a result of their density and size. This in turn means that the microscopic structure in Figure 69 (tier 1) must have been built up by self-assembly of nanoparticle building units at the microscopic construction site itself. The complete, sophisticated structure is formed by self-organization, the mode of which is encoded in the primary nanoparticles, and no secondary processes are involved. A similar hierarchical system was recently found for potassium hydrogen phthalate and PAA. Again, platelike units were composed of aligned crystalline nanocrystals.[430]

The above example already shows that mesocrystals do not necessarily exhibit morphologies with defined external faces. A mesocrystal can adopt virtually any shape provided that it is molded by a suitable external template. Oaki and Imai compared the macroscopic mesocrystal morphology to a nanoscale LEGO construction kit, because it has no restrictions in its external shape.[127] A simple example for shaping a mesocrystal by an external template is the production of a calcite mesocrystal film formed on a glass substrate by pouring a precursor solution containing Ca^{2+} and PAA into a plastic vessel and exposing a glass slide vertically into this solution before the carbonate is slowly added.[127] This results in a mesocrystal film with the calcite *c*-axis oriented perpendicular to the glass slide.

It is also remarkable that mesocrystals can be produced using polymers extracted from natural biominerals.[127] This was demonstrated for sea urchin spines that had been previously cleaned of all external organic matter. Subsequent dissolution of the $CaCO_3$ biomineral produced a Ca^{2+} solution containing the soluble biopolymers. Reprecipitation of $CaCO_3$ after carbonate addition to this mixture resulted in the formation of calcite mesocrystals, as shown in Figure 70. The nanoparticle substructure of the mesocrystal products was obvious in the high-magnification SEM images (Figure 70b), while TEM experiments confirmed the polycrystalline but oriented mesocrystal structure with the typical electron-diffraction pattern of a single crystal (Figure 70c). Higher-magnification images show that each calcite nanocrystal of ca. 20 nm size is a single crystal (Figure 70 parts d and e). This example beautifully demonstrates the similarities in the reaction conditions and mechanisms, as well as in the mesocrystal products produced in biomineralization and synthetic (or biomimetic) mesocrystallization.

Although these experiments did not succeed in replicating the complex, spongelike shape of sea urchin spine mesocrystals (see section 3.2.3), the nanometer structure of the mesocrystal was nicely mimicked in this synthesis. An outer, shape-defining template would be required to define the gross morphology on the micron scale. This result demonstrates that (a) the mesocrystal structure on the nanometer scale is controlled by polymer additives and (b) the shape on the micron scale cannot be reproduced without the application of a template acting as scaffold for the mesocrystal assembly.

Amorphous precursors can also form mesocrystalline-structured thin films. Kato and co-workers[432] have reported the formation of uniaxially oriented $CaCO_3$ thin-film crystals (Figure 71) on chitin matrices by using a natural peptide

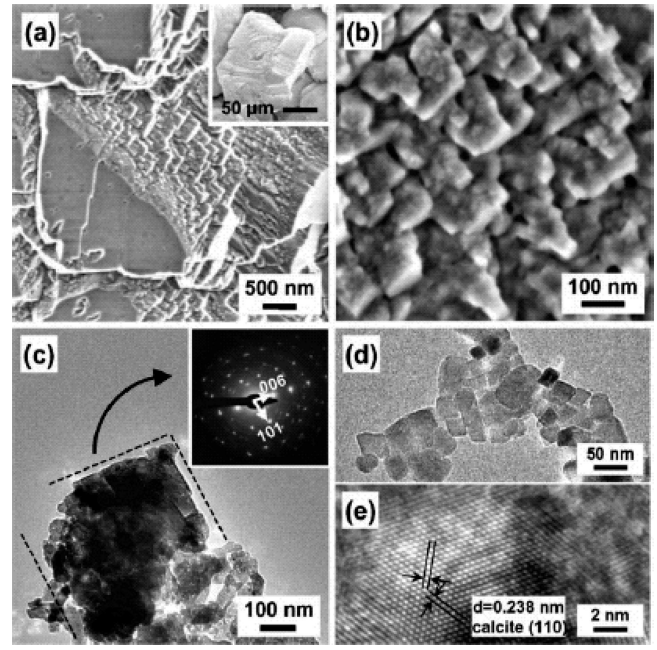

Figure 70. Nanoscopic architectures in the reproduction of sea urchin spine: (a) FESEM images of the macroscopic morphology; (b) magnified FESEM image of the nanoscopic structure; (c) FETEM and the corresponding SAED pattern (inset); (d) FETEM image of the bridged nanocrystals ca. 20 nm in size; (e) HRTEM image, showing that each nanocrystal is a single calcite crystal. Reprinted with permission from ref 127. Copyright 2006 Wiley-VCH.

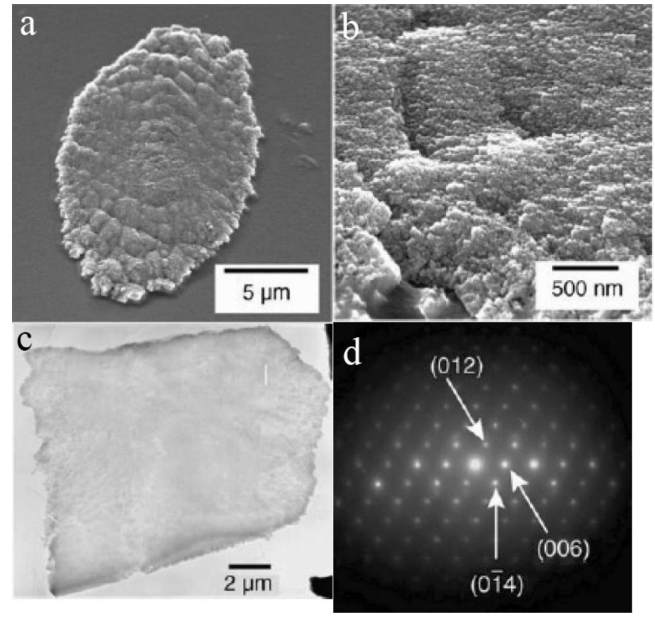

Figure 71. (a) SEM image of $CaCO_3$ crystals grown on a chitin matrix in the presence of CAP-1 for 20 h (3.0×10^{-3} wt %). (b) Magnified image of the crystal surface in (a). (c) TEM image and (d) the corresponding selected-area electron diffraction image of the uniaxially oriented crystal grown on a chitin matrix in the presence of CAP-1. Reproduced with permission from ref 432. Copyright 2006 Wiley-VCH.

(CAP-1) isolated from the exoskeleton of a crayfish. This film is formed in patches of ca. 10 and 1 μm thickness and is composed of an assembly of ca. 20 nm calcite nanocrystals (Figure 71b). The peptide CAP-1 used is thought to exhibit several functions: (i) It may bind $CaCO_3$ to the α-chitin fibrils on the surface through the action of a binding domain. (ii) Through the specific protein interaction with chitin, its acidic

groups get arranged. (iii) It may stabilize amorphous $CaCO_3$. Synergetic combinations of these functions led to the formation of the uniaxially oriented $CaCO_3$ patches in the films. The uniform textures of the $CaCO_3$ patches were confirmed by electron diffraction (Figure 71d). While the crystalline patches show different crystallographic orientations, each consists of iso-oriented calcite nanocrystals as shown by polarization microscopy.

Mesocrystal films composed of bridged $CaCO_3$ nanocrystals were also obtained with poly(acrylic acid) (PAA), and the influence of the PAA molar mass and concentration was systematically studied.[433] Low concentrations of a low-molar-mass PAA led to facetted calcite with rough surfaces, while round mesocrystals were obtained with increasing concentration of the PAA additive.[433] A binary mixture of a high- and low-molecular-weight PAA led to $CaCO_3$ films that developed calcite spines and cones with time.[129] These structures consisted of small bridged $CaCO_3$ nanocrystals with mutual crystallographic orientations. The formation of these structures was tentatively explained with a diffusion field, which is built up by consumption of dissolved material through crystal growth near the crystal surface. This concentration gradient is highest at the tip of a developing structure, and therefore, the tip will grow faster than the other parts of the structure.[129]

4.1.5. Polymer Additives and Oriented Attachment

Oriented attachment is usually applied to generate one-dimensional single-crystalline nanostructures. Most of the reported examples exploit the natural differences in surface energies of different nanocrystal faces as a driving force for directed aggregation, followed by fusion of the high-energy faces. This is described in section 2.1.3. Nevertheless, face-selective additive adsorption can also change the surface energies of crystal faces leading to a subsequent oriented-attachment process. For this, polymers can be advantageously applied. However, for $CaCO_3$, oriented attachment is very difficult to realize because of the strong aggregation tendency of unstabilized nanoparticles. Temporary stabilization can be achieved by polymer adsorption, but to date, fiber formation by oriented attachment has not yet been reported.

Fiber formation has, however, been reported for $BaSO_4$ and $BaCrO_4$, and fibers were found via three different pathways: (a) inverse microemulsion,[384,434] (b) with a double hydrophilic block copolymer,[435,436] and (c) with a polyacrylate homopolymer.[378] For case (a), the filaments grow through the linear coalescence and fusion of the primary nanoparticle building blocks, formed in the micelles of a reverse AOT microemulsion. This results in displacement of AOT molecules and subsequent nanoparticle fusion and formation of a surfactant bilayer between the forming nanofibers.[434] These fibers were elongated along their (010) axis. In the case of the polymers,[72,73,205,435−440] polymer adsorption to all faces parallel to the [210] axis was discussed for the fusion of temporarily stabilized $BaSO_4$ nanoparticles toward [210] elongated fibers.[436,440]

This is demonstrated in Figure 72, showing that the fibers are elongated along [210], suggesting about perfect mutual two-dimensional order of the nanofibers. The atomic surface structure modeling data for the surface cleavage of the $BaCrO_4$ crystal (hashemite) shows that the faces $(1\bar{2}2)$, $(1\bar{2}1)$, $(1\bar{2}0)$, $(\bar{1}20)$, which are parallel to the [210] axis, contain barium ions slightly elevated from the surface. It is reasonable to assume that the negatively charged $-PO_3H_2$, $-COOH$

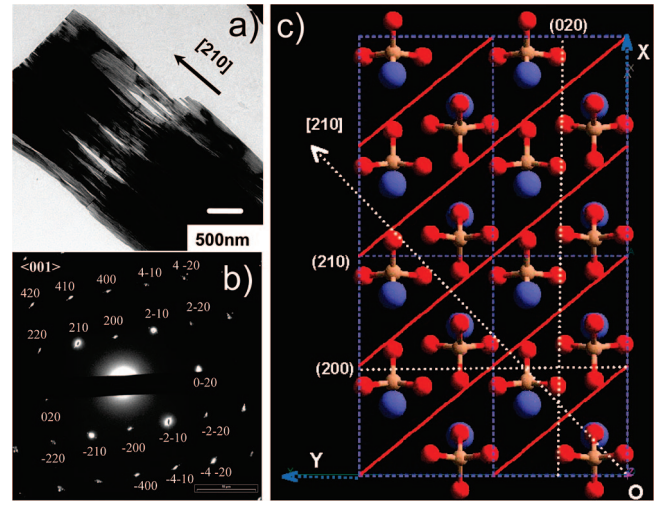

Figure 72. (a) TEM image of highly ordered $BaCrO_4$ nanofibers obtained in the presence of PEO-*b*-PMAA-PO_3H_2, pH 5. (b) Electron diffraction pattern taken along the <001> zone, showing the fiber bundles are well-crystallized single crystals and elongated along [210]. (c) Plot of the $BaCrO_4$ crystal structure as calculated with the Cerius^2 software viewed perpendicular to the [210] axis (indicated by white dashed arrow): blue = Ba, red = O, light brown = C. (210) faces (red lines) are always rich in negative chromate, while the top face is terminated by elevated Ba^{2+} ions. (a) and (b) reprinted with permission from ref 436, and (c) reprinted with permission from ref 440. Copyright 2002 and 2003 Wiley-VCH.

groups of the applied PEO-*b*-PMAA-PO_3H_2 block copolymer or the polyacrylate preferentially adsorb onto these faces by electrostatic condensation and block these faces from further growth. In contrast, the surface cleavage of the (210) face shows no addressable barium ions on the surface (red lines); meaningful cuts are always rich in chromate, as shown in Figure 72c. The negatively charged functional polymer group will certainly not favorably adsorb on this face, making the (210) face a high-energy face and, thus, favorable for further growth by oriented attachment. The resulting nanoparticle fusion finally results in the defect-free fibers oriented along [210].

$BaSO_4$ and the isomorphous $BaCrO_4$ provide nice model systems for nonclassical crystallization because their equilibrium solubility over a wide range of pH conditions is very low, thus suppressing molecular redissolution/crystallization events. The whole mechanism of oriented nanoparticle assembly relies on the absence of flow, which would disturb the directed aggregation. Indeed, no fiber bundles or cones are obtained when the solutions are stirred continuously at room temperature after mixing the reactants. Instead, only irregular and nearly spherical particles were obtained.[205,438] The fiber bundle structures obtained in the presence of the polymer additives are complex and display self-similar structures. They are compact on the micrometer scale, in the case of block copolymers,[435] but porous in the case of polyacrylate additives (Figure 73).[378,392] These species are indeed composed of defect-free single-crystalline fibers as revealed by microtoming (Figure 73).[435] A thin cut perpendicular to the fiber-bundle axis shows individual single-crystalline fibers that are interspaced by a polymer layer due to the preparation process. Variation of temperature and additive concentration allowed control of the finer details of the architecture, such as the length, axial ratio, opening angle, and mutual packing.[436]

The kinetics of formation of such structures has been studied in detail. At the early experimental stages, the

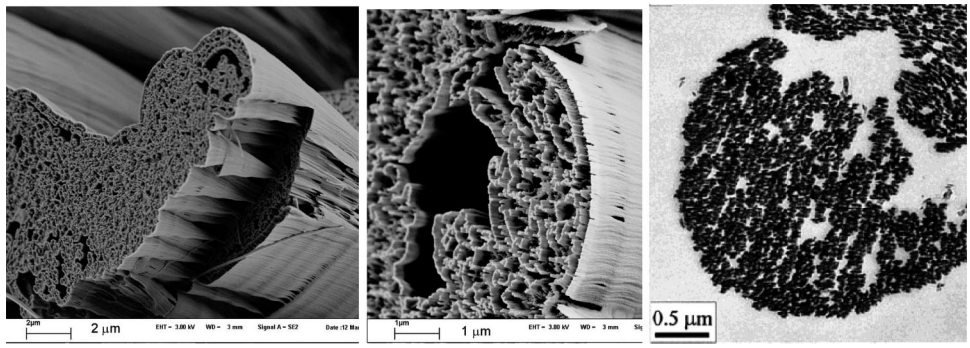

Figure 73. Complex forms of $BaSO_4$ fiber bundles produced in the presence of sodium polyacrylate, at room temperature. Reprinted with permission from ref 378. Copyright 2005 Materials Research Society (left and center). The right figure is reproduced with permission from ref 435. Copyright 2000 American Chemical Society.

polymer forms complexes with Ba^{2+} ions, which serve as ion depots for subsequent crystallization. As a next step, amorphous nanoparticles and aggregates of these particles can be observed, which occasionally attach to a polar surface and heterogeneously nucleate.[72,73] Fiber growth then occurs by attachment of nanoparticles to the (210) faces of the fibers even if the supersaturation has already dropped to 1, a level at which no further particle nucleation occurs.[73] This provides a clear experimental proof of a nanoparticle-mediated crystal-growth process. Interestingly, at least three different formation mechanisms could be identified, which lead to different structures of the fibers. At the early experimental stages where there is a high concentration of building material, the fiber bundles nucleate with their broad tips on the polar surface. At later stages, in contrast, the bundles are nucleated from a single nucleation spot. At the end of the reaction when the lowest concentrations of building material are present, striation patterns are observed that indicate a simultaneous self-limiting growth of several fibers in a bundle.[71]

This example demonstrates how complex a nanoparticle-mediated crystallization reaction can be. Interestingly, fibrous vaterite, formed by bacterial activity, has been reported. Here, crystals grew on the bacterial cell walls with their *c*-axes normal to the cell wall.[441] This provides a recent indication that similar structures to the above-reported $BaSO_4$ fibers might become available for $CaCO_3$.

4.1.6. 2D Templates

4.1.6.1. Morphological Control of Single Crystals at an Organic Matrix. Growth of crystals in association with ordered organic matrices has also been demonstrated to modulate crystal morphologies. It is a common observation that calcite single crystals precipitated on organized organic matrices such as Langmuir monolayers[182,442] and self-assembled monolayers (SAMs)[236,443] exhibit morphologies that are distorted as compared with an idealized rhombohedral morphology. This effect can be attributed to an anisotropic mismatch between the lattice of the organic matrix and the lattice of the calcium ions in the nucleating crystal face. [444] Nucleation of calcite crystals in a range of orientations on SAMs comprising ω-terminated thiols on gold and silver was considered, and the lattice mismatch between the calcium ions in the nucleating crystal face and the underlying SAM calculated. The anisotropic lattice mismatch results in anisotropy in the induced strain, which in turn affects the rate of crystal growth in different crystallographic directions. Predicted crystal morphologies were determined for a range of substrate/SAMs, based on the strain-derived anisotropic growth rates, and excellent agreement with experimentally observed crystal morphologies was achieved (Figure 74).

Interestingly, although little morphological variation was observed for (001) oriented crystals on Au and Ag substrates, there was a significant difference in the contact area of the crystals with the substrate in both of these systems, with crystals grown on Au exhibiting a larger nucleating face than those on Ag. This can be attributed to the magnitudes of the lattice mismatches along the *a* and *b* axes. The misfits are significantly larger on the Ag than on the Au, such that a higher energy is required for growth on the (001) plane on Ag than on Au. Consequently, the system minimizes the higher-energy interface by reducing the crystal/monolayer contact area. The effect of the stiffness of the monolayer itself in accommodating strains arising from crystal/monolayer mismatch was also considered. Because the monolayer itself is significantly softer than the calcite crystal, it will necessarily accommodate some of the induced strain. This effect was observed in comparing the morphologies of crystals grown on carboxylate-terminated SAMs with 10 and 15 carbon atoms in the chains. Although both sets of crystals showed identical orientations, a lower degree of morphological anisotropy was observed on the longer SAMs, an effect attributed to the greater stiffness of the longer, as compared with the shorter, SAMs.

This work, therefore, demonstrates that nucleation at an organized organic matrix has the potential to determine not only the orientation of crystals but also their morphologies. Significantly, this effect can lead to differences in size between symmetry-related crystal faces.

4.1.7. 3D Templates

The previous sections demonstrate the limitations of using soluble additives to modify the morphology of single crystals. Necessarily, the form of the product crystal must reflect the symmetry of the crystal lattice, and it is impossible to generate complex 3D morphologies using a simple additive-based approach. By direct analogy with biological systems, production of morphologically complex crystals relies upon templating strategies where the shape of a crystal is defined by the confines of the environment in which it precipitates. Templating therefore provides unique access to single crystals with noncrystallographic morphologies. In discussing the morphological control of single crystals via templating routes, we here highlight two distinct synthetic approaches: "direct precipitation", in which crystals form in the absence of a precursor phase, and "crystallization via an amorphous precursor phase", in which a mold is filled with an

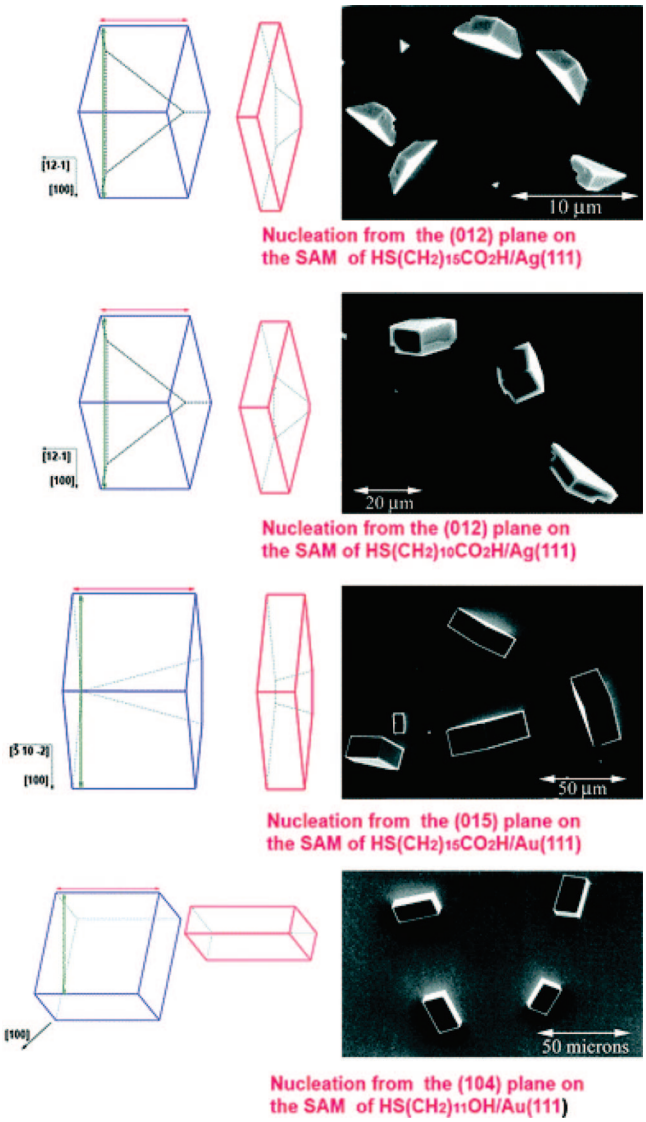

Figure 74. Comparison of the shapes of calcite crystals grown in different orientations with and without strain. (Left column) Theoretical isotropic shapes reconstructed using the SHAPE program (blue). The crystal lengths *A* (red) and *B* (green) that were used for determining the extent of shape anisotropy are shown. (Center) Calculated anisotropic shapes that develop as a result of mismatch strains at the interface and that are reconstructed using the SHAPE program (red). (Right column) Scanning electron micrographs (SEMs) of calcite crystals: experimental results. (a) Calcite nucleated from the (012) plane grown on $HS(CH_2)_{15}CO_2H$/Ag(111). (b) Calcite nucleated from the (012) plane grown on $HS(CH_2)_{10}CO_2H$/Ag(111). (c) Calcite nucleated from the (015) plane grown on $HS(CH_2)_{15}CO_2H$/Au(111). (d) Calcite nucleated from the (104) plane grown on $HS(CH_2)_{11}OH$/Au(111). Reprinted with permission from ref 444. Copyright 2007 The Royal Society of Chemistry.

amorphous material, which subsequently crystallizes to give a single crystal with identical morphology.

On the basis of the currently available information on biological calcification mechanisms, it would appear that calcite and aragonite precipitation can be generally classified as occurring either directly from solution or via an amorphous precursor phase. Interestingly, *both* of these routes have been used to produce single crystals with complex morphologies in biomimetic syntheses. Macroporous single crystals of calcite that were indistinguishable in form from sea urchin skeletal plates were produced by direct precipitation in macroporous polymer templates.[234,295] The surface chemistry of the polymer template appeared to play a pivotal role in defining the structure of the product particles by determination of the spatial distribution of nucleation sites.[297] Application of the same methodology to a range of alternative crystals demonstrated the generality of the approach.[296] As an alternative synthetic strategy, amorphous calcium carbonate has also been used as a precursor material to calcite single crystals with noncrystallographic forms.[9−11] Under this approach, the amorphous precursor material, which has no preferred geometry, is shaped within a suitable mold and then crystallized to give a single crystal of identical form. Again, control over nucleation was essential to give single-crystal products, and a high degree of morphological control was achieved in these systems.

There is increasing evidence that calcification via an amorphous precursor phase is a widespread strategy in biology—and therefore, one has to examine the potential benefits of this route over precipitation via an ion-by-ion growth mechanism.[5] On the basis of the result that single crystals with complex form and smooth, curved surfaces can readily be produced in the absence of an amorphous precursor phase, it is clear that ACC does not provide an organism with a unique route to morphological control. However, in precipitating single crystals from solution, the supersaturation must be maintained at relatively low values to prevent multiple nucleation events, which results in slow growth rates. In using ACC to fill a mold and then triggering crystallization, an organism can potentially achieve higher rates of delivery of reagents to the growth environment, as well as faster crystallization rates.

4.1.7.1. Spongelike Single Crystals via Direct Precipitation. Single crystals with complex, spongelike structures identical in form to sea urchin skeletal plates were produced by precipitation of a range of minerals including $CaCO_3$, $SrSO_4$, and $CuSO_4 \cdot 5H_2O$ in polymer replicas of urchin plates.[296] Echinoid skeletal plates, which were discussed in some detail in section 3.2.3, offer a uniquely ordered macroporous structure in which the calcium carbonate and porous fractions of the plates possess identical sizes and shapes. In filling the pores with polymer monomer, curing, and subsequently dissolving the calcium carbonate, a porous polymer with identical geometry and size to the original urchin is generated (Figure 75). Subsequent use of this template as an environment in which to precipitate single crystals then creates a unique opportunity for investigating whether shape constraint alone is sufficient to cast the morphology of single crystals, or whether the interplay of more complex variables such as the presence of organic additives is additionally required, thereby providing insight into biological crystallization mechanisms.

Precipitation of $CaCO_3$ in the urchin polymer replicas provides an immediate comparison with calcification in sea urchins. Calcite was precipitated using a double-diffusion protocol where a membrane was placed between two half U-tube arms filled with equimolar $CaCl_2$ and Na_2CO_3 solutions, and the crystals formed were isolated by dissolution of the membrane. Evidence of templating of the morphologies of the $CaCO_3$ particles was observed at all solution concentrations applied, although the quality of replication of the polymer morphology varied considerably.[295] At higher reagent concentrations (>0.1 M), large, porous, polycrystalline calcite networks were produced with overall structures that were defined by the polymer template (Figure 76a). Reduction in the reagent concentrations to 0.06

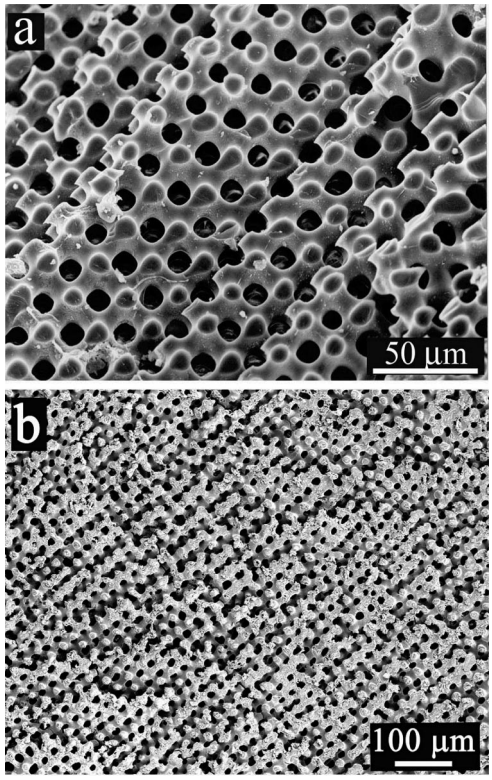

Figure 75. (a) Cross section through a sea urchin skeletal plate and (b) a polymer membrane taken as a replica of a sea urchin skeletal plate. Reprinted with permission from ref 445. Copyright 2007 Wiley-VCH.

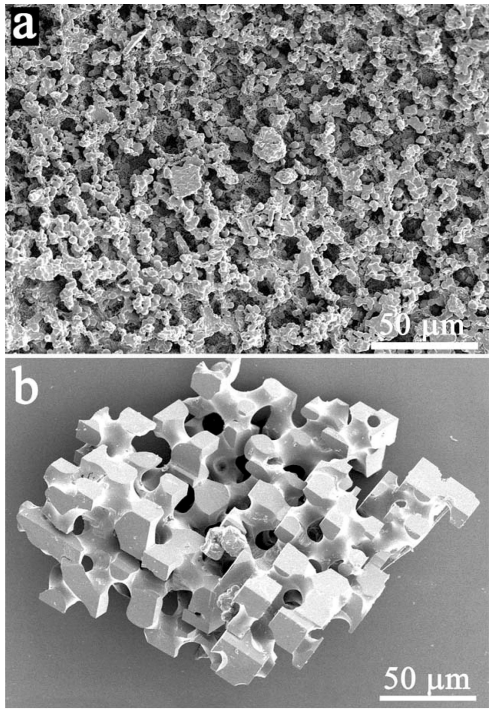

Figure 76. Crystals precipitated in a spongelike polymer membrane (a) polycrystalline calcite, precipitated from 0.4 M reagents; (b) a templated single crystal of calcite precipitated from 0.02 M reagents. Reprinted with permission from ref 295. Copyright 2002 Wiley-VCH.

M and below caused marked structural changes such that single crystals of calcite with structures perfectly replicating the morphology of the polymers template were obtained (Figure 76b). Particles of sizes up to 150−200 μm were

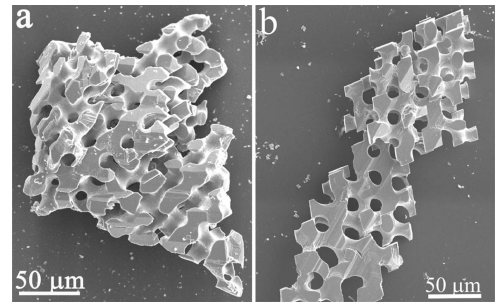

Figure 77. Crystals precipitated in a spongelike polymer membrane (a) a $SrSO_4$ single crystal precipitated from 0.05 M reagents and (b) a $PbSO_4$ single crystal precipitated from 0.05 M reagents.

produced after 1−2 days of incubation. These crystals showed both noncrystallographic curved surfaces, which were defined by contact with the polymer mold, and planar faces characteristic of crystalline materials, which represented the growth front of the crystal. Their single-crystal character was confirmed by the presence of aligned rhombohedral faces present on the perimeter of the particles and using single-crystal XRD.

The generality of this experimental approach was explored by precipitating a wide range of minerals within the urchin polymer membranes, and templated single crystals of a range of minerals were successfully obtained.[296] Large, macroporous single crystals or oligocrystals (comprising a small number of large particles) of strontium sulfate were again produced by a double-diffusion technique and typically reached sizes of 150−200 μm after 1−2 days (Figure 77a). In common with the $CaCO_3$ system, the formation of templated single crystals was strongly concentration-dependent, with single crystals being produced at low reagent concentrations and a transition to polycrystalline structures occurring with increasing concentrations. Analysis of the structures of the $SrSO_4$ particles using single-crystal XRD showed that some "single-crystal" particles were actually "oligocrystalline", comprising a few large crystals. The observed structural concentration-dependence is entirely consistent with the increased nucleation rates associated with higher supersaturations. At low supersaturations, crystal nuclei are well-separated and can grow without impinging on other developing particles such that single crystals are produced. Intergrowth occurs at high supersaturations where a high density of nuclei are formed, leading to polycrystalline products. Both $PbSO_4$ and $PbCO_3$ were also successfully templated using double-diffusion to produce macroporous single crystals (Figure 77b).[296] However, while single crystals of lead sulfate were observed over a wide concentration range, the conditions required to produce templated lead carbonate single crystals were considerably more restrictive, and $PbCO_3$ single crystals always coprecipitated with polycrystalline particles.

Contrasting these results with high-solubility ionic crystals, NaCl and $CuSO_4 \cdot 5H_2O$ were precipitated in the polymer replicas using an "evaporation method" in which crystals were precipitated on controlled evaporation of a saturated solution.[296] Again, templated single crystals were successfully produced, demonstrating that such morphological control of single crystals is not restricted either to the double-diffusion technique or to crystals with low solubilities. In common with the $SrSO_4$, $PbSO_4$, and $PbCO_3$, the single-crystal particles were often oligocrystalline. Interestingly, while it was clearly possible to template the morphology of these ionic crystals, the surfaces of the NaCl and

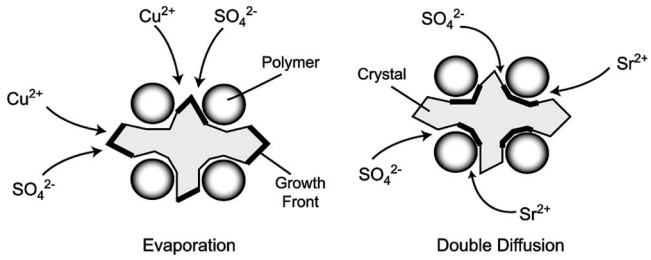

Figure 78. Schematic diagram illustrating the influence of the precipitation route on the surface structure of the templated particles formed. Reprinted with permission from ref 296. Copyright 2006 The American Chemical Society.

$CuSO_4 \cdot 5H_2O$ crystals were typically rougher than those of the single crystals produced by double-diffusion, suggesting that the surfaces had not been defined by close contact with the polymer template. This difference probably arises from the geometries of the experimental setup in both methods, as described schematically in Figure 78. In the double-diffusion method, crystal growth occurs by diffusion of ions from *opposite directions*, such that growth of the crystal proceeds from the point where the anions and cations meet, providing a driving force for ion diffusion throughout the membrane. The 3D spongelike structure of the membrane facilitates access of the ions to the growth front, and pores in the polymer membrane become entirely filled with the crystal. In contrast, in the evaporation technique, the anions and cations can diffuse to the growth front of the crystal from the *same direction*, such that there is no driving force for ions to diffuse throughout the entire membrane. Crystal growth will, therefore, continue on the nearest crystal face, rather than diffusing further into the membrane interior and combining with the inner crystal surfaces. The crystal will, therefore, not continue to grow to impinge upon the polymer membrane, resulting in the rougher crystal faces observed.

A range of other materials including $MgCO_3$, $ZnCO_3$, $BaCO_3$, and $SrCO_3$ were also precipitated within the polymer templates, but all yielded polycrystalline structures under the experimental conditions investigated.[296] In all cases, the crystallites formed in these systems were significantly smaller than the template length scale. This illustrates a fundamental requirement for the templating of single crystals, that the equilibrium size of the crystal under the selected growth conditions exceeds the length scale of the template.

The mechanism of formation of the templated single crystals was investigated by isolating particles from the polymer template with time and by studying the role of the template surface chemistry in dictating the structure of the templated crystals. In order to produce single crystals of complex morphology, control must be exerted not only during growth but also at nucleation. Single crystals must derive from individual nucleation sites and be free to grow without impinging on neighboring particles. While the nucleation rate will be defined by the solution supersaturation, it is also expected that the polymer surface chemistry may be active in directing crystal nucleation, providing a site where heterogeneous nucleation can occur. Taking $CaCO_3$ as a model system, precipitation from 0.02 M reagents yielded templated calcite single crystals and polycrystalline vaterite particles in approximately equal proportions at early times, while longer incubation times resulted in an increase in the ratio of calcite to vaterite, reaching $>80\%$ calcite after 3 days.[234] Results suggested that a dissolution-reprecipitation mechanism was operative. There

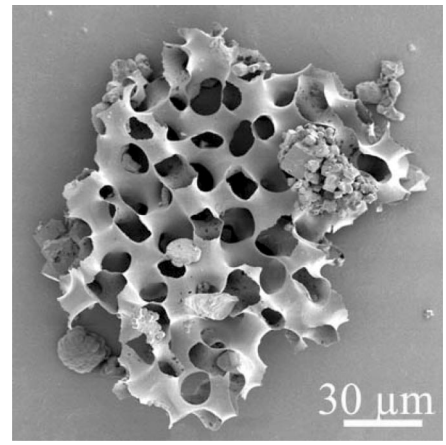

Figure 79. Calcium carbonate particle formed as a thin film over the membrane surface from 0.02 M reagents and isolated after 6 h. Reprinted with permission from ref 234. Copyright 2004 The Royal Society of Chemistry.

was also evidence that amorphous calcium carbonate (ACC) was present at early times, producing fragile, two-sided particles as a coating of ACC on the polymer membranes (Figure 79).[234]

The influence of the polymer surface chemistry in directing the formation of the templated particles was investigated through control of the polymer surface chemistry, either by treatment with an oxygen plasma or through coating with gold and subsequent modification with functionalized self-assembled monolayers (SAMs).[297] In common with the untreated membranes, the polymer modified with Au/hexadecanethiol and Au/mercaptopropanol SAMs supported the formation of templated single crystals. The charged SAMs (Au/mercaptohexadecanoic acid and Au/mercaptopropanesulfonic acid), in contrast, directed the formation of polycrystalline calcite particles (Figure 80). These particles showed spongelike morphologies and principally comprised intergrown calcite rhombohedra of size $\approx 10\ \mu$m, which were randomly oriented over the volume of the particle, indicating multiple nucleation sites. Similar results were obtained with the oxygen plasma-treated membranes. As intuitively expected, the untreated membranes offer few ionizable groups and exert little influence on crystal nucleation, while introduction of ionizable groups generates surfaces that actively promote nucleation.

This phenomenon was further investigated by repeating the surface-dependence studies with $SrSO_4$.[297] In this case, an unexpected result was obtained—templated single crystals were obtained with all of the surface-modified membranes. Analysis of the experimental conditions for the $SrSO_4$ and $CaCO_3$ systems showed that the crystals in fact grew under very similar conditions. A significant difference does exist between $CaCO_3$ and $SrSO_4$, however—the polymorphism of $CaCO_3$. Amorphous calcium carbonate (ACC) is anticipated to be the first phase precipitated in the calcite system and is likely to associate with the membrane surface, either via heterogeneous nucleation or through adsorption of particles formed by homogeneous nucleation in solution. The ACC precursor phase will generate a high density of Ca^{2+} and CO_3^{2-} ions at the membrane/solution interface, and subsequent recrystallization may be directed by the membrane, resulting in multiple nucleation sites and a polycrystalline product when ionizable surface groups are present. That little

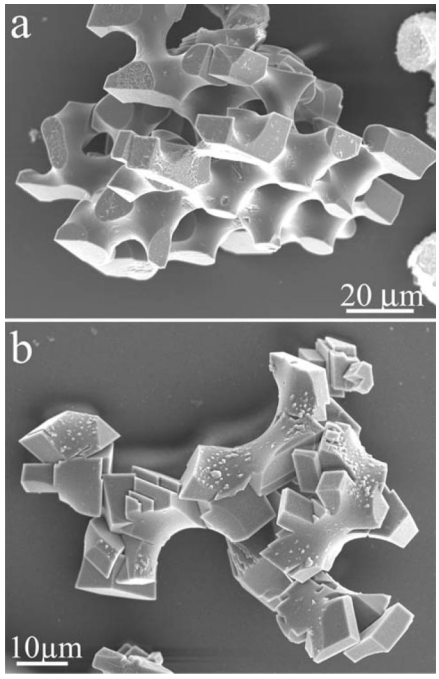

Figure 80. Calcite particles grown within surface treated polymer membranes (a) Au/hexadecanethiol-treated membrane and (b) Au/mercaptohexadecanoic acid-treated membrane. Reprinted with permission from ref 297. Copyright 2007 The American Chemical Society.

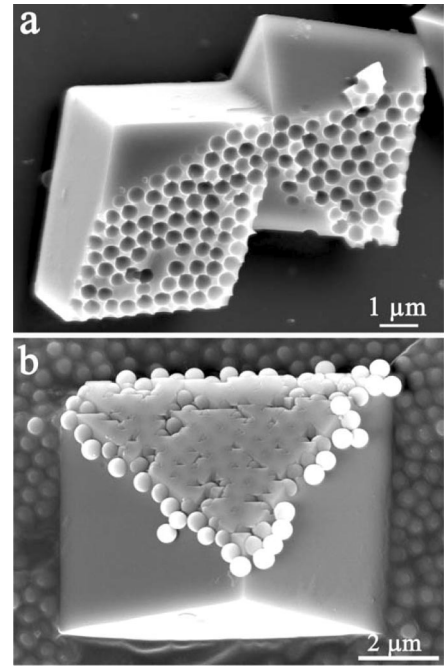

Figure 81. (a) Nucleation face of calcite crystal that grew in contact with the colloidal monolayer of 0.5 μm PS spheres after dissolution of the polymer spheres and (b) continued crystal growth resulting in encapsulation of PS spheres inside calcite single crystal. Reprinted with permission from ref 446. Copyright 2006 The American Chemical Society.

influence of the membrane over $SrSO_4$ precipitation occurs can, therefore, be attributed to the high supersaturation values.

This work, therefore, demonstrates that single crystals with complex morphologies and smooth, curved surfaces can be produced by shape constraint only, without any requirement for soluble additives or an amorphous precursor phase. While it was suggested that ACC was probably produced in the early stages of $CaCO_3$ precipitation, its short lifetime under the experimental conditions clearly excludes its participation in the formation of the large single crystals whose morphologies develop over long time periods. The surface chemistry of the environment in which the crystal forms also appears to play a pivotal role in defining the structure of the product particles.

4.1.7.2. Nanoscale Templating of Single-Crystal Morphologies. That such control of single-crystal morphologies can be achieved down to nanoscale levels was demonstrated by precipitating calcite single crystals in association with close-packed monolayers of polystyrene or silica spheres and on patterned polymer thin films.[446] Both systems provide easy access to pattern length scales ranging from the micron to the nanometer scale. All of the colloidal monolayers investigated supported the growth of rhombohedral calcite crystals, and the templating effect of these substrates was apparent on viewing the crystal face in contact with the particle monolayer, after dissolution of the particles. In all cases, the monolayer structure was perfectly replicated in the nucleating crystal face, producing a motif of close-packed hemispherical cavities (Figure 81). Examination of the crystal growth process over time suggested that the calcite crystals initially grew with a planar face in contact with the particle monolayers, and that growth then continued through the monolayer to produce the hemispherical cavities. Longer precipitation times resulted in continued growth through the monolayer and entrapment of the colloidal particles within the calcite single crystals (Figure 81b). Variation of the sizes of the colloidal particles within the range 5 μm to 50 nm showed that morphological templating could be achieved down to these very small length scales. While the large 5 μm particles were similar in size to the calcite crystals such that only one or two particles were typically associated with each crystal, the small particles templated entire crystal faces in a close-packed pattern.

Access to pattern length scales down to 10 nm in size was achieved using structured polymer films.[447] Calcite crystals were precipitated on polymer thin films, prepared by demixing of mixtures of low-molecular-weight poly(styrene) (PS) and poly(methyl methacrylate) (PMMA) during spin-casting. Dissolution of the PMMA then generated porous PS films (Figure 82a). In common with the colloidal crystal templates, the polymer film pattern was translated into the nucleating crystal face, resulting in patterning of features down to 10 nm in size (Figure 82b). Interestingly, crystallization did not terminate on penetration of the pores in the polymer film but continued on the opposite side of the film, producing a sheetlike crystal linked to the parent crystal through mineral bridges spanning the entire thickness of the polymer film (Figure 82c). That this process occurs indicates that the polymer film must separate from the substrate during crystallization. The polymer film, therefore, becomes fully encapsulated within a single crystal of calcite, producing a hybrid inorganic/organic material (Figure 82d).

4.1.8. Amorphous Precursors

4.1.8.1. Single Crystals via an Amorphous Precursor Phase. As an alternative approach to producing single crystals with noncrystallographic morphologies, single crystals of calcite have also been precipitated within rigid molds via an amorphous precursor phase. This methodology directly mimics the strategy employed by sea urchin embryos in

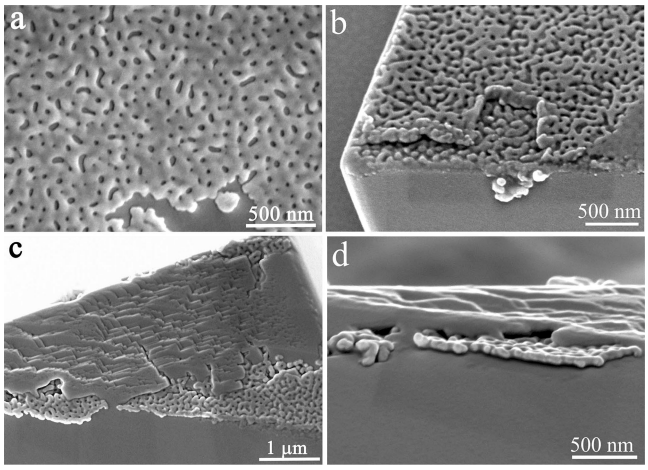

Figure 82. (a) Porous polystyrene (PS) film prepared by phase separation during spin-coating of a PS/PMMA (poly(methyl methacrylate)) blend and selective removal of the PMMA; (b) nucleating crystal face of a calcite crystal grown on the polymer film shown in (a); (c) continued crystal growth results in encapsulation of the polymer film within a single crystal of calcite and (d) side view of the crystal shown in (c) showing the encapsulation of the structured polymer film. Reprinted with permission from ref 447. Copyright 2006 Wiley-VCH.

which amorphous calcium carbonate (ACC) precipitated within a triradiate vesicle crystallizes to give a single crystal of calcite with an identical triradiate form.[50] ACC was precipitated within the confines of the pores of track-etch membranes, and subsequent crystallization yielded single crystals of calcite with rodlike morphologies and curved surfaces, as defined by the geometry of the pores.[9,10] Further, control of the pore size was shown to play a major role in defining the single-crystal/polycrystalline structure of the product particles in this system.[9] In an alternative system, additional control of the nucleation event of ACC maintained within a complex mold enabled the production of large, perforated, single crystals of calcite.[11] Again, the geometry of the mold was key in determining the single crystal/polycrystalline structure of the product particle. Both of these sets of experiments, therefore, show the potential of using an amorphous precursor phase to produce single crystals with complex form and curved surfaces—although as shown by the work described in section 4.1.7, an amorphous precursor phase is certainly *not a prerequisite* to achieving such morphological control. Aizenberg's experiments however, beautifully demonstrate one clear advantage of precipitating crystals via an amorphous precursor rather than by direct ion-by-ion growth—that a significantly higher crystallization rate can be achieved with this precipitation route. Ultimately, this may provide the basis for biology's adoption of an ACC precipitation route, rather than ease of morphological control.

4.1.8.2. Crystallization of ACC in Confinement. Calcium carbonate was precipitated within the cylindrical pores of polycarbonate track-etch membranes, both directly as calcite and via an ACC precursor phase.[9,10] With the initial constraint and subsequent transformation of ACC within the confined volumes provided by the membrane pores, this system was considered to provide a model for biological calcification in organisms such as sea urchin embryos. A simple experimental setup was employed in which a membrane with 3 μm pores was mounted between two half U-tube arms, which were filled with Na_2CO_3 and $CaCl_2$ solutions at ~4 °C. At this low temperature, ACC was stabilized and the rate of transformation to calcite was reduced. Isolation

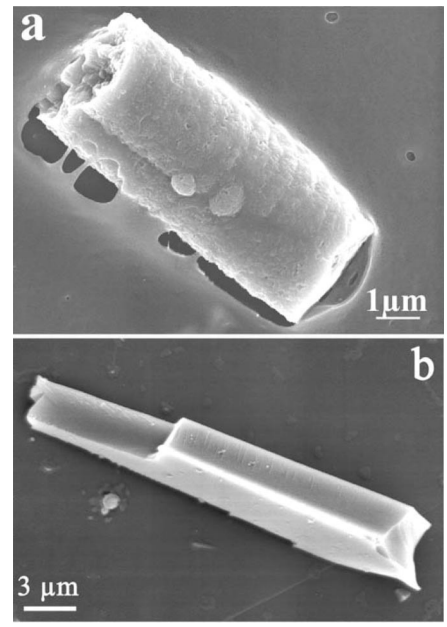

Figure 83. Calcium carbonate crystals precipitated in 3 μm pores (a) from 0.1 M reagents at low temperature with incubation time 24 h in membrane pores of diameter and (b) from 0.008 M reagents at room temperature after 24 h. Adapted with permission from ref 9. Copyright 2004 Wiley-VCH.

of the intramembrane crystals showed that they possessed rodlike morphologies and dimensions identical to the membrane pores, demonstrating the role of the confining environment in dictating the transformation product of the ACC particle (Figure 83a). That the particles were single crystals of calcite, or sometimes oligocrystalline, comprising a few large crystals, was confirmed through single-crystal XRD (synchrotron source) of individual particles. In order to investigate whether a precursor ACC phase was essential to morphological definition of the particles, the experiment was repeated under conditions where no ACC was precipitated in bulk solution. In this case, crystals with irregular rather than rodlike morphologies, which displayed well-defined crystal faces characteristic of calcite, were observed (Figure 83b).

The influence of the membrane pore size on the crystal product was also investigated by precipitating $CaCO_3$ in pores of sizes 10−0.2 μm. Interestingly, while single-crystal-type products were obtained in all pores of diameter 5 μm and under, polycrystalline particles were precipitated in the 10 μm pores (Figure 84). The basis for the size-dependence was determined on isolation of the intramembrane particles with time, which showed that, in the smaller pores, spherical ACC particles initially coated the walls of the pores, before filling in the entire volume and generating the final rodlike form (Figure 83). In the case of the 10 μm pores, the ACC did not fill the entire pore volume prior to the onset of recrystallization, such that multiple nucleation sites occurred due to the large particle/solution interface. It is also likely that the smaller pores offer greater stabilization of the ACC due to the larger membrane/particle contact area-to-volume ratio.

4.1.8.3. ACC-Mediated Formation of Large, Complex, Calcite Single Crystals. Large, patterned, single crystals of calcite were formed by a 2-fold strategy involving (i) crystallization of an ACC precursor phase in a well-defined environment and (ii) control of the nucleation event.[11] A template comprising a square array of posts, sandwiched

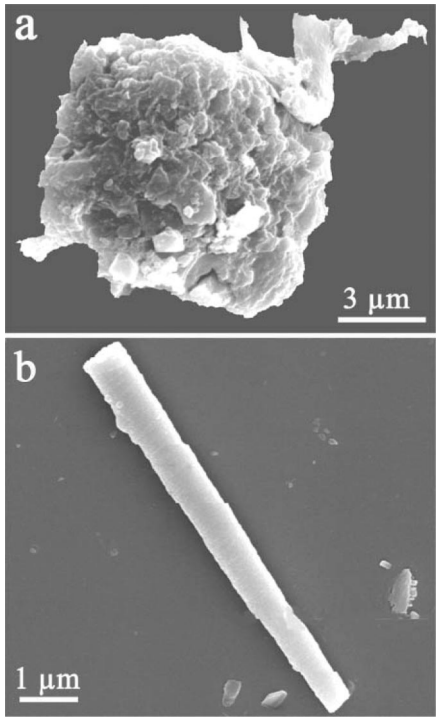

Figure 84. Intrapore calcium carbonate particles produced from 0.1 M reagents at low temperature with incubation time of 24 h in membrane pores of diameter (a) 10.0 μm and (b) 0.8 μm. Adapted with permission from ref 9. Copyright 2004 Wiley-VCH.

between two substrates, was employed (Figure 86). While one substrate was coated with a thin gold film and was functionalized with a mixture of phosphate-, methyl-, and hydroxyl-terminated thiols to promote the stabilization of ACC, the second substrate was a gas-permeable polymer film. Crucially, a single nucleation center comprising an area of hydroxyl-, carboxyl-, or sulfonate-terminated thiols was inscribed on the functionalized substrate using an AFM tip. Immersion of the prepared template in a solution of calcium chloride and exposure to an atmosphere of CO_2 released from solid ammonium carbonate resulted in initial precipitation of ACC. Nucleation of a calcite crystal at the designated nucleation center occurred within approximately 1 h, and growth proceeded within the boundaries presented by the network of posts, producing patterned single crystals of calcite up to 1 mm in size (Figure 86b). The crystals were specifically oriented with respect to the substrate according to the functional group expressed by the SAM nucleation center.

This system also provided valuable information on the mechanism of the ACC−calcite transformation. Variation in the pattern dimensions had a marked and systematic effect on the structure of the crystal product (Figure 87). Substrates with large channels did not support the formation of micropatterned single crystals, giving instead polycrystalline samples with domains 15−25 μm in size, when the nucleation event was located at distances >15 μm from the channel edge (Figure 87b). It was suggested that the micropattern provided a "microsump action" for the release of excess water during the ACC-to-calcite transition, enabling also relaxation of stress in the forming crystal. The expulsion of water from the ACC on crystallization was demonstrated through uniform incorporation of a fluorescent dye in the amorphous phase. On crystallization, the dye/water was expelled from the crystal phase (Figure 87 parts c and d). The crystallization process, therefore, appears to occur by

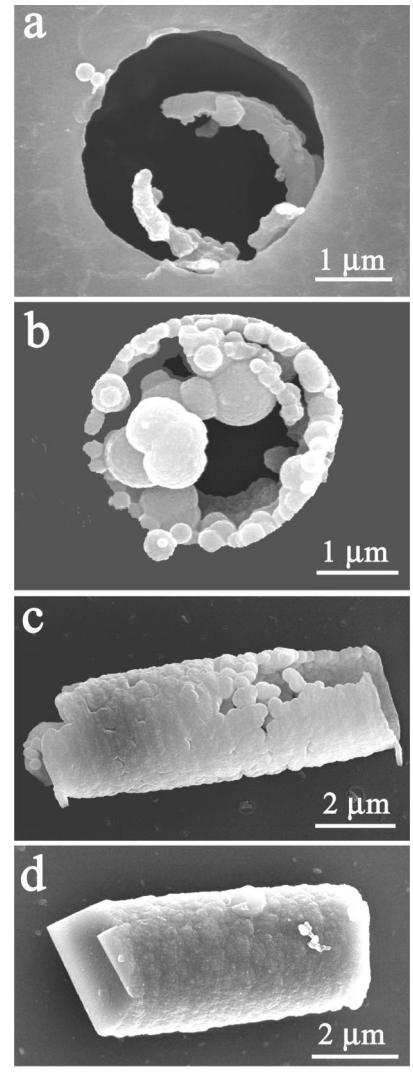

Figure 85. Micrographs showing the developmental stages of particles forming from 0.1 M reagents at low temperature in 3.0 μm pores after incubation times of (a) 5 min, (b) 15 min, (c) 15 min, and (d) 1 h. Reprinted with permission from ref 9. Copyright 2004 Wiley-VCH.

mass transport between the amorphous and crystalline phases, rather than by a solid-state transformation. Further, it was suggested that the porosity of the single crystal may provide a regular release of this stress and that porosity may indeed be a requirement for the growth of large single crystals via an amorphous precursor phase.

This interesting suggestion is supported by the observation that all large biological single crystals are indeed porous. A very recent work by Qi and Li even extended the above Aizenberg 2D approach toward 3D patterned single crystals with a very simple and straightforward approach. These authors successfully infiltrated a colloidal crystal on a filter with a freshly prepared ACC dispersion using vacuum suction through the template. Subsequent crystallization yielded a single crystal whose morphology replicated the shape of the colloidal crystal template (Figure 88).[13]

The approach of Li and Qi is a significant step toward large 3D macroporous single crystals and combines several desirable features of an easy and versatile synthesis via amorphous precursor particles. These include ease of preparation at room temperature with standard laboratory equipment, preparation without additives from cheap starting chemicals, and a template feature size well below the critical

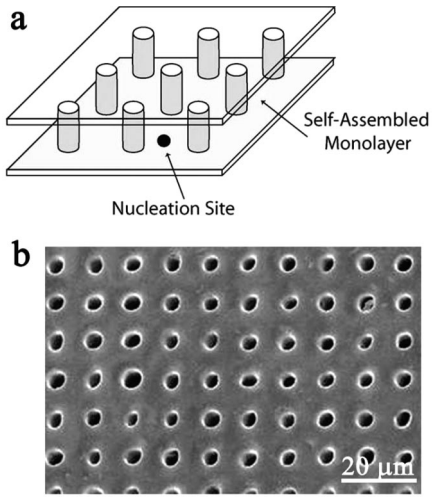

Figure 86. (a) Schematic diagram of template comprising an array of posts, in which ACC was precipitated and (b) SEM image of a patterned single calcite crystal fabricated in such a mold. In the experiment shown, the photoresist pattern was a square array of 3 μm posts separated by 8 μm spaces, and the nucleation site was a SAM of $HS(CH_2)_{11}SO_3H$ on Au. The size of the holes increased from 3 μm in the amorphous film to 4.2 $\pm$ 0.5 μm in the crystal. Adapted with permission from ref 11. Copyright 2003 American Association for the Advancement of Science.

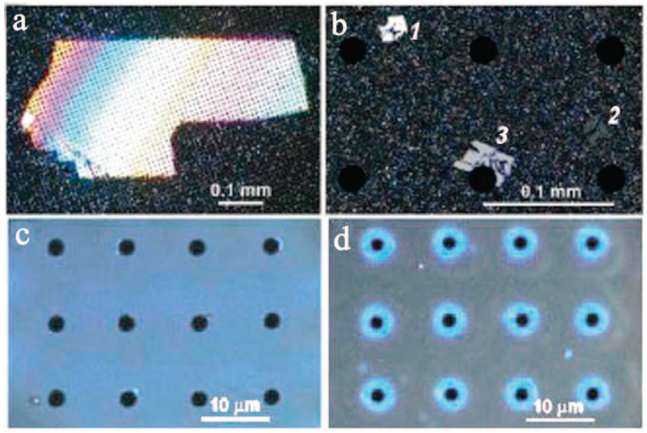

Figure 87. (a) Polarized light micrograph of a micropatterned single calcite crystal in the [104] orientation produced in a square array of 3 μm posts separated by 8 μm spaces. (b) Polarized light micrograph of the crystallized ACC layer in a framework with larger feature sizes. In the experiment shown, three nucleation sites (1−3) were imprinted on a template consisting of an array of 20 μm posts with a periodicity of 100 μm. The formation of crystals of a characteristic size 15−25 μm is observed. (c) ACC produced in the template incorporating a phosphate-containing dye, 4-methylumbelliferyl phosphate, showing even distribution of the dye. (d) After crystallization, the dye is excluded from the growing crystal and builds up at the post/crystal interface, hinting at the "microsump" function of the micropatterned framework. Reprinted with permission from ref 11. Copyright 2003 American Association for the Advancement of Science.

value for the production of a large patterned single crystal.[448] This easy and versatile method can be applied to a number of templates that can be infiltrated by amorphous precursor particles and to a large number of systems that can be produced by kinetic precipitation.

4.1.9. Crystallization in Gels

Biomineralization and, thus, the formation of complex organic−inorganic morphologies can take place in extracellular gel matrices, as in the case of the insoluble layer of the aragonitic nacreous layer of mollusks,[178,357,361] the insoluble matrix of fish otholiths,[449] and amelogenins, which are a major tooth component.[450] Although gels are a controlled reaction environment, they do not provide a confined space in the form of a template and are probably better considered as a scaffold.[451] Depending on the chemical functionality of gels, they can not only provide nucleation sites but also can control the growth or assembly of inorganic nanoparticles. Therefore, gels can be used as a medium for classical crystallization events and also for nanoparticle-based nonclassical crystallization pathways.[114] This chapter is, therefore, divided into two principal sections, one of which considers single-crystal formation via classical crystallization and the other of which considers mesocrystal formation by nonclassical crystallization pathways. It is important to emphasize, however, that no clear boundary exists between these two categories of crystals and that mesocrystals can transform into continuous single crystals.[122]

4.1.9.1. Single Crystals in Gels. Crystallization in gels is a classical technique for the formation of large, high-quality, and often defect-free single crystals.[55,56,58] The reason for this is the gel structure, which is a network with variable pore sizes that can be adjusted according to the cross-linking density. A high cross-linking density results in pore sizes in the range of a few nanometers, while lower cross-linking degrees can result in much larger pores, as seen for example in 1% agarose gels where pores can be as large as 140 nm.[452] The network structure of the gel restricts the ion diffusion depending on the cross-linking degree, typically by at least a factor of 2.[453] Thus, a large single crystal can slowly grow under idealized growth conditions as convective material transport is suppressed, which leads to the generation of concentration gradients in the gel. Furthermore, the formation of critical crystal nuclei can be retarded, such that the high supersaturations support the growth of a few large single crystals rather than the formation of many nanoparticles. This is usually achieved in counterdiffusion experiments, lowering the temperature or allowing a liquid in which the crystal is less soluble to diffuse into the gel medium.

The gel also serves to establish stable concentration gradients and supports the growth of a single crystal without exerting too high of forces upon it. There are three mechanisms that simultaneously determine the final crystal size:[55]

(a) The reagents are progressively exhausted.

(b) The diffusion gradients decrease when the reaction boundary moves along the gel column, which reduces the growth speed.

(c) The crystals, which involve acidic or basic ions like the alkaline CO_3^{2-} in $CaCO_3$, change pH, which makes the local pH more acidic on consumption of the CO_3^{2-} ions. The pH change with rapidly diffusing hydrogen ions is associated with a solubility change of these crystals. Thus, a steady state may be reached where growth and dissolution of the crystals are in balance

Because of these considerations, large crystals can be grown if nucleation can be limited to avoid the interaction of the diffusion fields between two growing crystals. This ensures a constant reagent supply and removes the waste products. An example is given in Figure 89.

The crystal morphology can be adjusted by changing the supersaturation in the gel. This can be done by changing the cross-linking degree in the gel or by limiting the reactant

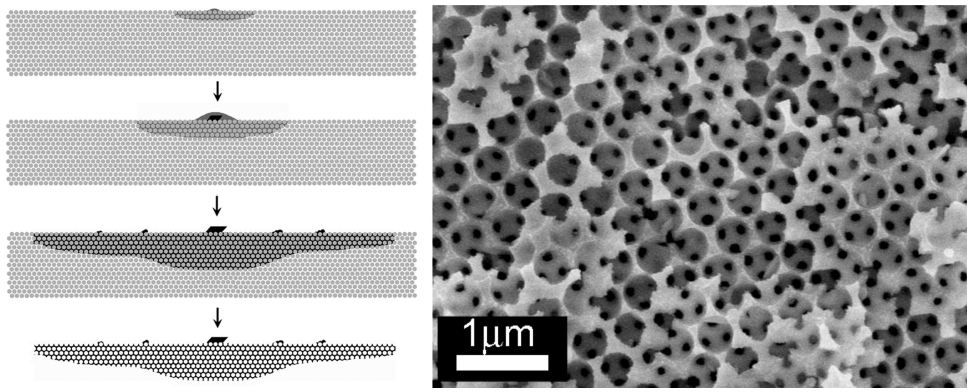

Figure 88. (Left) Schematic illustration of the formation process of flat nanopatterned calcite single crystals; (Right) SEM image of a calcite single crystal templated by a colloidal crystal of 450 nm latex particles showing the *hcp* order of the initial colloidal crystal template. Reprinted with permission from ref 13. Copyright 2008 Wiley-VCH.

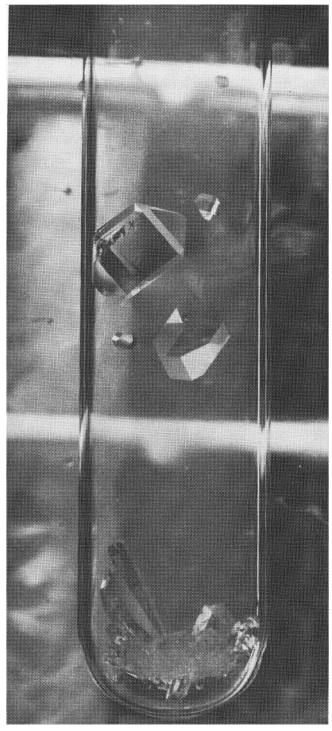

Figure 89. Potassium diphosphate (KDP) crystals grown in a 7% supersaturated tetramethoxysilane gel after lowering the temperature from 35 to 20 °C after 8 days. Reprinted with permission from ref 454. Copyright 1982 Elsevier.

supply followed by a decrease in supersaturation after nucleation of the first crystals. The effect of the supersaturation on the shape of the formed crystals is schematically shown in Figure 12 for the example of the highly insoluble PbS in Figure 90.[455]

Associated with the above considerations concerning the dependency of crystal morphology on supersaturation are the eight-arm, star-shaped calcite single crystals obtained in inert agarose gels.[456] This special shape of a single crystal is clearly a result of the restricted ion diffusion in an inert gel matrix (see Figure 91). In these experiments, an agarose gel was prepared in the presence of Ca^{2+}. Many small calcite nuclei rapidly formed on diffusion of CO_3^{2-} ions into the gel, and growth of these nuclei then depletes the reactant concentrations in the direct environment of the growing crystal (Figure 91a). Further crystal growth is then limited by the diffusion of further ions to the growing crystal. The eight edges of the nuclei are spatially favored and have a higher probability of accumulating ions from the surroundings than the six {104} faces. The edges, therefore, grow layerwise, as can be nicely seen in Figure 91b, and with time, the eight edges gradually extrude and extend outward, leading to the final star-shaped crystals (Figure 91c). Higher magnification shows many rhombohedral {104} faces in crystallographic register, which is supportive of the single-crystal nature of these star-shaped crystals.[456]

The shape of gel-grown crystals can also drastically change with time. Estroff et al. demonstrated that the appearance of calcite crystals in a self-assembled, carboxyl-functionalized hydrogel changed with time.[451] This morphological change is caused by slow dissolution due to nonspecific occlusion of gelator aggregates at imperfect crystal sites. A similarly increased solubility as compared with the perfect crystal is also observed for several $CaCO_3$ biominerals,[248,457−459] which might be the effect of occluded macromolecules. More recently, Estroff and Li crystallized $CaCO_3$ in an agar hydrogel on top of a carboxy-functionalized self-assembled monolayer (SAM) as a mimic of biological mineralization conditions.[460] Introduction of the functionalized SAM provides a substrate which can promote a high nucleation density and which can induce oriented nucleation. Rhombohedral calcite crystals nucleated with their (012) face on the monolayer, as is observed on crystallization from solution, in contrast to the star-shaped calcite crystals, which are characteristic of crystallization in agar gels in the absence of the effective nucleation sites provided by the SAM.[456] The calcite crystals contain the gel network, and their aspect ratio is significantly reduced compared to the solution case and decreases with increasing gel concentration.

The gel itself can also directly interact with the growing single crystals. Falini and co-workers demonstrated the growth of oriented octacalciumphosphate (OCP) platelets in a gelatin Xerogel.[461] The crystals preferentially grew as thin plates that were elongated along their *c*-axes and that showed large {100} faces parallel to the sheets of gelatin films. When the gelatin films were uniaxially deformed, the OCP crystals grew with their *c*-axes almost parallel to the direction of deformation.[461]

4.1.9.2. Mesocrystals in Gels. Crystallization in gels appears also to be well-suited to the generation of mesocrystals, due to the high supersaturation levels.[462] In order for large single crystals to grow, nucleation must be effectively suppressed by the gel. If this is not the case, small nanoparticles will nucleate that can serve as the building units for the mesocrystals. Simultaneously, convection or turbu-

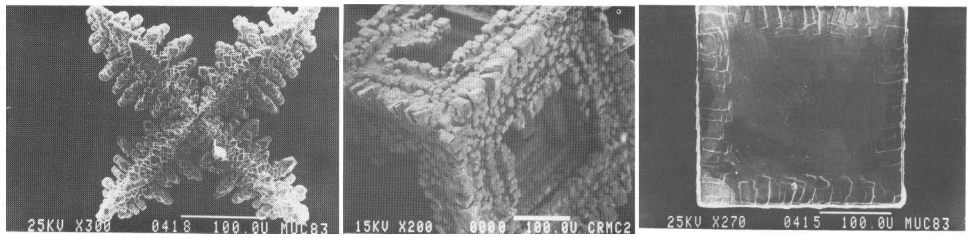

Figure 90. SEM of gel-grown PbS progressing from (left) dendritic crystal grown at very high supersaturation to (center) hopper crystal grown at moderately high supersaturation and (right) polyhedral crystal grown at low supersaturations. Reprinted with permission from ref 455. Copyright 1986 Elsevier.

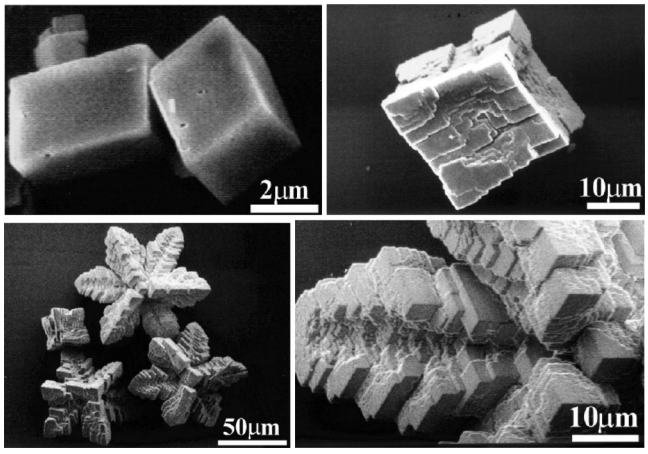

Figure 91. SEM images of calcite crystals grown in agarose gels at 30 °C after (upper left) 1 min, (upper right) 10 min, and (lower left) and (lower right) 24 h. Reprinted with permission from ref 456. Copyright 2003 Royal Society of Chemistry.

lence throughout crystallization can be suppressed, thus allowing the mutual interaction potentials to control the mutual alignment of particles. The diffusion of the mesocrystal building units is also significantly lowered in gels and is much lower than the diffusion rates of ions. This leads to a slow growth process and, therefore, the possibility of observing time-resolved structure formation. An alternative and likely crystallization pathway of mesocrystal formation in gels is the formation of mineral bridges, as shown in Figure 21b. Here, the crystals nucleate in the compartments between the network chains and can grow partially including the network chains into the crystal but also partly pushing the network chains away with the growing crystal surface. This will terminate nanoparticle growth at some stage, and a mineral bridge can develop at a site with poor polymer coverage. This mineral bridge can nucleate the next nanocrystal and so forth. In any case, mesocrystal formation in gels is slow because of the diffusion restrictions of the reactants. These are the reasons why many of the most defined mesocrystals are indeed observed in gels. In addition, gels can be prepared as inert structures that do not chemically interact with the growing crystals. They can, therefore, be prepared such that they simply provide diffusion control (for example, poly(acrylamide) or agarose gels) or they can be equipped with function groups that can interact with the forming crystal structures.

One of the most-investigated synthetic mesocrystals is the hexagonal prismatic seed crystal of fluoroapatite. These have been formed in a gelatin gel where they grow to spherical particles via dumbbell intermediates.[463−465] The first well-defined crystal form precipitated in the gel is a seed crystal with a hexagonal morphology. This seed crystal shows all of the typical features of a mesocrystal and, thus, provides

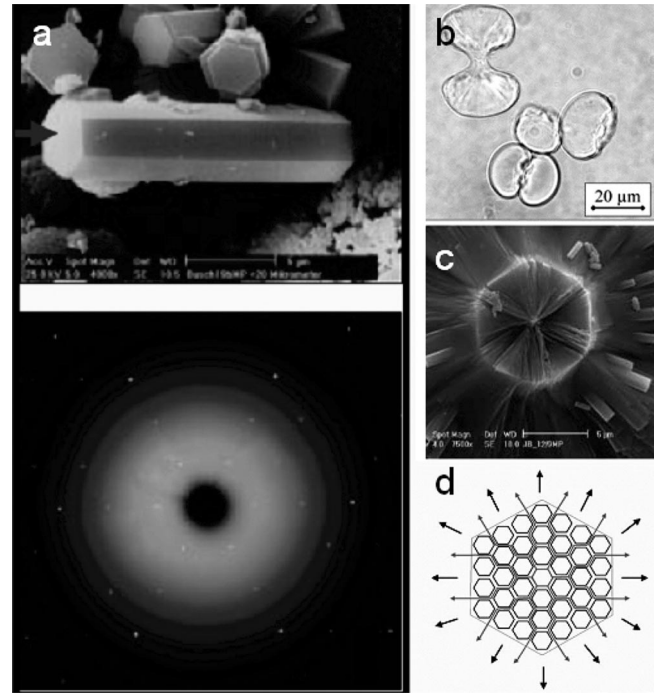

Figure 92. Fluoroapatite grown in a gelatin gel. (a) SEM of the hexagonal prismatic seed together with the corresponding X-ray diffraction pattern. The arrow indicates the direction of the incident X-ray beam; (b) gelatinous residue of the composite; (c) SEM image of the fracture area of a central seed; and (d) arrangement of hexagonal nanoparticles forming a superstructure. The lines and arrows indicate preferred cleaving directions. Figures (a), (b), and (d) are reproduced with permission from ref 466. Copyright 2003 Wiley-VCH. Figure (c) is reprinted with permission from ref 467. Copyright 2004 Royal Society of Chemistry.

a nice example to demonstrate the basic properties of a mesocrystal and the problems associated with mesocrystal identification (Figure 92a). X-ray diffraction of the seed crystal showed features of a fluoroapatite single crystal oriented along the *c*-axis,[466] due to the very high vectorial order of its nanoparticulate building units (Figure 92a). Only high-resolution TEM revealed the internal structure of the hexagonal seed crystals (Figure 92c) and a superstructure periodicity of 10 nm, in good agreement with a primary nanoparticle size of about 10 nm.[467] Although the hexagonal crystals contain ca. 2 wt % intracrystalline gelatin, the polymer does not modulate the crystal structure, suggesting that the gelatin adapts to the fluoroapatite structure.[466] The gelatin occluded in the crystals could be visualized as a ghost after removing the mineral component (Figure 92b). Because this review is focused on $CaCO_3$, silica, and morphogenesis, we will not discuss this beautiful example in depth here. Instead, the reader is referred to the original literature[463−472] as well as reviews that discuss the mesocrystal properties in more detail.[23,114,473]

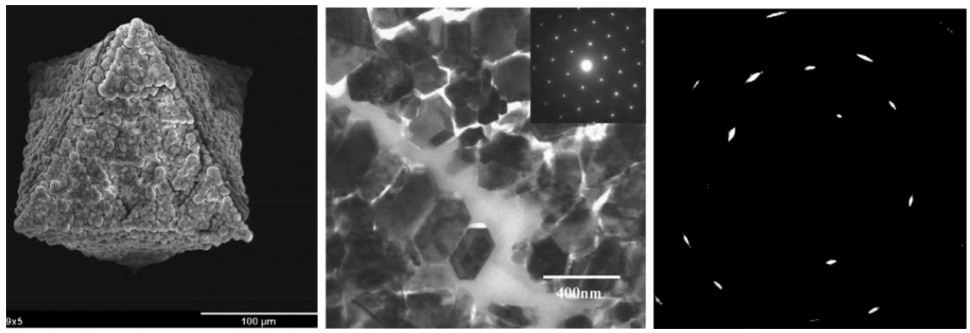

Figure 93. (left) SEM image of a calcite aggregate grown in a polyacrylamide gel with characteristic pseudo-octahedral morphology; (center) TEM image of the microstructure of a polyacrylamide-grown aggregate showing alignment of individual crystallites. An electron-diffraction pattern of an individual calcite crystal is inserted. (Right) Single crystal-like diffraction pattern of the calcite aggregate. Reprinted with permission from ref 369. Copyright 2003 American Mineralogical Society.

Gelatin gels have also been used to synthesize porous vaterite hexagonal particles.[474] Observation of the time-dependent structure-formation process revealed the nanoparticle-mediated, nonclassical crystallization process where vaterite nanocrystals underwent an ordered assembly to form a mesocrystal, and the nanoparticle subunits then fused to give a porous single crystal. This underlines the observation that porosity in single crystals can be an indication for a nonclassical crystallization process.

While gelatin gels can be considered to interact with inorganic crystals at least via their charged groups, polyacrylamide gels can be taken to be essentially inert. Growth of $CaCO_3$ in polyacrylamide gels led to remarkable pseudo-octahedral calcite mesocrystal morphologies built up of rhombohedral primary nanocrystallites, as shown in Figure 93.[369,370] It must be noted that the octahedral morphology is not possible for a calcite single crystal. As already observed for the fluoroapatite hexagonal seeds described above, the crystallographic orientation of the subcrystallites is almost perfect, and the organic matrix appears to be interspaced between individual crystallites (Figure 93).[369] However, the calcite mesocrystals exhibited a slight orientational distortion of the diffraction spots (Figure 93), corresponding to an average mosaic spread of 3.9 ± 1.1 degrees. Introduction of charge into the inert hydrogels by copolymerization with charged acrylamidopropanesulfonate (AMPS) to give polyacrylamide-co-acrylamidopropanesulfonate (PAAm-co-PAMPS) resulted in a modification of the crystal morphologies. Here, the morphologies of the calcite mesocrystals could be tuned from pseudo-octahedral[369] to cubooactahedral by increasing the amount of the charged AMPS in the copolymer gel (Figure 94).[475] The substructure of the mesocrystals that comprise smaller, aligned crystals could again be nicely visualized (Figure 94 lower images).

Alteration of the functional groups in the hydrogel changed the morphogenesis process rather than the mechanism of mesocrystal formation. The morphologies of the mesocrystals grown in gels with 1 mol % sulfonate only slightly deviate from the pseudo-octahedra shown in Figure 93, while increasing the content up to 10 mol % led to the gradual morphology variation to the cuboctahedra shown in Figure 94. This sheds some light on the questions as to why mesocrystals can exhibit defined outer faces and how their morphology can be influenced.[475]

Agar gel, which was successfully used to prepare star-shaped single $CaCO_3$ crystals under diffusion-controlled conditions,[456] has also been used for the preparation of hierarchical self-similar calcite mesocrystals. These structures formed when sufficient reactant was available through slow

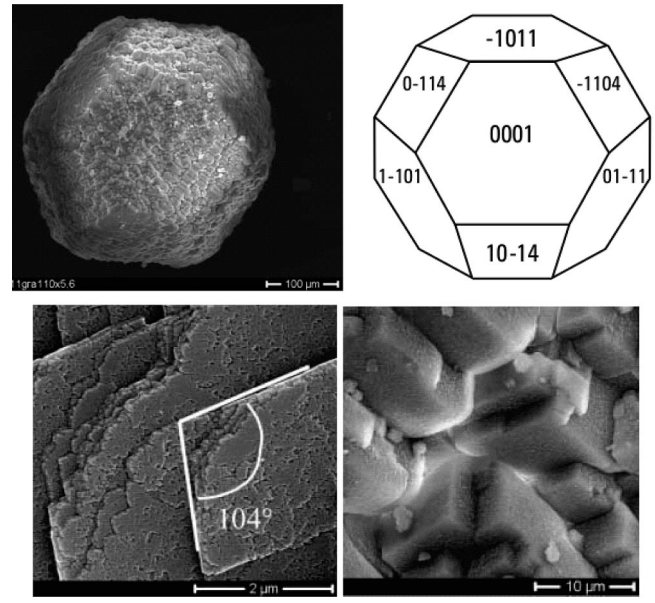

Figure 94. Pseudocubooctahedral calcite mesocrytals grown in a PAAm-co-PAMPS hydrogel containing 10 mol % of sulfonate group bearing monomers. (Upper left) SEM micrograph; (Upper right) schematic illustration of the pseudocubooctaedral morphology; (Lower left) flattened vertices of pseudocubooctahedral particles showing calcite rhombohedra faces; and (Lower right) orientation of rhombohedral subcrystals on aggregate faces. The lower images clearly show the substructure of the mesocrystal. Reprinted with permission from ref 475. Copyright 2003 Wiley-VCH.

introduction of carbonate via the gas phase.[476] The typical calcite rhombohedral habit could be generated on three different levels from the micron to the nanometer scale, and mineral bridges were suggested as connections between the nanocrystals. In contrast to the octahedral calcite mesocrystal shapes obtained in a noninteracting polyacrylamide gel, the rhombohedral shape was ascribed to a weak interaction of the agarose hydroxyl groups with calcite during the stepwise growth. [476]

Mesocrystals with a clusterlike surface morphology of mutually oriented calcite rhombohedra have been grown on an initially formed calcite single-crystal core.[477] The reason for mesocrystal formation on the single-crystal surface was seen in the compression of the gel, which resulted in the formation of a membrane due to displacement of the gel from the growing crystal. Restricted ion permeability also produced high ion concentration gradients at the crystal−gel interface.[477] Occlusion of macromolecules leads to porosity in mesocrystals as demonstrated for calcite grown in an agar

gel matrix.[478] Although the crystals look like rhombohedral calcite single crystals, they were shown to be mesocrystals by electron back-scattered diffraction, which demonstrated the same crystal orientation in an area with >1000 crystallites. The reported pores range in size from 190 ± 82 nm, and the presence of an occluded gel network was demonstrated by etching of the crystals. This approach could, therefore, be useful to alter the porosity of calcite crystals such that the porosity of the calcined crystals can be controlled according to the extent of the gel cross-linking.

4.2. Polycrystalline Structures

Polycrystalline structures are aggregates of unoriented or not uniformly oriented nanoparticles, which do not show the scattering behavior of single crystals but rings or arcs in a diffraction pattern. This distinguishes them from mesocrystals, which exhibit 3D nanoparticle orientation. There are a large number of reports on the action of additives or ions on polycrystalline $CaCO_3$ precipitation. However, although the morphology of the particles can be altered using this approach, the mechanism of formation of these structures is often unclear and there are still many questions to be answered regarding the formation of complex superstructures via nanoparticle self-assembly. Additive-based morphogenesis strategies are, therefore, not usually exploited for targeted product morphology selection. We will, therefore, focus on examples here where structure-formation mechanisms can at least be partly deduced.

4.2.1. Low-Molar-Mass Additive-Controlled Mineralization

As briefly discussed for Mg^{2+} in biominerals in section 3.2.1.2, simple ions and molecules can have a remarkable effect on $CaCO_3$ precipitation. The best-known example is Mg^{2+}, which leads to aragonite rather than calcite at high Mg^{2+} concentrations. Meldrum and Hyde showed that Mg^{2+}, in combination with citric or malic acid, has a large effect on the morphologies of precipitated magnesian calcite crystals, demonstrating that organized organic matrices are not essential for directed crystal growth of dumbbell-shaped particles.[310] Dumbbell-shaped particles were also found under varying pH and malic acid concentrations, and the transition of the dumbbell structures to spheres with time was reported.[406] The organic dicarboxylates malonate, succinate, glutarate, and adipate have also been used in a hydrothermal reaction to switch the polymorph of $CaCO_3$, according to the additive concentration and the reaction temperature.[479] Chelating carboxylato ligands yielded more profound changes in calcite morphology as compared to the dicarboxylates. Rounded calcite crystals with shapes similar to those of otoliths were formed, and the formation of microtrumpets constructed from bundles of nanocrystals of calcite was observed (see also Figure 95). Spherulite and dumbbell morphologies were also observed for high magnesian calcites with magnesium contents much greater than the thermodynamically maximum possible amount for calcite of 10 mol % Mg.[52] For this extreme situation, most unusual core−shell composite particles consisting of two different $CaCO_3$ polymorphs in direct contact to each other were observed and were shown to form via an ACC precursor phase.

In addition to soluble molecules, particle additives can also be used to direct the crystallization of $CaCO_3$. This was reported for vaterite and aragonite particles that were nucleated with mercaptobenzoic acid-capped gold particles and that displayed their characteristic morphologies.[480] The inclusion of gold particles makes the described materials an interesting metal−organic−inorganic hybrid material. Fascinating trumpetlike $CaCO_3$ morphologies, which are similar in structure to the coccolithophore *Discosphaera tubifera*, were obtained with 1,3-diamino-2-hydroxypropane-*N*,*N*,*N*A,*N*A-tetraacetate as a chelating additive.[481] These structures show an order of the primary calcite nanoparticles and are very sensitive to the $CaCO_3$−additive ratio. The mechanism of formation of these structures is as yet unknown but serves to demonstrate that even simple additives can mediate the organization of complex nanoparticle superstructures.

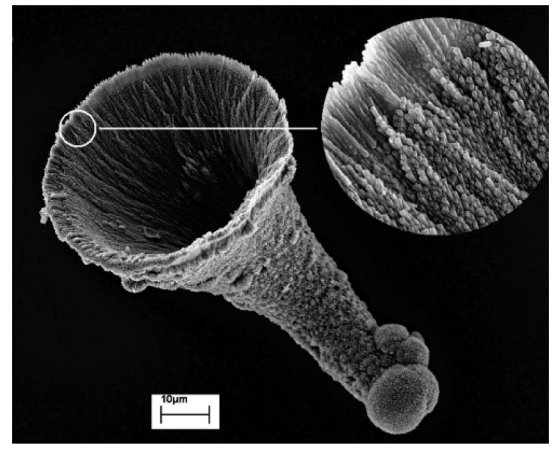

Figure 95. SEM close-up of a calcite microtrumpet formed in the presence of 1,3-diamino-2-hydroxypropane-*N*,*N*,*N*A,*N*A-tetraacetate after 24 h. Reprinted with permission from ref 481. Copyright 2004 Royal Society of Chemistry.

4.2.2. Polymer Additive-Controlled Mineralization

Polymers are very effective additives for the morphological control of crystalline substances, and particularly in the case of polycrystalline structures, there is a plethora of reported polymer-modified crystal morphologies. It is, therefore, impossible to summarize this topic in a comprehensive manner—even if only $CaCO_3$ is considered. In fact, crystal morphologies are typically modified with the addition of almost any soluble polymer additive, although very large differences exist in the effectiveness of different polymers. Polymers usually only temporarily stabilize the nanoparticle building units, and aggregation or controlled self-assembly of these units usually follows. However, the nanoparticles inside the nanocrystal superstructure do not necessarily need to be fixed in their position due to the surface polymer layer on the nanocrystals. Because the polymer is soft, such aggregates can have a soft character, as reported for $CaCO_3$ vaterite spheres obtained in the presence of polyaspartic acid.[482] Even a rearrangement of the nanoparticles in an aggregate is possible, which can lead to larger aggregate structures[482] in a similar process to the Ostwald ripening of molecules/ions/atoms dissolving from nanopaticles.

4.2.2.1. Homopolymers, Random Copolymers, and Dendrimers. Homopolymers and random copolymers offer a simple choice of polymer additive, as a wide range are already commercially available, thus circumventing the need for the researcher to synthesize them. A polymer additive that has received significant attention is poly(acrylic acid) (PAA) because it is an important scale inhibitor and, thus, significantly affects $CaCO_3$ crystallization.[38,115,204] The first

formed species in the presence of PAA are usually amorphous nanoparticles,[38,115] while the final products are typically polycrystalline and can show a variety of complex morphologies. These can be both mesocrystals (see section 4.1.4) or polycrystalline structures with unoriented nanocrystal units. The polycrystalline structures formed via liquid precursors (see section 2.2.2 and the review by Gower in this issue) fall within this category of structures. Indeed, seeded $CaCO_3$ crystallization allowed a systematic morphogenesis of calcite and vaterite, and the particle morphology could be varied from cuboid (low PAA concentrations) to ricelike ellipsoids according to the concentration of PAA used.[483]

Calcium carbonate structures displaying regular, surface-relief patterns were prepared by Kato et al. using the cooperative action of a directing agent of soluble poly(acrylic acid) (PAA) and a matrix of cholesterol-bearing pullulans (CHP-3).[484] At low temperatures (20 °C) and low concentrations of PAA and cholesteryl groups, high-quality periodic calcite structures were formed by a self-organization process. These structures formed in a reaction-diffusion regime, where precipitation and ion diffusion are in competition. These self-organized structures could also be tuned according to the molecular weight and concentration of PAA used.[485] The synthesis of $CaCO_3$ containing composites where the $CaCO_3$ is in the form of a desired polymorph is of importance from the viewpoint of materials science. A film of $CaCO_3$ crystals formed using the cooperation of insoluble polysaccharides and soluble acidic polymers was reported.[486−491] $CaCO_3$ thin-film composites containing pure calcite and vaterite were synthesized by using the cooperation of chitin/poly(acrylic acid)[486] and chitosan/poly(glutamic acid),[487] respectively. A polymorphic switching from vaterite to calcite was also realized in a chitosan matrix by changing the concentration of poly(acrylic acid).[488] Thin films with an aragonite phase have been prepared in the presence of Mg^{2+} ions and/or by using the templating effect of poly(vinyl alcohol).[489−491]

Dendrimers have also recently been shown to act as active additives for controlled $CaCO_3$ precipitation.[492−494] A motivation for this experimental approach is the defined dendrimer structure, shape, and chemical functionality. Anionic starburst dendrimers were found to stabilize spherical vaterite particles for up to 1 week, with the particle size varying in the range of 2.3−5.5 nm, according to the generation number of the dendrimer used.[494] Polystyrene sulfonate (PSS) was reported to be applicable for the synthesis of monodisperse spherical vaterite and calcite polycrystals.[495] Crystallization of spherical $CaCO_3$ particles in the presence of PSS has also been reported by Jada et al.[496] Homopolymers complexed with surfactants can also be applied for $CaCO_3$ morphogenesis.[495] Aggregates between PEO and the surfactant sodiumdodecylsulfate (SDS) were used for the generation of hollow calcite spheres.[497]

Chiral copolymers of phosphorylated serine and aspartic acid with molar masses between 15 000−20 000 g/mol have also been shown to be very efficient additives for the generation of helical calcite superstructures. These amazing structures were formed from a highly aligned array of elongated, 70 nm wide, uniform calcite nanoparticles, and the helix turn corresponded to the enantiomer (D or L) of the applied polymers.[498−500] A narrow experimental window was required for the formation of these morphologies. The helical structures formed when a high degree of phosphorylated Ser (75 mol %) and 25 mol % Asp in the copolymer were adopted in combination with a 10-fold Ca^{2+} concentration with respect to the monomer—conditions that are believed to closely resemble those that exist when a shellfish forms a shell. Very recently, a formation mechanism for these helical structures was proposed based on nonclassical crystallization.[500] Similar structures, but of purely organic nature, were found during "biomorph" synthesis and were reported to be an organic polymer, representing plastic abrasion caused by scratching glass pipettes along plastic surfaces.[501]

4.2.2.2. Biopolymers. In addition to these synthetic homopolymers, biopolymers have also been successfully used for the polymer-controlled formation of $CaCO_3$ polycrystals. Because of their role in biomineralization, biopolymers are often a natural choice of soluble additive for the morphogenesis of complex superstructures. Nevertheless, in vitro experiments have so far typically failed to reproduce the complex shapes of many biominerals. Looking at $CaCO_3$ precipitation, biopolymers including cationic, anionic, and nonionic dextran[502] and collagen[503] have been employed. Protein secondary structures where the spatial orientation of functional groups can be determined have been investigated so that the protein can bind to a targeted crystal face.[413] Alternatively, a combinatorial approach has been applied to select peptides from a 15-mer peptide library for use as additives for $CaCO_3$ crystallization.[504] These strategies reflect the problems associated with the complexity of biomineralization processes, which usually involve structural (insoluble) and functional (soluble) components, which are likely to work together in many biomineralization processes. Commonly, the structural matrix is neglected and investigations just focus on the soluble crystallization additives—an approach that can lead to significant control over mineralization reactions. The structural complexity already obtained in the presence of a single polymer additive can be high, and possible synergistic combinations between the different components in the organic matrix are difficult to assess and imitate.

4.2.2.3. Double Hydrophilic Block Copolymers. Probably the most effective class of polymers for controlling the crystallization of polycrystalline minerals are the so-called double hydrophilic block copolymers (DHBCs). There are a number of reviews available on their synthesis and application.[162,163,378,389,392,419] DHBCs provide a simplified model system for the proteins that are active in biomineralization.[419] They consist of a hydrophilic block that does not, or only weakly, interacts with crystal surfaces, thereby providing steric stabilization in water, and a second polyelectrolyte block, which interacts with inorganic surfaces. However, because the water-soluble blocks are short (usually between 2 000−10 000 g/mol), they only temporarily stabilize the primary nanoparticles. These nanoparticles are often kinetic products such as ACC or vaterite and have typical sizes of 10−30 nm. They provide the building units for higher-order assembly processes, leading to the formation of remarkably well-defined microparticles, whose shapes predominately depend on the chemical functionality of the polyelectrolyte block[424,505] and the functionalization degree.[506]

In addition to the structure of the polymer itself, the experimental conditions also play a significant role in determining the morphologies and structures of the particles precipitated in the presence of DHBCs. At low polymer concentrations or pH, the polymer selectively adsorbs onto specific crystal surfaces, leading to single crystals with

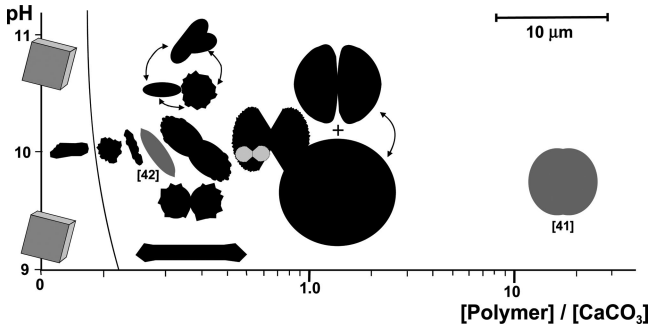

Figure 96. Morphology map of $CaCO_3$ in presence of PEG-PMAA showing the morphology dependence of $CaCO_3$ in dependence of pH and the ratio [509]/[$CaCO_3$] where the unit for both concentrations is g/L. The particles are drawn to scale. Arrows indicate when several morphologies were observed simultaneously. Morphologies reported for the same system in refs 510 and 511 are also included and drawn in gray. Reprinted with permission from ref 507. Copyright 2001 Wiley-VCH.

modified morphologies. In contrast, higher-order assembly of temporarily stabilized $CaCO_3$ nanoparticles can be observed at high polymer concentrations or pH values. By variation of experimental parameters like pH, polymer/$CaCO_3$ concentration, and ionic strength for a given system, a so-called morphology map can be obtained that allows the empirical prediction of the $CaCO_3$ morphology for known experimental conditions. This has been carried out for the polymer PEO-*b*-PMAA (see Figure 96).[507] For this system, a similar rod−dumbbell−sphere transition was observed, as was observed for fluoroapatite (discussed in section 4.1.9.2). Such structures including rods, dumbbells, and spheres can be overgrown by calcite rhombohedra in a further crystallization step.[508] The morphology development sequence from rods to spheres was also observed for other carbonates including $BaCO_3$ in the presence of PEG-*b*-PMAA, indicating the morphogenesis mechanism in Figure 96 to be more universal.[41] The observation of such a morphological map clearly demonstrates that a single polymer−mineral system can be tuned to produce a whole spectrum of particle aggregate morphologies. These particles are predominantly nanocrystal superstructures with complex morphologies, and it can be assumed that similar growth mechanisms operate to form many of these superstructures.

PEO-*b*-PMAA is probably the most extensively studied block copolymer to date. Its application was first independently reported in refs 510 and 511, although different structures were reported (dumbbells and spheres in ref 510 and elongated overgrown calcite rhombohedra in ref 511). Nevertheless, these structures fit well to the morphology, which is expected for the applied experimental conditions from the empirical morphology map (see Figure 96). Spherical vaterite microparticles were found if acidic polypeptide blocks such as PGlu were used as functional blocks in a PEO-based DHBC.[512] However, in contrast to the calcite rod−dumbbell−sphere morphology transition, which is observed for calcite with a PEO-*b*-PMAA additive, in the vaterite case, spherical particles are directly formed without any rod or dumbbell precursors. In addition, it could be shown that a random coil conformation of the polypeptide chain allowed for better crystallization control than the ordered α-helix conformation,[512] which is in agreement with the finding that biomineralization proteins tend to adopt the unfolded structures for their interacting motifs.[513]

A hollow, spherical, vaterite nanoparticle aggregate was reported in the presence of a DHBC with a strongly chelating poly(EDTA) block.[510] The final hollow-sphere morphology developed from a solid sphere by dissolution from the inside out. This could indicate the existence of a radial gradient of the $CaCO_3$ nanoparticle density or possibly a radially decreasing polymer-concentration gradient, where the DHBC would appear to play a chemically active role even after inclusion into the nanoparticle aggregate. The same principle has also been exploited for the formation of vaterite microrings.[514] Here, however, the PEO-*b*-PEDTA polymer was modified with C_{17} chains to enable polymer self-assembly. The microrings and a proposed formation mechanism are shown in Figure 97. The formation of the microrings starts with crystallization inside unstructured polymer aggregates, which results in the formation of an aggregate of polymer−inorganic hybrid nanocrystallites. Because the polymer concentration is greatest at the beginning of the precipitation process, the occluded polymer concentration will be highest inside these aggregates. The chelating polymer will then slowly dissolve from the $CaCO_3$ particles from the inside out, following its concentration gradient, and ultimately forming the $CaCO_3$ rings.

Hollow calcite spheres exhibiting surfaces comprising small calcite rhombohedra have been reported when PEO-*b*-PMAA was used as an additive together with SDS surfactant.[515] Here, hollow calcite aggregates were reported for the first time, as well as hollow vaterite disks composed of aggregated nanoparticles. These vaterite disks dissolved from the inside out, in analogy to the results reported in ref 510. The rhombohedral calcite surface structures are very similar to those reported by Tremel et al., where Au nanocolloids were used as nuclei for crystallization of calcite spherules with sizes about 10−15 μm.[516,517] In contrast, the cationic surfactant CTAB, which can complex to the anionic PMAA groups of the DHBC, yielded unusual calcite pine cone-shaped particles. [515]

When a DHBC with a rigid polyelectrolyte block was applied—in this particular case, a cyclic hexaethyleneimine ring—a stack of pancakelike $CaCO_3$ layers was obtained.[427] Computer simulations suggested that the crystal morphologies were not influenced by epitaxial match between polymer and exposed crystal surface but that nanoparticle stabilization, crystallization time, time for polymer rearrangement, and surface ion density were all important parameters in the morphogenesis process. Cationic DHBCs have also been successfully employed for the morphogenesis of vaterite particles.[518] Here, stratified morphologies were formed at the air−water interface and could be influenced by the poly(ethylene imine) (PEI) block length as well as pH.

The above studies indicate that DHBCs constitute a versatile class of model compounds for the study and generation of a wide variety of complex $CaCO_3$ morphologies. These structures are typically generated through higher-order assembly of temporarily stabilized $CaCO_3$ nanoparticles. Related copolymer architectures, for example, widely available graft copolymers, are likely to exhibit similar effects and facilitate the higher-order assembly of $CaCO_3$ nanoparticles. This is clearly a topic for future studies.

4.2.2.4. Double Hydrophilic Graft Copolymers. Graft copolymers are in many ways similar to DHBCs. They are significantly easier to prepare than block copolymers, and their composition can also be tailored over a wide range, although in a more random manner than is possible for block copolymers. Given then the possibility of upscaling, graft copolymers are also interesting as crystallization additives

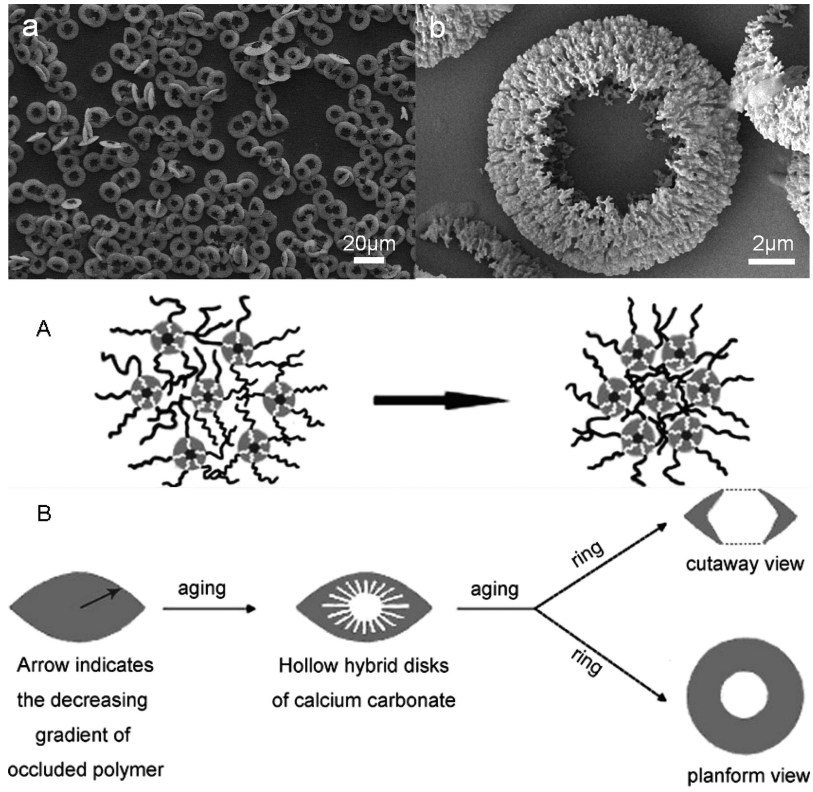

Figure 97. SEM images of $CaCO_3$ microrings grown in the presence of PEO-*b*-PEDTA and their proposed formation mechanism: grey, calcium carbonate; red, hydrophobic block; blue, soluble neutral block; and yellow, charged block. Red arrow indicates the decreasing gradient of occluded polymer within the disklike structure. Reprinted with permission from ref 514. Copyright 2006 American Chemical Society.

for industrial applications. Nevertheless, only a few examples have been reported to date of the use of graft copolymers as additives to control crystallization processes. $CaCO_3$ precipitation has been investigated in the presence of double hydrophilic graft copolymers in aqueous solution.[67] Graft copolymers with functional carboxy groups along the main chain were were applied as additives in the crystallization of $CaCO_3$.[519] Poly(ethylene oxide) graft copolymers with a polyacetal backbone were used to investigate the influence of the molecular parameters on $CaCO_3$ crystallization.[520] Variation of the block lengths of the hydrophilic and ceramophilic blocks resulted in altered calcite particle sizes, shapes, and dispersion stabilities with respect to aggregation. An optimal balance between both moieties in the graft copolymer was found to be essential for maximum effect on the $CaCO_3$ crystallization behavior.

4.2.3. Amorphous Precursor Phases

Amorphous precursor phases appear to provide the principal mechanism of polymer-controlled bioinspired mineralization processes. It has already been shown in section 2.2.2 that polymer-induced liquid precursor (PILP) phases can be used to generate polycrystalline $CaCO_3$ superstructures with moldable shapes. In most other cases of polymer-controlled mineralization, amorphous $CaCO_3$ nanoparticles are formed first and rapidly aggregate to form rather unstructured masses.[503,507] Application of DHBCs with concentrations in the range of only a few ppm can, however, stabilize individual spherical ACC nanoparticles with sizes in the range of ca. 100 nm.[521] Addition of polyelectrolytes with the ability to strongly inhibit crystallization can stabilize the amorphous nanoparticle in the early stages of the precipitation reaction. A mesoscale transformation[36] can then take place, providing a transition from the amorphous phase to crystalline forms. This has been demonstrated in a time-resolved study of the scale-inhibition efficiency of polycarboxylates, where amorphous nanoparticles were detected in the initial stages.[204] The ACC nanoparticles serve as material depots for subsequent crystallization events, and transformation into crystalline material probably takes place by dissolution-recrystallization, although solid-state reactions cannot be ruled out despite their high activation energy barrier (see discussion in section 2.1.5).

The formation of polycrystalline solids via amorphous precursors also overlaps with section 4.2.2, where amorphous precursors are omnipresent even if not explicitly stated there. In this section, we will focus on two selected cases: the formation of synthetic nacre in a demineralized organic nacre matrix via ACC precursors, and the transformation of stable ACC particles formed in reverse microemulsions into polycrystalline superstructures by the addition of water.

It is possible to use the demineralized matrix of nacre as a template for the synthesis of a structured organic/$CaCO_3$ composite material. In this model system, the demineralized insoluble matrix of nacre was remineralized with amorphous $CaCO_3$ nanoparticles, which were formed in the presence of μg/mL amounts of polyaspartic acid.[522] The amorphous precursors were able to completely fill the compartments of the insoluble organic matrix with $CaCO_3$. This was possible via nanosized holes in the interlamellar layers. Calcite was obtained instead of the natural aragonite, and the single-crystalline domains were found to be smaller than for the natural material (Figure 98). In addition, the synthetic nacre was morphologically indistinguishable from its natural

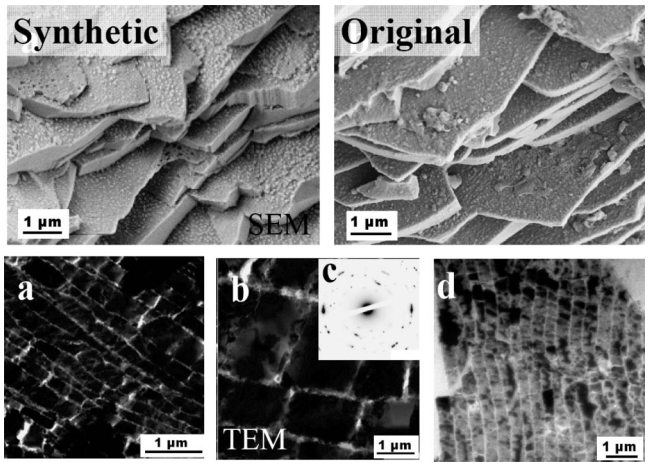

Figure 98. Nacre retrosynthesized in the insoluble organic matrix of a *Haliotis laevigata* shell via transformation of amorphous precursor particles. The upper pictures show the comparison of the SEM morphology of natural and synthetic nacre, and the lower line shows the corresponding transmission electron micrographs (TEMs) of microtomed samples: (a) synthetic nacre, (b) synthetic nacre in higher zoom, (c) electron-diffraction pattern taken in this region and showing an almost single crystalline calcite domain, and (d) TEM thin cut of natural nacre. Reprinted with permission from ref 522. Copyright 2005 American Chemical Society.

archetype by electron microscopy (SEM and TEM), as shown in Figure 98. This experiment suggests that natural nacre can indeed be fabricated from amorphous precursor particles, which can even be nucleated outside the matrix. For the generation of ACC, a simple polyelectrolyte function is sufficient.

A very efficient way to systematically change the crystal morphology of $CaCO_3$ was described via water-induced mesoscale transformation of surfactant-stabilized ACC. ACC precipitated in reverse microemulsions was used to generate self-assembled vaterite superstructures.[523] The structures could be adjusted from monodisperse spheroidal aggregates at low water amounts, via spindle-shaped aggregates and coaligned high-aspect ratio nanofilaments, to large vaterite nanoparticles at high water contents. This shows that water-triggered $CaCO_3$ crystallization and electrostatic mineral surfactant interactions can lead to coupled mesoscopic processes that result in the in situ higher-order assembly of complex morphologies. This microemulsion-based approach involving ACC dissolution and recrystallization was also successfully applied to the synthesis of well-defined, doughnut-shaped aragonite microparticles.[524]

4.2.4. Templating Routes to Polycrystalline Solids

The previous sections clearly show that, in removing the restriction of a required single-crystal structure, additives can direct the formation of polycrystalline particles with a huge range of morphologies. However, even in the production of polycrystalline solids, the application of additives is limited to the formation of relatively small structures. Again, access to complex 3D morphologies can only be achieved via templating, where the shape of the template defines the form of the product material. In this section, we provide an overview of the application of templating routes to producing polycrystalline solids with morphologies that could not be generated directly. Clearly, morphological control using this strategy relies upon the existence of suitable templates, and a wide range of templates had been explored including ice,[525−527] colloidal crystals,[528−530] filter paper,[531] and

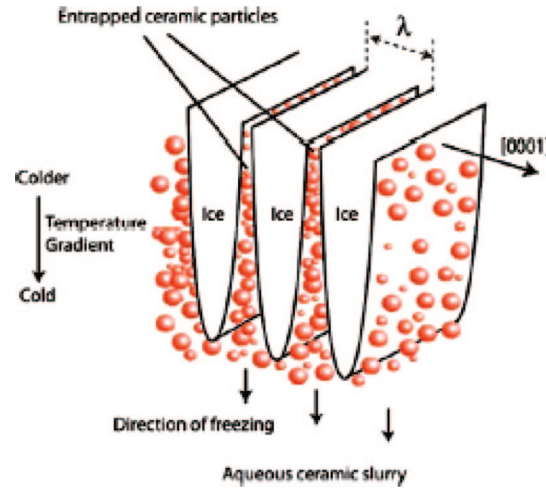

Figure 99. Pattern formation and particle segregation during freeze-casting of ceramic slurries. The ice platelets grow in a direction perpendicular to the *c*-axis of hexagonal ice. The interlamellar separation of the structure is represented by λ. Reprinted with permission from ref 527. Copyright 2008 The American Chemical Society.

microemulsion systems.[212,532,533] Moving to the production of more complex morphologies, the subject comes full circle and looks to biology for suitable templates. A wide range of biological templates including pollen grains,[534] sea urchin skeletal plates,[353,535−538] and wood[539−542] have been used to produce structures with intricate morphological form.

Necessarily, the topic of templating is enormous in scope. The intention of this section is, therefore, not to provide a comprehensive review of templating methodologies but to illustrate the potential and range of the approach. Again, in order to avoid unnecessary repetition, templating routes to some amorphous materials are considered here and are not discussed under section 2.2.2.

4.2.4.1. Ice Templating. Ice templating has been used as an elegant route to produce a range of inorganic and organic solids with controlled morphologies.[525−527] As a general methodology, an aqueous solution or dispersion is frozen to produce an array of ice crystals, and the rate of freezing is controlled such that the solute particles are expelled to the interfaces between the ice crystals (Figure 99). Subsequent removal of the ice by sublimation (freeze-drying) then generates a porous or fibrous solid with a morphology that is a replica of the ice crystal array.[525,527,543] Back-filling of this structure can then be carried out to achieve greater control over structure.[526] One of the principal strengths of this method is that the structure of the ice itself can be varied through selection of the freezing temperature and rate, or through application of "directional solidification" methods. This provides a basis for controlling the structure and morphology of the product materials and has been employed to produce a range of oriented porous materials, as will be briefly described here.[525,527] The specific case of silica-templating is considered in section 4.3.

Unidirectional freezing of sols or hydrogels of particles can be used to produce microchannelled structures that show a high degree of alignment along the freezing direction. For example, honeycomblike macroporous structures of $SiO_2-Al_2O_3$ were produced by directional freezing of a sol produced on combining $Al(NO_3)_3 \cdot 9H_2O$ and sodium silicate at pH 3,[544] with porous fibers of ceramics such as TiO_2,[545] ZrO_2,[546] and alumina.[547] Ice-templating has also been used

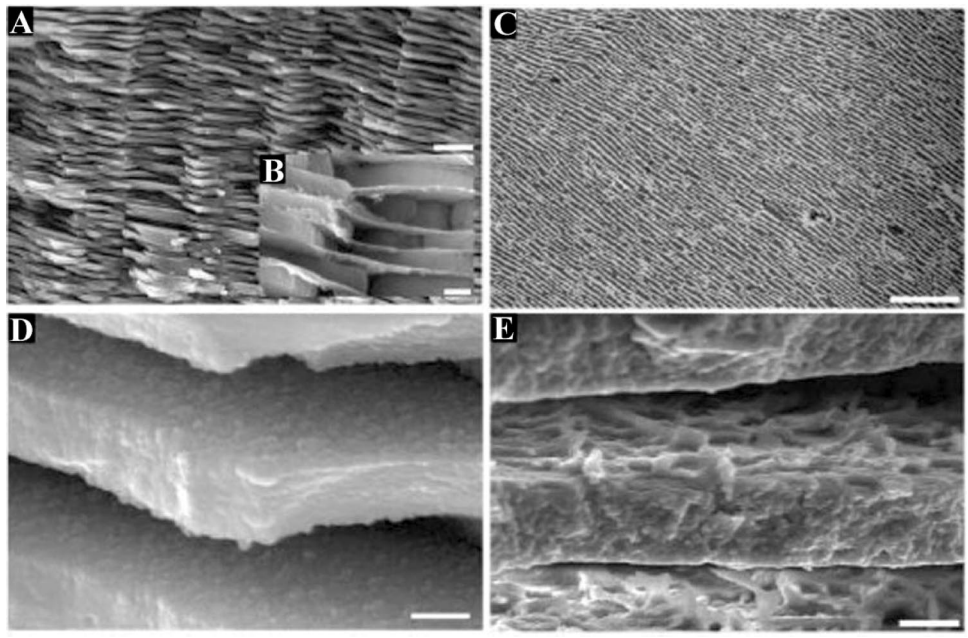

Figure 100. Natural nacre has a brick−mortar−bridges microstructure where inorganic calcium carbonate layers are held together by organic protein "glue" (B and C); the roughness of the inorganic walls (D) is a key contributor to the final mechanical properties of nacre. The layered microstructure of the ice-templated dense composites resembles that of nacre [for example, the alumina−Al−Si composite in (E)]. The particles entrapped between the ice dendrites generate a characteristic roughness on the lamella surface (F) that mimics that of the inorganic component of nacre. Scale bars indicate (B) 5 μm, (C) 0.5 μm, (D) 0.3 μm, (E) 300 μm, and (F) 10 μm. Reprinted with permission from ref 526. Copyright 2006 American Association for the Advancement of Science.

to fabricate ceramic-based composites with nacre-like structures.[526] Directional freezing of aqueous slurries of ceramic particles yielded a lamellar microstructure where the ceramic particles were concentrated between, and sometimes within, ice crystals. Dense composites were then produced by infiltrating the lamellar ceramic with a second phase such as a polymer or liquid metal. The solids produced exhibited marked structural similarities to nacre, such that the inorganic layers were parallel to each other and were homogeneous throughout the sample (Figure 100).

4.2.4.2. Micellar and Microemulsion Systems. Micellar and microemulsion systems have been extensively explored as systems with which to control the nucleation and growth of crystals and to produce nanoparticles of defined sizes and morphologies. Particle morphologies are principally defined by the confines of the organic template, and the sizes are defined by the dimensions of the organic aggregates, the reactant concentrations, and the reaction times. The application of micellar systems to nanoparticle synthesis has been summarized in a number of review articles.[548,549] Illustrating with calcite, which cannot be produced as nanoparticles using direct precipitation methods, $CaCO_3$ particles with diameters of 5.4 nm were produced in water-in-oil (W/O) microemulsions, prepared by solubilizing $Ca(OH)_2$ solution in the cores of reverse micelles of the nonionic surfactant hexaethyleneglycol dodecyl ether (DP-6) in cyclohexane and bubbling carbon dioxide through the solution.[550] A similar method was used to precipitate calcium carbonate in reverse micelles of calcium 1,2-bis-(2-ethylhexylcarbonyl)-1-ethane sulfonate (CaOT) in cyclohexane, and particles of diameters in the range 48 to 130 nm were produced according to the ratio of water and CaOT.[551] A highly uniform population of non-aggregated 25 nm $CaCO_3$ particles was produced by addition of a solution of $Ca(CH_3COO)_2$ to reverse microemulsions of $NaHCO_3$ solution/*n*-dodecane/cetyltrimethylammonium-bromide (CTAB)/hexan-1-ol, reflux of the solution for 1−2 h, and final addition of diethylene glycol (DEG).[552] It is noteworthy that the particles were reported to have an aragonite-like structure.

Small $CaCO_3$ particles of diameters $\approx$ 4 nm were also produced by combination of two sets of water/cyclohexane/Marlipan microemulsions containing calcium chloride and sodium carbonate, respectively.[553] Similar particle sizes were obtained for a wide range of Ca^{2+} and CO_3^{2-} concentrations and droplet sizes. Interestingly, prolonged incubation of the system resulted in the formation of needlelike $CaCO_3$ particles with lengths of 2−8 μm and widths of $\sim$100 nm. Formation of rod-shaped calcite crystals was also observed in a CTAB/1-pentanol/cyclohexane microemulsion system, where $CaCl_2$ solution provided the aqueous phase in the microemulsion and precipitation was induced through addition of $(NH_4)_2HCO_3$ solution.[554] Solutions were then left unstirred for 10 days. Examination of the precipitate with time showed that hexagonal vaterite platelets were produced after 1 day, and that crystallization proceeded to yield rod-shaped single crystals of calcite with time.

Some more complex crystal morphologies have also been produced in microemulsion systems. Stacked superstructures of 20 nm thick pseudohexagonal calcite plates were produced by addition of sodium carbonate-containing NaAOT (AOT = bis(2-ethylhexyl)sulfosuccinate) microemulsions to reverse micelles of calcium dodecylbenzene sulfonate under conditions of high pH (Figure 101).[555] Structural examination suggested crystallographic registry between the plates, and the observation of a spiral growth pattern on end plates suggested that the stacks developed by spiral outgrowth from a basal plate. That separate plates were observed rather than a single crystal unit was attributed to interaction with the surfactant molecules. Fibers of $CaCO_3$ comprising aggregates of crystals were also produced on precipitation of $CaCO_3$ from $CaCl_2$/CTAB/toluene reverse microemulsions on addition of sodium bicarbonate solution and subsequent reflux.[556] Here, the results suggested that rod-shaped aragonite crystals were formed first, and that vaterite crystals subse-

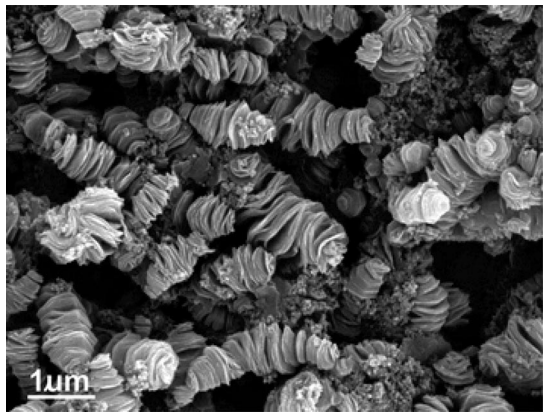

Figure 101. SEM image showing stacked lamellar calcite superstructures. Reprinted with permission from ref 555. Copyright 2004 The Royal Society of Chemistry.

quently grew on these to give the observed product morphology. Combining the effect of confinement provided by microemulsions with that of soluble additives, calcium carbonate was precipitated on combination of $Ca(AOT)_2$ reverse micelles and carbonate-containing NaAOT microemulsions, to which the growth modifier sodium polyphosphate had been added.[557] In the absence of sodium polyphosphate, micrometer-sized doughnut-shaped structures of densely packed layers of platelike aragonite crystals were formed. These appeared to form from aggregates of surfactant-stabilized ACC particles, which subsequently crystallized to give either single crystals of aragonite or highly oriented polycrystalline arrays. Further aging in solution led to overgrowth by calcite nanofilaments (Figure 102). Addition of polyphosphate at concentrations of 0.5 g L^{-1} and above had a significant effect on the particles precipitated. Calcite was the principal polymorph produced at concentrations of 1 g L^{-1}, while vaterite and calcite were produced at 2 g L^{-1}. The effect of the additive was also apparent in the particle morphologies, such that platelike, rather than doughnut-shaped, particles were produced at 2 g L^{-1}.

The use of surfactant systems has also been extended to produce some remarkable calcium carbonate morphologies. Spherical vaterite particles with spongelike microstructures and diameters of 4−16 μm were prepared by evaporation of sodium dodecyl sulfate (SDS)/octane/supersaturated calcium bicarbonate solution water-in-oil microemulsions (Figure 103).[212] The particles were patterned with a random array of hemispherical surface depressions and pores. Many were highly porous with a perforated outer shell and a partially hollow center, while others were more highly mineralized, with one large hole or indentation. These structures were considered to form by precipitation of mineral on micron-scale water droplets, generating perforated hollow shells with smooth surfaces. Bubbles of CO_2 released from the saturated bicarbonate solution then form at the oil/water interface of the aqueous droplets, where they remain due to their low diffusion rate through the oil phase. Precipitation of calcium carbonate around the bubbles then generates the observed surface patterns, and further growth proceeds inward as the droplets progressively decrease in volume (Figure 105b).

Calcium phosphate materials with reticulated structures were formed by precipitation of calcium phosphate in a microemulsion system of composition DDAB(didodecyldimethylammonium bromide)/oil/metastable calcium phosphate solution, where the oil phase selected was either dodecane, tetradecane, or hexadecane.[558] The prepared microemulsions

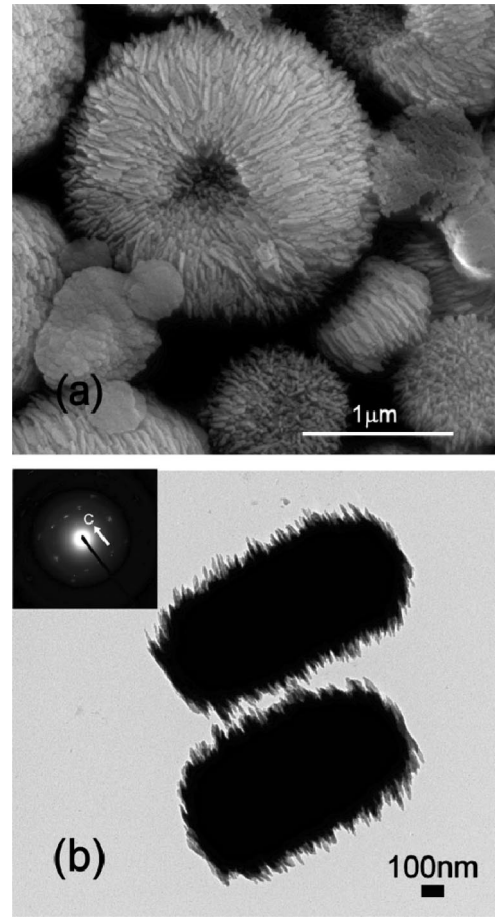

Figure 102. (a) SEM image showing doughnut-shaped aragonite particles overgrown with calcite nanofilaments after 7 days; (b) TEM image showing side view of doughnut-shaped particles and elongated calcitic outgrowths parallel to the morphological radial axis. The inset shows corresponding electron-diffraction pattern from the particle in the upper part of the TEM image. Reprinted with permission from ref 557. Copyright 2006 The American Chemical Society.

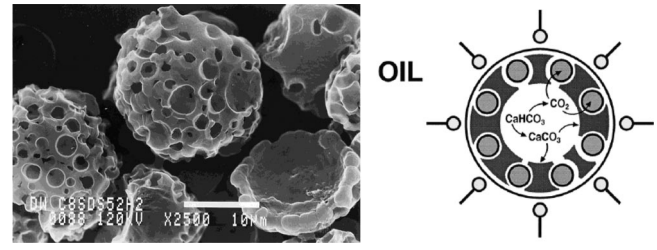

Figure 103. (a) SEM image of spongelike vaterite spheroids from a reverse microemulsion showing complex surface and internal patterning, with microemulsion composition octane/SDS/$CaHCO_3$ = 71:4:25 wt %; (b) the formation mechanism. Reprinted with permission from ref 212. Copyright 1999 Wiley-VCH.

were frozen for a period of several weeks at temperatures where the oil phase was frozen but the water remained liquid. The inorganic product material was then isolated by centrifugation and washing in hot hexane. Macroporous frameworks with pores of up to several microns in diameter and wall thicknesses of 50−130 nm were typically obtained. The fine structure of the frameworks was determined by the oil and reagent concentrations used, with the constituent particles varying from needles to sheets of hydroxyapatite. The overall skeletal structure of these materials was attributed to nucleation of the mineral within the confines of the water channels of the bicontinuous microemulsion. Further growth

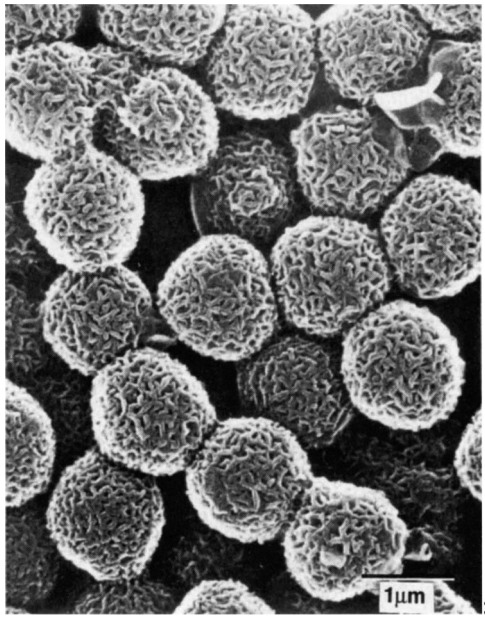

Figure 104. Hollow shells of mesoporous aragonite. Reprinted with permission from ref 532. Copyright 1995 Nature Publishing Group.

then results in a reorganization of the microemulsion system, such that the product mineral shows structuring at a significantly longer length scale than the original microemulsion system.

Polycrystalline aragonite exhibiting an intergrown, "skeletal" structure has also been precipitated from bicontinuous microemulsions. Here, microemulsions of DDAB, tetradecane, and hexadecane, and a saturated calcium/magnesium bicarbonate solution were employed, and the mineral was precipitated as thin films on selected substrates.[532] Films of aragonite were deposited on solid substrates by placing a drop of the microemulsion solution on a substrate, immersing it in hot chloroform and finally evaporating any residual solvent. The films formed possessed honeycomb microstructures of irregularly shaped columnar pores with interconnecting crystalline walls, often at ~120° to each other, and pore sizes were determined by the composition of the microemulsions. Hollow shells of skeletal aragonite were formed using a similar strategy, where polystyrene spheres were dipped into the microemulsion solution, prior to washing in hexane and finally dissolving away the spheres (Figure 104). The morphology of the aragonite films appeared to form during the solvent-extraction step. This may have induced phase separation, which in turn resulted in the production of a close-packed array of oil droplets on the substrate. Facile outgassing of CO_2 from the supported thin film then results in rapid mineralization and complete removal of the oil, which leaves an inorganic replica of the self-assembled foam. Although the overall structures of the bicontinuous microemulsions and the continuous mineral network are similar, the length scales are totally not commensurate, which suggests that phase separation and reorganization of the microemulsions structure must occur during crystallization.

Similar systems were also explored to produce similar "cellular frameworks" of a range of transition metal oxides.[533] Thin films with skeletal structures of lepidocrocite (γ-FeOOH), Mn(III/IV) oxide ($Mn_7O_{13}\cdot 5H_2O$) and cobalt(III) oxide were prepared using a similar methodology to that described above for aragonite, with the exception that

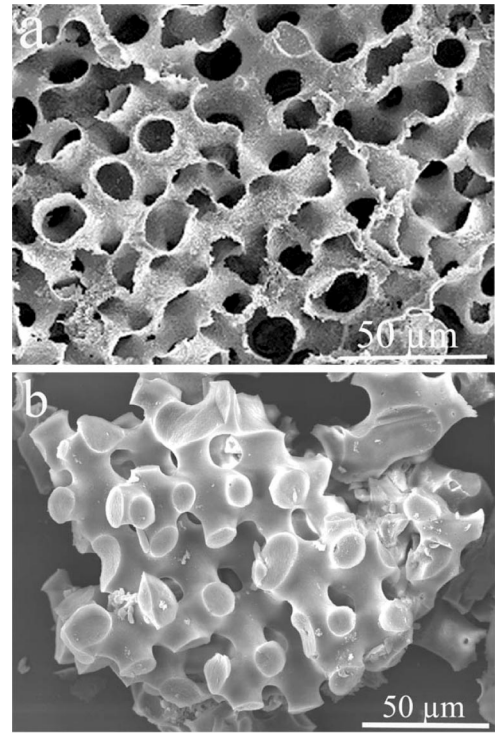

Figure 105. (a) Templated macroporous silica produced by a "filtration method", showing double-sided structure, and (b) by a "particle/hydrolysis method", producing a solid replica. Reprinted with permission from ref 537. Copyright 2006 Elsevier.

crystallization of the inorganic phase now occurred on oxidation of a metal-ion-containing microemulsion, rather than outgassing of CO_2. Here, the structured inorganic thin films were produced when the rate of oxidation and hydrolytic condensation of the metal ions was comparable to the lifetime of the oil-droplet-based foams. The branched network structure was in turn determined by the constrained growth of the metal oxides within the phase-separated microemulsion film.

4.2.4.3. Biotemplating. We have previously described the use of selected biotemplates in producing single-crystal structures (section 4.1). There are many similarities in the techniques used to template polycrystalline and amorphous structures, and in an effort to avoid excessive repetition, this section will address the application of biotemplates to form both polycrystalline and amorphous mineral structures, using both solution-based and gas-phase synthetic methods. Demonstrating the versatility of the approach, we will initially use the example of the application of sea urchin skeletal plates as templates, showing how these structures can be used to direct the formation of macroporous amorphous and polycrystalline ceramics and metals. An overview of biotemplating methods is then provided, which shows the diversity of morphologies that can be generated based on biological structures.

4.2.4.3.1. Sea Urchin Skeletal Plates. Sea urchin plates offer truly remarkable structures, the surfaces of which resemble a triply periodic minimal surface (TPMS), a Schwartz P-surface, which possesses zero mean curvature and exhibits periodicity in structure in three independent directions (see also section 3.2.3).[14,351] While TPMS are common throughout the natural world, occurring, for example, in surfactant−water systems and cell membranes, the sea urchin plate structure is on a significantly larger length scale.[351,352] Employing urchin skeletal plates as templates

therefore gives access to structures that cannot as yet be prepared de novo.

A wide range of amorphous and polycrystalline macroporous solids including silica, gold, copper, nickel, and titania were prepared using templating approaches based on sea urchin skeletal plates.[353,535−537] The $CaCO_3$ plates were either used directly or polymer replicas with identical structures were employed, providing greater chemical stability. A variety of templating procedures was used, tailored to the product material, and excellent structural reproduction was achieved. Looking first at the example of amorphous silica, a number of synthetic techniques were applied. Suction-filtration of a dilute sol of 0.2−0.3 μm pre-prepared silica particles through a skeletal plate, subsequent annealing, and removal of the $CaCO_3$ yielded a two-sided macroporous silica structure deriving from surface coverage of the urchin plate by the silica particles (Figure 106a). Two further methods were also investigated, namely, a "hydrolysis method" in which either a sea urchin plate or polymer replica was immersed in tetraethoxyorthosilicate (TEOS) or silicon tetrachloride and then subjected to controlled hydrolysis and a "particle/hydrolysis method" where the selected template was initially immersed in a solution of pre-prepared silica particles to give partial filling of the pores and then dried before applying the hydrolysis method. While the "hydrolysis method" was in general of limited success, leading to poor structural replication, the "particle/hydrolysis method" enabled excellent templating of both the sea urchin plates and polymer replicas (Figure 105b). Macroporous, spongelike structures that were almost identical in morphology to the original template were produced, indicating that complete filling of the template pore structure had occurred. The average size of the SiO_2 particles produced varied according to the template used, and the 100 μm particles produced in the sea urchin plates were typically significantly larger than the 50 μm or smaller particles produced in the polymer membranes.

Bicontinuous, macroporous titania structures were formed using polymer replicas of sea urchin skeletal plates as templates as the low pH values present during hydrolysis of the titania precursors resulted in dissolution of the native $CaCO_3$ plates.[537] Similar methods were applied as described for silica. Using the "hydrolysis method", the template was immersed in titanium ethoxide or titanium tetrachloride and then subjected to controlled hydrolysis, while with the "particle/hydrolysis method", the template was initially immersed in a solution of titania nanoparticles and then dried, before applying the hydrolysis method. Both of these methods were successful in achieving extensive filling of the membrane pores. Using the hydrolysis method, far greater structural perfection was achieved using titanium tetrachloride than titanium ethoxide, and macroporous solids with sizes often exceeding 200 μm and structures identical to the original urchin plates were produced (Figure 106a). The "particle/hydrolysis" method enabled excellent templating of the polymer replicas using both reagents, and very large macroporous monoliths of TiO_2, very close in structure to the original plate and often exhibiting sizes in excess of 1 mm, were produced (Figure 106b). While the immediate hydrolysis products were in all cases amorphous titania, subsequent calcination at 600 °C yielded crystalline anatase, with maintenance of the original macroporous structure.

Sea urchin plates have also been used to template the formation of a range of macroporous metals, using a number of synthetic techniques. Bicontinuous gold structures were

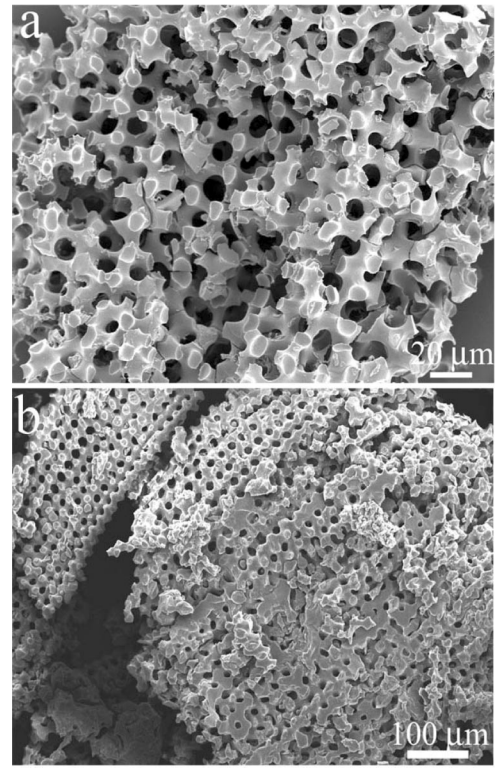

Figure 106. Macroporous titania produced by (a) hydrolysis of titanium tetrachloride in a polymer replica of a sea urchin skeletal plate, and (b) the particle/hydrolysis method in the polymer replica, in which the polymer was initially immersed in a solution of TiO_2 particles prior to hydrolysis. Reprinted with permission from ref 537. Copyright 2006 Elsevier.

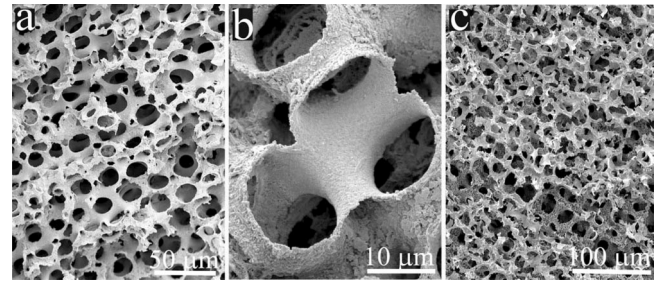

Figure 107. (a) Macroporous gold produced from a sea urchin skeletal plate template and (b) a higher-magnification image showing the rough surface originally in contact with the pore and the smooth surface originally in contact with the urchin plate; (c) macroporous nickel produced via electroless deposition showing a skeletal structure. Adapted with permission from ref 537. Copyright 2006 Elsevier.

prepared directly from $CaCO_3$ urchin plates by immersing one end of a dry plate into a gold paint comprising organostabilized gold particles, such that the paint was absorbed into the plate.[535] The plate was then heated to burn off the protective organic matter in the paint, and the dipping/heating cycle was repeated. Finally, the gold-coated plate was annealed, and the $CaCO_3$ was dissolved to give a macroporous gold product that possessed a double-sided structure, comprising two nonintersecting porous networks (Figure 107 parts a and b). This structure derived from coating of the template with gold particles, and the two sets of networks were readily distinguished because the gold surface originally in contact with the urchin plate was entirely smooth, while the surface directed into the pore was rough. As an alternative experimental method, electroless deposition was used to produce macroporous nickel and yielded a

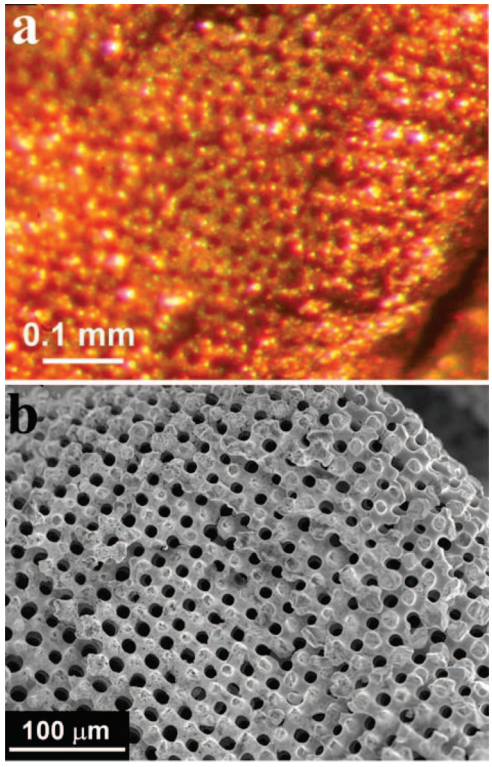

Figure 108. (a) Optical micrograph of macroporous copper produced in urchin polymer template and (b) SEM image of the templated macroporous copper. Reprinted with permission from ref 353. Copyright 2007 The Royal Society of Chemistry.

macroporous product with skeletal structure (Figure 107c).[537] The surface of an urchin plate was initially covered with a thin layer of gold, to enable a high-quality nickel film to be deposited, and the plating solution was then slowly drawn through the urchin plate under suction. Sintering of the Ni-filled plate and dissolution of the $CaCO_3$ template then yielded a macroporous solid with pore sizes of ~30−40 μm. This difference in structure as compared with the gold may have derived from weaker adherence of the nickel than the gold to the calcium carbonate or from a higher percentage filling of the pore volume with the nickel.

Demonstrating the application of these templating techniques in producing functional materials, the unique structure of the urchin plates has also been used as the basis for generating materials with superior mechanical and optical properties.[353,538] In replicating the structure in copper rather than the mechanically inferior $CaCO_3$, the unique sea urchin structure was used to prepare a porous metal with excellent mechanical properties,[353] while a periodic porous tellurium solid, with photonic properties, was prepared using an urchin plate template.[538] An electrochemical deposition method was explored to produce copper replicas of the sea urchin structures.[353] Here, polymer templates were employed to give stability at the low pH values generated during electrolysis. Application of electrochemical deposition techniques enabled the entire porous network to be filled with copper, yielding macroporous copper identical in form to the original sea urchin skeletal plates (Figure 108). The mechanical properties of these porous solids were evaluated and were compared with nonperiodic porous copper sample of similar porosity.[353] The stress−strain curve for the TPMS copper showed that not only did this material have a higher elastic modulus and yield stress but that it also lacked a defined plateau region, suggesting that the compressive force is distributed uniformly over the material structure and is not focused at specific points in the lattice. This work, therefore, provides experimental evidence to support theoretical predictions suggesting that materials with a TPMS structure will exhibit high compressive strengths, with optimal stress distribution and significant strain reduction,[351,559] thereby providing insight into the structure/function relationship of the sea urchin test.

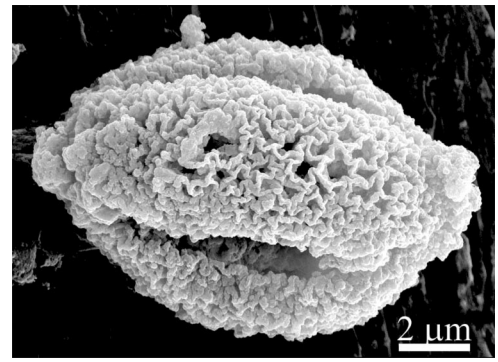

Figure 109. SEM image of a silica replica of a pollen grain. Reprinted with permission from ref 534. Copyright 2003 The Royal Society of Chemistry.

Sea urchin skeletal plates have also been used as the basis for fabricating a periodic porous solid (of the semimetal tellurium) with photonic properties.[538] An isomorphic size reduction of the original urchin structure was required to achieve mid-IR reflectivity. This was achieved by creating a replica of the urchin plates in PDMS (poly(dimethyl siloxane) and then shrinking the structure by ~50% using pyrolysis of the PDMS to SiOC. Back-filling with poly(styrene) (PS), removing the SiOC by etching in HF, and repeating the cycle generated a porous SiOC solid with structure identical to the original urchin plates, but with a reduced periodicity of ~8 μm. Finally, a tellurium replica of the porous SiOC was formed, and the SiOC was removed. Examination of the optical properties of this structure showed a low-absorption, high-dielectric-constant photonic crystal with a stop band in the mid-IR region.

4.2.4.3.2. General Biotemplating. Sol−gel techniques provide an extremely versatile strategy for templating biological structures. Pollen grains were used as the basis for forming ~25 μm porous, hollow ceramic particles whose surface structures closely approached that of the original pollen grains (Figure 109).[534] Silica replicas were produced using a straightforward synthetic approach in which the pollen grains were immersed in a solution of silicic acid, filtered and then suspended in ethanol to induce silica precipitation. Calcination at 600 °C removed the original organic template, leaving the silica replica. Surface area analysis of these structures showed data consistent with mesoporosity and a relatively high Brunauer−Emmett−Teller (BET) surface area of 817 $m^2\ g^{-1}$. Calcium carbonate and calcium phosphate replicas of the pollen grains were also produced using similar methodologies, where pollen grains were soaked in calcium chloride solution, and excess solution was washed off prior to immersing the grains in carbonate or phosphate solution, respectively. Again, a final calcination step yielded the pure inorganic replicas.

The multicellular filaments of the bacterium *Bacillus subtilis* have been used to direct the formation of porous silicas.[560] Coaligned bundles of bacterial filaments were drawn from solution and allowed to dry, prior to immersion of one end of the bacterial thread in a silica sol. Subsequent

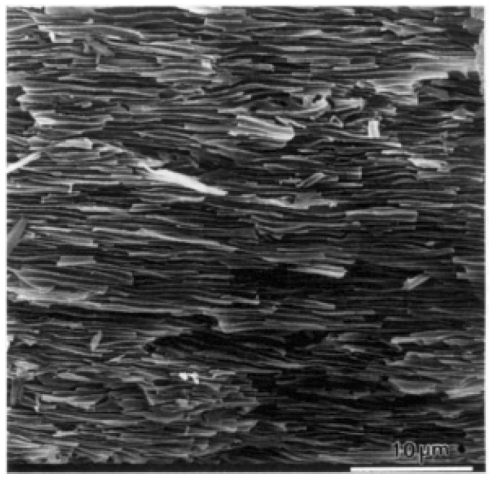

Figure 110. SEM image of a silica-infiltrated bacterial thread after heating to 600 °C and fracturing parallel to the fiber axis. The internal architecture consists of an organized array of uniform-sized 0.5 μm wide silica-walled channels oriented parallel to the fiber axis. Reprinted with permission from ref 560. Copyright 1997 Nature Publishing Group.

drying, and then calcination at 600 °C, yielded a macroporous framework comprising 0.5 μm wide channels with curved walls 50−200 nm in thickness (Figure 110). A similar procedure was also followed to template the bacterial thread with mesoporous silica (MCM-41), thus generating a solid with a hierarchical porous structure. Bacteria have also been employed as templates to form an array of silica-based wires on a substrate.[561] Magnetic nanoparticles were attached to the surfaces of the bacterium *Bacillus megaterium* via carbodiimide coupling between amine groups on the nanoparticles and surface carboxylic acid groups on the bacteria. The magnetically labeled bacteria were then aligned into wirelike formations through application of a magnetic field. Finally, these structures were stabilized by coverage with silica using a sol−gel protocol.

A range of biological materials with fine structural detail were also explored as possible templates for a range of structured ceramics.[562] Materials including spider silk, hair, cotton wool and silk fiber, and mushroom gills were employed, and these structures were coated with titania, silica iron oxide, and copper oxide using sol−gel techniques. After drying, the coated materials were calcined at 450 °C. A good degree of replication of the mushroom gill morphology was achieved, although the structure underwent considerable shrinkage during calcination. The spider silk and silk fibers templated the formation of fibers, while hollow tubules were generated from the hair and cotton wool. The difference in behavior of these fibers as templates was attributed to the structure of the individual fibers; hair and cotton wool have tubular structures at their core, while the silk and spider silk do not.

Wood has been widely explored as a template for producing macroporous ceramics such as SiO_2,[539,540] Al_2O_3,[541] iron oxide,[563] and zirconia[564] and constitutes a natural composite material with cellular structure, which requires little treatment to make it suitable for mineralization.[539,540,542,565] Depending on the product desired, the wood (which may be preprocessed to give superior infiltration) is infiltrated with gaseous or liquid organometallic of metalorganic precursors and then oxidized to remove the template. Looking at some examples, silica replicas of poplar and pine woods were prepared by a surfactant-templated

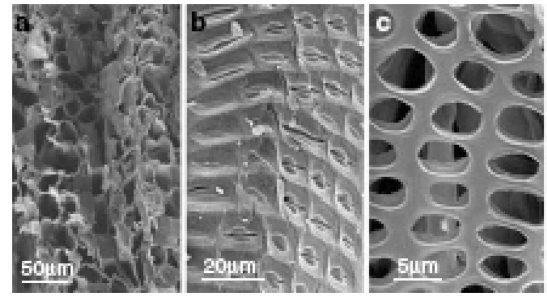

Figure 111. SEM images of poplar samples prepared under acidic conditions after calcination at 550 °C for 6 h. Images (a), (b), and (c) show the structure at different degrees of magnification. Reprinted with permission from ref 539. Copyright 2007 Elsevier.

sol−gel process in which the wood was soaked in the sol−gel solution at 60 °C for up to 6 days, before being calcined at 550 °C.[539,540] The product structure strongly depended on the conditions under which silica condensation was performed and on the presence of the surfactant. Precipitation of silica under acid conditions in the presence of surfactant yielded a product material whose structure replicated the cellular structure of the wood (Figure 111). In this case, the silicate material infiltrated the cell walls rather than filling the pores. In contrast, under neutral solution conditions, negative wood replicas were produced in which the cavities were filled with silica. Here, rapid condensation of the silica prevents penetration into the cell walls, resulting in the production of the negative replica. The presence of the surfactant was also key to enabling the production of the direct silica replicas. The nanoporous channels in the surfactant-templated silica were considered to provide a mechanism for the release of the degradation products of the organic matrix on calcinations, thus preserving the structural integrity of the silica replica.

As an alternative route to fabricating materials with morphologies resembling those of biological systems, diatom frustules have been converted into anatase via direct chemical reaction.[566] Rather than using the biological structure as a cast, as the vast majority of the templating processes described above have done, this approach leads to duplication of the original material in the morphology of the product. The methodology used relied upon a halide gas/solid displacement reaction where silica diatom frustules were converted into titania by exposure to gaseous TiF_4 for 2 h at 350 °C, followed by O_2 for 2 h at 350 °C. Under these conditions, the predominant mineral phase was anatase, and the original morphologies of the diatom frustules were well-preserved in the product ceramic (Figure 112).[566]

Diatom frustules have also been used to produce structured ceramics via more conventional templating procedures. Formation of a barium titanate-coated ceramic with complex morphology was achieved by initial reaction of silica diatom frustules with gaseous magnesium, forming a MgO-rich phase.[567] Subsequent coating of this intermediate material with a continuous layer of barium titanate by a sol−gel process, followed by annealing at 700 °C for 1.5 h, then led to a crystalline coating of barium titanate on a composite mixture of MgO, Si, and Mg_2Si. As an alternative approach, sol−gel chemical methods were used to produce crystalline zirconia from diatom templates, with preservation of the original morphology and fine structure.[568] After coating the frustules in zirconia, the silica was selectively removed by immersion in sodium hydroxide, leaving a pure zirconia

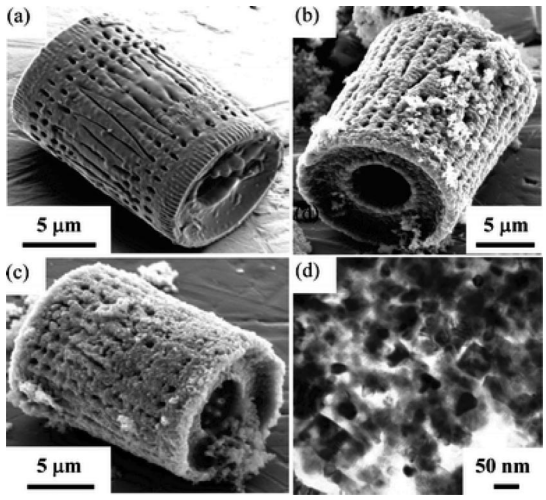

Figure 112. Secondary electron images of *Aulacoseira* diatom frustules: (a) before treatment; (b) after exposure to TiF_4(g) for 2 h at 350 °C; (c) exposure to TiF_4(g) for 2 h at 350 °C and then to pure O_2 for 2 h at 350 °C. (d) A transmission electron image of a cross section of a frustule after exposure to TiF_4(g) for 2 h at 350 °C and then to pure O_2 for 2 h at 350 °C. Reprinted with permission from ref 566. Copyright 2004 The Royal Society of Chemistry.

phase. Structured boron nitride, a nonoxide ceramic, was also prepared based on diatom templates.[569] Here, a solution of polyborazylene was vacuum-filtered through the silica frustules, prior to pyrolysis at 1250 °C and subsequent dissolution of the silica in HF solution. Again, the overall fine structure of the original silica morphology was preserved.

Again employing gas-phase deposition methods to achieve structural reproduction, chemical vapor deposition (CVD) has also been employed to replicate a number of biological structures in silica.[570] Reaction of vaporized hydrogen peroxide with gaseous silane in the presence of the biological template resulted in uniform coverage of the selected material to a thickness defined by the silane concentration and the reaction time. Calcination was then employed to remove the organic template, leaving the silica replica. This experimental technique enabled precise replication of the fine structural detail of biotemplates including a butterfly wing (Figure 113), the wing of a housefly, and the surface of a leaf of the self-cleaning plant *Colocasia esculenta* in the product silica structure, although some shrinkage of the structure was observed on calcination.

4.2.5. Coded and Programmed Self-Assembly

An enormous number of fascinating structures can be produced via controlled self-organization processes. These include mesocrystals and structures arising from oriented-aggregation processes. Because these categories of materials have been discussed in previous sections, we will here focus on other polycrystalline structures, namely, those which form in a controlled manner. An advanced way to encode nanoparticle self-assembly in the earliest stages of the assembly process would be to selectively adsorb additives onto specific crystal surfaces of the primary building units and, thus, to program their self-assembly. This morphogenesis process, although attractive, is not yet predictable. Consequently, we will instead focus on just two examples of a polymer-encoded self-assembly process. One example is given by $BaCO_3$ crystallization in the presence of a stiff, large, and shape-persistent phosphonated DHBC.[571] Here,

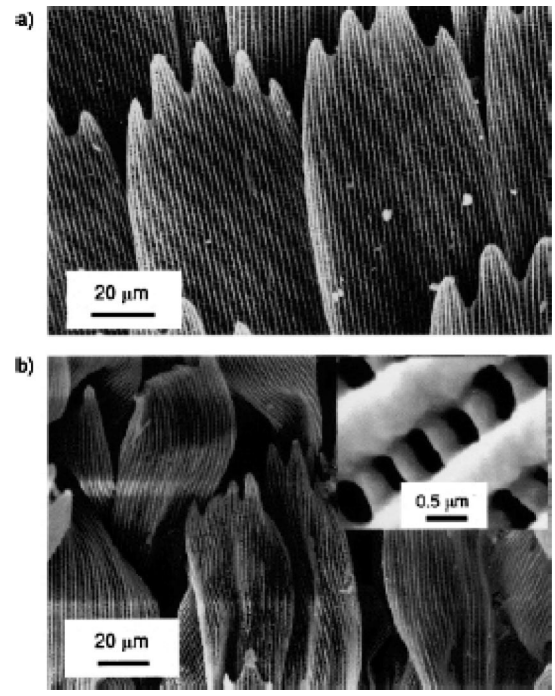

Figure 113. (a) Details of a peacock butterfly wing revealed by SEM; (b) calcined silica replica showing a slight degree of creasing as a consequence of heat treatment. The insert is a high-magnification image. Reprinted with permission from ref 570. Copyright 2003 Wiley-VCH.

the selective adsorption of the DHBC onto the (110) witherite surfaces leads to the tectonic arrangement of the elongated orthorhombic $BaCO_3$ by programmed self-assembly. This resulted in the formation of remarkable helical structures from a nonchiral mineral crystal system and a racemic polymer (Figure 114). As expected, the number of left- and right-handed helices was found to be similar.[571] Not only is the degree of alignment of the elongated nanoparticles in these helices remarkable, but the obvious "communication" between the two helices is also striking (Figure 114a). Identical morphologies and irregular helix pitch strongly indicate that physical fields also provide a driving force for ordering, in addition to face-selective polymer adsorption.

The involvement of the polymer in two processes results in the observed tectonic arrangement via coded self-assembly of elongated witherite nanoparticles:

(1) There exist favorable (110) surfaces with a possible purely cationic surface, which can favorably interact with the stiff polyanion via electrostatic interaction. The other three surfaces shown in Figure 114h not only expose cations at their surfaces but also show mostly tilted carbonate ions. Thus, these three surfaces are not favored for polymer adsorption. The exclusive polymer adsorption onto favorable (110) faces leads to a staggered arrangement of aggregating nanoparticles, which defines the mode of assembly after the aggregation of just the first three particles (Figure 114 parts d−g). The driving force for this process is the prevention of bending of the sterically crowded polymer after aggregation of another nanoparticle building unit into an unfavorable position. The polymer acts as a steric block. The result is an aggregation of nanoparticles along a common growth direction, which is determined by the aggregation of the first three building units.

(2) Considering then the perpendicular direction (Figure 114i), a particle approaching an aggregate can also experi-

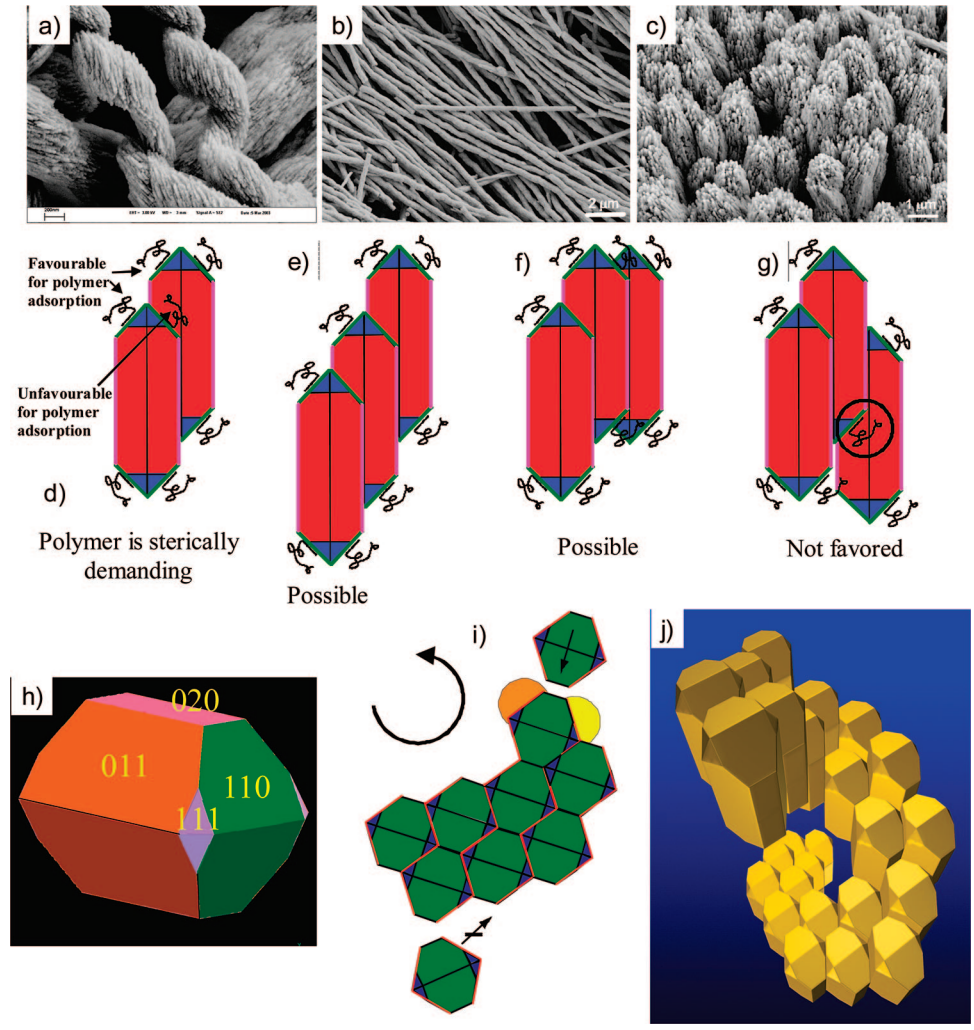

Figure 114. (a−c) SEM micrographs of $BaCO_3$ nanoparticle superstructures obtained under control of a stiff phosphonated DHBC, $[Ba^{2+}]$ = 10 mM: (a) helices formed at starting pH 4, $c_{Polymer}$ = 1 g/L; (b) starting pH 5.6, $c_{Polymer}$ = 1 g/L; (c) starting pH 4, $c_{Polymer}$ = 2 g/L. The colors in (d−g) correspond to the indexed faces of the primary nanocrystal witherite building block in (h). (d) Interparticle aggregation along the (011) and (020) faces makes the adsorption faces at the tip different, allowing the particles to differentiate between favorable and unfavorable arrangements. The (partially) staggered arrangement is preferred [(e) and (f), with (f) being much more improbable] over the probable but energetically excluded arrangement with unfavorable polymer adsorption sites [circle shown in (g)] and predetermines addition of subsequent particles resulting in directed aggregation of subsequent particles either upward or downward as defined by the first three aggregated particles. (i) Perpendicular view along the helix growth axis: the alternation of particle aggregation by (011) (red lines) and (020) (black lines) faces breaks the linear character and brings in helicity [only one (020) face sterically accessible in a favorable way]. The yellow and orange spots indicate different (011) faces for an attaching particle. The orange spot is more favorable for subsequent particle attachment, and thus, the helix turn is continued. Overlay of processes (d−g) and (i) leads to the helical superstructure (j), which even tolerates some mismatched particles. Please note that, in this figure, the polymer is not drawn as a stiff rod and is also not to scale. Figure partly reproduced with permission from refs 571 and 378. Copyright 2005 Nature Publishing Group and 2005 Materials Research Society.

ence both favorable and unfavorable adsorption sites. If a particle aggregates along (020), a linear arrangement will result, whereas two possibilities exist for an approaching particle to aggregate along the (011) faces (Figure 114i). These possibilities are indicated by a yellow (unfavorable) and orange (favorable) spot in Figure 114i. The yellow position is unfavorable because the approaching particle has to be oriented along two faces, whereas for the orange position, the orientation along (011) is sufficient. Therefore, this will be the preferred adsorption site. This introduces a counterclockwise turn in the particle aggregate in the example in Figure 114i.

Application of both of these processes leads to the helix formation shown in Figure 114j. The pitch of the helices can be controlled by influencing the counterplay between the above two processes. If the pH is increased (Figure 114b), the nucleation of nanoparticle building units is favored. Simultaneously, the nanoparticle building units become less charged as the pH approaches the isoelectric point of $BaCO_3$ of 10.0−10.5. At these pH values, the interparticle repulsion is decreased and the particle assembly is favored. Consequently, the on-axis particle aggregation is favored over polymer adsorption and the helix pitch is increased, which results in salt-stick-like morphologies (Figure 114b). Increase of the polymer concentration, in contrast, results in the formation of a back-biting helix, without a pitch (similar to that shown in Figure 114c.) In this case, increased polymer adsorption to all (110) faces—including the unfavorable ones—prevents axial aggregation. These extreme cases show that even the pitch of the tectonic helix arrangements can be controlled by a parameter as simple as the pH or the polymer concentration. This shows that a delicate balance

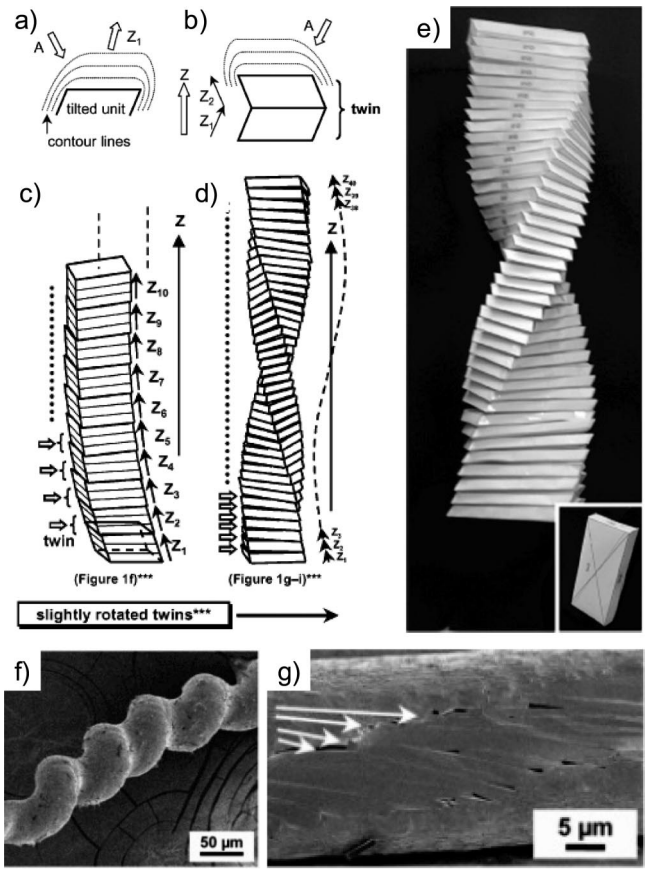

Figure 115. Two-dimensional assembly of a tilted unit in a diffusion field: (a) diffusion field around the tilted unit and (b) formation of the twin. A nonsymmetric diffusion field is produced around the tilted unit. The concentration of PAA provides a specified concentration gradient or intensity of the diffusion field around the growing crystals. (c, d) Curved and helical morphology with the accumulation of slightly rotated twins, respectively, as a result of a 3D diffusion field. The key aspect of the curved and helical forms is the slightly rotated twins within the limit of mutual lattice matching to achieve faster growth. Slightly rotated twins also adjust the original growth directions (Z_1, Z_2, Z_3,..., Z_{40}) to direction Z. (e) A simple model of a helical backbone. The replicas of the tilted platy unit (inset) connected with a rotation angle of about 4.5° reproduced the helical backbone. (f, g) SEM of experimentally observed helical K_2SO_4 morphologies and backbone. White arrows in (g) show the tilted subunits. Reprinted with permission from ref 572. Copyright 2005 American Chemical Society.

of conditions is required for programmed particle self-assembly and demonstrates the possibilities of such an approach, which can even create chirality from nonchiral/racemic compounds.

A further example of controlled nanoparticle assembly leading to helical structures from twisted twin subunits was reported for orthorhombic K_2SO_4 in a viscous poly(acrylic acid) solution.[572] Here, the crystal morphology was modified by selective PAA adsorption, leading to tilted, platelike crystals. Polymer-induced diffusion also limited the growth and controlled the assembly of the tilted subunits (Figure 115). In common with the above example of assembly in the orthorhombic $BaCO_3$ system, face-selective polymer adsorption—in this case onto 010 faces—changed the morphology of the primary building units (tectons) and coded them for subsequent assembly/growth. However, in contrast to the $BaCO_3$ helices, which were constructed from elongated building units, the tectons comprising the K_2SO_4 system had a tilted, platelike shape (Figure 115a). More importantly, the polymer fulfilled a different second role from the above $BaCO_3$ case. While the stiff and shape-persistent polymer coded the self-assembly of the $BaCO_3$ tectons, the PAA was believed to form a viscous matrix around the growing primary units, thus creating a diffusion field in which reactant diffusion is reduced (Figure 115a,b). This means that no self-assembly of individual nanoparticles is observed, but instead, growth of a second nanoparticle occurs on an existing one. This explanation of helix formation therefore fundamentally differs from that proposed for $BaCO_3$ helix formation, although both mechanisms describe the polymer-coded assembly of helical structures.

If a tilted, platelike unit is placed in a two-dimensional diffusion field, the concentration contour lines will be distributed nonsymmetrically, as shown in Figure 115a. The driving force of growth is, in this case, anisotropic, due to the nonsymmetric concentration gradients and diffusion fields around the tilted unit (Figure 115a). Although the original growth direction of the tilted unit is in direction Z_1 (Figure 115 parts a and b), the higher crystallization driving force is along direction A due to the higher concentration gradient. Thus, a twin consisting of the reversed unit along direction Z_2 would be introduced to achieve faster growth (Figure 115b), and the original growth direction (Z_1) would then be adjusted to direction Z (Figure 115b). Therefore, in a diffusion field, which is, in this case, generated by the polymer around the primary crystals, faster growth with the formation of the twins is favorable rather than growth in the original direction even though excess interfacial energy is introduced at the interface. The whole morphology is, therefore, determined by the concentration gradient in a diffusion field around the growing crystals.

Particularly at high PAA concentrations, the formation of reversed twins along direction Z_2 is preferred to achieve faster growth in a relatively high concentration gradient. However, the nucleation probability of the completely reversed twin would be relatively small under a steep concentration gradient, which is generated by a high PAA concentration. The formation of slightly rotated twins would then be more favorable because faster growth is preferred to the most stable state under that condition.[572] However, the rotation angle of the subunits is not variable and determined by lattice matching on the twin plane. The accumulation of slightly rotated twins adjusts the orientation of the growth of the individual subunits (Z_1, Z_2, Z_3,..., Z_{40}, as shown in Figure 115 parts c and d) into the direction of the diffusion (direction Z).[572] Therefore, the assembly of rotated twins induces the formation of curved and helical morphologies that comprise tilted units. If the tilted units were aligned along the *b*-axis (*Z*-direction in this discussion) with a rotation angle of about 4.5°, which is realistic if lattice matching is to be maintained between the tilted units, a helical backbone is produced according to the model shown in Figure 115e. In this model, the thickness of the platelike subunits determines the helical pitch. The tilted subunit plates were experimentally observed (Figure 115g), and the whole helix is shown in Figure 115f.[572] In addition to the helical assembly program, a zigzag assembly was also encoded at lower PAA concentrations in the same experimental system.[572] In this way, the system is similar to the $BaCO_3$ case where the assembly of the tectons can be controlled by modification of simple experimental variables such as the polymer concentration or the pH. Further, it also demonstrates the subtle control that can be

achieved in a coded assembly program by face-selective polymer adsorption.

4.2.6. Polycrystalline Structures in Gels

In addition to their use in the crystallization of large, defect-free single crystals and mesocrystals, gels can also be used for the generation of polycrystalline structures with complex morphologies. Many of these studies are driven by the finding that a considerable number of biominerals grow in gel matrices. Both natural and synthetic gel systems have, therefore, been applied to the crystallization of polycrystalline materials. The particles produced in gels in this way often have remarkable forms, such as the chiral H_3BO_3, $K_2Cr_2O_7$, and $CuSO_4 \cdot 5H_2O$ helices grown from these triclinic crystals in pectin or agar gels.[60] The proportion of left- and right-handed helices in these systems could even be precisely tuned by molecular recognition of added amino acid enantiomers.[573] There are a number of other interesting examples, but we will focus here on the crystallization of polycrystalline $CaCO_3$ in gels.

The question of whether collageneous matrices are involved in crystal nucleation and crystallite alignment of $CaCO_3$ or whether this is achieved by other proteins was addressed by Falini and co-workers.[321,574] Oriented calcite crystals could be grown in/on gelatin films containing poly-L-aspartate,[574] and the polymorph could be switched between calcite and aragonite using these films.[321] Vaterite was also be obtained at high concentrations of poly-L-aspartate.[575] Gelatin gels containing poly-L-aspartate can, therefore, be used to synthesize all three anhydrous $CaCO_3$ polymorphs.[576] The type, density, and structural geometry of the charged groups responsible for the crystallization of calcium carbonate can be easily regulated by changing the kind and amount of acidic polyelectrolytes in the starting gelatin solution. Further, the structure of the polyelectrolyte−gelatin assembly can be changed through mechanical deformation, which modifies the microenvironments of the nucleation and growth sites. In these studies, the poly-L-aspartate served as a model substance for acidic proteins with β-sheet conformation. While poly-L-aspartate induced the orientation of the formed crystallites, this was not observed for poly-L-glutamic acid.[575] If gelatin gels were used without any additives, barrel-shaped polycrystals were obtained that contained a significant amount of occluded gelatin, inhomogeneously distributed throughout the particles.[370] Within these barrels, three regions with equal orientations of calcite crystallites were found. If a polyaspartate additive is added to the gel, the polyelectrolyte appears to overcompensate for the physical properties of the organic matrix, leading to morphologies that are independent of which hydrogel is used.

A limited degree of polymorph control between calcite and aragonite was also reported for $CaCO_3$ grown in agar gels in the presence of calcium-binding polysaccharides extracted from algae, a phosphonic acid scale inhibitor,[577] and several bivalent cations,[172] mono- and trivalent cations,[578] and carboxylic acids.[579] Both the polymorph and the morphological development of the calcite crystals were found to be related to supersaturation conditions and the amount of added Mg^{2+} for $CaCO_3$ precipitated in silica gels.[323] At high supersaturation levels, spherical calcite crystals containing up to 15 mol % $MgCO_3$ were formed. At lower supersaturations, the Mg content decreased and the morphologies changed progressively through a sequence from spheres to dumbbell-like forms, to wheat-sheaf-like bundles, and finally to single crystals with steep rhombohedral faces. These examples show that polymorph and morphology control of polycrystals can be achieved in gels, although the detailed morphogenesis process is not know. This contrasts with the development of mesocrystals in gels, where a reasonable picture of the mechanism of structure formation exists.

4.2.7. Biomorphs

"Biomorphs" are a fascinating and beautiful category of polycrystalline, self-assembled minerals, which are so-called because their morphologies are highly reminiscent of the shapes of primitive life—and yet they are purely inorganic in origin. Biomorphs are self-assembled silica−alkaline earth carbonate composite materials, which are usually obtained by performing a (carbonate, mostly $BaCO_3$) mineralization reaction in the presence of an alkaline solid or solidifying silica gel. They are characterized by complex, curved morphologies and hierarchical structures that resemble many biominerals, and are considered to form by self-organization processes.[580−582] Biomorphs could also be discussed under the framework of section 4.2.6 because a silica gel is used for their production. However, as changes in the silica gel structure are coupled to the mineralization of the alkaline earth carbonates, a synergistic morphogenesis process operates that is peculiar to the formation of biomorphs. These structures will, therefore, be discussed separately here.

Biomorphs exhibit a hierarchical structural organization over many length scales, including scales as large as several mm, which is significantly greater than most of the systems discussed in this review. Their structural and morphological similarity to many biominerals is often so close that it is discussed whether the morphology of a mineral can be used as an indicator of biogenicity at all.[583] Biomorphs were, to our knowledge, first observed by Herrera as far back as 1912,[584] and, therefore, belong to the oldest nonexplained observations in structural crystallization. Biomorphs also serve to demonstrate that inorganic abiotic materials can display a wide range of curved morphologies that are usually considered to be exclusive to the biological world. These includes complex helical structures, twisted ribbons, worms, sheets, flowerlike spherulithic objects, orchidlike cones, coral-like bent plates, trumpets, mushroom bundles, and many other morphologies[580−583,585−594] A gallery of some of these fascinating structures is given in Figure 116.

The morphology of biomorphs can be influenced by various parameters including pH, NaCl addition,[586,591,593] temperature,[588,593] carbonate concentration,[589] Ba^{2+} concentration,[593] silicate concentration,[593,594] CTAB surfactant,[593] ethanol,[595] or L-amino acid additives.[590] The morphologies of $BaCO_3$ biomorphs are, for example, highly temperature-dependent such that a gradual change from globular structures → globular worms → globular, worms, helices (sheets) → helices, sheets → complex mixture of sheets, corals, bands is observed with an increasing reaction temperature.[593] An increase in temperature, pH, and Ba^{2+} results in an increase in the number of nuclei, as well as a decrease in the silicate concentration, which suggests that the formation of barium silicate prevents nucleation of the $BaCO_3$. Nevertheless, barium silicate particles may serve as nuclei for the heterogeneous nucleation of $BaCO_3$ and as depots of barium and silicate during the biomorph growth. As silicate poisons the growth of witherite ($BaCO_3$), nanosized crystals encapsulated in silica are formed as building

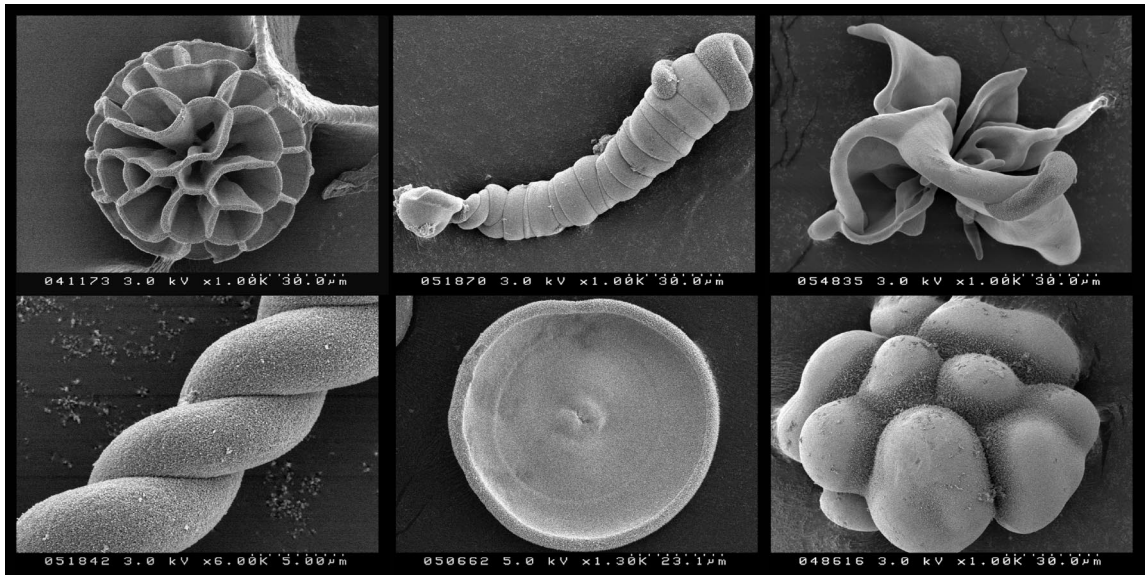

Figure 116. Different biomorph morphologies showing the large range of complex morphologies that are possible. The shown particles are generally in the range greater than several tens of micrometers. Images kindly supplied by Dr. Anne Carnerup. Copyright 2008 Anne Carnerup, Canberra.

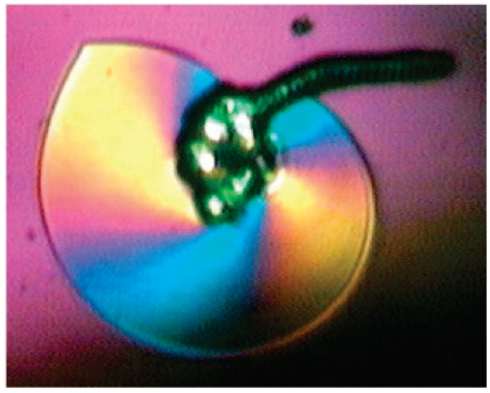

Figure 117. Optical micrograph of a sheet viewed under crossed polarizers. The extinction pattern is indicative of radial orientational ordering of the optically anisotropic witherite nanocrystals within a biomorph sheet. Reprinted with permission from ref 581. Copyright 2004 Elsevier

units. Biomorph growth itself is strongly dependent on the reaction conditions such that slow growth produces more globular morphologies, while fast growth can yield a greater range of morphologies including helical and sheetlike structures, which were believed to grow under diffusion-limited conditions.[593] Overall, this suggests that the complex morphogenesis process is coupled to crystallographic as well as reaction-diffusion relationships.

The perfection of the alignment of the primary nanocrystals in curved biomorphs, which is achieved in the absence of any organic molecule or biological action, can be nicely visualized by polarized light microscopy, as shown in Figure 117. Figure 117 shows a snail-like structure with a helical stem. It is clearly seen that the crystal superstructure perfectly follows the radial assembly program of the optically anisotropic witherite components, which is reflected in the interference colors due to the birefringence of witherite ($BaCO_3$).

The mechanisms of formation of biomorphs are manifold, and a unifying general mechanism has not yet been detemined, due in part to the complexity of the coupled processes of silica polycondensation/gelation and the interplay of changes in the gel structure that occur during nucleation and growth of the inorganic carbonate mineral. Although much of the understanding of these systems remains rather empirical in nature, recent work has revealed some aspects of the morphogenesis process. The first stage of biomorph formation involves the formation of small, 10−50 nm nanoparticles, which also provide the pathway of material transport. They are instantly formed after mixing, as revealed by light scattering, and form a conglomerate of smaller globular nanoparticles a few minutes after mixing.[593] The particle core has a higher electron density after hours, indicating a higher Ba^{2+} content in the core of a Ba-rich phase that is later covered by a silicate phase. The particles in these aggregates are still amorphous.[593] These primary blocks first aggregate to give an embryo microsphere, which then grows, presumably by field effects from the crystallizing superspheres, in a number of distinct directions. Helix formation, for example, can be categorized into a number of different stages: (i) the growth of an initial globular aggregate, from which a tongue is extruded; (ii) the curling of the edges of the tongue in different directions; (iii) the continued growth of a double helix; and (iv) the development of a wormlike aggregate on the pre-existing double helix.

The fact that the helix maintains a constant diameter throughout the growth process indicates that matter is only added at the growth zone, i.e., at the tip of the helix. Besides directional transport, the experimental data also strongly support a possible influence of mechanical stress fields and dipolar interactions. The soft silica gel appears to suppress turbulence and—via the sol fraction—stabilize primary nanoparticles until they can interact and adhere. In any case, the original gel nanostructure is broken throughout the growth of the biomorphs. Very recent work highlights the application of alkoxysilanes like tetraethoxysilane (TEOS) as precursors for the controlled generation of silicic acid, which leads to a much higher experimental reproducibility of the biomorph structures obtained. The previously used water glass silica sources are compositionally less well-defined water and can suffer from partial condensation.[595] This may help to better elucidate the relationship between experimental parameters and the formed biomorph morphologies and aid the search

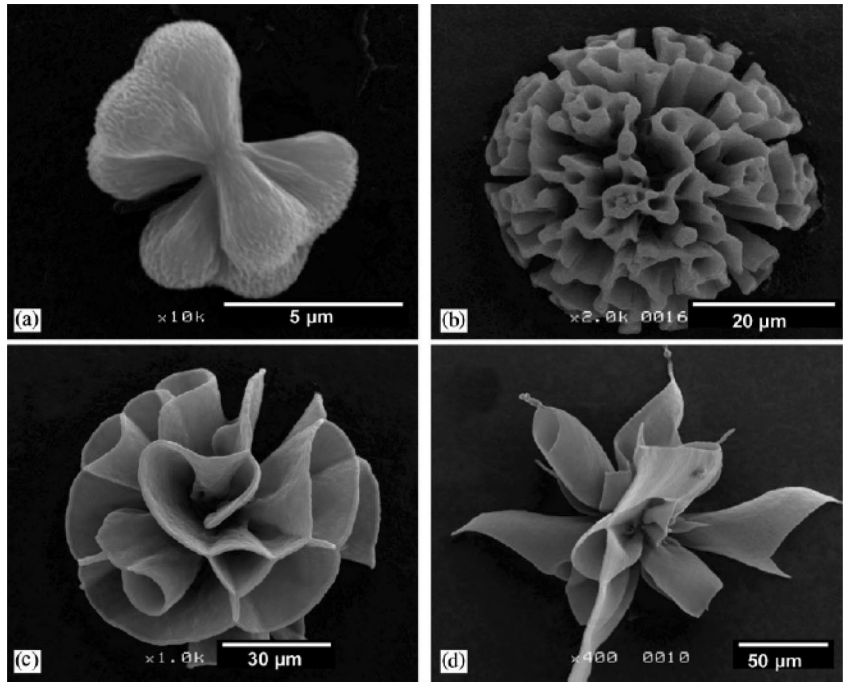

Figure 118. SEM images of $SrCO_3$ biomorphs indicating morphological evolution of the clusters prepared in silica gel at pH 10.5 containing 0.01 M of carbonate ions in the early stage: (a) 0.5 h, (b) 2 h, (c) 6 h, and (d) 9 h. Reprinted with permission from ref 591. Copyright 2003 Elsevier.

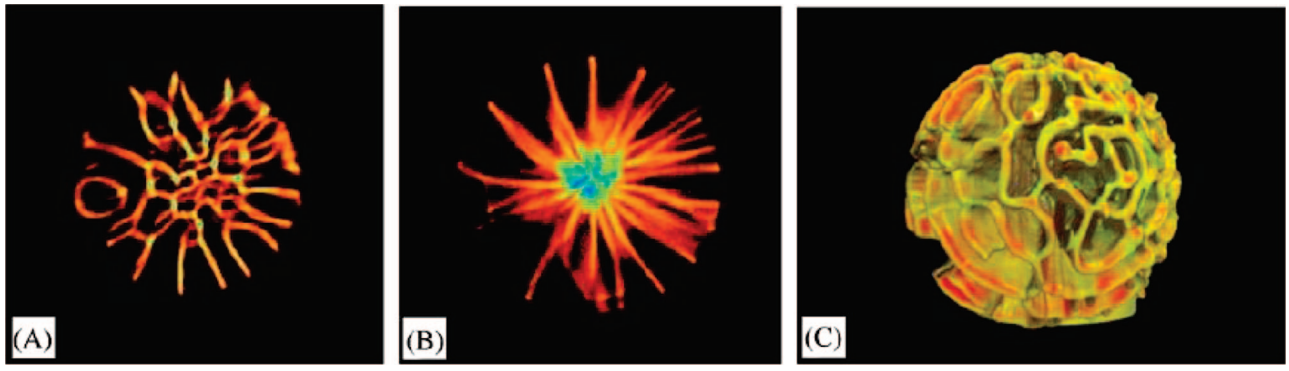

Figure 119. X-ray CT images (A, B) and the 3D rendered surface (C) of a floral $BaCO_3$ biomorph spherulite. Reprinted with permission from ref 581. Copyright 2004 Elsevier

for a universal mechanism for the formation of biomorphs under various experimental conditions.

A rather nice growth sequence of $SrCO_3$ biomorphs is shown in Figure 118. This figure also serves to illustrate the degree of structural complexity that can be achieved from a self-organized, dynamic growth regime. The first observed precipitate (Figure 118a) showed multiple dumbbell-like morphology, which closed with time into the porous spherical structure shown in Figure 118b. Further growth resulted in the pitted aggregates observed in Figure 118c. Preferential growth at the tips finally results in petal formation (Figure 118d), from which helical extensions frequently developed (Figure 118d). TEM analysis showed that the petal sheets consisted of oriented nanocrystalline units that comprised 10−20 nm $SrCO_3$ crystals, which were covered by an amorphous silica phase to yield fibrous subunits with a diameter of 40−60 nm.[591] Increase in pH decreased the size of the crystallite subunits. The morphological evolution can, therefore, be attributed to the reduction of the crystal subunit size by adsorption of silicate anions. The subsequent emergence of elaborate complex forms, involving sheets and helical forms, occurs due to instability of the growth of a spherulite consisting of nanoscale fibrous subunits enveloped by a silicate sheath. Indeed, dissolution of the carbonate yielded a silica ghost, and the internal substructure of the sheets and helical ribbons was preserved with the silica framework.[591] This can be compared with the external silica skin reported in earlier studies.[585,586,589,592,596] In contrast, selective dissolution of the silica component of the biomorphs in dilute NaOH leaves the $BaCO_3$ skeleton intact as dense aggregates of small witherite crystallites.[581] Biomorphs are, therefore, dual composites of intergrown witherite and silica structures.

Looking in turn at the $BaCO_3$ system, the structure of "floral" biomorphs with the morphology-type shown in Figure 118c was investigated using X-ray computed tomography.[593] These analyses showed a high degree of complexity, even on the micron scale, as shown in Figure 119. These images show that the central core and the connection points between the sheets have a higher X-ray contrast (blue) than the sheets themselves (red), which is indicative of a higher Ba^{2+} content inside the aggregate.

$CaCO_3$ biomorphs can also be formed, although they have not been investigated as extensively as the $BaCO_3$ biomorphs.

$CaCO_3$ biomorphs reported by Garcia Ruiz showed a *"sheaf of wheat"* morphology,[597] as well as fingerlike structures.[589,597] In the *sheaf of wheat* structures, concentric banding of the substructures was observed, which corresponded to fibers of calcite rhombohedra, linearly aligned along their *c*-axes. Imai et al. also observed unusual porous and coral-like $CaCO_3$ morphologies on precipitating $CaCO_3$ in silica gels.[598,599]

4.3. Amorphous Minerals

4.3.1. Morphological Control of Amorphous Minerals

This section addresses the morphological control of amorphous materials. Necessarily this is an enormous topic, and as such we have elected to exemplify possible control mechanisms by considering morphological control of amorphous silica only. Silica provides an excellent model compound as it is both important synthetically and an abundant biomineral. Given its amorphous structure, silica morphogenesis principally relies upon templating techniques and, therefore, ultimately depends upon the existence of suitable templates. Because it is well-beyond the scope of this article to review all of the templating approaches that have been described in the literature, the methods described here are intended to be illustrative of the types of synthetic approaches applied and the range of possible morphological products, rather than providing an exhaustive review of the area. For more detailed information covering the breadth of the topic, the reader is directed to alternative, existing reviews.[397,528,600−605] Necessarily, there is also significant overlap of topics covered in this section with templating methods used to produce polycrystalline solids as described earlier in section 4.2.4. In order to prevent excessive repetition, the topic of biotemplating, which was considered previously in section 4.2.4.3, will not be repeated here.

Templating processes giving rise to silica particles with sizes from nano- to micrometer in size range and with structures varying from solid to hollow to porous are discussed first. There is considerable academic and industrial interest in the fabrication of porous solids, and many templates, including colloidal crystals, condensed arrays of emulsion droplets, and directionally frozen ice, have been used to direct the formation of these structures. Templating on the mesoscale gives rise to mesoporous solids, which represent an extremely important category of materials. Here, two principal synthetic strategies are applied that rely either on the formation of a preassembled organic template ("nanocasting") or on the cooperative assembly of silica precursor species and the structure-directing organic molecules.[601] Again, the subject area of mesoporous solids is so large as to warrant a review in its own right and, thus, will not be covered here. We then consider how the confinement offered by the template itself can affect silica precipitation and morphological development. Finally, the use of self-assembled organic molecules to direct silica morphologies is briefly considered. There is considerable overlap of this topic with biological silicification processes in organisms such as diatoms, where there is strong evidence that pattern-formation arises due to self-assembly processes driven by molecular self-assembly and phase-separation processes. The topic of biogenic silicification was considered previously in detail in section 3.4 and is not repeated again here.

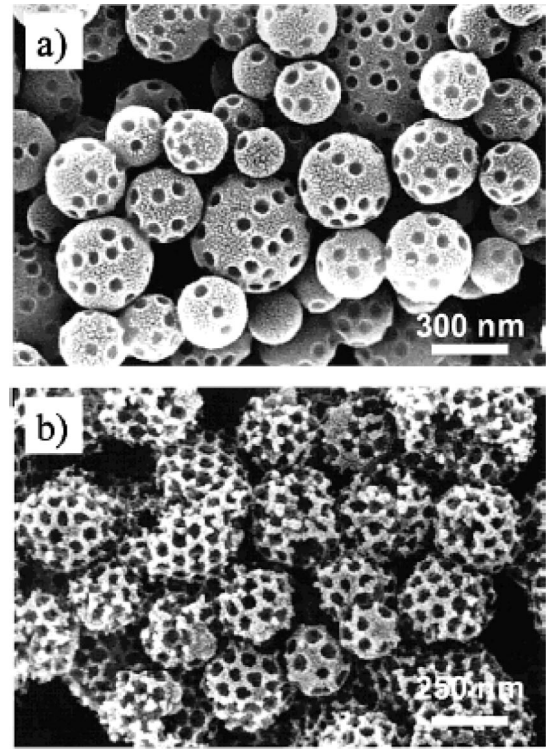

Figure 120. SEM images of a spherical silica powder produced by varying the content ratio of PS latex and silica: 10 mL of silica colloids (0.05%) mixed with (a) 0.5 mL and (b) 1 mL of PS latex colloid (3.6×10^{13} particles/ mL). The size of PS latex particles was maintained at 79 nm. Reprinted with permission from ref 608. Copyright 2001 American Chemical Society.

4.3.2. Spherical Silica Particles via Templating

Silica particles and shell structures have been prepared by coating a range of suitable spherical organic particles such as polymer colloids, vesicles, emulsion droplets, and gel particles with silica and then removing the template. The layer-by-layer method was used to deposit alternate layers of poly(diallyldimethylammonium chloride) (PDADMAC) and 25 nm silica nanoparticles on sulfate-stabilized polystyrene colloids.[606] Complete hollow silica spheres were produced after calcination after deposition of two or more multilayers. Using a similar approach, silica particle/polymer multilayers were formed on red blood cells (echinocytes). Removal of the organic material then generated hollow silica particles covered with blunt spicules, as dictated by the form of the original template.[607] Latex particles were also used by Okuyama and co-workers to create spherical silica particles containing spherical mesopores.[608] In this case, a mixture of silica nanoparticles and latex colloidal particles was sprayed as droplets into a vertical reactor containing two temperature zones. The solvent evaporates in the first zone, generating primary silica particles containing the PS latex particles, and the PS is burnt off in the second zone, giving the product silica particles. The density and packing of the cavities in the silica particles was defined by the original concentration of the PS particles and varied from disordered to close-packed in structure (Figure 120).

A number of methods have been used to prepare hollow silica shells from dispersed emulsion droplets. Monodisperse, micrometer-sized hollow particles were obtained by encapsulation of an emulsion droplet in a silica shell, followed by removal of the organic core by evaporation or dissolution in ethanol.[609] Here, highly monodisperse oil-in-water droplets

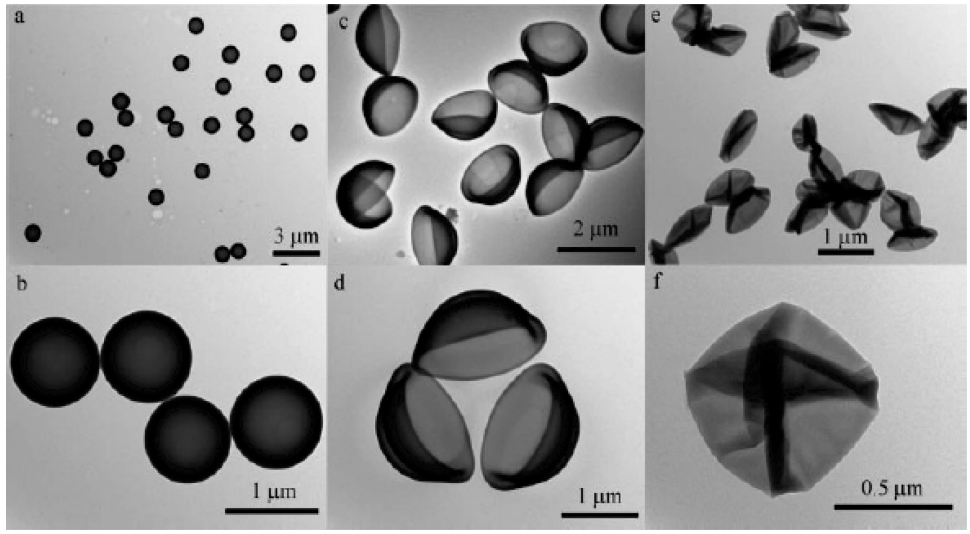

Figure 121. Transmission electron micrographs showing different hollow particles: (a, b) hollow microspheres formed by adding TEOS 24 h after DMDES, (c, d) microcapsules, formed by adding TEOS after 48 h; and (e, f) microballoons, formed on addition of TEOS after 72 h. Reprinted with permission from ref 609. Copyright 2005 Wiley-VCH.

of low molecular weight polydimethylsiloxane (PDMS) silicone oil were produced, and encapsulated in a solid silica shell by adding a solution of tetraethoxysilane (TEOS) to the emulsions with stirring. The product obtained depended on the time at which the TEOS was added and, therefore, the size of the emulsion particles, which increased with incubation time. Three general particles were produced, termed microspheres, capsules, and microballoons (Figure 121), according to the ratio of the shell thickness to the shell radius. While the microspheres exhibited thick, rigid shells, the microballoons had very thin shells and, thus, deformed easily. Silica microcapsules have also been produced by silicification of a water/oil/water emulsion system.[610] Sodium silicate solution was used as one water phase, an *n*-hexane solution of Tween 80 and Span 80 was used as the oil phase, and most successfully NH_4HCO_3 was used as a precipitant and the second water phase. Silica deposition occurred at the interface between the two aqueous phases, at the outer W/O interface when NH_4HCO_3 was used as a precipitant, and at the inner interface between the O/W when NH_4Cl was employed. The greatest control over the hollow silica particle size was achieved using NH_4HCO_3 as precipitant according to the composition of the reaction solution.

Emulsion-based templating using the pluronic block copolymer $EO_{76}-PO_{29}-EO_{76}$ has also been successfully used to generate hollow silica spheres with hierarchical porosity.[611−613] Here, the block copolymer functioned both to stabilize the emulsion and to catalyze silica condensation on the droplet surface. Silicification of a trimethylbenzene/$EO_{76}-PO_{29}-EO_{76}$/ethanol/water system using sodium silicate and an aging temperature of 80 °C produced hollow silica particles with diameters ≈ 1 μm. The particles exhibited uniform wall thicknesses of ~100 nm, and the shells exhibited a multilamellar structure.[614] Further investigation of this system demonstrated that similar hollow silica spheres of diameters ≈ 1 μm, in which the walls were perforated with wormlike pore structures, could be produced using an aging temperature of 40 °C.[613] The formation mechanism was investigated using confocal laser scanning microscopy by incorporating a fluorescent dye in the emulsion droplets. These studies suggested that the silica particles were not produced from a templating process, but that the process was driven by complexation of the polymer chains with silicate ions. This led to a decreased emulsifying action of the block copolymer, producing larger, but stable emulsion droplets that subsequently became mineralized.

This system was also modified to produce "gigantic" hollow silica spheres of diameters up to 30 μm, where the silica shell was constructed from aggregated 1 μm silica particles. Synthesized using an $EO_{76}-PO_{29}-EO_{76}$/butanol/ethanol/water system, the product spheres showed bimodal pore-size distributions with smaller pores of 4 nm and larger pores of diameter of 40 nm.[612] Examination of the mechanism of formation of these structures suggested that initial addition of sodium silicate to the emulsion system results in swelling of the emulsion droplets and condensation of silica around micelles of $EO_{76}-PO_{29}-EO_{76}$ in the aqueous core of the emulsion droplets. This process results in destabilization of the emulsion droplets, which then fuse on collision in solution to generate larger particles with smaller surface areas. As the silica nanoparticles are somewhat hydrophobic, they remain at the particle surface, generating a hollow product structure.

Silica particles with highly ordered, porous structures have been prepared using oil-in-water (O/W) emulsion droplets as confined geometries in which to form well-defined clusters of template poly(styrene) (PS) particles.[615] Silica nanoparticles and PS spheres were codispersed in O/W emulsion droplets, using toluene as the oil phase and as a stabilizer, and the droplets were dried out to give well-defined clusters comprising a symmetrical or "patchy" organization of polystyrene spheres embedded in a matrix of silica particles. Removal of the PS spheres by calcination then produced porous silica particles with symmetric porous morphologies and large surface pores. The structure of the porous particles could be defined according to the number of PS particles per cluster (*n*), which was defined by the composition of the solution, and the complexity of the structure evolved with increasing *n* (Figure 122).

More unusual particle morphologies have also been generated from the templating of emulsion droplets. Hollow silica particles with porous surfaces have been produced on addition of some water-soluble polymers such as polymethylmethacrylate to a water−oil−water emulsion system.[610] The polymers were added to the inner water phase, and silica was deposited at the oil−water interface. Introduction of

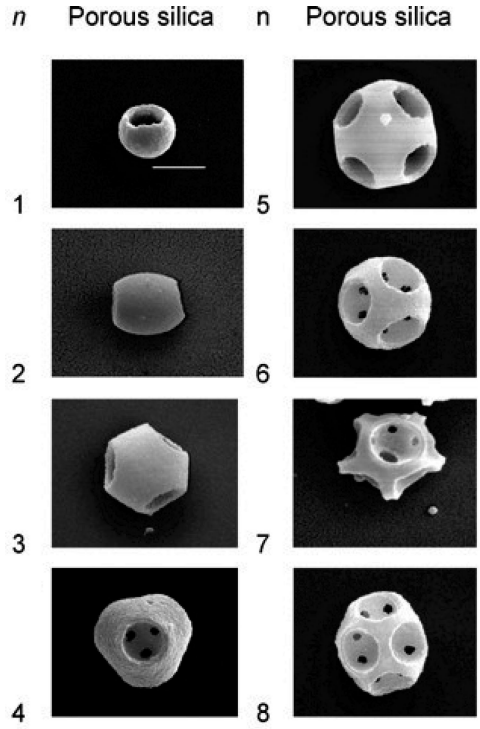

Figure 122. (a) Scanning electron micrographs of the porous silica particles produced by burning out the PS microspheres from the composite particles; scale bar is 1 μm. (b) Cagelike porous silica particles; scale bars are 1 μm. (c) Structural evolution of the porous silica for $n = 3$; scale bars are 1 μm. Reprinted with permission from ref 615. Copyright 2007 American Chemical Society.

polymer to the inner water phase generated silica particles permeated with holes of up to ~0.5 μm in size according to the type, molecular weight, and concentration of the polymer used, an effect that was attributed to release of the encapsulated polymer from the emulsion interior into the continuous phase. Budded mesoporous silica spheres were formed using an emulsion-templating method where the anionic surfactant *N*-lauroylsarcosine (Sar-Na) is used both as a surfactant and as an oil phase after acidification to Sar-H. Emulsion droplets were formed on acidification of Sar-Na to Sar-H, and silica was deposited on these particles.[616] The surfactant directs the formation of a mesoporous silica shell, and on heating, the Sar-H oil diffuses through the silica/organic shell, causing swelling of the micelles in the shell and leading to the vesicular mesostructured buds on the shell surface. Variation in the composition of the solution and particularly the amount of TEOS present led to more complex morphologies, where the product silica particles were covered with "spines", creating a structure similar to radiolaria skeletons (Figure 123).[616] The silica particles were approximately 3 μm in diameter, and spines varied in length from 2 to 15 μm. Examination of broken spines showed that they possessed hollow, multicellular structures. Again, formation of these structures was attributed to release of surfactant from the oil droplets and subsequent coassembly of the surfactant and silica precursors.

An alternative route to producing spherical silica particles is the templating of microgel particles. Uniform ~230 silica particles were synthesized using polyacrylamide gels as templates, and the photoluminescence was investigated.[617] Porous silica particles have also been produced based on porous cationic poly(acrylamide-co-2-(dimethylamino)ethyl methacrylate), methyl chloride quaternized cationic microgels. These gel particles were produced by inverse emulsion polymerization and were used as templates for silica deposition using a tetramethylorthosilicate (TMOS) silica precursor.[618] Silica was deposited exclusively on the gel particles, leading to submicron, silica−microgel particles.

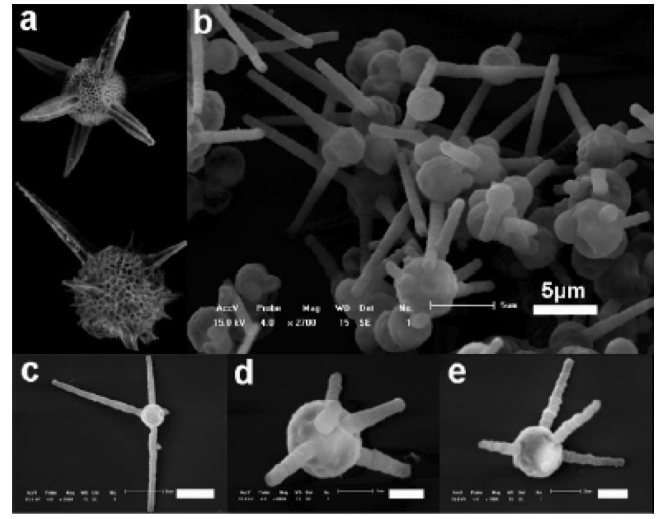

Figure 123. (a) Images of natural skeletons of radiolaria (from www.radioliaria.org), (b) SEM images of the as-synthesized silica, and (c, d, e) particles with different numbers of radial spines. The scale bar is 5 μm in (c) and 2 μm in (d) and (e). Reprinted with permission from ref 616. Copyright 2006 Wiley-VCH.

Employing a protein, hollow spherical silica particles that were perforated with pores of varying sizes and interconnectivity were formed by sonication of a mixture of TEOS and lysozyme.[619] Drying of this solution at 60 °C produced lysozyme−silica hybrid particles, which were subsequently calcined at 700 °C to generate hollow silica shells. Characteristically, the silica particles had shell thicknesses of ~100 nm that contained through-holes of sizes 50−250 nm. Considerable variation of the sizes and connectivity of the pores was observed. Where shell thicknesses exceeded 100 nm, pores often did not completely penetrate the shell, and bilayer shell structures were sometimes observed. Examination of the porosity of the particles prior and subsequent to calcinations showed the presence of pores of 3 nm diameters in samples calcined at 500 °C and larger pores at higher calcination temperatures. The 3 nm mesopores are consistent with the size of the lysozyme molecules, indicating that the lysozyme molecules are uniformly distributed throughout the silica. Restructuring of the silica network then occurs after removal of the lysozyme template, leading to a morphological change and generating the observed surface pores.

Micelles and vesicles have also been widely explored as templates for the production of spherical silica particles. In an early example of the use of vesicles to direct the formation of silica particles, silica was deposited on multilamellar vesicles formed from diamine bola-amphiphile surfactants.[620] The spherical form of the vesicle template was preserved on removal of the organic material by calcination or solvent extraction, leading to spherical silica particles of diameter 300−800 nm. Examination of the silica wall revealed a porous lamellar structure, which was considered to form on penetration of the neutral silica oligomers into the vesicle wall, where they underwent further hydrolysis and polymerization. Using instead unilamellar vesicles prepared from dioctadecyldimethylammonium bromide (DODAB) or didodecyldimethylammonium bromide (DDAB), silica-stabi-

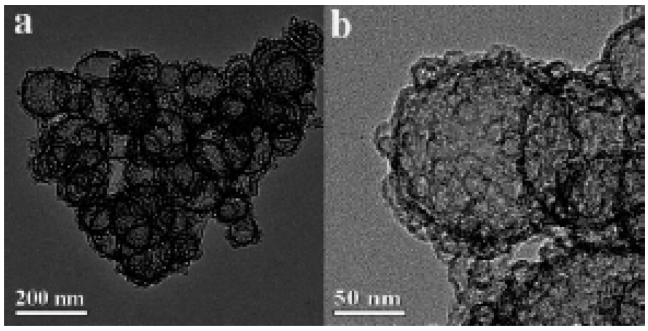

Figure 124. TEM images (a, b) of calcined raspberrylike hollow silica structures. Reprinted with permission from ref 624. Copyright 2007 American Chemical Society.

lized particles of average diameters 156 and 134 nm, respectively, were produced.[621] Silica was deposited using silicon alkoxide reagents to give a shell thickness of ~6 nm, and the deposition was mediated by the quaternary ammonium groups on the vesicle surfaces. In this preparation, the silica shell was too thin to maintain mechanical stability after removal of the organic template.

Providing greater stability, catanionic surfactant vesicles have also been used to produce hollow silica particles.[622,623] Mixtures of (i) cetyltrimethylammonium bromide (CTAB) and sodium perfluorooctanoate (FC_7) and (ii) cetyltrimethylammonium tosylate (CTAT) and sodium dodecylbenzenesulphonate (SBAS) spontaneously formed unilamellar vesicles in dilute HCl, which were coated with silica using tetramethoxysilane (TMOS).[622] Hollow silica particles with sizes in the range 60−120 nm were produced according to the composition of the vesicles, and more complex, multilamellar structures were formed within the biphasic lamellar/vesicular region of the CTAB/FC7 phase diagram. Catanionic vesicles formed from a mixture of cetyltrimethylammonium hydroxide (CTAOH) and myristic acid ($C_{13}COOH$) templated the formation of facetted, rounded, or damaged hollow silica particles according to the surface charge of the vesicles, the rate of silica deposition, and the rate of ethanol production (generated on hydrolysis of the tetraethoxysilane (TEOS) reagent).[623] Derived from the high stiffness of cationic bilayers, the vesicles exhibited facetted icosahedral morphologies when the anionic surfactant was in excess, according to the solution pH. Under acidic pH, the facetted vesicles templated silica particles of the same shape, while rounded particles were observed at higher pH values.

Block copolymers that self-assemble into micellar and vesicular structures have proven to provide effective and versatile templates for the production of hollow silica particles. Hierarchical silica hollow spheres have been produced by a one-pot method in which silica was deposited on micelles and vesicles of the block copolymer $PEO_{39}PPO_{47}PEO_{39}$ (B50−6600), which coexisted in the reactant solution.[624] Controlled hydrolysis of TEOS in the presence of the polymer aggregates at room temperature, subsequent incubation at 100 °C, and finally calcination generated product particles with "raspberrylike" hollow structures (Figure 124). These structures were attributed to aggregation of silica-coated vesicles and micelles, such that 100−200 nm silica particles formed on the silica coating of the vesicles, and 20−25 nm diameter particles formed on the coating of the micelles. Subsequent aggregation of the small to the large particles, followed by calcinations, generated the particle morphologies observed. The commercially available copolymer poly(ethylene oxide)−poly(propylene oxide−poly(ethylene oxide) (PEO−PPO−PEO) has also been used to direct the formation of a range of silica structures, including silica spheres.[625] According to the pH, the solution concentrations, and the reaction temperature, siliceous tubules, spheres, and nanofoams were produced. Because this copolymer has not been previously recognized to form unilamellar vesicles, it was suggested that the silicification process itself played a role in directing their formation. In turn, the foams were generated on aggregation of soft vesicles.

Employing block copolymers to template nanosized silica particles, PDMA−PDPA block copolymer micelles were used to direct the formation of a homogeneous population of ~35 nm hollow silica particles by a similar procedure. Diblock copolymer micelles comprising cationic poly(2-(dimethylamino)ethyl methacrylate) (PDMA) and hydrophobic poly(2-(diisopropylamino)ethyl methacrylate) (PDPA) cores were silica-coated using tetramethylorthosilicate (TMOS) such that silica deposition was confined to the cationic PDMA chains, leading to core−shell particle structures.[626] The silica nanoparticles were stable in solution over a wide range of pH values and were considered for potential controlled-release applications.

4.3.3. Porous Solids via Emulsion Templates

There has been enormous interest in the formation of structured porous solids of materials including silicates, metals, metal chalogenides, and carbon allotropes through the use of colloidal crystals and emulsions as templates.[528,605,627−629] As such, we aim here only to provide a brief overview of the technique and its application to the preparation of porous silica. Emulsion templating relies upon the use of a highly uniform dispersion of liquid emulsion droplets as a template, and inorganic materials are deposited using sol−gel techniques.[629,630] The technique can lead to porous solids with uniform pores with a high degree of order, although considerable shrinkage of the pore size is typically observed as compared with the original emulsion droplet size, and many of the monoliths produced show disordered pore distributions and fairly large pore-size distributions. A considerable advantage of emulsion templating, however, as compared with using rigid colloidal crystals as templates is that, because the emulsion droplets are deformable, samples are able to accommodate the stresses and strains associated with gelation and calcination. Emulsion templating can, therefore, lead to much larger sample sizes than colloidal crystal templating.[605]

Initial work employed oil-in-formamide, nonaqueous emulsions stabilized with a triblock copolymer of general structure $(\text{ethylene oxide})_n-(\text{propylene oxide})_m-(\text{ethylene oxide})_n$ that were produced with a polydispersity of a few percent and below through a repeated fractionation/shearing procedure.[630,631] A silica replica of the structure of the emulsion droplets was then formed by addition of the emulsion to a sol of silica particles in formamide followed by centrifugation to adjust the porosity and induce self-assembly of the emulsion droplets. Subsequent increase in the pH to induce gelation, aging, and finally calcination to burn off the organic material then yields a macroporous silica monolith. Extending this methodology, a range of techniques has been employed to prepare porous silicates from emulsion templates. Macroporous silica was prepared from oil-in-water emulsions using sodium dodecyl sulfate (SDS) as a stabilizer, although a nonuniform distribution of pore sizes was

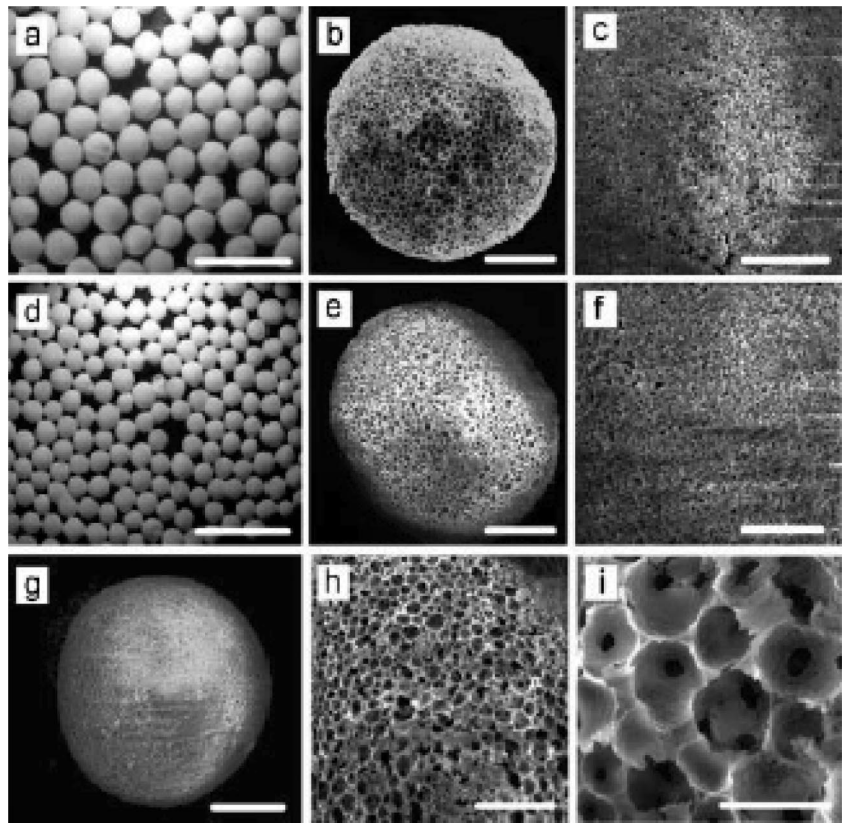

Figure 125. (a−c) Polymer/silica composite beads: (a) optical micrograph, scale bar = 5 mm; (b) SEM of a cross-sectioned composite bead, scale bar = 500 μm; (c) SEM of the bead surface, scale bar = 100 μm. (d−i) Silica beads: (d) optical micrograph, scale bar = 5 mm; (e) SEM of a cross-sectioned bead, scale bar = 500 μm; (f) SEM of the bead surface, scale bar = 200 μm; (g) SEM of a single bead, scale bar = 500 μm; (h) SEM of porous internal structure, scale bar = 200 μm; (i) SEM of porous internal structure, scale bar = 50 μm. Reprinted with permission from ref 634. Copyright 2007 Wiley-VCH.

obtained.[632] Emulsions have also been used to template macroporous silica in the absence of surfactants using nanosized silica particles of controlled wettability to stabilize the emulsion droplets.[633] Macroporous silica was then produced by evaporation of the liquids in the emulsions.

Hierarchically ordered porous silica structures have also been prepared by a number of routes based on emulsion templating. Meso/macroporous silica monoliths were formed on condensation of silica around the oil droplets of a CTAB (cetyl trimethylammonium bromide) stabilized emulsion. Here, the CTAB acted both to stabilize the emulsion and to direct the formation of mesoporous silica.[635,636] Silica/polymer composite beads have been formed by sedimentation polymerization of a high internal-phase emulsion, and subsequent calcination then generated silica beads with retention of the original structure (Figure 125).[634] Extending the application of polymers further, hierarchically porous silica beads were prepared using porous polymer beads as templates, which were themselves synthesized by oil-in-water-in-oil sedimentation polymerization.[637] Infiltration of the sol−gel precursor solution into the porous polymer beads, followed by gelation and calcination, then generated the product porous beads that exhibited 2−5 nm mesopores and micropores and 5−10 μm macropores. Using a similar principle, meso/macroporous silica monoliths were prepared using a polystyrene foam template, which was formed by polymerization of styrene either in the continuous or dispersed phase of an oil-in-water emulsion.[638] Formation of mesoporous silica in this porous template and removal of the organic material then generated the hierarchically structured silica.

4.3.4. Porous Solids via Colloidal Crystal Templates

Colloidal crystals provide access to porous solids with an extremely high level of order such that the product inverse opal material is a precise inverse replica of the initial colloidal crystal.[528,639,640] The methodology relies upon formation of a colloidal crystal from uniform colloidal particles (typically either polymer or silica) and deposition the selected material in the void space (Figure 126). While complete filling of the void space leads to a perfect negative replica of the colloidal crystal, incomplete filling results in additional porosity in the product structure. Further, the form of the skeletal solid produced from the colloidal crystal template can vary considerably, depending on the deposition method.[528] When the precursor material interacts strongly with the template surface ("surface templating"), the material deposits on the spheres, and the pores in the structure can become blocked prior to filling of the entire pore volume, giving rise to additional holes. In many solvent-based infiltration methods, "volume" templating occurs such that the solid fills the void space. Incomplete filling, or shrinkage during calcination, typically yields skeletal structures. Silica reverse opal structures have typically been prepared using sol−gel methods or through deposition of fine silica sols in the pore structure. A range of techniques have been applied to achieve uniform infiltration into the template structure, including, for example, filtration of the reagents through the colloidal crystal or infiltration based on capillary effects[641,642] and control of the rate of silicification through adsorption of surfactant onto latex spheres.[642]

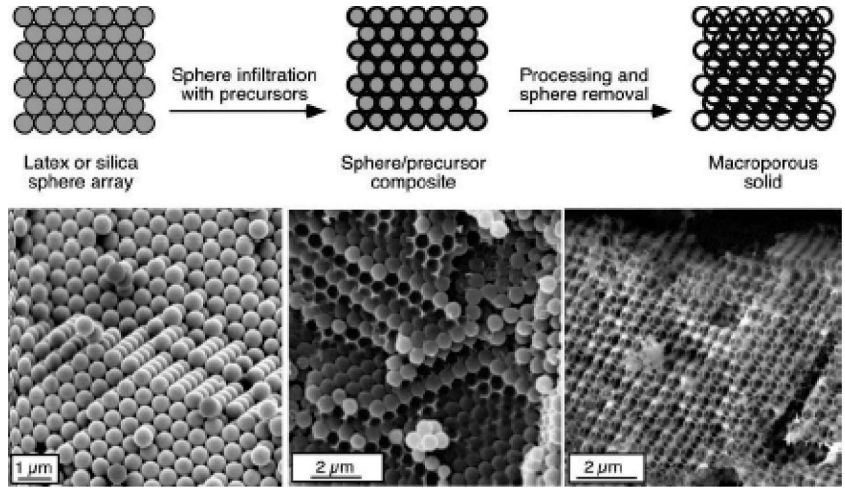

Figure 126. General synthesis scheme for ordered macroporous solids and the corresponding SEM images for a polystyrene/silica system prepared with tetraethylorthosilicate. Reprinted with permission from ref 627. Copyright 2001 Elsevier.

Colloidal crystal templates have also been extensively used as the basis for preparing solids with hierarchical porous structures (reviewed in refs 528 and 605). Depositing mesoporous silica in the void space of the colloidal crystal provides an immediate strategy for generating a solid with porosity on both the macroscopic and mesoscopic length scales.[643,644] In this case, the confinement of the pores in the colloidal crystal can give rise to structural changes in the mesoporous silica as compared with the bulk. Silica samples with hierarchical porosity have also been produced from colloidal crystal templates using additional synthetic strategies. Colloidal crystals formed from colloidal particles with different sizes have been used to generate complex porous structures. Employing bimodal populations of beads, colloidal crystals with different superlattice structures were formed according to the ratio of the diameters and the proportions of the two types of beads.[645] These colloidal crystals then acted as suitable templates to form silicates with binary macroporous structures and mesoporous walls. Colloidal crystals containing three bead sizes have also been employed, where 465 nm PS beads generated the gross structure of the colloidal crystal, and 84 nm PMMA and 6 nm beads silica partly occupied the pore volume.[646] Calcination of this structure then generated a silica reverse opal structure, where the pore walls were perforated by pores generated by the PMMA beads. Finally, micromolding techniques have been combined with colloidal crystal templating to generate porous silicas with well-defined gross morphologies and patterned over multiple length scales.[647]

Porous single crystals can also be prepared via colloidal crystal templates if an amorphous precursor phase of the mineral is used. This strategy is discussed in section 4.1.8.3.

Colloidal particles have also been used to direct the formation of porous solids without the prior formation of a colloidal crystal.[648−650] Lukens et al. employed polystyrene particles coated with cationic surfactants to direct the formation of silica foams,[649] while Vaudreuil et al. allowed a uniform population of polystyrene beads to sediment in an ethanolic solution of TEOS (tetraethyl orthosilicate), before evaporating off excess solution. After calcination to remove the polymer beads, macrostructured silicas were produced where the structure was based on interconnected silica shells, resulting from incomplete filling of the interparticle space. Similar skeletal silica structures were generated by Oh et al.[648] on the self-assembly of aggregates of polystyrene beads in a mesoporous silicate sol−gel solution (Figure 127). After formation of the mesoporous silicate and removal of the polymer beads, skeletal structures were generated whose form was attributed to initial coating of the beads with silicate particles (Figure 127). Interparticle, doughnut-type structures then developed through drying and shrinking of the sol−gel precursor solution, and these structural units then assembled to generate an FCC lattice. The product silicates, therefore, exhibit bimodal meso/macroporous structures.

4.3.5. Alternative Templating Routes to Porous Solids

A number of other templating systems have been used to produce porous silica solids including, for example, polymer membranes and starch gels. Cellulose acetate and polyamide membranes have been used to prepare meso/macrostructured silica films, where the mesostructure was defined by surfactant aggregates and the macrostructure was defined by the polymer membrane.[651] Polyurethane foams have also been coated with preformed mesoporous silica particles, with subsequent calcination removing the organic framework to generate a cellular silica foam with trimodal pore sizes.[652] Profiting this time from a biopolymer, starch gels have been used to direct the formation of micromeso-macroporous silicates.[653] A number of approaches were applied, in which the structure of the gel was controlled according to the composition of the solution and the preparation conditions. The gels were infiltrated with 50 nm zeolite nanoparticles, and the starch framework could be removed without significant disruption to the structure, generating pores of up to 100 μm in size. Also employing a biopolymer, mesoporous silica has been prepared using nematic suspensions of cellulose as templates.[654] Structural examination of the product material suggested that the silica exhibited a pattern based on the helically ordered cellulose rods. Bicontinuous microemulsions based on didodecyldimethylammonium bromide (DDAB) and C_{14}/C_{16} oil provided a suitable environment in which to generate macroporous silica frameworks.[655] Silicification was carried out at temperatures ranging from −20 °C to room temperature. According to the reagent concentrations and reaction temperature, structures ranging from a continuous silica network to aggregated silica particles were produced.

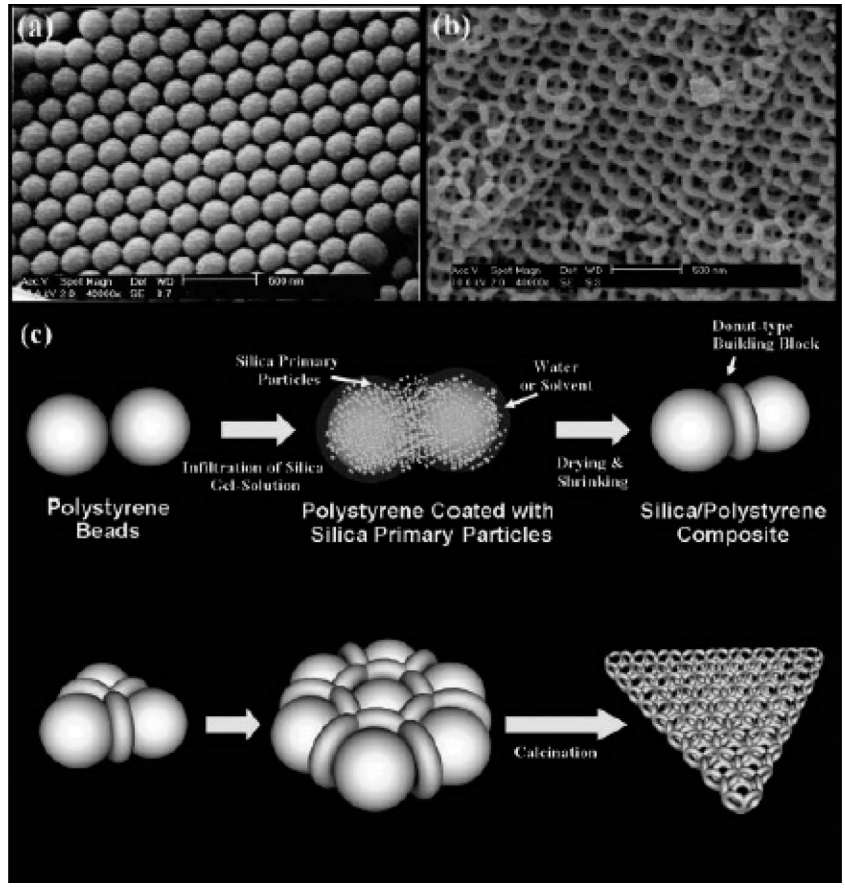

Figure 127. SEM images of (a) an array of polystyrene latex spheres and (b) macrostructured MCM-41. (c) Suggested scheme for the skeletal macrostructure formation. Reprinted with permission from ref 648. Copyright 2005 Wiley-VCH.

4.3.6. Ice Templates

The use of ice as an effective and versatile template for producing structured solids was introduced in section 4.2.4.1. We will here provide a number of examples of the application of this method to templating silica. Silica fibers with unique cross-sectional geometries and typical dimensions of 50 μm $\times$ 15 cm were produced through controlled freezing of silicic acid in water, followed by melting to remove the residual water.[543] In the method applied, the pH of a solution of silicic acid was adjusted to produce a gel, which was aged, and then directionally frozen. The solution and freezing conditions defined the dimensions of the product fibers such that thinner fibers were produced with lower silicic acid concentrations, colder freezing temperatures, and faster freezing rates. Control of the polymerization rate with the silicic acid concentration and the pH, as well as the aging time, yielded a range of different product structures, including fibers with star-shaped cross sections, flakes patterned with parallel ridges, or honeycomb structures (Figure 128). Polygonal cross-sectioned fibers were promoted by high gel strengths, low electrolyte concentrations, and unidirectional freezing. This approach has been extended to produce silica monoliths with microhoneycomb structures comprising unidirectionally aligned homogeneous channels, perforated by micro- and mesopores.[656,657] Again, the structure of the ice, which comprises a polycrystalline assembly of continuous rod-shaped crystal domains with polygonal cross section, defines the morphology of the templated material. Freshly gelled silica hydrogels were unidirectionally frozen under conditions where pseudo-steady-state growth of ice crystals occurs. Subsequent thawing of the frozen samples, exchange of the water for *t*-butanol, and freeze-drying resulted in the production of these honeycomb monoliths with microporous/mesoporous walls.[656,657] Refinement of structural parameters such as the macropore size and the thickness and porosity of the silica walls could be made by changing the rate of freezing, the freezing temperature, and the silica concentration and by hydrothermal treatment of the prepared macroporous silica monoliths under basic conditions.[657]

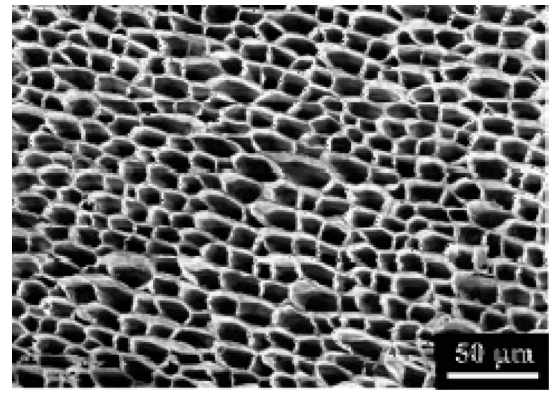

Figure 128. SEM image of the cross section of a silica microhoneycomb formed via templating of directionally frozen ice. Reprinted with permission from ref 657. Copyright 2005 American Chemical Society.

4.3.7. Membrane Pores

The rod-shaped pores of track-etch membranes have been used as templates to mold the formation of silica particles and to investigate the effect of confinement on silica

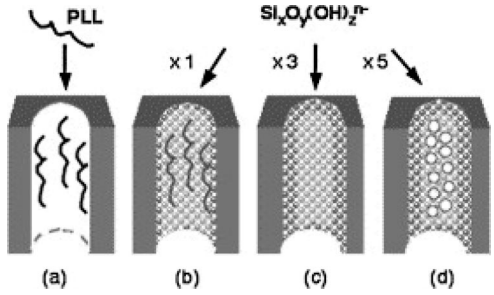

Figure 129. Schematic representation of silica tube formation. Poly L-lysine (PLL) is first adsorbed on the pore internal surface (a). First addition of silicates ($Si_xO_y(OH)^{n-}_z$) leads to the formation of a silica shell (b), which thickens with further impregnations (c). Further silicate addition leads to core particle growth (d). Reprinted with permission from ref 662. Copyright 2007 Elsevier.

formation, from a biomimetic perspective.[658] Anodic alumina membranes have been used to template the formation of mesoporous silicas.[659−661] This work has clearly demonstrated a strong influence of confinement on the structure of the product particles.

Silica was deposited within the pores of polycarbonate track-etch membranes with pore sizes in the range 0.2−1.2 μm, using sequential cycles of filtration of a silicate solution through the pores, immersion in a silicate solution, and washing.[658] Deposition of silica within the membranes pores was investigated by studying the intact membranes and after isolation of the silica by dissolution of the membranes in chloroform. Silica tubes with dense walls were produced in all the pore sizes investigated, suggesting that silica deposition is primarily defined by the silica/membrane surface interactions rather than by the pore dimensions. Repeated cycles increased the thickness of the tube walls, resulting in a core/shell structure where the dense silica shell became filled with silica aggregates. The size of the silica nanoparticles comprising the tubule cores was dependent on the pore size, and an increase in the primary particle size from ~10 to ~15 nm was observed on transition from 0.2 to 1.2 μm pore. This effect was attributed to gel formation (particle aggregation) being favored as compared with nanoparticle growth in confinement, such that the size of particles forming the gel decreases with confinement. The influence of the pore surface chemistry on the silica deposition process was also investigated by adsorbing poly-L-lysine on the membrane surface prior to silica precipitation.[662] The process is shown schematically in Figure 129. Some significant differences were observed as compared with the unmodified membranes; build-up of the silica shell was slower in the modified membranes, the thickness of the tube shell decreased with a decrease in the pore diameter, and the particle size was independent of the membrane-channel diameter. These observations were attributed to variations in the amount of poly-L-lysine adsorbed in different-sized pores, rather than to any conformational modification of the polymer that could have given rise to different surface/silicate interactions.

In an elegant demonstration of the effect of confinement on structure and morphology, mesoporous silica with markedly different structures was produced within the pores of anodic alumina, according to the pore size (Figure 130).[661] Mesostructured silica, templated with a block copolymer (Pluronic 123, P123), was deposited within nanochannels of diameters ranging from 18 to 80 nm. Markedly different structures were produced according to the dimensions of the confining pores. With channels in the range 55−73 nm, the enclosed mesostructure comprised three coaxial layers, of which the innermost forms a straight core while the outer two consist of concentric mesochannels with morphologies ranging from stacked doughnuts, to single or double helices. On reduction of the channel size to 49−54 nm, the particle structure becomes a coaxial double-layer helix in which the inner core is a single helix with 30 nm pitch and the outer layer is a single helix with 13 nm pitch. Further reduction in the pore diameter to 34−45 nm produced particles with a straight channel at the core and an outer layer consisting of stacked doughnuts, single or double helices. Channels with 31 nm diameters supported the formation of particles with a single-layer double-helix structure, while 28 nm pores yielded a new structure comprising linearly packed spherical cages. Finally, at a pore size of 18 nm, a single line of aligned cages is produced. Formation of these structures was interpreted in terms of the influence of the confined pore on the organization of the cylinder-forming mesophase. For example, the stacked doughnuts and single-helix structures can be constructed by regular stacking of coiled cylindrical micelles and springlike curling of cylindrical micelles respectively. Indeed, the periodicity of the coiled structures produced in confinement is in excellent agreement with the lattice spacing of the normal hexagonal phase of P123 in water, providing a vindication of this model.

Alternative studies on the formation of mesoporous silicas in confined geometries have also demonstrated the effect of confinement on the architecture of the product silica.[659,663,664] Mesoporous silica nanotubes and nanofibers were produced by precipitation of a block-copolymer (Pluronic F-127) templated silica in the pores of anodic alumina membranes.[660] In the absence of surface-treatment, the alumina membranes supported the formation of silica nanotubes only. Hydrophobically treated membranes, in contrast, templated the formation of silica fibers with hexagonally ordered pores where the pores were arranged perpendicular to the long axis of the fiber in a circular structure along the axis. Precipitation of mesoporous silica in the pores of anodic alumina membranes in the presence of a Pluronic P123 surfactant resulted in curvature of the silica mesopore channels along the membrane pores.[659] No preferential alignment of the hexagonal pores with respect to the channel axis was observed. The mesostructure produced depended on the pore size, and structures such as circular hexagonal, coaxial lamellar, and helices extended along the length of the membrane pores were produced. These structures were suggested to derive from nucleation of the mesoporous silica on alumina pore surface, followed by growth inward. Nanorods of mesoporous silica have also been precipitated in the pores of an alumina membrane in the presence of Pluronic 123, producing particles in which the mesochannel orientation was perpendicular to the membrane.[663] Influence of the confines of 200 nm alumina membrane pores on the ordering of mesoporous silica was also observed in that the mesopores were hexagonally ordered at the silica/membrane interface but became more disordered to the interior of the fiber, suggesting that the pore walls mediated the growth of the mesoporous structure in a 1D direction.[665]

Extensive studies have been carried out investigating silica deposition within the confines of inverse opal crystals of polymeric beads. An excellent recent review of this topic is provided in ref 528. While much of the focus of the work carried out on silica deposition in colloidal crystals has been on the generation of ordered macroporous solids, an overview

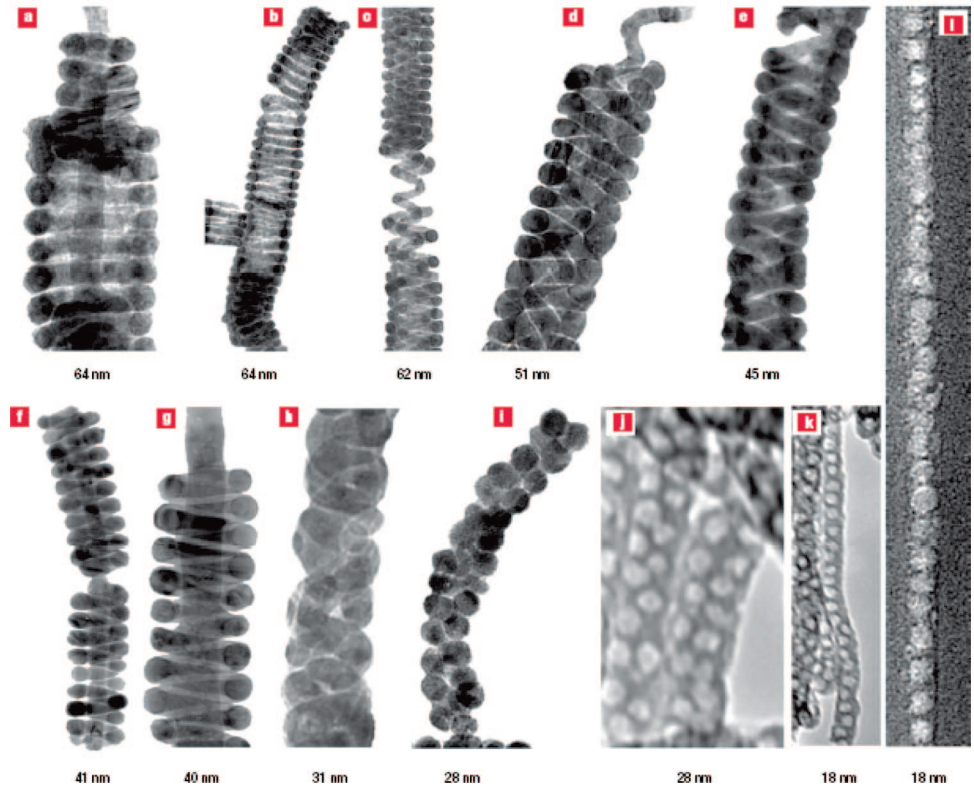

Figure 130. Representative TEM images of mesostructures formed inside alumina nanochannels with differing confinement dimensions. The confining nanochannel diameter is indicated underneath each image. (a−i) Silver inverted mesostructures prepared by backfilling the confined mesoporous silica; (j−k) free-standing mesoporous silica fibers; (l) mesoporous silica embedded inside the alumina nanochannels obtained using a focused-ion beam for sample preparation. The structures are (a) three-layer stacked doughnuts; (b) S-helix; (c) core−shell D-helix, in which the core and the shell are both S-helix; (d) core−shell triple-helix, in which the shell is a D-helix and the core is an S-helix; (e) D-helix; (f, g) S-helix with a straight core channel; (h) D-helix; (i, j) inverted peapod structure with two lines of spherical cages packed along the long axis of the alumina nanochannel; and (k, l) inverted peapod with one line of cages. Reprinted with permission from ref 661. Copyright 2007 Nature Publishing Group.

of which will be provided in section 4.3.4, this system has also enabled study of the effects of confinement on the structure of mesoporous silicates.[528] Providing a few examples, silica colloids were formed in the presence of a Pluronic F127 triblock copolymer within the spherical cavities of a colloidal crystal, and the diameter, surface chemistry, and connectivity of the cavities were shown to influence the internal structure of the silica particles.[666] When the template polymer was hydrophilic in nature, the colloids exhibited a circularly wound mesostructure, while an intermediate surface energy yielded particles in which the mesostructure exhibited a pseudorhombohedral dodecahedral organization. In contrast, disordered mesostructures were produced in hydrophobic polymer environments.

In a detailed study of the effects of confinement on surfactant-templated mesoporous solids precipitated in colloidal crystals, the phase diagram for the structured silica was shown to differ from that of the same material precipitated in bulk.[667] Further, the orientation of the mesochannels with respect to the polymer beads differed according to whether the surfactant Brij56 ($C_{16}H_{33}(OCH_2CH_2)_nOH$, $n \approx 10$) or Pluronic P123 ($EO_{20}PO_{70}EO_{20}$) was used, as well as the presence of a cosurfactant. Using Brij56 and dodecane as structure-directing agents, mesoporous silicas with either wormlike pores or cubic or hexagonal structures were produced according to the solution composition. In the hexagonal structure, the pores were oriented perpendicular to the surfaces of the polymer spheres. In contrast, hexagonal structures were produced in the presence of P123 such that the columnar mesopores ran parallel to the surfaces of the polymer beads.

4.3.8. Silica Mineralization Based on Assemblies of Organic Molecules

This section will focus on the use of assemblies of organic molecules as structure-directing templates. There has been considerable interest in this area, partly driven by the direct analogy with biogenic silicification processes. The mechanisms active in biosilicification, and most importantly the roles played by organic molecules in directing both silica precipitation and morphogenesis, have been best-studied in diatoms and siliceous sponges.[668] Characterization of the key macromolecules involved in silicification in these species then provides an inspiration for the design of synthetic polypeptides to control silica formation in vitro and an opportunity to probe the mechanisms of morphology control. Some discussion of the influence of organic macromolecules isolated from diatom frustrules on in vitro silica precipitation has already been made in section 3.4.2. Here, we will provide an overview of the wide range of systems that have been used to direct silica morphogenesis, which ranges from the assembly of block copolymers and block copolypeptides, peptide-based amphiphiles, surfactants, and organogels.

Analyses of the axial protein filaments present in the siliceous spicules of the sponge *Tethya aurantia* have demonstrated that they comprise three silcatein protein subunits, whose key structural features were mimicked in a series of cystein-lysine block copolypeptides.[669] The co-

polypeptides self-assembled into aggregates in solution, which both catalyzed the hydrolysis of TEOS and directed the product silica morphology. While lysine groups were active in mediating silica formation, the cysteine block directed the morphology of the silica structures, directing the formation of a range of structures including fibers and hollow spheres. Variation of the block sizes, and control over the oxidation of the cysteine sulfydryl groups, enabled the aggregation of the polymers and, therefore, the morphology of the silica particles to be determined. Hollow silica particles ~100 μm in diameter were produced using the polymer poly(L-cysteine$_{30}$-*b*-L-lysine$_{200}$) under an inert environment. Similar results were obtained on reducing the size of the cysteine block to poly(L-cysteine$_{10}$-*b*-L-lysine$_{200}$), while increase to poly(L-cysteine$_{60}$-*b*-L-lysine$_{200}$) led to elongated silica particles. By performing the experiment under oxidative conditions where intra- and interchain cross-links formed on oxidation of the cysteine sulfydryl groups, ordered columns of silica were observed rather than silica spheres.

Further studies have also examined the influence of poly(lysine)-based copolymers on silica precipitation. Lysine/phenylalanine block copolymer vesicles were used as templates for the preparation of hollow and solid spherical silica particles.[670] The mismatch in solubility between the lysine and phenylalanine blocks (which are highly and poorly water soluble at pH 7, respectively) leads to their aggregation in solution. The structure of the product particles could be varied according to the sizes of the copolymer blocks, such that hollow shells of size 114 nm were produced using Lys$_{23}$-*b*-Phe$_{23}$ while solid silica particles were formed if the block ratio of Lys/Phe was increased above 1:1. Lys-*b*-Gly copolypeptides, in contrast, supported the formation of silica spheres and platelets, according to the reaction conditions and the size of the block copolymer blocks.[671] It was suggested that the Lys-*b*-Gly block copolypeptides could aggregate to form structures with both high and low curvatures, such that they could template the formation of both spheres and platelets.

poly-L-Lysine (PLL) has also been used as a structure-directing additive, showing that the silica product can be controlled according to the molecular weight of the PLL, the reaction conditions, and the presence of additives.[672−678] Silica particles were produced in the presence of PLL (with a maximum degree of polymerization of 72) and hydrophobic amines, using TEOS as the silica source.[675] According to the pH value and the amine used, either granular silica particles or hollow silica spheres were produced. At pH values of 11.6, rapid silica precipitation occurred in the presence of benzylamine, yielding hollow, spherical silica particles. Formation of these structures was attributed to the formation of PLL/benzylamine aggregates and subsequent transcription of this structure into silica, as driven by a hydrogen-bonding interaction between the negatively charged silica precursors and the amine moiety of the additive.

A wide range of silica morphologies have been generated in the presence of PLL by variation of the reaction conditions. Silica was precipitated in the presence of PLL, a phosphate buffer, and TMOS as the silica source, and in the absence of any perturbation, silica hexagons and spheres were typically produced.[673] Flowing the reaction mixture through a tube resulted in petal-like and fiberlike silica structures, while stirring the mixture induced the formation of unusual ladderlike structures, in addition to hexagons and spheres. Looking specifically at the influence of the PLL chain length,

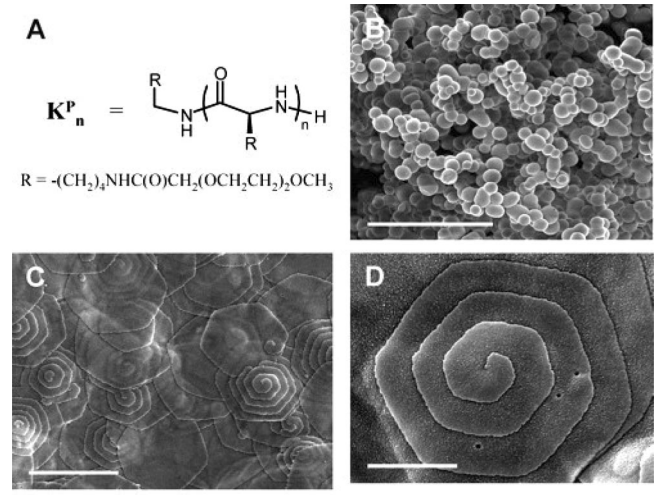

Figure 131. Morphologies of silica−K^P_n polypeptide composites and K^P_n homopolymer: (A) chemical structure of K^P_n; (B) SEM image of silica−K^P_{56} (40 wt % polypeptide) composite spheres (bar = 50 μm); (C) SEM top view image of silica−K^P_{264} (85 wt % polypeptide) composite hexagonal plates (bar = 10 μm); and (D) close-up SEM image of a silica−K^P_{264} (65 wt % polypeptide) composite hexagonal plate (bar = 2 μm). Reprinted with permission from ref 679. Copyright 2006 American Chemical Society.

for silica formation in the presence of a phosphate buffer, PLL molecules with chain lengths of <100 amino acids were shown to support the formation of a network of fused silica particles, while chain lengths of between 100−840 residues produced fused silica plates with hexagonal morphologies.[672,676] The hexagonal platelets were believed to form because of the formation of helical chains of PLL that develop due to a change in the secondary structures of the long-chain PLL molecules in the presence of silicate and phosphate ions. These chains in turn assemble into a hexagonal lattice during the silicification process, ultimately giving rise to the fused hexagonal silica platelets.[672] This mechanism was confirmed using in situ circular dichroism measurements, which demonstrated that the formation of PLL helices was a prerequisite to the formation of the hexagonal silica particles and that only silica particles formed in the presence of β-sheet PLL.[677] The conformation of the PLL, therefore, acts as a "molecular switch" that dictates the morphology of the silica product. Further demonstrating the importance of the PLL secondary structure in directing silica deposition, silicas were precipitated in the presence of PLL with different conformations, in the absence of further additives.[678] Silicas with pore sizes of 1.5 nm were produced when PLL was in an α-helical form, while larger pores (the sizes of which were determined by the PLL concentration) were observed in the presence of β-sheet PLL. In both cases, the pore sizes reflected the size of PLL aggregates in solution, demonstrating their templating effect.

Looking beyond poly(lysine)-based polymers, soluble α-helical polypeptides (termed K^P_n and shown in Figure 131) have also been used to prepare aggregates of well-defined, silica−polypeptide tablets (Figure 131 parts c and d).[679] These structures were formed in concentrated solutions of longer polypeptide chains, while either irregular morphologies or spherical particles were precipitated in solutions of shorter (K^P_{56}) polypeptides. That the hexagonal tablets form in concentrated polymer solutions demonstrates the influence of the charged silica species in driving the crystallization of the polypeptide. Silica condensation mediates growth of polypeptide crystals due to aggregation of the rodlike,

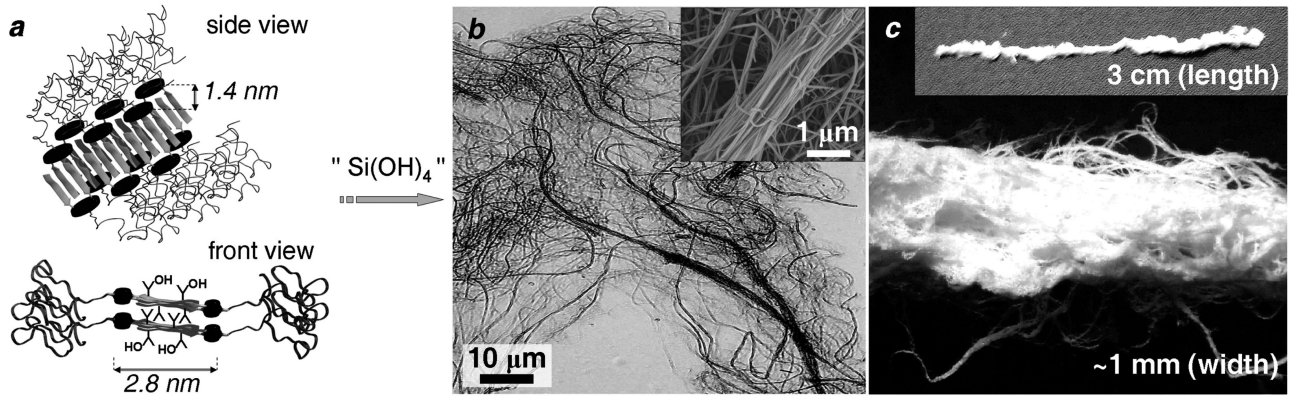

Figure 132. Spontaneous formation of silica composite fibers by the addition of "silicic acid" to a dilute solution of PEO−peptide nanotapes. (a) Schematic representation of nanotapes with a functional peptide β-sheet core and a PEO shell; (b) Optical microscopy image of the composite fibers; inset: SEM image of protocomposite fibers in bundles. (c) Macrocomposite fibers resulting in macroscopic threads (2 μm). Modified and reprinted with permission from ref 683. Copyright 2007 Wiley-VCH.

α-helical peptides, and the crystals then act as templates for silica deposition.

Assemblies of peptide-based molecules have also been explored as templates for the production of silica nanotubes.[680−682] Hollow silica nanotubes, hundreds of nanometres long and with a central pore of ~3.5 nm, were produced by condensation of silica on designed self-assembled β-sheet fibrils, followed by calcination to remove the organic template.[680] Using peptide amphiphiles as templates, hollow silica nanotubes were produced whose wall thickness could be adjusted according to the reaction conditions and the size of the peptide amphiphile.[681] The peptide amphiphiles self-assembled to give a fiber with hydrophobic core, surrounded by a structured β-sheet region, and an outer layer containing conformationally flexible groups. Silica deposition then occurs on the positively charged/neutral groups on the fiber surface, with growth also occurring inward into the fiber. Peptidic lipids that assembled to give fibers also proved to be suitable templates for the production of silica nanotubes, where the diameter could be tuned to between 30 and 80 nm according to the dimensions of the fiber templates.[682]

Remarkable silica fibers exhibiting up to six levels of hierarchical organization were produced on silica-coating of nanotapes. [683] The nanotapes themselves had a width of 15 nm, height of 1.4 nm, and length of up to 2 μm and were produced by self-assembly of peptide−polymer conjugates comprising a peptide β-sheet core and a PEO shell. The structure of these nanotapes is such that the PEO shell shields the peptide core, therefore minimizing lateral interactions and assembly, while the hydroxy groups from the threonine residues were active in directing silica deposition. Addition of prehydrolyzed TMOS to the fibers resulted in rapid formation of macroscopic fibers of widths 400 nm−2 μm, each of which comprised bundles of smaller, ~100 nm wide fibers (Figure 132). Silica condensation was suggested to occur on both sides of the β-sheet faces, giving rise to charged silica patches that induce aggregation. Depending on conditions, further entanglement also occurred to give macroscopic fibers with diameters up to ~1 mm and lengths up to ~3 cm. Such length scales are quite extraordinary for self-assembly-driven processes, which are usually self-limiting on the micron scale. This technology was further applied to produce silica nanocomposites and fiber networks.[684] In this case, the self-assembled PEO−peptide nanotapes were used as ink, using a 2D-plotting process to define the fiber width and the network structure and initiating silicification by injecting the nanotape solution into a thin layer of prehydrolyzed TMOS. Calcination of the silica/fiber composites then generated a silica fiber network with high-surface-area mesoporous structure with aligned cylindrical pores.

A wide range of helical silica structures have been formed based on the self-assembly of chiral cationic surfactants in solution.[685,686] According to the reagent concentrations and the solvent, particle morphologies ranging from helical mesoporous nanostructures to double helical mesoporous nanofibers, to single-stranded coiled mesoporous nanofibers, to twisted mesoporous silica ribbons have been produced. Examples of the range of silica structures produced using 2-propanol as a solvent are shown in Figure 133, which varied from double-helical mesoporous fibers (Figure 133a) to single-stranded, loosely coiled nanofibers (Figure 133 parts c and d) to twisted ribbons (Figure 133f). Formation of mesoporous structures was considered in terms of competition between the rate of condensation of the silica oligomers and the rate of aggregation of the surfactant. When the condensation rate is such that the silica species absorb and polymerize on the surface of single organic fibers, mesoporous products are formed, while silica condensation on the surface of ribbons or fibers yields silica ribbons or nanotubes.[685]

Finally, some remarkable silica morphologies have been prepared using organogels as templates.[604] A considerable volume of work has been carried out in this area, so we will not attempt here to be comprehensive, but rather to give some illustrative examples of the types of structures that can be formed and the mechanisms of their formation. Poly(ethylene imine) polymers with a number of different architectures were used to direct the deposition of silica, producing a range of morphologies including flower-, plate-, bundle-, leaf-, and spherelike morphologies according to the structure of the polymers and the reagent concentrations.[687,688] A wide range of other silica architectures including fibers, rolled-paper structures, and helical ribbons have also been generated according to the structure of the gel and the reaction conditions.[604] An acetic acid organogel of compound **1** (Figure 134) comprising fibers with diameters ranging from 50 to 200 nm was produced in the presence of TEOS and water and successfully templated the formation of hollow silica nanotubes (produced after calcination).[689] Here, the precursor anionic silica species are adsorbed on the cationic organic fibrils, where the surface of the fibrils directs the

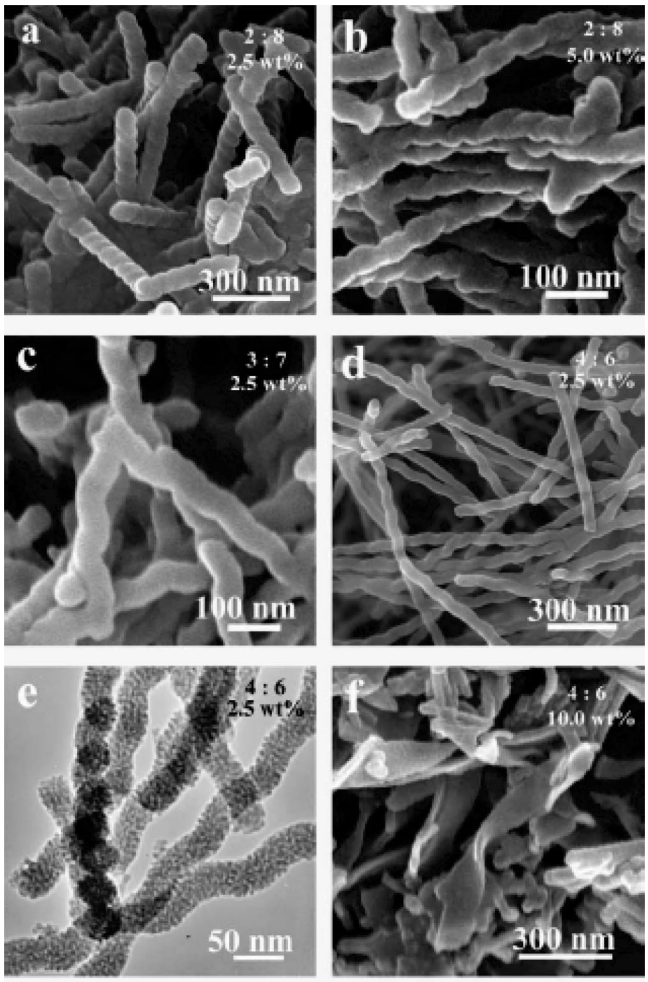

Figure 133. FESEM (a, b, c, d, f) and TEM (e) images of calcined nanostructured silica prepared in a mixture of water and 2-propanol. The top right values in the figures show the volume ratios of 2-propanol to water and the weight concentrations of NH_3. Preparation conditions were as follows: (a) 10 mg of L-4PyCl, 0.2 mL of 2-propanol, 0.8 mL of 2.5 wt % NH_3 aq, and 20 mg of TEOS; (b) 10 mg of L-4PyCl, 0.2 mL of 2-propanol, 0.8 mL of 5.0 wt % NH_3 aq, and 20 mg of TEOS; (c) 10 mg of L-4PyCl, 0.3 mL of 2-propanol, 0.7 mL of 2.5 wt % NH_3 aq, and 20 mg of TEOS; (d and e) 10 mg of L-4PyCl, 0.4 mL of 2-propanol, 0.6 mL of 2.5 wt % NH_3 aq, and 20 mg of TEOS; and (f) 10 mg of L-4PyCl, 0.4 mL of 2-propanol, 0.6 mL of 2.5 wt % NH_3 aq, and 20 mg of TEOS. Reprinted with permission from ref 685. Copyright 2006 Royal Society of Chemistry.

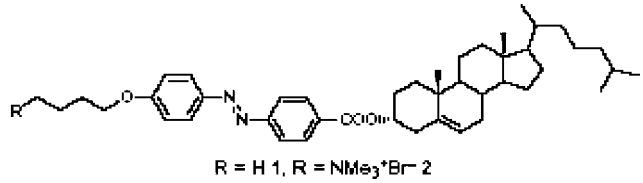

Figure 134. Structures of compounds **1** and **2**. Reprinted with permission from ref 689. Copyright 1998 Royal Society of Chemistry.

polmerization process. Cholesterol-based organogelators such as **1** and **2** (Figure 135) also assemble to form chiral structures, whose morphologies could be transcribed into silica. At specific ratios of compounds **1** and **2**, the chiral organic fibers templated chiral, helical, silica fibers.[690,691] When the organic fibers exhibit a high negative charge, the anionic silica precursors are randomly adsorbed onto the fiber surfaces, while moderate cationic charge leads to excellent

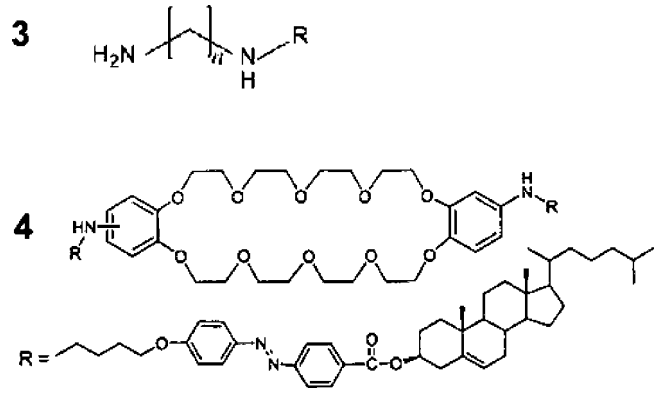

Figure 135. Structures of molecules **3** and **4**. Reprinted with permission from ref 693. Copyright 2007 American Chemical Society.

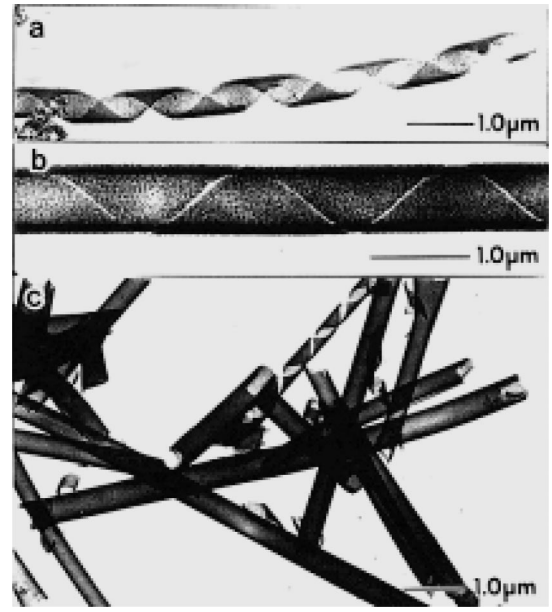

Figure 136. TEM images of tubular and ribbonlike structures after transcription of the acetic acid gel of **4**. Reprinted with permission from ref 696. Copyright 2000 American Chemical Society.

transcription of the fiber structure into the silica product. Silica fibers with a "rolled-paper" structure have been produced using a gel of the cholesterol/crown ether compound **4** (Figure 135) in the presence of cations such as K^+ or Cs^+, where the positive charge of the fibers again drives the silica adsorption and polymerization process.[692]

Similar structures have also been produced with templates under basic conditions (i.e., in the absence of a positive charge). Gels prepared from compound **3** yielded a range of structures including rollder-paper-like silica according to the structure of the gel (the size of *n*), where the strength of interaction between the amine group on the gel and the silica precursor species drove the transcription process.[694,695] Gels of compound **4** formed helical ribbon structures under specific conditions, and these morphologies were perfectly transcribed into silica ribbons with identical structures (Figure 136).[693] Indeed, close examination of these silica ribbons showed that they consisted of two independent layers separated by 8−9 nm, resulting from removal of the organogel template. As a straightforward, and highly controllable, route to helical, chiral silica fibers, a series of bis(ureido)cyclohexane-based compounds were prepared in enantiomericaly pure forms. While a chiral organogel

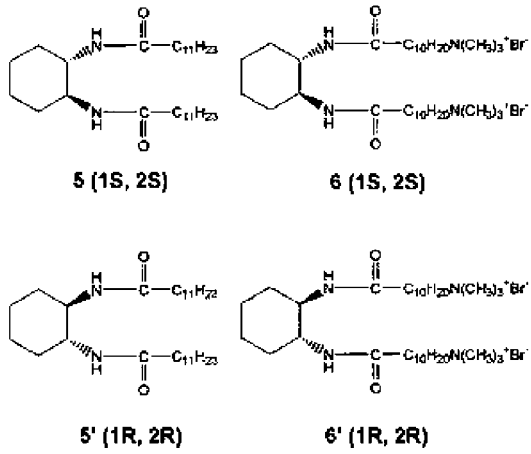

Figure 137. Structures of molecules **5** and **6**. Reprinted with permission from ref 696. Copyright 2000 Wiley-VCH.

prepared from a mixture of 1*S*,2*S*-diamines **5** and **6** (Figure 137) templated right-handed silica helices only, left-handed helices were exclusively produced from a mixture of 1*R*,2*R*-diamides **5′** and **6′**.[696,697] Successful templating of the fiber structure into silica only occurred when the ratio of the noncharged to the charged gelator was lower than 70:30.

4.3.9. Amorphous Macroporous Solids via Templating

Amorphous macroporous silica and titania solids were formed using either sea urchin skeletal plates or polymer replics of the plates of these templates, and excellent structural reproduction was achieved in both cases. A number of techniques were applied to form macroporous silica, including suction-filtration of a dilute sol of 0.2−0.3 μm preprepared silica particles through a skeletal plate. Subsequent annealing of the plate and removal of the $CaCO_3$ yielded a two-sided macroporous silica structure, derived from surface coverage of the urchin plate by the silica particles. Two further methods were also investigated, termed a "hydrolysis method", in which either a sea urchin plate or polymer replica was immersed in tetraethoxyorthosilicate (TEOS) or silicon tetrachloride and then subjected to controlled hydrolysis and a "particle/hydrolysis method", where the selected template was initially immersed in a solution of preprepared silica particles to give partial filling of the pores and was then dried, before applying the hydrolysis method.

While the hydrolysis method was in general of limited success, leading to poor structural replication, the particle/hydrolysis method enabled excellent templating of both the sea urchin plates and polymer replicas. Macroporous, spongelike structures that were almost identical in morphology to the original template were produced, indicating that complete filling of the template pore structure had occurred. The average size of the SiO_2 particles produced varied according to the template used, and the 100 μm particles produced in the sea urchin plates were typically significantly larger than the 50 μm or smaller particles produced in the polymer membranes. All of the macroporous silicas were amorphous, as anticipated for room-temperature hydrolysis.

The same methods were also used to produce macroporous titania in the polymer templates. Large macroporous TiO_2 particles were produced on hydrolysis of either titanium ethoxide or titanium tetrachloride as reagents, although greater structural perfection was achieved using titanium tetrachloride. Casts almost identical in morphology to the original sea urchin were produced with sizes often exceeding 200 μm. The particle/hydrolysis method, using an anatase sol to partially infiltrate the polymer template, also yielded macroporous titania solids with structures identical to the original sea urchin plates. Very large macroporous monoliths of TiO_2, very close in structure to the original plate, were produced that often exhibited sizes in excess of 1 mm. Examination of the operative mechanism suggested that the precursor particles initially coated the polymer, partially filling the pores and possibly promoting the subsequent hydrolysis step. The hydrolysis step then leads to complete filling of the porous network. The hydrolysis method, operating at room temperature, yielded an entirely amorphous product, while the particle/hydrolysis method showed partial crystallinity due to the presence of the entrapped anatase particles used in the infiltration step. Subsequent calcination of both of these samples at 600 °C resulted in crystallization of the amorphous TiO_2 to give crystalline anatase.

4.3.10. Microgels as ACC Templates. Besides crystallization control by bulk gels, microgels can also used as templates for controlled precipitation. Copolymer hydrogels of poly(*N*-isopropylacrylamide-co-(4-vinylpyridine)) (termed PNIPVP) have been used as a localized precipitation medium for amorphous $CaCO_3$. Spherical, $CaCO_3$ filled hydrogels were formed after infiltration with Ca^{2+} and exposure to a slow supply of CO_2 (as shown in Figure 138).[698] The particles did not retain their spherical shapes after drying, but rather collapsed into monodisperse disklike nanoparticles, which were organized as a nonclose hexagonal packing array. This contrasts with the packing of hard spheres and soft hydrogels (see Figure 138 center).[698] The disks also showed doughnutlike shapes when the PNIPVP microgels were first loaded with 3 nm, carboxy-functionalized CdTe nanoparticles. These particles served as nuclei for $CaCO_3$, resulting in subsequent agglomeration of the $CaCO_3$ coated CdTe nanoparticles in the shells of the gel spheres and blocking further CO_2 transport into the center. This process results in the observed central hole.[698] This hydrogel system offers the possibility of tuning the separation of the $CaCO_3$ disks,[699] which can be achieved by variation of simple parameters such as the dip-coating speed and the concentration of the spheres.

4.3.11. Direct Synthesis of Monodisperse Spherical ACC Microparticles. Amorphous calcium carbonate can also be directly synthesized without any templates as reported in a number of papers by Wegner et al.[142,143,700] They were able to obtain monodisperse ACC micro- and nanoparticles via the alkaline decomposition of dialkylcarbonate as carbonate source. It is notable that liquid−liquid phase separation is discussed for the formation of the ACC particles. The particle size could be controlled by the reaction conditions such as temperature, concentration of components, and presence of polymers.[142,143,700] Because of the amorphous character, ACC is deformable, and therefore, it is not surprising that individual ACC nano- and microparticles adopt spherical shapes that show minimal surface areas. In the dry state, such nano- and microparticles can be kept stable for months and the synthesis could be upscaled—a rare case among the many reported morphogenesis strategies in this review.

ACC particles produced in the presence of polymeric additives such as PAA have already been discussed in section 4.2.2.1 and usually lead to the formation of ACC nanoparticles that rapidly aggregate. Naka et al. recently overcame

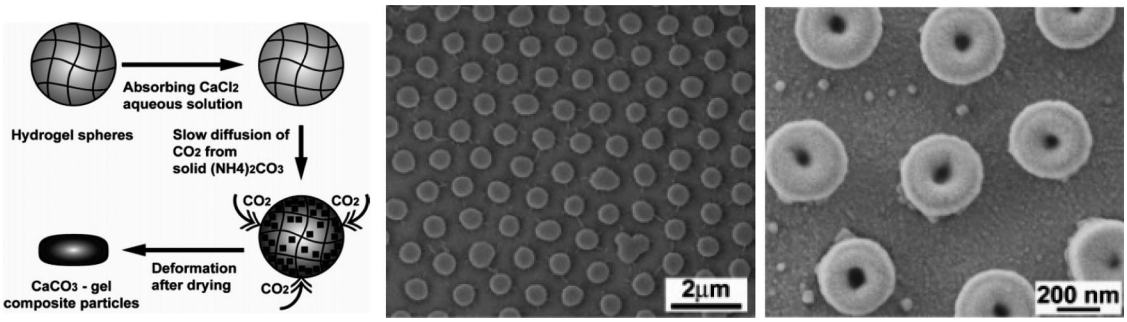

Figure 138. (left) Schematic illustration of the mineralization of $CaCO_3$ in a hydrogel particle matrix. (center) SEM image of the composite particles organized on the bottom of the reaction vial and (right) composite PNIPVP−$CaCO_3$−CdTe particles with doughnut shape. Reprinted with permission from ref 698. Copyright 2005 American Chemical Society.

this problem by incorporating a large amount of PAA into the nanoparticles, such that they were then stable in solution for up to 3 months. The sizes of the particles could be adjusted according to the PAA concentration. The PAA content of the nanoparticles was about 30 wt %, which is clearly the origin of the stabilization effect.[701] A much smaller amount of more potent PEO-*b*-PAA block copolymers in the ppm range was necessary to stabilize ACC nanoparticles in solution,[521] indicating the potential control of polymer structure of DHBCs for crystallization control (see section 4.2.2.3).

5. Summary

In this article, we have reviewed and discussed the topic of morphological development and control of biogenic and bioinspired minerals. Given the extent of morphological variation in both biology and synthetic systems, this is necessarily an enormous topic, and as such we have aimed to capture the principal elements of this subject by focusing on $CaCO_3$ and silica. $CaCO_3$ and silica are two of the most abundant biominerals, have been widely studied in biomimetic systems, and serve to illustrate the routes available for controlling the morphologies of crystalline and amorphous materials, respectively. One clear message delivered by our review of mineral morphologies in synthetic systems is that complex morphologies need not be restricted to nature; purely synthetic, inorganic minerals can adopt morphologies that are every bit as remarkable as their natural counterparts.

A very good example of this are the "biomorphs" discussed in section 4.2.7. Garcia Ruiz and Hyde, who are at the forefront of this field, have already addressed this question.[580,581,583] Entirely inorganic and abiotic biomorphs have been produced that display morphologies almost identical to the supposed cyanobacterial microfossils from the Precambrian Warrawoona chert formation in Western Australia. These are reputed to be the oldest terrestrial microfossils.[580] These findings have certainly also to be considered in the field of "nanobes",[702] which are reported to be dwarf forms of bacteria, 0.05−0.2 μm in size—that is, about one-tenth of the diameter and one-thousandth of the volume of ordinary bacteria. They would, thus, be the smallest form of life on earth. Interestingly, nanobes are found to be enormously abundant in minerals and rocks. The discussion of extraterrestrial magnetite, where the resemblance of these crystals to the magnetosomes found in magnetotactic bacteria is considered indicative of former life on Mars,[703] needs also to consider possible abiotic morphogenesis scenarios of the kind summarized in this review. Given the morphological and structural control of crystals that can be achieved in purely synthetic systems, it could be argued that the existing crystallographic and morphological evidence cannot conclusively support the existence of former life on Mars.[336]

A key issue arising from this discussion is that biology has devised ways to control mineral morphologies and structures with almost perfect reproducibility. Many of these "biological" morphologies can be produced synthetically and can be found in geological samples. However, the abiotic samples require a unique microenvironment that is often difficult to characterize and reproduce. This is still one of the major obstacles in the application of bioinspired approaches to mineralization reactions. A large number of potent additives have already been identified and used to control the crystallization and morphology of a wide range of minerals. However, the mechanisms by which these additives operate throughout the entire morphogenesis process are often time-dependent and are extremely difficult to access. Further, biomineralization processes, which form the inspiration for many strategies applied to mineralization in synthetic systems, are also very complex and difficult to study. Many questions remain to be answered on the structural, morphological, and orientational control of biominerals in vivo.

Study of mineral formation in both biological and synthetic systems clearly offers a challenging analytical problem, where a multicomponent system varies in time and space over orders of magnitude. Nevertheless, remarkable results have already been achieved. Morphogenesis processes certainly depend on the nature of the mineral—for example, whether it is amorphous, single crystalline, or polycrystalline. The production of complex morphologies from amorphous materials such as silica or ACC appears relatively straightforward, as these isotropic materials can me molded to any desired shape using templating approaches. A wider range of strategies are available for the morphological control of single-crystal and polycrystalline materials. Templating is again a general strategy and has been successfully applied to both single crystals and polycrystals. While it has been widely applied to polycrystalline materials, where it is clear that small units can be packed to form any selected morphology, templating of single crystals has received less attention. This is partly because this method is restricted by the requirement that the equilibrium size of the crystal under the applied growth conditions must exceed the length scale of the template and partly because it is often assumed that single crystals cannot be produced with complex morphologies by such a simple route.

Looking beyond templating approaches, soluble additives are widely used to control crystalline morphologies. In the thermodynamic regime, the action of additives can be understood in terms of face-selective additive adsorption, which is displayed in the final morphology as a consequence of Wulff's rule.[33] The mechanisms operating in the kinetic regime are often quite different. Amorphous or even liquid precursors are frequently found, and the reaction can proceed via several metastable polymorphs, following Ostwald's rule of stages. In this regime, the crystallization pathway often does not follow the classical textbook view of layerwise atom/ion/molecule addition to a critical crystal nucleus but instead proceeds via the self-assembly of nanoparticulate precursor units. Self-assembly mechanisms including "oriented attachment" and "mesocrystal formation", both of which have been identified in synthetic mineralization systems,[70] can be summarized under the term "nonclassical crystallization".[23,71] These mechanisms display the common feature that they lead to the formation of a single-crystal product by elimination of nanoparticle interfaces through crystallographic fusion. The distinction between single crystals formed by classical crystallization and nonclassical nanoparticle-mediated crystallization should, therefore, be based on the nature of the nucleation event. In the former case, a single nucleation event occurs, while nanoparticle-mediated crystallization is associated with multiple nucleation events. Nonclassical crystallization has also been reported for a number of biominerals and clearly offers a number of advantages over traditional ion-by-ion crystal-growth mechanisms. For example, nanoparticle-based crystallization scenarios where nanoparticles can be synthesized at one location prior to transportation to the mineralization site, avoids high salt concentrations with their associated high osmotic pressures and the transport of large solution volumes for the precipitation of sparingly soluble salts.

While the traditional approach is to use biological system as an inspiration for the synthetic, it is clear that the converse can also hold true, and mineralization in synthetic systems can provide insight into possible mechanisms active in biomineralization processes. This is especially important as it is generally far easier to identify mechanisms for controlled synthetic systems than it is for *in vivo* environments. Current developments undoubtedly demonstrate that it will probably be possible to control the morphologies of all inorganic and many organic crystals forming via ions. This can be achieved using a suite of methods including flexible molecular templates, rigid templates, tailored self-assembly mechanisms, and other strategies discussed in this review. These emerging bioinspired approaches may also provide a starting point for developing alternative pathways, leading to the formation of minerals and crystals with complex morphologies.

As an extension of this strategy, there is also a requirement to examine the relationship between the structural type and complexity (shape, size, phase, dimensionality, hierarchy, etc.) of materials and their properties. This is likely to result in novel applications in many areas of materials science and other related fields. Biominerals, with their complex morphologies and properties optimized for their function, also provide a unique inspiration for materials design. Despite being formed under ambient conditions from inorganic minerals with comparatively poor physical properties, nature creates materials whose properties challenge those of many synthetic products. Adopting a similar approach, it should be possible to optimize materials properties by controlling and defining their structures, organization, and morphologies. In this respect, morphosynthesis is an important component in the rapidly developing field of bottom-up synthesis in nanotechnology. As this review shows, although significant work remains to be carried out in this area, many significant mechanisms of morphological and structural control in biomineralization and bioinspired mineralization have already been identified that could be readily applied to the field of synthetic materials.

6. Acknowledgments

F.C.M. thanks the EPSRC and H.C. acknowledges the Max-Planck Society for financial support of this work.

7. References

(1) Thompson, D. W. *On Growth and Form*; Cambridge University Press: Cambridge, U.K., 2004.
(2) Perry, C. C.; Wilcock, J. R.; Williams, R. J. P. *Experientia* **1988**, *44*, 638.
(3) Mann, S. *Angew. Chem., Int. Ed.* **2000**, *39*, 3392.
(4) Wilt, F. H. *Dev. Biol.* **2005**, *280*, 15.
(5) Addadi, L.; Raz, S.; Weiner, S. *Adv. Mater.* **2003**, *15*, 959.
(6) Beniash, E.; Addadi, L.; Weiner, S. *J. Struct. Biol.* **1999**, *125*, 50.
(7) Weiss, I. M.; Tuross, N.; Addadi, L.; Weiner, S. *J. Exp. Zool.* **2002**, *293*, 478.
(8) Politi, Y.; Arad, T.; Klein, E.; Weiner, S.; Addadi, L. *Science* **2004**, *306*, 1161.
(9) Loste, E.; Park, R. J.; Warren, J.; Meldrum, F. C. *Adv. Funct. Mater.* **2004**, *14*, 1212.
(10) Loste, E.; Meldrum, F. C. *Chem. Commun.* **2001**, 901.
(11) Aizenberg, J.; Muller, D. A.; Grazul, J. L.; Hamann, D. R. *Science* **2003**, *299*, 1205.
(12) Cheng, X. G.; Gower, L. B. *Biotechnol. Prog.* **2006**, *22*, 141.
(13) Li, C.; Qi, L. M. *Angew. Chem., Int. Ed.* **2008**, *47*, 2388.
(14) Donnay, G.; Pawson, D. L. *Science* **1969**, *166*, 1147.
(15) Raup, D. M. *J. Geol.* **1959**, *67*, 661.
(16) Nissen, H.-U. *Science* **1969**, *166*, 1150.
(17) Towe, K. M. *Science* **1967**, *157*, 1048.
(18) LaMer, V. K.; Dinegar, R. H. *J. Am. Chem. Soc.* **1950**, *72*, 4847.
(19) Mullin, J. W. *Crystallization*, 4th ed.; Butterworth-Heinemann: Oxford, U.K., 2001.
(20) Berman, A.; Addadi, L.; Kvick, A.; Leiserowitz, L.; Nelson, M.; Weiner, S. *Science* **1990**, *250*, 664.
(21) Aizenberg, J.; Hanson, J.; Koetzle, T. F.; Weiner, S.; Addadi, L. *J. Am. Chem. Soc.* **1997**, *119*, 881.
(22) Kulak, A. N.; Iddon, P.; Li, Y.; Armes, S. P.; Cölfen, H.; Paris, O.; Wilson, R. M.; Meldrum, F. C. *J. Am. Chem. Soc.* **2007**, *129*, 3729.
(23) Cölfen, H.; Antonietti, M. *Mesocrystals and Non Classical Crystallization*; John Wiley & Sons: Chichester, U.K., 2008.
(24) Aizenberg, J.; Hanson, J.; Koetzle, T. F.; Leiserowitz, L.; Weiner, S.; Addadi, L. *Chem.—Eur. J.* **1995**, *1*, 414.
(25) Volmer, M. *Kinetik der Phasenbildung*; Steinkopff: Dresden, U.K., 1939.
(26) Kossel, W. *Ann. Phys.* **1934**, *21*, 457.
(27) Frenkel, J. *Phys. Z. (U.S.S.R.)* **1932**, *1*, 498.
(28) Burton, W. K.; Cabrera, N.; Frank, F. C. *Philos. Trans. R. Soc. London, Ser. A* **1951**, *243*, 299.
(29) Chernov, A. A. *Modern Crystallography III: Crystal Growth*; Springer: Berlin, 1984.
(30) Williams, E. D.; Bartelt, N. C. *Science* **1991**, *251*, 393.
(31) Barabási, A.-L.; Stanley, H. E. *Fractal concepts in surface growth*; Cambridge University Press: Cambridge, U.K., 1995.
(32) De Yoreo, J. J.; Vekilov, P. G. In *Reviews in Mineralogy and Geochemistry: Biomineralization*; Dove, P. M., De Yoreo, J. J., Weiner, S., Eds.; Mineralogical Society of America: Washington, DC, 2003; Vol. 54, p 57.
(33) Wulff, G. *Z. Kristallogr. Mineral.* **1901**, *34*, 449.
(34) Turnbull, D. *J. Appl. Phys.* **1950**, *21*, 1022.
(35) Luo, Y.; Sonnenberg, L.; Cölfen, H. *Cryst. Growth Des.* **2008**, *8*, 2049.
(36) Cölfen, H.; Mann, S. *Angew. Chem., Int. Ed.* **2003**, *42*, 2350.
(37) Mann, S. *Biomineralization: Principles and Concepts in Bioinorganic Materials Chemistry*; Oxford University Press: Oxford, U.K., 2001.
(38) Rieger, J.; Hädicke, E.; Rau, I. U.; Boeckh, D. *Tenside, Surfactants, Deterg.* **1997**, *34*, 430.
(39) Söhnel, O.; Mullin, J. W. *J. Cryst. Growth* **1982**, *60*, 239.

(40) Richter, A.; Petzold, D.; Hofmann, H.; Ullrich, B. *Chem. Technik* **1996**, *48*, 271.
(41) Yu, S. H.; Cölfen, H.; Antonietti, M. *J. Phys. Chem. B* **2003**, *107*, 7396.
(42) Yu, J. G.; Guo, H. T.; Davis, S. A.; Mann, S. *Adv. Funct. Mater.* **2006**, *16*, 2035.
(43) Tsortos, A.; Ohki, S.; Zieba, A.; Baier, R. E.; Nancollas, G. H. *J. Colloid Interface Sci.* **1996**, *177*, 257.
(44) Bolze, J.; Peng, B.; Dingenouts, N.; Panine, P.; Narayanan, T.; Ballauff, M. *Langmuir* **2002**, *18*, 8364.
(45) Taylor, M. G.; Simkiss, K.; Greaves, G. N.; Okazaki, M.; Mann, S. *Proc. R. Soc. London, Ser. B* **1993**, *252*, 75.
(46) Levi-Kalisman, Y.; Raz, S.; Weiner, S.; Addadi, L.; Sagi, I. *Adv. Funct. Mater.* **2002**, *12*, 43.
(47) Hasse, B.; Ehrenberg, H.; Marxen, J.; Becker, W.; Epple, M. *Chem.—Eur. J.* **2000**, *6*, 3679.
(48) Marxen, J. C.; Becker, W.; Finke, D.; Hasse, B.; Epple, M. *J. Molluscan Stud.* **2003**, *69*, 113.
(49) Nassif, N.; Pinna, N.; Gehrke, N.; Antonietti, M.; Jager, C.; Cölfen, H. *Proc. Natl. Acad. Sci. U.S.A.* **2005**, *102*, 12653.
(50) Beniash, E.; Aizenberg, J.; Addadi, L.; Weiner, S. *Proc. R. Soc. London, Ser. B* **1997**, *264*, 461.
(51) Aizenberg, J.; Lambert, G.; Addadi, L.; Weiner, S. *Adv. Mater.* **1996**, *8*, 222.
(52) Raz, S.; Weiner, S.; Addadi, L. *Adv. Mater.* **2000**, *12* (1), 38.
(53) Lowenstam, H. A.; Weiner, S. *Science* **1985**, *227*, 51.
(54) Ziegler, A. *J. Struct. Biol.* **1994**, *112*, 110.
(55) Henisch, H. K. *Crystals in Gels and Liesegang Rings*; Cambridge University Press: Cambridge, U.K., 1988.
(56) Dennis, J.; Henisch, H. K. *J. Electrochem. Soc.* **1967**, *114*, 263.
(57) Henisch, H. K.; Dennis, J.; Hanoka, J. I. *J. Phys. Chem. Solids* **1965**, *26*, 493.
(58) Oaki, Y.; Imai, H. *Cryst. Growth Des.* **2003**, *3*, 711.
(59) Suda, J.; Nakayama, T.; Nakahara, A.; Matsushita, M. *J. Phys. Soc. Jpn.* **1996**, *65*, 771.
(60) Imai, H.; Oaki, Y. *Angew. Chem., Int. Ed.* **2004**, *43*, 1363.
(61) Muller, S. C.; Kai, S.; Ross, J. *Science* **1982**, *216*, 635.
(62) Imai, H.; Tatara, S.; Furuichi, K.; Oaki, Y. *Chem. Commun.* **2003**, 1952.
(63) Bogoyavlenskiy, V. A.; Chernova, N. A. *Phys. Rev. E* **2000**, *61*, 1629.
(64) Davey, R. J.; Mullin, J. W. *J. Cryst. Growth* **1974**, *26*, 45.
(65) Blank, S.; Arnoldi, M.; Khoshnavaz, S.; Treccani, L.; Kuntz, M.; Mann, K.; Grathwohl, G.; Fritz, M. *J. Microsc.* **2003**, *212*, 280.
(66) Walters, D. A.; Smith, B. L.; Belcher, A. M.; Paloczi, G. T.; Stucky, G. D.; Morse, D. E.; Hansma, P. K *Biophys. J.* **1997**, *72*, 1425.
(67) Wegner, G.; Baum, P.; Müller, M.; Norwig, J.; Landfester, K. *Macromol. Symp.* **2001**, *175*, 349.
(68) Lu, C. H.; Qi, L. M.; Cong, H. L.; Wang, X. Y.; Yang, J. H.; Yang, L. L.; Zhang, D. Y.; Ma, J. M.; Cao, W. X. *Chem. Mater.* **2005**, *17*, 5218.
(69) Rieger, J.; Frechen, T.; Cox, G.; Heckmann, W.; Schmidt, C.; Thieme, J. *Faraday Discuss.* **2007**, *136*, 265.
(70) Niederberger, M.; Cölfen, H. *Phys. Chem. Chem. Phys.* **2006**, *8*, 3271.
(71) Cölfen, H. In *Biomineralization: From Paleontology to Materials Science*; Arias, J. L., Fernandez, M. S., Eds.; Editorial Universitaria, Universidad de Chile: Santiago, Chile, 2007; p 515.
(72) Wang, T. X.; Cölfen, H. *Langmuir* **2006**, *22*, 8975.
(73) Wang, T. X.; Reinecke, A.; Cölfen, H. *Langmuir* **2006**, *22*, 8986.
(74) Penn, R. L.; Banfield, J. F. *Geochim. Cosmochim. Acta* **1999**, *63*, 1549.
(75) Penn, R. L.; Banfield, J. F. *Am. Mineral.* **1998**, *83*, 1077.
(76) Huang, F.; Zhang, H.; Banfield, J. F. *Nano Lett.* **2003**, *3*, 373.
(77) Penn, R. L. *J. Phys. Chem. B* **2004**, *108*, 12707.
(78) Ribeiro, C.; Lee, E. J. H.; Longo, E.; Leite, E. R. *ChemPhysChem* **2006**, *7*, 664.
(79) Banfield, J. F.; Welch, S. A.; Zhang, H. Z.; Ebert, T. T.; Penn, R. L. *Science* **2000**, *289*, 751.
(80) Alivisatos, A. P. *Science* **2000**, *289*, 736.
(81) Lee, E. J. H.; Ribeiro, C.; Longo, E.; Leite, E. R. *J. Phys. Chem. B* **2005**, *109*, 20842.
(82) Read, W. T.; Shockley, W. *Phys. Rev.* **1950**, *78*, 275.
(83) Dunn, C. G.; Lionetti, F. *Trans. Am. Inst. Min. Metall. Eng.* **1949**, *185*, 125.
(84) Collier, A. P.; Hetherington, C. J. D.; Hounslow, M. J. *J. Cryst. Growth* **2000**, *208*, 513.
(85) Polleux, J.; Pinna, N.; Antonietti, M.; Niederberger, M. *Adv. Mater.* **2004**, *16*, 436.
(86) Polleux, J.; Pinna, N.; Antonietti, M.; Hess, C.; Wild, U.; Schlögl, R.; Niederberger, M. *Chem.—Eur. J.* **2005**, *11*, 3541.
(87) Antonietti, M.; Breulmann, M.; Goltner, C. G.; Colfen, H.; Wong, K. K. W.; Walsh, D.; Mann, S. *Chem.—Eur. J.* **1998**, *4*, 2493.
(88) Penn, R. L.; Banfield, J. F. *Science* **1998**, *281*, 969.
(89) Pacholski, C.; Kornowski, A.; Weller, H. *Angew. Chem., Int. Ed.* **2002**, *41*, 1188.
(90) Lou, X. W.; Zeng, H. C. *J. Am. Chem. Soc.* **2003**, *125*, 2697.
(91) Gehrke, N.; Cölfen, H.; Pinna, N.; Antonietti, M.; Nassif, N. *Cryst. Growth Des.* **2005**, *5*, 1317.
(92) Liu, B.; Zeng, H. C. *J. Am. Chem. Soc.* **2003**, *125*, 4430.
(93) Yang, H. G.; Zeng, H. C. *Angew. Chem., Int. Ed.* **2004**, *43*, 5930.
(94) Liu, B.; Zeng, H. C. *J. Am. Chem. Soc.* **2004**, *126*, 8124.
(95) Liu, B.; Zeng, H. C. *J. Am. Chem. Soc.* **2005**, *127*, 18262.
(96) Yao, K. X.; Zeng, H. C. *J. Phys. Chem. C* **2007**, *111*, 13301.
(97) Song, J. M.; Zhan, Y. J.; Xu, A. W.; Yu, S. H. *Langmuir* **2007**, *23*, 7321.
(98) Ribeiro, C.; Longo, E.; Leite, E. R *Appl. Phys. Lett.* **2007**, *91*, . article Number: 103105.
(99) Penn, R. L.; Oskam, G.; Strathmann, T. J.; Searson, P. C.; Stone, A. T.; Veblen, D. R. *J. Phys. Chem. B* **2001**, *105*, 2177.
(100) Guyodo, Y.; Mostrom, A.; Penn, R. L.; Banderjee, S. K. *Geophys. Res. Lett.* **2003**, *30*, 19.
(101) Burleson, D. J.; Penn, R. L. *Langmuir* **2006**, *22*, 402.
(102) He, T.; Chen, D.; Jiao, X. *Chem. Mater.* **2004**, *16*, 737.
(103) Yao, W.-T.; Yu, S.-H.; Zhou, Y.; Jiang, J.; Wu, Q.-S.; Zhang, L.; Jiang, J. *J. Phys. Chem. B* **2005**, *109*, 14011.
(104) Penn, R. L.; Stone, A. T.; Veblen, D. R. *J. Phys. Chem. B* **2001**, *105*, 4690.
(105) Si, R.; Zhang, Y. W.; You, L. P.; Yan, C. H. *J. Phys. Chem. B* **2006**, *110*, 5994.
(106) Du, N.; Zhang, H.; Chen, B. G.; Ma, X. Y.; Yang, D. R. *J. Phys. Chem. C* **2007**, *111*, 12677.
(107) Giersig, M.; Pastoriza-Santos, I.; Liz-Marzan, L. M. *J. Mater. Chem.* **2004**, *14*, 607.
(108) Yu, J. H.; Joo, J.; Park, H. M.; Baik, S.-I.; Kim, Y. W.; Kim, S. C.; Hyeon, T. *J. Am. Chem. Soc.* **2005**, *127*, 5662.
(109) Xu, A.-W.; Antonietti, M.; Cölfen, H.; Fang, Y.-P. *Adv. Funct. Mater.* **2006**, *16*, 903.
(110) Cho, K.-S.; Talapin, D. V.; Gaschler, W.; Murray, C. B. *J. Am. Chem. Soc.* **2005**, *127*, 7140.
(111) Yamauchi, Y.; Momma, T.; Fuziwara, M.; Nair, S. S.; Ohsuna, T.; Terasaki, O.; Osaka, T.; Kuroda, K. *Chem. Mater.* **2005**, *17*, 6342.
(112) Ye, M. F.; Zhong, H. Z.; Zheng, W. J.; Li, R.; Li, Y. F. *Langmuir* **2007**, *23*, 9064.
(113) Zeng, H. C *Int. J. Nanotechnol.* **2007**, *4*, 329.
(114) Cölfen, H.; Antonietti, M. *Angew. Chem., Int. Ed.* **2005**, *44*, 5576.
(115) Rieger, J.; Franke, D.; Frechen, T.; Haberkorn, H.; Goesele, W. 9th Workshop on Industrial Crystallization, Halle-Wittenberg, Germany, 2002; p 13.
(116) Judat, B.; Kind, M. *J. Colloid Interface Sci.* **2004**, *269*, 341.
(117) Ma, Y.; Cölfen, H.; Antonietti, M. *J. Phys. Chem. B* **2006**, *110*, 10822.
(118) Gower, L. A.; Tirrell, D. A. *J. Cryst. Growth* **1998**, *191*, 153.
(119) Wohlrab, S.; Cölfen, H.; Antonietti, M. *Angew. Chem., Int. Ed.* **2005**, *44*, 4087.
(120) tenWolde, P. R.; Frenkel, D. *Science* **1997**, *277*, 1975.
(121) Anwar, J.; Boateng, P. K. *J. Am. Chem. Soc.* **1998**, *120*, 9600.
(122) Schwahn, D.; Ma, Y.; Cölfen, H. *J. Phys. Chem. C* **2007**, *111*, 3224.
(123) Cuif, J. P.; Dauphin, Y. *Biogeosciences* **2005**, *2*, 61.
(124) Ma, Y. R.; Börner, H. G.; Hartmann, J.; Cölfen, H. *Chem.—Eur. J.* **2006**, *12*, 7882.
(125) Wang, T. X.; Antonietti, M.; Cölfen, H. *Chem.—Eur. J.* **2006**, *12*, 5722.
(126) Schäffer, T. E.; Ionescu-Zanetti, C.; Proksch, R.; Fritz, M.; Walters, D. A.; Almqvist, N.; Zaremba, C. M.; Belcher, A. M.; Smith, B. L.; Stucky, G. D.; Morse, D. E.; Hansma, P. K. *Chem. Mater.* **1997**, *9*, 1731.
(127) Oaki, Y.; Kotachi, A.; Miura, T.; Imai, H. *Adv. Funct. Mater.* **2006**, *16*, 1633.
(128) Oaki, Y.; Imai, H. *Small* **2006**, *2*, 66.
(129) Miura, T.; Kotachi, A.; Oaki, Y.; Imai, H. *Cryst. Growth Des.* **2006**, *6*, 612.
(130) Inumaru, K. *Catal. Surv. Asia* **2006**, *10*, 151.
(131) Kitano, Y. *Bull. Chem. Soc. Jpn.* **1962**, *35*, 1973.
(132) Page, M. G.; Colfen, H. *Cryst. Growth Des.* **2006**, *6*, 1915.
(133) Johannes, W.; Puhan, D. *Contrib. Mineral. Petrol.* **1971**, *31*, 28.
(134) Bagdassarov, N. S.; Slutskii, A. B. *Phase Transitions* **2003**, *76*, 1015.
(135) Shahar, A.; Bassett, W. A.; Mao, H. K.; Chou, I. M.; Mao, W. *Am. Mineral.* **2005**, *90*, 1835.
(136) Han, Y. S.; Hadiko, G.; Fuji, M.; Takahashi, M. *J. Cryst. Growth* **2006**, *289*, 269.
(137) Koga, N.; Nakagoe, Y. Z.; Tanaka, H. *Thermochim. Acta* **1998**, *318*, 239.
(138) Han, Y. S.; Hadiko, G.; Fuji, M.; Takahashi, M. *J. Eur. Ceram. Soc.* **2006**, *26*, 843.
(139) Schwertmann, U.; Cornell, R. M. *Iron oxides in the Laboratory*; Wiley-VCH: Weinheim, Germany, 2000.
(140) Lindskog, S. *Pharmacol. Ther.* **1997**, *74*, 1.

(141) Covarrubias, A. S.; Bergfors, T.; Jones, T. A.; Hogbom, M. *J. Biol. Chem.* **2006**, *281*, 4993.
(142) Faatz, M.; Gröhn, F.; Wegner, G. *Adv. Mater.* **2004**, *16*, 996.
(143) Faatz, M.; Grohn, F.; Wegner, G. *Mater. Sci. Eng., C* **2005**, *25*, 153.
(144) Dickinson, S. R.; McGrath, K. M. *J. Mater. Chem.* **2003**, *13*, 928.
(145) Chen, S. F.; Yu, S. H.; Yu, B.; Ren, L.; Yao, W. T.; Cölfen, H. *Chem.—Eur. J.* **2004**, *10*, 3050.
(146) Falini, G.; Gazzano, M.; Ripamonti, A. *Chem. Commun.* **1996**, 1037.
(147) Seo, K. S.; Han, C.; Wee, J. H.; Park, J. K.; Ahn, J. W *J. Cryst. Growth* **2005**, *276*, 680.
(148) Qi, L. M.; Li, J.; Ma, J. M. *Chem. J. Chin. Univ. Chin.* **2002**, *23*, 1595.
(149) Cong, H. P.; Yu, S. H. *Chem.—Eur. J.* **2007**, *13*, 1533.
(150) Chen, H. I.; Chang, H. Y. *Colloids Surf., A* **2004**, *242*, 61.
(151) Guo, X. H.; Yu, S. H. *Cryst. Growth Des.* **2007**, *7*, 354.
(152) Manoli, F.; Dalas, E. *J. Cryst. Growth* **2000**, *218*, 359.
(153) Chen, S. F.; Yu, S. H.; Jiang, J.; Li, F. Q.; Liu, Y. K. *Chem. Mater.* **2006**, *18*, 115.
(154) Guo, X. H.; Yu, S. H.; Cai, G. B. *Angew. Chem., Int. Ed.* **2006**, *45*, 3977.
(155) Wöhler, F.; Liebig, J. *Ann. Pharm.* **1832**, 249.
(156) Brittain, H. G. In *Polymorphism in Pharmaceutical Solids*; Brittain, H. G., Ed.; Marcel Dekker, Inc.: New York, 1999; p 227.
(157) Cabri, W.; Ghetti, P.; Pozzi, G.; Alpegiani, M. *Organic Process Res. Dev.* **2007**, *11*, 64.
(158) Dupont, L.; Portemer, F.; Figlarz, M. *J. Mater. Chem.* **1997**, *7*, 797.
(159) Price, C. P.; Grzesiak, A. L.; Matzger, A. J. *J. Am. Chem. Soc.* **2005**, *127*, 5512.
(160) Lang, M. D.; Grzesiak, A. L.; Matzger, A. J. *J. Am. Chem. Soc.* **2002**, *124*, 14834.
(161) Davey, R. J.; Blagden, N.; Potts, G. D.; Docherty, R. *J. Am. Chem. Soc.* **1997**, *119*, 1767.
(162) Cölfen, H. *Macromol. Rapid Commun.* **2001**, *22*, 219.
(163) Yu, S.-H.; Colfen, H. *J. Mater. Chem.* **2004**, *14*, 2124.
(164) Marland, G. *Geochim. Cosmochim. Acta* **1975**, *39*, 83.
(165) Marland, G. *Geochim. Cosmochim. Acta* **1975**, *39*, 1193.
(166) Wolf, G.; Konigsberger, E.; Schmidt, H. G.; Konigsberger, L. C.; Gamsjager, H. *J. Therm. Anal. Calorim.* **2000**, *60*, 463.
(167) Hu, Z. S.; Deng, Y. L. *Powder Technol.* **2004**, *140*, 10.
(168) Zhou, G. T.; Zheng, Y. F. *Neues Jahrb. Mineral., Abh.* **2001**, *176*, 323.
(169) Wray, J. L.; Daniels, F. *J. Am. Chem. Soc.* **1957**, *79*, 2031.
(170) Falini, G.; Gazzano, M.; Ripamonti, A. *J. Cryst. Growth* **1994**, *137*, 577.
(171) Xie, A. J.; Shen, Y. H.; Li, X. Y.; Yuan, Z. W.; Qiu, L. G.; Zhang, C. Y.; Yang, Y. F. *Mater. Chem. Phys.* **2007**, *101*, 87.
(172) Wada, N.; Yamashita, K.; Umegaki, T. *J. Cryst. Growth* **1995**, *148*, 297.
(173) Heywood, B. R.; Mann, S. *Chem. Mater.* **1994**, *6*, 311.
(174) Rushdi, A. I.; Pytkowicz, R. M.; Suess, E.; Chen, C. T. *Geol. Rundsch.* **1992**, *81*, 571.
(175) Davis, K. J.; Dove, P. M.; De Yoreo, J. J. *Science* **2000**, *290*, 1134.
(176) Deleuze, M.; Brantley, S. L. *Geochim. Cosmochim. Acta* **1997**, *61*, 1475.
(177) Tai, C. Y.; Chen, F. B. *AIChE J.* **1998**, *44*, 1790.
(178) Addadi, L.; Joester, D.; Nudelman, F.; Weiner, S. *Chem.—Eur. J.* **2006**, *12*, 981.
(179) Belcher, A. M.; Wu, X. H.; Christensen, R. J.; Hansma, P. K.; Stucky, G. D.; Morse, D. E. *Nature* **1996**, *381*, 56.
(180) Falini, G.; Albeck, S.; Weiner, S.; Addadi, L. *Science* **1996**, *271*, 67.
(181) Hiremath, R.; Basile, J. A.; Varney, S. W.; Swift, J. A. *J. Am. Chem. Soc.* **2005**, *127*, 18321.
(182) Heywood, B. R.; Mann, S. *Adv. Mater.* **1994**, *6*, 9.
(183) Aizenberg, J.; Black, A. J.; Whitesides, G. H. *J. Am. Chem. Soc.* **1999**, *121*, 4500.
(184) Fricke, M.; Volkmer, D. In *Biomineralization I: Crystallization and Self-Organization Process*; Topics in Current Chemistry: Springer-Verlag: Berlin, 2007; Vol. 270, p 1.
(185) Fricke, M.; Volkmer, D.; Krill, C. E.; Kellermann, M.; Hirsch, A. *Cryst. Growth Des.* **2006**, *6*, 1120.
(186) Volkmer, D.; Fricke, M.; Agena, C.; Mattay, J. *J. Mater. Chem.* **2004**, *14*, 2249.
(187) Xu, A. W.; Ma, Y.; Cölfen, H. *J. Mater. Chem.* **2007**, *17*, 415.
(188) Mitchell, C. A.; Yu, L.; Ward, M. D. *J. Am. Chem. Soc.* **2001**, *123*, 10830.
(189) Kuther, J.; Nelles, G.; Seshadri, R.; Schaub, M.; Butt, H. J.; Tremel, W. *Chem.—Eur. J.* **1998**, *4*, 1834.
(190) Kim, I. W.; Collino, S.; Morse, D. E.; Evans, J. S. *Cryst. Growth Des.* **2006**, *6*, 1078.
(191) Collino, S.; Kim, I. W.; Evans, J. S. *Cryst. Growth Des.* **2006**, *6*, 839.
(192) Balz, M.; Barriau, E.; Istratov, V.; Frey, H.; Tremel, W. *Langmuir* **2005**, *21*, 3987.
(193) Sato, K.; Boistelle, R. *J. Cryst. Growth* **1984**, *66*, 441.
(194) Boistelle, R.; Abbona, F.; Madsen, H. E. L. *Phys. Chem. Mineral.* **1983**, *9*, 216.
(195) Kitamura, M.; Furukawa, H.; Asaeda, M. *J. Cryst. Growth* **1994**, *141*, 193.
(196) Suzuki, M.; Ogaki, T.; Sato, K. *J. Am. Oil Chem. Soc.* **1985**, *62*, 1600.
(197) Peric, J.; Vucak, M.; Krstulovic, R.; Brecevic, L.; Kralj, D. *Thermochim. Acta* **1996**, *277*, 175.
(198) Wolf, G.; Gunther, C. *J. Therm. Anal. Calorim.* **2001**, *65*, 687.
(199) Gunther, C.; Becker, A.; Wolf, G.; Epple, M. *Z. Anorg. Allg. Chem.* **2005**, *631*, 2830.
(200) Nebel, H.; Epple, M. *Z. Anorg. Allg. Chem.* **2008**, *634*, 1439.
(201) Kotachi, A.; Miura, T.; Imai, H. *Cryst. Growth Des.* **2006**, *6*, 1636.
(202) Naka, K.; Keum, D. K.; Tanaka, Y.; Chujo, Y. *Chem. Commun.* **2000**, 1537.
(203) Xu, A. W.; Dong, W. F.; Antonietti, M.; Colfen, H. *Adv. Funct. Mater.* **2008**, *18*, 1307.
(204) Rieger, J. *Tenside, Surfactants, Deterg.* **2002**, *39*, 221.
(205) Qi, L.; Cölfen, H.; Antonietti, M.; Li, M.; Hopwood, J. D.; Ashley, A. J.; Mann, S. *Chem.—Eur. J.* **2001**, *7*, 3526.
(206) Decker, G. L.; Morrill, J. B.; Lennarz, W. J. *Development* **1987**, *101*, 297.
(207) Yu, S. H.; Cölfen, H. *J. Mater. Chem.* **2004**, *14*, 2124.
(208) Towe, K. M.; Lowenstam, H. A. *J. Ultrastruct. Res.* **2005**, *17*, 1.
(209) Mann, S. In *Magnetite Biomineralization and Magnetoreception in Organisms*; Kirschvink, J. L., Jones, D. S., MacFadden, B. J., Eds.; Plenum Press: New York, 1985; p 311.
(210) Meibom, A.; Cuif, J.-P.; Hillion, F.; Constantz, B. R.; Juillet-Leclerc, A.; Dauphin, Y.; Watanabe, T.; Dunbar, R. B. *Geophys. Res. Let.* **2004**, *31*, L23306.
(211) Dillaman, R.; Hequembourg, S.; Gay, M. *J. Morphol.* **2005**, *263*, 356.
(212) Walsh, D.; Lebeau, B.; Mann, S. *Adv. Mater.* **1999**, *11*, 324.
(213) Rudloff, J.; Antonietti, M.; Cölfen, H.; Pretula, J.; Kaluzynski, K.; Penczek, S. *Macromol. Chem. Phys.* **2002**, *203*, 627.
(214) Rudloff, J.; Cölfen, H. *Langmuir* **2004**, *20*, 991.
(215) Pan, Y.; Zhao, X.; Guo, Y. P.; Lv, X. T.; Ren, S. X.; Yuan, M. R.; Wang, Z. C. *Mater. Lett.* **2007**, *61*, 2810.
(216) Kuznetsov, Y. G.; Malkin, A. J.; McPherson, A. *J. Cryst. Growth* **2001**, *232*, 30.
(217) Brooks, R.; Clark, L. M.; Thurston, E. F. *Philos. Trans. R. Soc. London, Ser. A* **1950**, *243*, 145.
(218) von Lengyel, E. *Z. Kristallogr. Mineral.* **1937**, *97*, 67.
(219) Hunt, T. S. *Am. J. Sci.* **1866**, *XLII*, 49.
(220) Gower, L. B.; Odom, D. J. *J. Cryst. Growth* **2000**, *210*, 719.
(221) Olszta, M. J.; Odom, D. J.; Douglas, E. P.; Gower, L. B. *Connect. Tissue Res.* **2003**, *44*, 326.
(222) Cheng, X. G.; Varona, P. L.; Olszta, M. J.; Gower, L. B. *J. Cryst. Growth* **2007**, *307*, 395.
(223) Volkmer, D.; Harms, M.; Gower, L. B.; Ziegler, A. *Angew. Chem., Int. Ed.* **2005**, *44*, 639.
(224) Kim, Y. Y.; Douglas, E. P.; Gower, L. B. *Langmuir* **2007**, *23*, 4862.
(225) Amos, F. F.; Sharbaugh, D. M.; Talham, D. R.; Gower, L. B.; Fricke, M.; Volkmer, D. *Langmuir* **2007**, *23*, 1988.
(226) Patel, V. M.; Sheth, P.; Kurtz, A.; Ossenbeck, M.; Shah, D. O.; Gower, L. B. In *Concentrated Dispersions: Theory, Experiments, and Applications*; Somansundaran, P., Markovic, B., Eds.; ACS Symposium Series 878; American Chemical Society: Washington, DC, 2004.
(227) Olszta, M. J.; Douglas, E. P.; Gower, L. B. *Calc. Tissue Int.* **2003**, *72*, 583.
(228) Balz, M.; Therese, H. A.; Li, J. X.; Gutmann, J. S.; Kappl, M.; Nasdala, L.; Hofmeister, W.; Butt, H. J.; Tremel, W. *Adv. Funct. Mater.* **2005**, *15*, 683.
(229) Loges, N.; Graf, K.; Nasdala, L.; Tremel, W. *Langmuir* **2006**, *22*, 3073.
(230) Han, J. T.; Xu, X. R.; Cho, K. W. *J. Cryst. Growth* **2007**, *308*, 110.
(231) Lowenstam, H. A.; Weiner, S. *On Biomineralization*; Oxford University Press: New York, 1989.
(232) Weiner, S.; Addadi, L. *J. Mater. Chem.* **1997**, *7*, 689.
(233) Bäuerlein, E. *Angew. Chem., Int. Ed.* **2003**, *42*, 614.
(234) Park, R. J.; Meldrum, F. C. *J. Mater. Chem.* **2004**, *14*, 2291.
(235) Hunter, G. K. *Curr. Opin. Solid State Int. Sci.* **1996**, *1*, 430.
(236) Travaille, A. M.; Donners, J. J. J. M.; Gerritsen, J. W.; Sommerdijk, N. A. J. M.; Nolte, R. J. M.; van Kempen, H. *Adv. Mater.* **2002**, *14*, 492.
(237) Aizenberg, J.; Black, A. J.; Whitesides, G. M. *Nature* **1999**, *397*, 4500.
(238) Berman, A.; Ahn, D. J.; Lio, A.; Salmeron, M.; Reichert, A.; Charych, D. *Science* **1995**, *269*, 515.

(239) Travaille, A. M.; Kaptijn, L.; Verwer, P.; Hulsken, B.; Elemans, J. A. A. W.; Nolte, R. J. M.; van Kempen, H. *J. Am. Chem. Soc.* **2003**, *125*, 11571.
(240) Wheeler, A. P.; George, J. W.; Evans, C. R. *Science* **1981**, *212*, 1397.
(241) Wheeler, A. P.; Sikes, C. S. *Am. Zool.* **1984**, *24*, 933.
(242) Wheeler, A. P.; Low, K. C.; Sikes, S. In *Surface Reactive Peptides and Polymers*; Sikes, S., Wheeler, A. P., Eds.; American Chemical Society: Washington, DC, 1991; Vol. 444, p 72.
(243) Campbell, A. A.; Ebrahimpour, A.; Perez, L.; Smesko, S. A.; Nancollas, G. H. *Calcif. Tissue Int.* **1989**, *45*, 122.
(244) Albeck, S.; Addadi, L.; Weiner, S. *Connect. Tissue Res.* **1996**, *35*, 419.
(245) Albeck, S.; Weiner, S.; Addadi, L. *Chem.—Eur. J.* **1996**, *2*, 278.
(246) Albeck, S.; Aizenberg, J.; Addadi, L.; Weiner, S. *J. Am. Chem. Soc.* **1993**, *115*, 11691.
(247) Fu, G.; Qiu, S. R.; Orme, C. A.; Morse, D. E.; De Yoreo, J. J. *Adv. Mater.* **2005**, *17*, 2678.
(248) Aizenberg, J.; Albeck, S.; Weiner, S.; Addadi, L. *J. Cryst. Growth* **1994**, *142*, 156.
(249) Fu, G.; Valiyaveettil, S.; Wopenka, B.; Morse, D. E. *Biomacromolecules* **2005**, *6*, 1289.
(250) Pokroy, B.; Zolotoyabko, E.; Adir, N. *Biomacromolecules* **2006**, *7*, 550.
(251) Gotliv, B.-A.; Addadi, L.; Weiner, S. *ChemBioChem* **2003**, *4*, 522.
(252) Gotliv, B.-A.; Kessler, N.; Sumerel, J. L.; Morse, D. E.; Tuross, N.; Addadi, L.; Weiner, S. *ChemBioChem* **2005**, *6*, 304.
(253) Livingston, B. T.; Killian, C. E.; Wilt, F.; Cameron, A.; Landrum, M. J.; Ermolaeva, O.; Sapojnikov, V.; Maglott, D. R.; Buchanan, A. M.; Ettensohn, C. A. *Dev. Biol.* **2006**, *300*, 335.
(254) Marin, F.; Luquet, G. *C. R. Palevol* **2004**, *3*, 469.
(255) Zhang, C.; Zhang, R. *Marine Biotechnol.* **2006**, *8*, 572.
(256) Sollner, C.; Burghammer, M.; Busch-Nentwich, E.; Berger, J.; Schwarz, H.; Riekel, C.; Nicolson, T. *Science* **2003**, *302*, 282.
(257) Weiner, S.; Hood, L. *Science* **1975**, *190*, 987.
(258) Addadi, L.; Moradian, J.; Shay, E.; Maroudas, N. G.; Weiner, S. *Proc. Natl. Acad. Sci. U.S.A.* **1987**, *84*, 2732.
(259) Aizenberg, J.; Lambert, G.; Weiner, S.; Addadi, L. *J. Am. Chem. Soc.* **2002**, *124*, 32.
(260) Kröger, N.; Deutzmann, R.; Bergsdorf, C.; Sumper, M. *Proc. Natl. Acad. Sci. U.S.A.* **2000**, *97*, 14133.
(261) Kröger, N.; Lorenz, S.; Brunner, E.; Sumper, M. *Science* **2002**, *298*, 584.
(262) Sumper, M.; Lehmann, G. *ChemBioChem* **2006**, *7*, 1419.
(263) Sumper, M.; Kroger, N. *J. Mater. Chem.* **2004**, *14*, 2059.
(264) Perry, C. C.; Keeling-Tucker, T. *Colloid Polym. Sci.* **2003**, *281*, 652.
(265) Cha, J. N.; Shimizu, K; Zhou, Y.; Christiansen, S. C.; Chmelka, B. F.; Stucky, G. D.; Morse, D. E. *Proc. Natl. Acad. Sci. U.S.A.* **1999**, *96*, 361.
(266) Shimizu, K.; Cha, J. N.; Stucky, G. D.; Morse, D. E. *Proc. Natl. Acad. Sci. U.S.A.* **1998**, *95*, 6234.
(267) Kröger, N.; Deutzmann, R.; Sumper, M. *Science* **1999**, *286*, 1129.
(268) Kröger, N.; Deutzmann, R.; Bergsdorf, C.; Sumper, M. *J. Biol. Chem.* **2001**, *276*, 26066.
(269) Sumper, M.; Brunner, E. *Adv. Funct. Mater.* **2006**, *16*, 17.
(270) Poulsen, N.; Sumper, M.; Kröger, N. *Proc. Natl. Acad. Sci. U.S.A.* **2003**, *100*, 12075.
(271) Sumper, M.; Lorenz, S.; Brunner, E. *Angew. Chem., Int. Ed.* **2003**, *42*, 5192.
(272) Chasteen, N. D.; Harrison, P. M. *J. Struct. Biol.* **1999**, *126*, 182.
(273) Harrison, P. M.; Arosio, P. *Biochim. Biophys. Acta Bioenergy* **1996**, *1275*, 161.
(274) Towe, K. M.; Lowenstam, H. A. *J. Ultrastruct. Res.* **1967**, *17*, 1.
(275) Levi, Y.; Albeck, S.; Brack, A.; Weiner, S.; Addadi, L. *Chem.—Eur. J.* **1998**, *4*, 389.
(276) Politi, Y.; Levi-Kalisman, Y.; Raz, S.; Wilt, F. H.; Addadi, L.; Weiner, S.; Sagi, I. *Adv. Funct. Mater.* **2006**, *16*, 1289.
(277) Becker, A.; Ziegler, A.; Epple, M. *J. Chem. Soc., Dalton Trans.* **2005**, *10*, 1814.
(278) Becker, A.; Bismayer, U.; Epple, M.; Fabritius, H.; Hasses, B.; Shi, J.; Ziegler, A. *J. Chem. Soc., Dalton Trans.* **2003**,
(279) Levi-Kalisman, Y.; Raz, S.; Weiner, S.; Addadi, L.; Sagi, I. *J. Chem. Soc., Dalton Trans.* **2000**, *21*, 3977.
(280) Kwak, S. Y.; DiMasi, E.; Han, Y. J.; Aizenberg, J.; Kuzmenko, I. *Cryst. Growth Des.* **2005**, *5*, 2139.
(281) Han, Y.; Aizenberg, J. *J. Am. Chem. Soc.* **2003**, *125*, 4032.
(282) Han, Y. J.; Wysocki, L. M.; Thanawala, M. S.; Siegrist, T.; Aizenberg, J. *Angew. Chem., Int. Ed.* **2005**, *44*, 2386.
(283) Volkmer, D.; Fricke, M.; Gleiche, M.; Chi, L. F. *Mater. Sci. Eng., C* **2005**, *25*, 161.
(284) Fricke, M.; Volkmer, D. *Top. Curr. Chem.* **2007**, *270*, 1.
(285) Weiner, S.; Traub, W. *Philos. Trans. R. Soc. London, Ser. B* **1984**, *304*, 425.
(286) Weiner, S.; Traub, W. *FEBS Lett.* **1980**, *111*, 311.
(287) Checa, A. G.; Rodriguez-Navarro, A. B. *Biomaterials* **2005**, *26*, 1071.
(288) Checa, A. G.; Okamoto, T.; Ramirez, J. *Proc. R. Soc. London, Ser. B* **2006**, *273*, 1329.
(289) Raup, D. *The endoskeleton*; J. Wiley & Sons, Interscience: New York, 1966.
(290) Berman, A.; Hanson, J.; Leiserowitz, L.; Koetzle, T. F.; Weiner, S.; Addadi, L. *Science* **1993**, *259*, 776.
(291) Dutour Sikiric, M.; Furedi-Milhofer, H. *Adv. Colloid Interface Sci.* **2006**, *128−130*, 135.
(292) Aizenberg, J.; Hanson, J.; Ilan, M.; Leiserowitz, L.; Koetzle, T. F.; Addadi, L.; Weiner, S *FASEB J.* **1995**, *9*, 262.
(293) Weiner, S.; Addadi, L.; Wagner, H. D. *Mater. Sci. Eng., C* **2000**, *11*, 1.
(294) Young, J. R.; Henriksen, K. In *Reviews in Mineralogy and Geochemistry: Biomineralization*; Dove, P. M., De Yoreo, J. J., Weiner, S., Eds.; Mineralogical Society of America: Washington, DC, 2003; Vol. 54, p 189.
(295) Park, R. J.; Meldrum, F. C. *Adv. Mater.* **2002**, *14*, 1167.
(296) Yue, W. B.; Kulak, A. N.; Meldrum, F. C. *J. Mater. Chem.* **2006**, *16*, 408.
(297) Wucher, B.; Yue, W.; Kulak, A. N.; Meldrum, F. C. *Chem. Mater.* **2007**, *19*, 1111.
(298) Raz, S.; Hamilton, P. C.; Wilt, F. H.; Weiner, S.; Addadi, L. *Adv. Funct. Mater.* **2003**, 13.
(299) Addadi, L.; Weiner, S. *Proc. Natl. Acad. Sci. U.S.A.* **1985**, *82*, 4110.
(300) De Yoreo, J. J.; Wierzbicki, A.; Dove, P. M. *CrystEngComm* **2007**, *9*, 1144.
(301) Teng, H. H.; Dove, P. M.; Orme, C. A.; De Yoreo, J. J. *Science* **1998**, *282*, 724.
(302) Berman, A.; Addadi, L.; Weiner, S. *Nature* **1988**, *331*, 546.
(303) Orme, C. A.; Noy, A.; Wierzbicki, A.; McBride, M. T.; Grantham, M.; Teng, H. H.; Dove, P. M.; DeYoreo, J. J. *Nature* **2001**, *411*, 775.
(304) Aizenberg, J.; Ilan, N.; Weiner, S.; Addadi, L. *Connect. Tissue Res.* **1996**, *35*, 17.
(305) Berman, A.; Hanson, J.; Leiserowitz, L.; Koetzle, T.; Weiner, S.; Addadi, L. *J. Phys. Chem.* **1993**, *97*, 5162.
(306) Treccani, L.; Mann, K.; Heinemann, F.; Fritz, M *Biophys. J.* **2006**, *91*, 2601.
(307) Elhadj, S.; De Yoreo, J. J.; Hoyer, J. R.; Dove, P. M. *Proc. Natl. Acad. Sci. U.S.A.* **2006**, *103*, 19237.
(308) Elhadj, S.; Salter, E. A.; Wierzbicki, A.; De Yoreo, J. J.; Han, N.; Dove, P. M. *Cryst. Growth Des.* **2006**, *6*, 197.
(309) van der Leeden, M. C.; Kashchiev, D.; van Rosmalen, G. M. *J. Cryst. Growth* **1993**, *130*, 221.
(310) Meldrum, F. C.; Hyde, S. T. *J. Cryst. Growth* **2001**, *231*, 544.
(311) Falini, G.; Fermani, S.; Gazzano, M.; Ripamonti, A. *J. Mater. Chem.* **1998**, *8*, 1061.
(312) Goldsmith, J. R.; Graf, D. L.; Joensuu, O. I. *Geochim. Cosmochim. Acta* **1955**, *7*, 212.
(313) Chave, K. E. *J. Geol.* **1954**, *62*, 266.
(314) Weber, J. N. *J. Geol.* **1973**, *81*, 543.
(315) Bischoff, W. D.; Mackenzie, F. T.; Bishop, F. C. *Geochim. Cosmochim. Acta* **1987**, *51*, 1413.
(316) Lippmann, F. *Sedimentary Carbonate Minerals*; Springer Verlag: Berlin, 1973.
(317) Mucci, A.; Morse, J. W. *Geochim. Cosmochim. Acta* **1983**, *47*, 217.
(318) Katz, A. *Geochim. Cosmochim. Acta* **1973**, *37*, 1563.
(319) Reddy, M. M.; Nancollas, G. H. *J. Cryst. Growth* **1976**, *35*, 33.
(320) Reddy, M. M.; Wang, K. K. *J. Cryst. Growth* **1980**, *50*, 470. 1980.
(321) Falini, G.; Fermani, S.; Gazzano, M.; Ripamonti, A. *Chem.—Eur. J.* **1997**, *3*, 1807.
(322) Berner, R. A. *Geochim. Cosmochim. Acta* **1975**, *39*, 489.
(323) Fernandez-Diaz, L.; Putnis, A.; Prieto, M.; Putnis, C. V. *J. Sediment. Res.* **1996**, *66*, 482.
(324) Nancollas, G. H.; K, S. *J. Petrol. Technol.* **1982**, *34*, 645.
(325) Loste, E.; Wilson, R. M.; Seshadri, R.; Meldrum, F. C. *J. Cryst. Growth* **2003**, *254*, 206.
(326) Gayathri, S.; Lakshminarayanan, R.; Weaver, J. C.; Morse, D. E.; Kini, R. M.; Valiyaveettil, S. *Chem.—Eur. J.* **2007**, *13*, 3262.
(327) Folk, R. L. *J. Sediment. Petrol.* **1974**, *44*, 40.
(328) Davis, K. J.; Dove, P. M.; Wasylenki, L. E.; De Yoreo, J. J. *Am. Mineral.* **2004**, *89*, 714.
(329) Kralj, D.; Kontrec, J.; Brecevic, L.; Falini, G.; Nothig-Laslo, V. *Chem.—Eur. J.* **2004**, *10*, 1647.
(330) Bazylinski, D. A.; Frankel, R. B. *Nature Rev. Microbiol.* **2004**, *2*, 217.
(331) Bazylinski, D. A.; Frankel, R. B.; Konhauser, K. O *Geomicrobiol. J.* **2007**, *24*, 465.
(332) Komeili, A. *Annu. Rev. Biochem.* **2007**, *76*, 351.
(333) Mann, S.; Sparks, N. H. C.; Blakemore, R. P. *Proc. R. Soc. London, Ser. B* **1987**, *231*, 477.

(334) Meldrum, F. C.; Heywood, B. R.; Mann, S.; Frankel, R. B.; Bazylinski, D. A. *Proc. R. Soc. London, Ser. B* **1993**, *251*, 237.
(335) Devouard, B.; Posfai, M.; Hua, X.; Bazylinski, D. A.; Frankel, R. B.; Buseck, P. R. *Am. Mineral.* **1998**, *83*, 1387.
(336) Buseck, P. R.; Dunin-Borkowski, R. E.; Devouard, B.; Frankel, R. B.; McCartney, M. R.; Midgley, P. A.; Posfai, M.; Weyland, M. *Proc. Natl. Acad. Sci. U.S.A.* **2001**, *98*, 13490.
(337) Komeili, A.; Li, Z.; Newman, D. K.; Jensen, G. J. *Science* **2006**, *311*, 242.
(338) Frankel, R. B.; Papaefthymiou, G. C.; Blakemore, R. P.; O'Brien, W. *Biochim. Biophys. Acta* **1983**, *763*, 147.
(339) Mann, S.; Frankel, R. B.; Blakemore, R. P. *Nature* **1984**, *310*, 405.
(340) Schüler, D.; Bäuerlein, E. *J. Bacteriol.* **1998**, *180*, 159.
(341) Schüler, D.; Frankel, R. B. *Appl. Microbiol. Biotechnol.* **1999**, *52*, 464.
(342) Young, J. R.; Davis, S. A.; Brown, P. R.; Mann, S. *J. Struct. Biol.* **1999**, *126*, 195.
(343) Mann, S.; Sparks, N. H. C. *Proc. R. Soc. London, Ser. B* **1988**, *234*, 441.
(344) Didymus, J. M.; Young, J. R.; Mann, S. *Proc. R. Soc. London, Ser. B* **1994**, *258*, 237.
(345) Westbroek, P.; van der Wal, P.; van Emberg, P. R.; de Vrind-de Jong, E. W.; de Bruijn, W. C. In *Biomineralization in Lower Plants and Animals*; Leadbeater, B. S. C., Riding, R., Eds.; Clarendon Press: Oxford, U.K., 1986; Vol. 304, p 189.
(346) Westbroek, P.; de Jong, E. W.; van der Wal, P.; de Vrind, J. P. M.; Kok, D.; de Bruijn, W. C.; Parker, S. B. *Philos. Trans. R. Soc. London, Ser. B* **1984**, *304*, 435.
(347) Marsh, M. E. *Protoplasma* **1994**, *177*, 108.
(348) Pautard, F. G. E. In *Biological Calcification*; Schraer, H., Ed.; Appleton-Century-Crofts: New York, 1970; p 105.
(349) Smith, A. B. *Spec. Pap.—Palaeontol.* **1980**, *25*, 1.
(350) Sethmann, I.; Putnis, A.; Grassmann, O.; Lobmann, P. *Am. Mineral.* **2005**, *90*, 1213.
(351) Hyde, S. T.; Andersson, S.; Larsson, K.; Blum, Z.; Landh, T.; Lidin, S.; Ninham, B. W. *The Language of Shape*; Elsevier Science B.V.: Amsterdam, The Netherlands, 1997.
(352) Klinowski, J.; Mackay, A. L.; Terrones, H. *Philos. Trans. R. Soc. London, Ser. A* **1996**, *354*, 1975.
(353) Lai, M.; Kulak, A. N.; Law, D.; Zhang, Z. B.; Meldrum, F. C.; Riley, D. J. *Chem. Commun.* **2007**, *34*, 3547.
(354) Wilt, F. H. *Zool. Sci.* **2002**, *19*, 253.
(355) Chateigner, D.; Hedegaard, C.; Wenk, H.-R. *J. Struct. Geol.* **2000**, *22*, 1723.
(356) Cartwright, J. H. E.; Checa, A. G. J. R. *Soc. Interface* **2006**, *4*, 491.
(357) Levi-Kalisman, Y.; Falini, G.; Addadi, L.; Weiner, S. *J. Struct. Biol.* **2001**, *135*, 8.
(358) Nudelman, F.; Gotliv, B. A.; Addadi, L.; Weiner, S. *J. Struct. Biol.* **2006**, *153*, 176.
(359) Nassif, N.; Gehrke, N.; Pinna, N.; Shirshova, N.; Tauer, K.; Antonietti, M.; Cölfen, H. *Angew. Chem., Int. Ed.* **2005**, *44*, 6004.
(360) Rousseau, M.; Lopez, E.; Coute, A.; Mascarel, G.; Smith, D. C.; Naslain, R.; Bourrat, X. *J. Struct. Biol.* **2005**, *149*, 149.
(361) Nudelman, F.; Chen, H. H.; Goldberg, H. A.; Weiner, S.; Addadi, L. *Faraday Discuss.* **2007**, *136*, 9.
(362) Weiner, S. *CRC Crit. Rev. Biochem.* **1986**, *20*, 365.
(363) Hemleben, C. H.; Anderson, O. R.; Berthold, W.; Spindler, M. In *Biomineralization in Lower Plants and Animals*; Leadbeater, B. S. C., Riding, R., Eds.; Clarendon Press: Oxford, U.K., 1986; Vol. 30, p 237.
(364) Debenay, J. P.; Guillou, J. J.; Geslin, E.; Lesourd, M. *Micropaleontology* **2000**, *46*, 87.
(365) Towe, K. M.; Cifelli, R. *J. Palaeontol.* **1967**, *41*, 742.
(366) Bentov, S.; Erez, J. *Geol.* **2005**, *33*, 841.
(367) Towe, K. M.; Berthold, W.-U.; Appleman, D. E. *J. Foraminiferal Res.* **1977**, *7*, 58.
(368) Murray, J. W. *Palaeontol. Electronica* **2003**, *5*, 31.
(369) Grassmann, O.; Neder, R. B.; Putnis, A.; Löbmann, P. *Am. Mineral.* **2003**, *88*, 647.
(370) Grassmann, O.; Müller, G.; Löbmann, P. *Chem. Mater.* **2002**, *14*, 4530.
(371) Löbmann, P. *Curr. Nanosci.* **2007**, *3*, 306.
(372) Hildebrand, M.; Wetherbee, R. In *Silicon biomineralization: Biology, biochemistry, molecular biology, biotechnology*; Müller, W. E. G., Ed.; Springer: Berlin, 2003; Vol. 33, p 11.
(373) Blake, D. F.; Peacor, D. R.; Allard, L. F. *Micron. Microsc. Acta* **1984**, *15*, 85.
(374) Crawford, R. M.; Schmid, A. M. In *Biomineralization in lower plants and animals*; Leadbeater, B. S., Riding, R., Eds.; Oxford University Press: Oxford, U.K., 1986; p 291.
(375) Schmid, A.-M. M.; Volcani, B. E. *J. Phycol.* **1983**, *19*, 387.
(376) Brunner, E.; Lutz, K.; Sumper, M. *Phys. Chem. Chem. Phys.* **2004**, *6*, 854.
(377) Mann, S.; Heywood, B. R. *Biomimetic Materials Chemistry*; VCH Publishers: New York, 1996.
(378) Cölfen, H.; Yu, S. H. *MRS Bull.* **2005**, *30*, 727.
(379) Jones, W.; Rao, C. N. R. *Supramolecular Organization and Materials Design*; Cambridge University Press: Cambridge, U.K., 2002.
(380) Antonietti, M.; Göltner, C. *Angew. Chem., Int. Ed.* **1997**, *36*, 910.
(381) Dabbs, D. M.; Aksay, I. A. *Annu. Rev. Phys. Chem.* **2000**, *51*, 601.
(382) Archibald, D. D.; Mann, S. *Nature* **1993**, *364*, 430.
(383) Yang, H.; Coombs, N.; Ozin, G. A. *Nature* **1997**, *386*, 692.
(384) Li, M.; Schnablegger, H.; Mann, S. *Nature* **1999**, *402*, 393.
(385) Estroff, L. A.; Hamilton, A. D. *Chem. Mater.* **2001**, *13*, 3227.
(386) Aizenberg, J. *Adv. Mater.* **2004**, *16*, 1295.
(387) Mann, S. *Nature* **1993**, *365*, 499.
(388) Davis, S. A.; Breulmann, M.; Rhodes, K. H.; Zhang, B.; Mann, S. *Chem. Mater.* **2001**, *13*, 3218.
(389) Cölfen, H. *Curr. Opin. Colloid Interface Sci.* **2003**, *8*, 23.
(390) Meldrum, F. C. *Int. Mater. Rev.* **2003**, *48*, 187.
(391) Garnweitner, G.; Niederberger, M. *J. Am. Ceram. Soc.* **2006**, *89*, 1801.
(392) Cölfen, H. *Top. Curr. Chem.* **2007**, *270*, 1.
(393) Imai, H.; Oaki, Y.; Kotachi, A. *Bull. Chem. Soc. Jpn.* **2006**, *79*, 1834.
(394) Sikiric, M. D.; Furedi-Milhofer, H. *Adv. Colloid Interface Sci.* **2006**, *128*, 135.
(395) Stoneham, M. *Rep. Prog. Phys.* **2007**, *70*, 1055.
(396) Antonietti, M.; Niederberger, M.; Smarsly, B. *J. Chem. Soc., Dalton Trans.* **2008**, 18.
(397) Sotiropoulou, S.; Sierra-Sastre, Y.; Mark, S. S.; Batt, C. A. *Chem. Mater.* **2008**, *20*, 821.
(398) Imai, H. In *Biomineralization I: Crystallization and Self-Organization Process*; Naka, K., Ed.; Springer: Berlin, 2007; Vol. 270, p 43.
(399) Azoury, R.; Randolph, A. D.; Drach, G. W.; Perlberg, S.; Garti, N.; Sarig, S. *J. Cryst. Growth* **1983**, *64*, 389.
(400) Kitano, Y.; Hood, D. W. *Geochim. Cosmochim. Acta* **1965**, *29*, 29.
(401) Weissbuch, I.; Popovitz-Biro, R.; Leiserowitz, L.; Lahav, M. *Lock and Key Processes at Crystalline Interfaces: Relevance to the Spontaneous Generation of Chirality*; John Wiley & Sons Ltd: New York, 1994.
(402) Didymus, J. M.; Oliver, P.; Mann, S. *J. Chem. Soc., Faraday Trans.* **1993**, *89* (15), 2891.
(403) Tian, Z. R.; Voigt, J. A.; Liu, J.; Mckenzie, B.; Mcdermott, M. J. *J. Am. Chem. Soc.* **2002**, *124*, 12954.
(404) Tian, Z. R.; Voigt, J. A.; Liu, J.; Mckenzie, B.; Mcdermott, M. J.; Rodriguez, M. A.; Konishi, H.; Xu, H. F *Nat. Mater.* **2003**, *2*, 821.
(405) Mann, S.; Didymus, J. M.; Sanderson, N. P.; Heywood, B. R.; Samper, E. J. A. *J. Chem. Soc., Faraday Trans.* **1990**, *86*, 1873.
(406) Mao, Z. F.; Huang, J. H. *J. Solid State Chem.* **2007**, *180*, 453.
(407) Altay, E.; Shahwan, T.; Tanoglu, M. *Powder Technol.* **2007**, *178*, 194.
(408) Kahr, B.; Gurney, R. W. *Chem. Rev.* **2001**, *101*, 893.
(409) Gaubert, P. *Bull. Soc. Mineral. France* **1905**, *28*, 286.
(410) Gaubert, P. *C. R. Hebd. Seances Acad. Sci.* **1910**, *151*, 1134.
(411) Bastin, L. D.; Kahr, B. *Tetrahedron* **2000**, *56*, 6633.
(412) Addadi, L.; Weiner, S. *Mol. Cryst. Liq. Cryst.* **1986**, *134*, 305.
(413) DeOliveira, D. B.; Laursen, R. A. *J. Am. Chem. Soc.* **1997**, *119*, 10627.
(414) Ilan, M.; Aizenberg, J.; Gilor, O. *Proc. R. Soc. London, Ser. B* **1996**, *263*, 133.
(415) Wolf, S. E.; Loges, N.; Mathiasch, B.; Panthofer, M.; Mey, I.; Janshoff, A.; Tremel, W. *Angew. Chem., Int. Ed.* **2007**, *46*, 5618.
(416) Kuang, D. B.; Xu, A. W.; Fang, Y. P.; Ou, H. D.; Liu, H. Q. *J. Cryst. Growth* **2002**, *244*, 379.
(417) Titiloye, J. O.; Parker, S. C.; Mann, S. *J. Cryst. Growth* **1993**, *131*, 533.
(418) Munoz-Espi, R.; Qi, Y.; Lieberwirth, I.; Gomez, C. M.; Wegner, G. *Chem.—Eur. J.* **2005**, *12*, 118.
(419) Cölfen, H. In *Macromolecular Engineering. Precise Synthesis, Materials Properties, Applications*; Matyjaszewski, K., Gnanou, Y., Leibler, L., Eds.; Wiley-VCH: Weinheim, Germany, 2007; Vol. 4, p 2597.
(420) Yu, S. H.; Cölfen, H.; Mastai, Y. *J. Nanosci. Nanotechnol.* **2004**, *4*, 291.
(421) Taubert, A.; Palms, D.; Weiss, O.; Piccini, M. T.; Batchelder, D. N. *Chem. Mater.* **2002**, *14*, 2594.
(422) Öner, M.; Norwig, J.; Meyer, W. H.; Wegner, G. *Chem. Mater.* **1998**, *10*, 460.
(423) Taubert, A.; Glasser, G.; Palms, D. *Langmuir* **2002**, *18*, 4488.
(424) Kaluzynski, K.; Pretula, J.; Lapienis, G.; Basko, M.; Bartczak, Z.; Dworak, A.; Penczek, S. *J. Polym. Sci., Part A: Polym. Chem.* **2001**, *39*, 955.
(425) Cölfen, H.; Qi, L. M.; Mastai, Y.; Börger, L. *Cryst. Growth Des.* **2002**, *2*, 191.
(426) Ofir, P. B. Y.; Govrin-Lippman, R.; Garti, N.; Furedi-Milhofer, H. *Cryst. Growth Des.* **2004**, *4*, 177.

(427) Chen, S. F.; Yu, S. H.; Wang, T. X.; Jiang, J.; Cölfen, H.; Hu, B.; Yu, B. *Adv. Mater.* **2005**, *17*, 1461.
(428) Yu, Q.; Ou, H. D.; Song, R. Q.; Xu, A. W. *J. Cryst. Growth* **2006**, *286*, 178.
(429) Wang, T.; Cölfen, H.; Antonietti, M. *J. Am. Chem. Soc.* **2005**, *127*, 3246.
(430) Oaki, Y.; Imai, H. *Chem. Commun.* **2005**, 6011.
(431) Oaki, Y.; Imai, H. *Adv. Funct. Mater.* **2005**, *15*, 1407.
(432) Sugawara, A.; Nishimura, T.; Yamamoto, Y.; Inoue, H.; Nagasawa, H.; Kato, T. *Angew. Chem., Int. Ed.* **2006**, *45*, 2876.
(433) Kotachi, A.; Miura, T.; Imai, H. *Chem. Mater.* **2004**, *16*, 3191.
(434) Li, M.; Mann, S. *Langmuir* **2000**, *16*, 7088.
(435) Qi, L.; Cölfen, H.; Antonietti, M. *Chem. Mater.* **2000**, *12*, 2392.
(436) Yu, S.-H.; Cölfen, H.; Antonietti, M. *Chem.—Eur. J.* **2002**, *8*, 2937.
(437) Qi, L.; Cölfen, H.; Antonietti, M. *Angew. Chem., Int. Ed.* **2000**, *39*, 604.
(438) Yu, S. H.; Antonietti, M.; Cölfen, H.; Hartmann, J. *Nano Lett.* **2003**, *3*, 379.
(439) Li, M.; Cölfen, H.; Mann, S. *J. Mater. Chem.* **2004**, *14*, 2269.
(440) Yu, S.-H.; Cölfen, H.; Antonietti, M. *Adv. Mater.* **2003**, *15*, 133.
(441) Rodriguez-Navarro, C.; Jimenez-Lopez, C.; Rodriguez-Navarro, A.; Gonzalez-Munoz, M. T.; Rodriguez-Gallego, M. *Geochim. Cosmochim. Acta* **2007**, *71*, 1197.
(442) Loste, E.; Diaz-Marti, E.; Zarbakhsh, A.; Meldrum, F. C. *Langmuir* **2003**, *19*, 2830.
(443) Aizenberg, J. *J. Chem. Soc., Dalton Trans.* **2000**, 3963.
(444) Pokroy, B.; Aizenberg, J. *CrystEngComm* **2007**, *9*, 1219.
(445) Meldrum, F. C.; Ludwigs, S. *Macromol. Biosci.* **2007**, *7*, 152.
(446) Hetherington, N. B. J.; Kulak, A. N.; Sheard, K.; Meldrum, F. C. *Langmuir* **2006**, *22*, 1955.
(447) Ludwigs, S.; Steiner, U.; Kulak, A. N.; Lam, R.; Meldrum, F. C. *Adv. Mater.* **2006**, *18*, 2270.
(448) Cölfen, H. *Angew. Chem., Int. Ed.* **2008**, *47*, 2351.
(449) Murayama, E.; Takagi, Y.; Ohira, T.; Davis, J. G.; Greene, M. I.; Nagasawa, H. *Eur. J. Biochem.* **2002**, *269*, 688.
(450) Moradian-Oldak, J. *Matrix Biol.* **2001**, *20*, 293.
(451) Estroff, L. A.; Addadi, L.; Weiner, S.; Hamilton, A. D. *Organic Biomol. Chem.* **2004**, *2*, 137.
(452) Bica, C. I. D.; Borsali, R.; Geissler, E.; Rochas, C. *Macromolecules* **2001**, *34*, 5275.
(453) Lee, R. E.; Meeks, F. R. *J. Colloid Interface Sci.* **1971**, *35*, 584.
(454) Lefaucheux, F.; Robert, M. C.; Manghi, E. *J. Cryst. Growth* **1982**, *56*, 141.
(455) Garcia Ruiz, J. M. *J. Cryst. Growth* **1986**, *75*, 441.
(456) Yang, D.; Qi, L. M.; Ma, J. M. *Chem. Commun.* **2003**, 1180.
(457) Brown, S. J.; Elderfield, H. *Paleoceanography* **1996**, *11*, 543.
(458) Ryves, D. B.; Juggins, S.; Fritz, S. C.; Battarbee, R. W. *Palaeogeogr., Palaeoclimatol., Palaeoecol.* **2001**, *172*, 99.
(459) Kennish, M. J.; Lutz, R. A. *Palaeogeogr., Palaeoclimatol., Palaeoecol.* **1999**, *154*, 293.
(460) Li, H. Y.; Estroff, L. A. *J. Am. Chem. Soc.* **2007**, *129*, 5480.
(461) Falini, G.; Gazzano, M.; Ripamonti, A. *J. Mater. Chem.* **2000**, *10*, 535.
(462) Putnis, A.; Prieto, M.; Fernandezdiaz, L. *Geol. Mag.* **1995**, *132*, 1.
(463) Kniep, R.; Busch, S. *Angew. Chem., Int. Ed.* **1996**, *35*, 2624.
(464) Busch, S.; Dolhaine, H.; DuChesne, A.; Heinz, S.; Hochrein, O.; Laeri, F.; Podebrad, O.; Vietze, U.; Weiland, T.; Kniep, R. *Eur. J. Inorg. Chem.* **1999**, 1643.
(465) Busch, S. Selbstorganisation und Morphogenese von Apatit-Gelatine-Kompositen unter biomimetischen Bedingungen. Ph.D. Dissertation, Technische Universität Darmstadt, Darmstadt, Germany, 1998.
(466) Busch, S.; Schwarz, U.; Kniep, R. *Adv. Funct. Mater.* **2003**, *13*, 189.
(467) Simon, P.; Carrillo-Cabrera, W.; Formanek, P.; Gobel, C.; Geiger, D.; Ramlau, R.; Tlatlik, H.; Buder, J.; Kniep, R. *J. Mater. Chem.* **2004**, *14*, 2218.
(468) Busch, S.; Schwarz, U.; Kniep, R. *Chem. Mater.* **2001**, *13*, 3260.
(469) Kniep, R. In *Facetten einer Wissenschaft*; Müller, A., Quadbeck-Seeger, H. J., Diemann, E., Eds.; Wiley-VCH: Weinheim, Germany, 2004; p 221.
(470) Simon, P.; Schwarz, U.; Kniep, R. *J. Mater. Chem.* **2005**, *15*, 4992.
(471) Volkert, C. A.; Busch, S.; Heiland, B.; Dehm, G. *J. Microsc.* **2004**, *214*, 208.
(472) Tlatlik, H.; Simon, P.; Kawska, A.; Zahn, D.; Kniep, R. *Angew. Chem., Int. Ed.* **2006**, *45*, 1905.
(473) Kniep, R.; Simon, P. In *Biomineralization I: Crystallization and Self-Organization Process*; Topics in Current Chemistry; Springer-Verlag: Berlin, 2007; Vol. 270, p 73.
(474) Zhan, J. H.; Lin, H. P.; Mou, C. Y. *Adv. Mater.* **2003**, *15*, 621.
(475) Grassmann, O.; Lobmann, P. *Chem.—Eur. J.* **2003**, *9*, 1310.
(476) Oaki, Y.; Hayashi, S.; Imai, H. *Chem. Commun.* **2007**, 2841.
(477) Sethmann, I.; Helbig, U.; Worheide, G. *CrystEngComm* **2007**, *9*, 1262.
(478) Li, H. Y.; Estroff, L. A. *CrystEngComm* **2007**, *9*, 1153.
(479) Mukkamala, S. B.; Anson, C. E.; Powell, A. K. *J. Inorg. Biochem.* **2006**, *100*, 1128.
(480) Lee, I.; Han, S. W.; Choi, H. J.; Kim, K. *Adv. Mater.* **2001**, *13*, 1617.
(481) Mukkamala, S. B.; Powell, A. K. *Chem. Commun.* **2004**, 918.
(482) Zhang, Z. P.; Gao, D. M.; Zhao, H.; Xie, C. G.; Guan, G. J.; Wang, D. P.; Yu, S. H. *J. Phys. Chem. B* **2006**, *110*, 8613.
(483) Donnet, M.; Bowen, P.; Jongen, N.; Lemaitre, J.; Hofmann, H. *Langmuir* **2005**, *21*, 100.
(484) Sugawara, A.; Ishii, T.; Kato, T. *Angew. Chem., Int. Ed.* **2003**, *42*, 5299.
(485) Sakamoto, T.; Oichi, A.; Sugawara, A.; Kato, T. *Chem. Lett.* **2006**, *35*, 310.
(486) Kato, T.; Suzuki, T.; Irie, T. *Chem. Lett.* **2000**, 186.
(487) Kato, T.; Suzuki, T.; Amamiya, T.; Irie, T.; Komiyama, M.; Yui, H. *Supramol. Sci* **1998**, *5*, 411.
(488) Hosoda, N.; Kato, T *Chem. Mater.* **2001**, *13*, 688.
(489) Sugawara, A.; Kato, T. *Chem. Commun.* **2000**, 487.
(490) Hosoda, N.; Sugawara, A.; Kato, T *Macromolecules* **2003**, *36*, 6449.
(491) Sugawara, A.; Kato, T. *Compos. Interfaces* **2004**, *11*, 287.
(492) Naka, K. *Top. Curr. Chem.* **2003**, *228*, 141.
(493) Keum, D. K.; Naka, K.; Chujo, Y. *Bull. Chem. Soc. Jpn.* **2003**, *76*, 1687.
(494) Naka, K.; Tanaka, Y.; Chujo, Y. *Langmuir* **2002**, *18*, 3655.
(495) Lei, M.; Tang, W. H.; Cao, L. Z.; Li, P. G.; Yu, J. G. *J. Cryst. Growth* **2006**, *294*, 358.
(496) Jada, J.; Verraes, A. *Colloids Surf., A* **2003**, *219*, 7.
(497) Ji, X.; Li, G.; Huang, X. *Mater. Lett.* **2008**, *62*, 751.
(498) Sugawara, T.; Suwa, Y.; Ohkawa, K.; Yamamoto, H. *Macromol. Rapid Commun.* **2003**, *24*, 847.
(499) Yamamoto, H.; Yamaguchi, M.; Sugawara, T.; Suwa, Y.; Ohkawa, K.; Shinji, H.; Kurata, S. In *Bioceramics 16*; Key Engineering Materials Series; Trans Tech Publications Ltd.: Zurich-Uetikon, Switzerland, 2004; Vol. 254-2, pp 603−606.
(500) Hayashi, S.; Ohkawa, K.; Suwa, Y.; Sugawara, T.; Asami, T.; Yamamoto, H. *Macromol. Biosci.* **2008**, *8*, 46.
(501) Glaab, F.; Kellermeier, M.; Kunz, W. *Macromol. Rapid Commun.* **2007**, *28*, 1024.
(502) Hardikar, V. V.; Matijevic, E. *Colloids Surf., A* **2001**, *186*, 23.
(503) Shen, F. H.; Feng, Q. L.; Wang, C. M. *J. Cryst. Growth* **2002**, *242*, 239.
(504) Li, C. M.; Botsaris, G. D.; Kaplan, D. L. *Cryst. Growth Des.* **2002**, *2*, 387.
(505) Sedlák, M.; Cölfen, H. *Macromol. Chem. Phys.* **2001**, *202*, 587.
(506) Kaluzynski, K.; Pretula, J.; Penczek, S. *J. Polym. Sci., Part A: Polym. Chem.* **2007**, *45*, 90.
(507) Cölfen, H.; Qi, L. *Chem.—Eur. J.* **2001**, *7*, 106.
(508) Yu, S.-H.; Cölfen, H.; Hartmann, J.; Antonietti, M. *Adv. Funct. Mater.* **2002**, *12*, 541.
(509) Napper. D. H. *Polymeric stabilization of colloidal dispersions*; Academic Press: New York, Paris, San Diego, San Francisco, Sao Paulo, Sydney, Tokyo, Toronto, 1983; pp 1−30.
(510) Cölfen, H.; Antonietti, M. *Langmuir* **1998**, *14*, 582.
(511) Marentette, J. M.; Norwig, J.; Stockelmann, E.; Meyer, W. H.; Wegner, G. *Adv. Mater.* **1997**, *9*, 647.
(512) Kasparova, P.; Antonietti, M.; Cölfen, H. *Colloids Surf., A* **2003**, *250*, 153.
(513) Evans, J. S. *Curr. Opin. Colloid Interface Sci.* **2003**, *8*, 48.
(514) Gao, Y. X.; Yu, S. H; Cong, H. P.; Jiang, J.; Xu, A. W.; Dong, W. F.; Cölfen, H. *J. Phys. Chem. B* **2006**, *110*, 6432.
(515) Qi, L.; Li, J.; Ma, J. *Adv. Mater.* **2002**, *14*, 300.
(516) Kuther, J.; Seshadri, R.; Nelles, G.; Assenmacher, W.; Butt, H. J.; Mader, W.; Tremel, W. *Chem. Mater.* **1999**, *11*, 1317.
(517) Küther, J.; Seshadri, R.; Tremel, W. *Angew. Chem., Int. Ed.* **1998**, *37*, 3044.
(518) Gao, Y. X.; Yu, S. H.; Guo, X. H. *Langmuir* **2006**, *22*, 6125.
(519) Basko, M.; Kubisa, P. *Macromolecules* **2002**, *35*, 8948.
(520) Basko, M.; Kubisa, P. *J. Polym. Sci., Part A: Polym. Chem.* **2004**, *42*, 1189.
(521) Guillemet, B.; Faatz, M.; Gröhn, F.; Wegner, G.; Gnanou, Y. *Langmuir* **2006**, *22*, 1875.
(522) Gehrke, N.; Nassif, N.; Pinna, N.; Antonietti, M.; Gupta, H. S.; Cölfen, H. *Chem. Mater.* **2005**, *17*, 6514.
(523) Li, M.; Mann, S. *Adv. Funct. Mater.* **2002**, *12*, 773.
(524) Li, M.; Lebeau, B.; Mann, S. *Adv. Mater.* **2003**, *15*, 2032.
(525) Zhang, H.; Cooper, A. I. *Adv. Mater.* **2007**, *19*, 1529.
(526) Deville, S.; Saiz, E.; Nalla, R. K.; Tomsia, A. P. *Science* **2006**, *311*, 515.
(527) Gutierrez, M. C.; Ferrer, M. L.; del Monte, F. *Chem. Mater.* **2008**, *20*, 634.
(528) Stein, A.; Li, F.; Denny, N. R. *Chem. Mater.* **2008**, *20*, 649.
(529) Yan, H.; Blanford, C. F.; Holland, B. T.; Smyrl, W. H.; Stein, A. *Chem. Mater.* **2000**, *12*, 1134.

(530) Holland, B. T.; Blanford, C. F.; Do, T.; Stein, A. *Chem. Mater.* **1999**, *11*, 795.
(531) Caruso, R. A. *Angew. Chem., Int. Ed.* **2004**, *43*, 2746.
(532) Walsh, D.; Mann, S. *Nature* **1995**, *377*, 320.
(533) Walsh, D.; Mann, S. *Adv. Mater.* **1997**, *9*, 658.
(534) Hall, S. R.; Bolger, H.; Mann, S. *Chem. Commun.* **2003**, 2784.
(535) Meldrum, F. C.; Seshadri, R. *Chem. Commun.* **2000**, 29.
(536) Seshadri, R.; Meldrum, F. C. *Adv. Mater.* **2000**, *12*, 1149.
(537) Yue, W.; Park, R. J.; Kulak, A. N.; Meldrum, F. C. *J. Cryst. Growth* **2006**, *294*, 69.
(538) Ha, Y. H.; Vaia, R. A.; Lynn, W. F.; Costantino, J. P.; Shin, J.; Smith, A. B.; Matsudaira, P. T.; Thomas, E. L. *Adv. Mater.* **2004**, *16*, 1091.
(539) Shin, Y.; Exarhos, G. J. *Cellulose* **2007**, *14*, 269.
(540) Shin, Y. S.; Liu, J.; Chang, J. H.; Nie, Z. M.; Exarhos, G. *Adv. Mater.* **2001**, *13*, 728.
(541) Rambo, C. R.; Andrade, T.; Fey, T.; Sieber, H.; Martinelli, A. E.; Greil, P. *J. Am. Ceram. Soc.* **2008**, *91*, 852.
(542) Greil, P. *J. Eur. Ceram. Soc.* **2001**, *21*, 105.
(543) Mahler, W.; Bechtold, M. F. *Nature* **1980**, *285*, 27.
(544) Nishihara, H.; Mukai, S. R.; Fujii, Y.; Tago, T.; Masuda, T.; Tamon, H. *J. Mater. Chem.* **2006**, *16*, 3231.
(545) Mukai, S. R.; Nishihara, H.; Shichi, S.; Tamon, H. *Chem. Mater.* **2004**, *16*, 4987.
(546) Kokubo, T.; Teranishi, Y.; Maki, T.; Sakka, S. *J. Mater. Sci.* **1988**, *23*, 1126.
(547) Maki, T.; Sakka, S. *J. Non-Cryst. Solids* **1986**, *82*, 239.
(548) Pileni, M. P. *Langmuir* **1997**, *13*, 3266.
(549) Eastoe, J.; Hollamby, M. J.; Hudson, L. *Adv. Colloid Interface Sci.* **2006**, *128*, 5.
(550) Kandori, K.; Kon-no, K.; Kitahara, A. *J. Colloid Interface Sci.* **1987**, *115*, 579.
(551) Kandori, K.; Kon-no, K.; Kitahara, A. *J. Colloid Interface Sci.* **1988**, *122*, 78.
(552) Buchold, D. H. M.; Feldmann, C. *Adv. Funct. Mater.* **2008**, *18*, 1002.
(553) Rauscher, F.; Veit, P.; Sundmacher, K. *Colloids Surf., A* **2005**, *254*, 183.
(554) Liu, D. X.; Yates, M. Z. *Langmuir* **2006**, *22*, 5566.
(555) Viravaidya, C.; Li, M.; Mann, S. *Chem. Commun.* **2004**, 2182.
(556) Sindhu, S.; Jegadesan, S.; Leong, R. A. E.; Valiyaveettil, S. *Cryst. Growth Des.* **2006**, *6*, 1537.
(557) Thachepan, S.; Li, M.; Davis, S. A.; Mann, S. *Chem. Mater.* **2006**, *18*, 3557.
(558) Walsh, D.; Hopwood, J. D; Mann, S. *Science* **1994**, *264*, 1576.
(559) Rajagopalan, S.; Robb, R. A. *Med. Image Anal.* **2006**, *10*, 693.
(560) Davis, S. A.; Burkett, S. L.; Mendelson, N. H. *Nature* **1997**, *385*, 420.
(561) Liu, S. T.; Wood, L. F.; Ohman, D. E.; Collinson, M. M. *Chem. Mater.* **2007**, *19*, 2752.
(562) Kim, Y. *Biomacromolecules* **2003**, *4*, 908.
(563) Liu, Z.; Fan, T.; Zhang, W.; Zhang, D. *Microporous Mesoporous Mater.* **2005**, *85*, 82.
(564) Sieber, H.; Rambo, C.; Cao, J.; Vogli, E.; Greil, P. In *Euro Ceramics VII, Pt. 1−3*; Key Engineering Materials Series; Trans Tech Publications Ltd.: Zurich-Uetikon, Switzerland, 2002; Vol. 206-2, pp 2009−2012.
(565) Zampieri, A.; Sieber, H.; Selvam, T.; Mabande, G. T. P.; Schwieger, W.; Scheffler, F.; Scheffler, M.; Greil, P. *Adv. Mater.* **2005**, *17*, 344.
(566) Unocic, R. R.; Zalar, F. M.; Sarosi, P. M.; Sandhage, K. H. *Chem. Commun.* **2004**, 796.
(567) Weatherspoon, M. R.; Allan, S. M.; Hunt, E.; Cai, Y.; Sandhage, K. H. *Chem. Commun.* **2005**, 651.
(568) Zhao, J. P.; Gaddis, C. S.; Cai, Y.; Sandhage, K. H. *J. Mater. Res.* **2005**, *20*, 282.
(569) Kusari, U.; Bao, Z.; Cai, Y.; Ahmad, G.; Sandhage, K. H.; Sneddon, L. G. *Chem. Commun.* **2007**, 1177.
(570) Cook, G.; Timms, P. L.; Göltner-Spickerman, C. *Angew. Chem., Int. Ed.* **2003**, *42*, 557.
(571) Yu, S. H.; Cölfen, H.; Tauer, K.; Antonietti, M. *Nat. Mater.* **2005**, *4*, 51.
(572) Oaki, Y.; Imai, H. *Langmuir* **2005**, *21*, 863.
(573) Oaki, Y.; Imai, H. *J. Am. Chem. Soc.* **2004**, *126*, 9271.
(574) Falini, G.; Gazzano, M.; Ripamonti, A. *Adv. Mater.* **1994**, *6*, 46.
(575) Falini, G.; Fermani, S.; Gazzano, M.; Ripamonti, A. *Chem.—Eur. J.* **1998**, *4*, 1048.
(576) Falini, G.; Fermani, S.; Gazzano, M.; Ripamonti, A. *J. Chem. Soc., Dalton Trans.* **2000**, 3983.
(577) Wada, N.; Okazaki, M.; Tachikawa, S. *J. Cryst. Growth* **1993**, *132*, 115.
(578) Wada, N.; Yamashita, K.; Umegaki, T. *J. Colloid Interface Sci.* **1998**, *201*, 1.
(579) Wada, N.; Yamashita, K.; Umegaki, T. *J. Colloid Interface Sci.* **1999**, *212*, 357.
(580) Garcia Ruiz, J. M.; Hyde, S. T.; Carnerup, A. M.; Christy, A. G.; Van Kranendonk, M. J.; Welham, N. J. *Science* **2003**, *302*, 1194.
(581) Hyde, S. T.; Carnerup, A. M.; Larsson, A. K.; Christy, A. G.; Garcia-Ruiz, J. M. *Physica A* **2004**, *339*, 24.
(582) Garcia Ruiz, J. M.; Amoros, J. L. *Bull. Mineral.* **1981**, *104*, 107.
(583) Garcia Ruiz, J. M.; Carnerup, A. M.; Christy, A. G.; Welham, N. J.; Hyde, S. T. *Astrobiology* **2002**, *2*, 353.
(584) Herrera, A. L. *Mem. Rev. Soc. Cient. "Antonio Alzate"* **1912**, *32*, 345.
(585) Garcia Ruiz, J. M.; Amoros, J. L. *J. Cryst. Growth* **1981**, *55*, 379.
(586) Baird, T.; Braterman, P. S.; Chen, P.; Garciaruiz, J. M.; Peacock, R. D.; Reid, A. *Mater. Res. Bull.* **1992**, *27*, 1031.
(587) Hyde, S. T.; Garcia-Ruiz, J. M. *Act. Chim.* **2004**, 4.
(588) Garcia Ruiz, J. M.; Moreno, A. *Anal. Quim. Int. Ed.* **1997**, *93*, 1.
(589) Garcia Ruiz, J. M.; Moreno, A. *J. Cryst. Growth* **1985**, *73*, 251.
(590) Reyes-Grajeda, J. P.; Jauregui-Zuniga, D.; Batina, N.; Salomon-Salazar, M.; Moreno, A. *J. Cryst. Growth* **2002**, *234*, 227.
(591) Terada, T.; Yamabi, S.; Imai, H. *J. Cryst. Growth* **2003**, *253*, 435.
(592) Garcia Ruiz, J. M. *Geology* **1998**, *26*, 843.
(593) Carnerup, A. M. Biomorphs: Morphology, chemistry, and implications for the identification of early life Ph.D. Dissertation, University of Canberra, Canberra, Australia, 2007.
(594) Bittarello, E.; Aquilano, D. *Eur. J. Mineral.* **2007**, *19*, 345.
(595) Voinescu, A. E.; Kellermeier, M.; Carnerup, A. M.; Larsson, A. K.; Touraud, D.; Hyde, S. T.; Kunz, W. *J. Cryst. Growth* **2007**, *306*, 152.
(596) Garcia Ruiz, J. M. In Origins of Life and Evolution of the Biosphere; Kluwer Academic Publishers: Dordrecht, The Netherlands, 1994; Vol. 24, p 451.
(597) Dominguez Bella, S.; Garcia-Ruiz, J. M. *J. Cryst. Growth* **1986**, *79*, 236.
(598) Imai, H.; Terada, T.; Yamabi, S. *Chem. Commun.* **2003**, 484.
(599) Imai, H.; Terada, T.; Miura, T.; Yamabi, S. *J. Cryst. Growth* **2002**, *244*, 200.
(600) Lopez, P. J.; Gautier, C.; Livage, J.; Coradin, T. *Curr. Nanosci.* **2005**, *1*, 73.
(601) Lu, A. H.; Schuth, F. *Adv. Mater.* **2006**, *18*, 1793.
(602) Caruso, R. A.; Antonietti, M. *Chem. Mater.* **2001**, *13*, 3272.
(603) Patwardhan, S. V.; Clarson, S. J.; Perry, C. C. *Chem. Commun.* **2005**, 1113.
(604) van Bommel, K. J. C.; Friggeri, A.; Shinkai, S. *Angew. Chem., Int. Ed.* **2003**, *42*, 980.
(605) Yuan, Z.-H.; Su, B.-L. *J. Mater. Chem.* **2006**, *16*, 663.
(606) Caruso, F.; Caruso, R. A.; Mohwald, H. *Science* **1998**, *282*, 1111.
(607) Caruso, F. *Chem.—Eur. J.* **2000**, *6*, 413.
(608) Iskandar, F.; Mikrajuddin; Okuyama, K. *Nano Lett.* **2001**, *1*, 231.
(609) Zoldesi, C. I.; Imhof, A. *Adv. Mater.* **2005**, *17*, 924.
(610) Fujiwara, M.; Shiokawa, K.; Sakakura, I.; Nakahara, Y. *Nano Lett.* **2006**, *6*, 2925.
(611) Sun, Y.; Mayers, B.; Xia, Y. *Adv. Mater.* **2003**, *15*, 641.
(612) Sun, Q.; Magusin, P.; Mezari, B.; Panine, P.; van Santen, R. A.; Sommerdiik, N. A. J. M. *J. Mater. Chem.* **2005**, *15*, 256.
(613) Botterhuis, N. E.; Sun, Q. Y.; Magusin, P.; van Santen, R. A.; Sommerdijk, N. A. J. M. *Chem.—Eur. J.* **2006**, *12*, 1448.
(614) Sun, Q. Y.; Kooyman, P. J.; Grossmann, J. G.; Bomans, P. H. H.; Frederik, P. M.; Magusin, P. C. M. M.; Beelen, T. P. M.; van Santen, R. A.; Sommerdijk, N. A. J. M. *Adv. Mater.* **2003**, *15*, 1097.
(615) Cho, Y.-S.; Yi, G.-R.; Kim, S.-H.; Jeon, S.-J.; Elsesser, M. T.; Yu, H. K.; Yang, S. M.; Pine, D. *Chem. Mater.* **2007**, *19*, 3183.
(616) Wang, J. G.; Xiao, Q.; Zhou, H. J.; Sun, P. C.; Yuan, Z. Y.; Li, B. H.; Ding, D. T.; Shi, A. C.; Chen, T. H. *Adv. Mater.* **2006**, *18*, 3284.
(617) Zhao, Q. C.; Chen, W. M.; Zhu, Q. R. *Nanotechnology* **2004**, *15*, 958.
(618) Zhou, F.; Li, S.; Vo, C. D.; Yuan, J. J.; Chai, S.; Gaol, Q.; Armes, S. P.; Lu, C.; Cheng, S. *Langmuir* **2007**, *23*, 9737.
(619) Shiomi, T.; Tsunoda, T.; Kawai, A.; Mizukami, F.; Sakaguchi, K. *Chem. Commun.* **2007**, 4404.
(620) Tanev, P. T.; Pinnavaia, T. J. *Science* **1996**, *271*, 1267.
(621) Hubert, D. H. W.; Jung, M.; Frederik, P. M.; Bomans, P. H. H.; Meuldijk, J.; German, A. L. *Adv. Mater.* **2000**, *12*, 1286.
(622) Hentze, H. P.; Raghavan, S. R.; McKelvey, C. A.; Kaler, E. W. *Langmuir* **2003**, *19*, 1069.
(623) Lootens, D.; Vautrin, C.; Van Damme, H.; Zemb, T. *J. Mater. Chem.* **2003**, *13*, 2072.
(624) Yu, M. H.; Wang, H. N.; Zhou, X. F.; Yuan, P.; Yu, C. Z. *J. Am. Chem. Soc.* **2007**, *129*, 14576.
(625) Wang, H. N.; Wang, Y. H.; Zhou, X.; Zhou, L.; Tang, J.; Lei, J.; Yu, C. *Adv. Funct. Mater.* **2007**, *17*, 613.
(626) Yuan, J. J.; Mykhaylyk, O. O.; Ryan, A. J.; Armes, S. P. *J. Am. Chem. Soc.* **2007**, *129*, 1717.
(627) Stein, A. *Microporous Mesoporous Mater.* **2001**, *44*, 227.

(628) Hoa, M. L. K.; Lu, M. H.; Zhang, Y. *Adv. Colloid Interf. Sci.* **2006**, *121*, 9.
(629) Zhang, H. F.; Cooper, A. I. *Soft Matter* **2005**, *1*, 107.
(630) Imhof, A.; Pine, D. J. *Adv. Mater.* **1998**, *10*, 697.
(631) Imhof, A.; Pine, D. J. *Nature* **1997**, *389*, 948.
(632) Yi, G. R.; Yang, S. M. *Chem. Mater.* **1999**, *11*, 2322.
(633) Binks, B. P. *Adv. Mater.* **2002**, *14*, 1824.
(634) Zhang, H. F.; Hardy, G. C.; Rosseinsky, M. J.; Cooper, A. I. *Adv. Mater.* **2003**, *15*, 78.
(635) Sen, T.; Tiddy, G. J. T.; Cascic, J. L.; Anderson, M. W. *Chem. Commun.* **2003**, 2182.
(636) Sen, T.; Tiddy, G. J. T.; Casci, J. L.; Anderson, M. W. *Microporous Mesoporous Mater.* **2005**, *78*, 255.
(637) Zhang, H.; Hardy, G. C.; Khimyak, Y. Z.; Rosseinsky, M. J.; Cooper, A. I. *Chem. Mater.* **2004**, *16*, 4245.
(638) Maekawa, H.; Esquena, J.; Bishop, S.; Solans, C.; Chmelka, B. F. *Adv. Mater.* **2003**, *15*, 591.
(639) Velev, O. D.; Kaler, E. W. *Adv. Mater.* **2000**, *12*, 531.
(640) Stein, A.; Schroden, R. C. *Curr. Opin. Solid State Mater. Sci.* **2001**, *5*, 553.
(641) Carbajo, M. C.; Gomez, A.; Torralvo, M. J.; Enciso, E. *J. Mater. Chem.* **2002**, *12*, 2740.
(642) Velev, O. D.; Jede, T. A.; Lobo, R. F.; Lenhoff, A. M. *Chem. Mater.* **1998**, *10*, 3597.
(643) Villaescusa, L. A.; Mihi, A.; Rodriguez, I.; Garcia-Bennett, A. E.; Miguez, H. *J. Phys. Chem. B* **2005**, *109*, 19643.
(644) Wang, Z. Y.; Stein, A. *Chem. Mater.* **2008**, *20*, 1029.
(645) Luo, Q.; Li, L.; Yang, B.; Zhao, D. *Chem. Lett.* **2000**, 378.
(646) Wang, J.; Li, Q.; Knoll, W.; Jonas, U. *J. Am. Chem. Soc.* **2006**, *128*, 15606.
(647) Yang, P. D.; Deng, T.; Zhao, D. Y.; Feng, P. Y.; Pine, D.; Chmelka, B. F.; Whitesides, G. M.; Stucky, G. D. *Science* **1998**, *282*, 2244.
(648) Oh, C. G.; Baek, Y. Y.; Ihm, S. K. *Adv. Mater.* **2005**, *17*, 270.
(649) Lukens, W. W.; Yang, P. D.; Stucky, G. D. *Chem. Mater.* **2001**, *13*, 28.
(650) Vaudreuil, S.; Bousmina, M.; Kaliaguine, S.; Bonneviot, L. *Adv. Mater.* **2001**, *13*, 1310.
(651) Caruso, R. A.; Antonietti, M. *Adv. Funct. Mater.* **2002**, *12*, 307.
(652) Huerta, L.; Guillem, C.; Latorre, J.; Beltran, A.; Beltran, D.; Amoros, P. *Chem. Commun.* **2003**, 1448.
(653) Zhang, B. J.; Davis, S. A.; Mann, S. *Chem. Mater.* **2002**, *14*, 1369.
(654) Dujardin, E.; Blaseby, M.; Mann, S. *J. Mater. Chem.* **2003**, *13*, 696.
(655) Sims, S. D.; Walsh, D.; Mann, S. *Adv. Mater.* **1998**, *10*, 151.
(656) Mukai, S. R.; Nishihara, H.; Tamon, H. *Chem. Commun.* **2004**, 874.
(657) Nishihara, H.; Mukai, S. R.; Yamashita, D.; Tamon, H. *Chem. Mater.* **2005**, *17*, 683.
(658) Gautier, C.; Lopez, P. J.; Hemadi, M.; Livage, J.; Coradin, T. *Langmuir* **2006**, *22*, 9092.
(659) Wang, D. H.; Kou, R.; Yang, Z. L.; He, J. B.; Yang, Z. Z.; Lu, Y. F. *Chem. Commun.* **2005**, 166.
(660) Yang, Z. L.; Niu, Z. W.; Cao, X. Y.; Yang, Z. Z.; Lu, Y. F.; Hu, Z. B.; Han, C. C. *Angew. Chem., Int. Ed.* **2003**, *42*, 4201.
(661) Wu, Y. Y.; Cheng, G. S.; Katsov, K.; Sides, S. W.; Wang, J. F.; Tang, J.; Fredrickson, G. H.; Moskovits, M.; Stucky, G. D. *Nat. Mater.* **2004**, *3*, 816.
(662) Gautier, C.; Lopez, P. J.; Livage, J.; Coradin, T. *J. Colloid Interface Sci.* **2007**, *309*, 44.
(663) Lu, Q. Y.; Gao, F.; Komarneni, S.; Mallouk, T. E. *J. Am. Chem. Soc.* **2004**, *126*, 8650.
(664) Kickelbick, G. *Small* **2005**, *1*, 168.
(665) Yamaguchi, A.; Uejo, F.; Yoda, T.; Uchida, T.; Tanamura, Y.; Yamashita, T.; Teramae, N. *Nat. Mater.* **2004**, *3*, 337.
(666) Chae, W. S.; Braun, P. V. *Chem. Mater.* **2007**, *19*, 5593.
(667) Li, F.; Wang, Z. Y.; Ergang, N. S.; Fyfe, C. A.; Stein, A. *Langmuir* **2007**, *23*, 3996.
(668) Foo, C. W. P.; Huang, J.; Kaplan, D. L. *Trends Biotechnol.* **2004**, *22*, 577.
(669) Cha, J. N.; Stucky, G. D.; Morse, D. E.; Deming, T. J. *Nature* **2000**, *403*, 289.
(670) Jan, J. S.; Lee, S. J.; Carr, C. S.; Shantz, D. F. *Chem. Mater.* **2005**, *17*, 4310.
(671) Jan, J. S.; Shantz, D. F. *Adv. Mater.* **2007**, *19*, 2951.
(672) Tomczak, M. M.; Glawe, D. D.; Drummy, L. F.; Lawrence, C. G.; Stone, M. O.; Perry, C. C.; Pochan, D. J.; Deming, T. J.; Naik, R. R. *J. Am. Chem. Soc.* **2005**, *127*, 12577.
(673) Patwardhan, S. V.; Mukherjee, N.; Steinitz-Kannan, M.; Clarson, S. J. *Chem. Commun.* **2003**, 1122.
(674) McKenna, B. J.; Birkedal, H.; Bartl, M. H.; Deming, T. J.; Stucky, G. D. *Angew. Chem., Int. Ed.* **2004**, *43*, 5652.
(675) van Bommel, K. J. C.; Jung, J. H.; Shinkai, S. *Adv. Mater.* **2001**, *13*, 1472.
(676) Rodriguez, F.; Glawe, D. D.; Naik, R. R.; Hallinan, K. P.; Stone, M. O. *Biomacromolecules* **2004**, *5*, 261.
(677) Patwardhan, S. V.; Maheshwari, R.; Mukherjee, N.; Kiick, K. L.; Clarson, S. J. *Biomacromolecules* **2006**, *7*, 491.
(678) Hawkins, K. M.; Wang, S. S. S.; Ford, D. M.; Shantz, D. F. *J. Am. Chem. Soc.* **2004**, *126*, 9112.
(679) Bellomo, E. G.; Deming, T. J. *J. Am. Chem. Soc.* **2006**, *128*, 2276.
(680) Meegan, J. E.; Aggeli, A.; Boden, N.; Brydson, R.; Brown, A. P.; Carrick, L.; Brough, A. R.; Hussain, A.; Ansell, R. J. *Adv. Funct. Mater.* **2004**, *14*, 31.
(681) Yuwono, V. M.; Hartgerink, J. D. *Langmuir* **2007**, *23*, 5033.
(682) Ji, Q.; Iwaura, R.; Shimizu, T. *Chem. Mater.* **2007**, *19*, 1329.
(683) Kessel, S.; Thomas, A.; Börner, H. G. *Angew. Chem., Int. Ed.* **2007**, *46*, 9023.
(684) Kessel, S.; Börner, H. G. *Macromol. Rapid Commun.* **2008**, *29*, 316.
(685) Yang, Y. G.; Suzuki, M.; Owa, S.; Shirai, H.; Hanabusa, K. *J. Mater. Chem.* **2006**, *16*, 1644.
(686) Yang, Y. G.; Suzuki, M.; Owa, S.; Shirai, H.; Hanabusa, K. *Chem. Commun.* **2005**, 4462.
(687) Jin, R. H.; Yuan, J. J. *Chem. Commun.* **2005**, 1399.
(688) Yuan, J. J.; Jin, R. H. *Adv. Mater.* **2005**, *17*, 885.
(689) Ono, Y.; Nakashima, K.; Sano, M.; Kanekiyo, Y.; Inoue, K.; Hojo, J.; Shinkai, S. *Chem. Commun.* **1998**, 1477.
(690) Ono, Y.; Nakashima, K.; Sano, M.; Hojo, J.; Shinkai, S. *Chem. Lett.* **1999**, 1119.
(691) Ono, Y.; Nakashima, K.; Sano, M.; Hojo, J.; Shinkai, S. *J. Mater. Chem.* **2001**, *11*, 2412.
(692) Jung, J. H.; Ono, Y.; Shinkai, S. *J. Chem. Soc., Perkin Trans.* **1999**, 1289.
(693) Jung, J. H.; Kobayashi, H.; Masuda, M.; Shimizu, T.; Shinkai, S. *J. Am. Chem. Soc.* **2001**, *123*, 8785.
(694) Jung, J. H.; Ono, Y.; Shinkai, S. *Chem. Lett.* **2000**, 636.
(695) Jung, J. H.; Shinkai, S. *J. Chem. Soc., Perkin Trans.* **2000**, 2393.
(696) Jung, J. H.; Ono, Y.; Shinkai, S. *Chem.—Eur. J.* **2000**, *6*, 4552.
(697) Jung, J. H.; Ono, Y.; Hanabusa, K.; Shinkai, S. *J. Am. Chem. Soc.* **2000**, *122*, 5008.
(698) Kuang, M.; Wang, D. Y.; Gao, M. Y.; Hartmann, J.; Möhwald, H. *Chem. Mater.* **2005**, *17*, 656.
(699) Zhang, G.; Wang, D. Y.; Gu, Z. Z.; Hartmann, J.; Möhwald, H. *Chem. Mater.* **2005**, *17*, 5268.
(700) Gorna, K.; Munoz-Espi, R.; Grohn, F.; Wegner, G. *Macromol. Biosci.* **2007**, *7*, 163.
(701) Huang, S. C.; Naka, K.; Chujo, Y. *Langmuir* **2007**, *23*, 12086.
(702) Uwins, P. J. R.; Webb, R. I.; Taylor, A. P. *Am. Mineral.* **1998**, *83*, 1541.
(703) McKay, D. S.; Gibson, E. K.; ThomasKeprta, K. L.; Vali, H.; Romanek, C. S.; Clemett, S. J.; Chillier, X. D. F.; Maechling, C. R.; Zare, R. N. *Science* **1996**, *273*, 924.

CR8002856